Experimental Verification of a Cracked Fuel Mechanical Model

Prepared by R. E. Williford

Pacific Northwest Laboratory
Operated by
Battelle Memorial Institute

Availability of Reference Materials Cited in NRC Publications

Most documents cited in NRC publications will be available from one of the following sources:

1. The NRC Public Document Room, 1717 H Street, N.W.
    Washington, DC 20555

2. The NRC/GPO Sales Program, U.S. Nuclear Regulatory Commission,
    Washington, DC 20555

3. The National Technical Information Service, Springfield, VA 22161

Although the listing that follows represents the majority of documents cited in NRC publications, it is not intended to be exhaustive.

Referenced documents available for inspection and copying for a fee from the NRC Public Document Room include NRC correspondence and internal NRC memoranda; NRC Office of Inspection and Enforcement bulletins, circulars, information notices, inspection and investigation notices; Licensee Event Reports; vendor reports and correspondence; Commission papers; and applicant and licensee documents and correspondence.

The following documents in the NUREG series are available for purchase from the NRC/GPO Sales Program: formal NRC staff and contractor reports, NRC-sponsored conference proceedings, and NRC booklets and brochures. Also available are Regulatory Guides, NRC regulations in the *Code of Federal Regulations*, and *Nuclear Regulatory Commission Issuances*.

Documents available from the National Technical Information Service include NUREG series reports and technical reports prepared by other federal agencies and reports prepared by the Atomic Energy Commission, forerunner agency to the Nuclear Regulatory Commission.

Documents available from public and special technical libraries include all open literature items, such as books, journal and periodical articles, and transactions. *Federal Register* notices, federal and state legislation, and congressional reports can usually be obtained from these libraries.

Documents such as theses, dissertations, foreign reports and translations, and non-NRC conference proceedings are available for purchase from the organization sponsoring the publication cited.

Single copies of NRC draft reports are available free upon written request to the Division of Technical Information and Document Control, U.S. Nuclear Regulatory Commission, Washington, DC 20555.

Copies of industry codes and standards used in a substantive manner in the NRC regulatory process are maintained at the NRC Library, 7920 Norfolk Avenue, Bethesda, Maryland, and are available there for reference use by the public. Codes and standards are usually copyrighted and may be purchased from the originating organization or, if they are American National Standards, from the American National Standards Institute, 1430 Broadway, New York, NY 10018.

GPO Printed copy price: $6.50

Experimental Verification of a Cracked Fuel Mechanical Model

Prepared by
R. E. Williford

Pacific Northwest Laboratory
P. O. Box 999
Richland, WA 99352

Experimental Verification
of a Cracked Fuel Mechanical
Model

Prepared by
R. E. Williford

Pacific Northwest Laboratory
P.O. Box 999
Richland, WA 99352

ABSTRACT

This report describes the results of a series of laboratory experiments conducted to independently verify a model that describes the nonlinear mechanical behavior of cracked fuel in pelletized UO_2/Zircaloy nuclear fuel rods under normal operating conditions. After a brief description of the analytical model, each experiment is discussed in detail.

Experiments were conducted to verify the general behavior and numerical values for the three primary independent modelling parameters (effective crack roughness, effective gap roughness, and total crack length), and to verify the model predictions that the effective Young's moduli for cracked fuel systems were substantially less than those for solid UO_2 pellets. In general, the model parameters and predictions were confirmed, and new insight was gained concerning the complexities of cracked fuel mechanics.

ABSTRACT

This report describes the results of a series of laboratory experiments conducted to independently verify a model that describes the nonlinear mechanical behavior of cracked fuel in pelletized UO_2/Zircaloy nuclear fuel rods under normal operating conditions. After a brief description of the analytical model, each experiment is discussed in detail.

Experiments were conducted to verify the general behavior and numerical values for the three primary independent modelling parameters (effective crack roughness, effective gap roughness, and total crack length), and to verify the model predictions that the effective Young's moduli for cracked fuel systems were substantially less than those for solid UO_2 pellets. In general, the model parameters and predictions were confirmed, and new insight was gained concerning the complexities of cracked fuel mechanics.

CONTENTS

FIGURES

TABLES

TABLES

1.0 SUMMARY

Thermally-induced cracking of fuel pellets occurs during the normal operation of nuclear fuel rods in reactor. This cracking causes some of the original fuel/cladding gap to be redistributed into the fuel in the form of cracks, and results in the fuel fragments moving radially outward to partially fill the gap (relocation). These fundamental changes in fuel geometry alter its bulk thermal and mechanical properties, and result in nonlinear behavior patterns as irradiation proceeds.

A model had been previously developed to describe this nonlinear behavior. The general approach was to model the cracked fuel in terms of effective Young's moduli and effective thermal conductivity. A basic assumption in this model was that these effective properties were controlled by the opening and closing of the fuel cracks, and thus that the fragments themselves behaved as rigid bodies. This appears justifiable for Light Water Reactors, where fuel temperatures are generally less than 1400°C.

This model of fuel behavior in terms of crack sizes required a suitable description of the cracks themselves. A "crack compliance" model was selected which related the crack width to the stress applied normal to the crack, the Meyer Hardness of the UO_2, and the effective roughnesses of the crack surfaces in contact. Thus fuel stresses could be related to average crack widths. The average crack width times the total crack length (in the transverse plane) determines the amount of crack void ("free area") within the fuel. The effective Young's moduli and effective thermal conductivity of the cracked fuel are related to this "free area." Also, fuel relocation is caused by the outward ratcheting of the fuel fragments, which results in an asymmetric fuel outer surface that is in partial contact with the cladding inner surface. The effective roughness concept was also used to describe the fuel outer surface, and thus the gap was considered as another crack.

In-reactor data from the NRC/PNL/Halden experiments IFA-431, IFA-432, and IFA-513 were analyzed with this cracked fuel model. The results were a series of predictions for the effective crack roughness (R_c), the effective gap roughness (R_g), the total crack lengths (L_{tc}), the effective Young's moduli, and the effective thermal conductivities for the cracked fuel systems of rods with a range of initial fuel/cladding gap sizes. A major result was that the effective moduli and conductivity for cracked fuel systems were significantly less than those for solid UO_2 pellets.

More recent efforts to quantify cracked fuel behavior have focused on the independent experimental verification of the above described model. A series of laboratory experiments was conducted to verify the values deduced for the three primary independent modelling parameters (R_c, R_g, L_{tc}), and to verify that the model results for reduced effective moduli were correct. The major results of these experiments are summarized below.

1

Single crack experiments performed on alumina samples verified the magnitude and behavior of effective crack roughnesses (R_c) estimated from in-reactor data. R_c decreases as crack width (free area) decreases or as stress increases, and also depends on crack surface macromorphology (waviness). Waviness also appears to control fragment rotations as the cracks close.

A laboratory simulation of cracked fuel relocation/fragment ratcheting mechanisms using alumina samples yielded effective gap roughnesses (R_g) that were twice the values deduced from in-reactor data. The distribution of relocated fuel outer surface asperities exhibited an extended tail for large asperities, a phenomenon that is suspected of occurring in reactor and may affect cladding stress concentrations or fuel failure analyses.

The total crack length (L_{tc} = 3.5 fuel diameters) in the transverse plane was verified by the quantitative optical analysis of post-irradiation-examination photomacrographs for 19 test reactor rods. It was also found that about 25% of "apparently closed" cracks may actively assist the "obviously open" cracks in reducing the effective modulus.

The reductions in effective moduli caused by fuel cracking were verified with a series of laboratory fuel rod mechanical compliance experiments designed to simulate in-reactor stress systems. Good agreement was found between these experiments, in-reactor data, and other laboratory experiments except in the case of very small initial gap sizes. Uncracked (unirradiated) and cracked (irradiated) fuel rods were tested at two different sites by applying axial loads to simulated and actual fuel columns in Zircaloy cladding. Increased fuel cracking was found to cause the fuel strain energy to be dissipated in the radial direction over progressively shorter axial distances by increased fuel/cladding friction and fuel shearing mechanisms. This may result in burnup-dependent limitations to the maximum desirable axial node length for adequate calculation of fuel rod stresses by fuel performance codes.

Axial slipping between cracked fuel and cladding was found to be of sufficient magnitude to affect the analysis of in-reactor fuel rod relaxation. Friction coefficients between simulated cracked fuel columns and Zircaloy cladding ranged between 0.5 and 2.0, depending on the distance of axial sliding. Initial gap size affected the load required to cause free sliding ("breakaway"). Fuel-induced rod bowing increased with initial gap size and decreased with fuel cracking. An apparently anomolous relationship between rod bowing and cladding diameter deformations indicated that the mechanics of load/moment transfer and frictional interactions in cracked fuel systems are not well understood.

2.0 INTRODUCTION: DESCRIPTION OF CRACKED FUEL MODEL

The purpose of this section is to provide the reader with some background information concerning the parameters of the mathematical model developed to describe the mechanical behavior of cracked fuel. A brief description of these modelling parameters will provide the perspective necessary to understand the motivation behind each of the verification experiments discussed in the following sections, and will also permit the experimental objectives to be stated in a more concise form.

It has long been recognized that pelletized nuclear fuel cracks during normal operation. This cracking is caused by the rather large radial temperature gradients which cause thermal stresses that exceed the UO_2 fracture stress. A schematic of cracked fuel is shown in Figure 1, which is similar to many transverse photomacrographs that result from postirradiation examination (PIE).

Cracking alters the basic geometric and structural state of the fuel pellets, and is believed to be closely related to the fuel rod thermal and mechanical performance. The outward motion of the fuel fragments partially closes the original fuel-cladding gap and results in random contact between the fuel fragments and the cladding inner surface. The partial (dispersed) contact between cracked fuel and cladding is responsible for much of the nonlinear mechanical behavior of the fuel rod. An example of this nonlinear behavior is shown in Figure 2, where total cladding axial elongation is plotted versus rod power. If the original fuel-cladding gap remained symmetrical, the cladding elongation would be expected to closely resemble the discontinuous curve in Figure 2. The abrupt change in slope of this curve is caused by the (theoretically uniform) fuel-cladding contact that occurs when fuel radial thermal
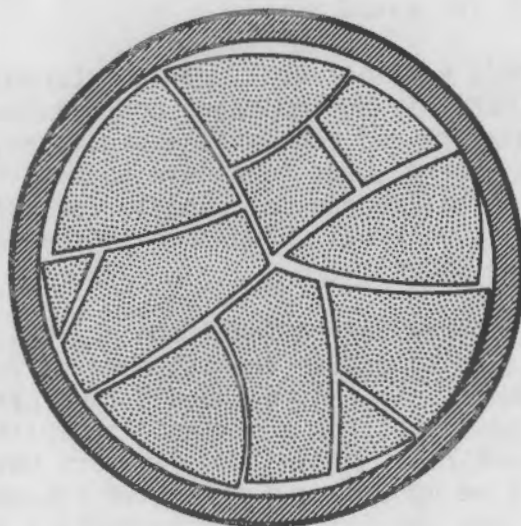
FIGURE 1. Cracked Fuel Schematic

DATA
— — SOLID CYLINDER MODEL

CLADDING AXIAL ELONGATION

FREE THERMAL EXPANSION

POINT OF CONTACT

ROD POWER
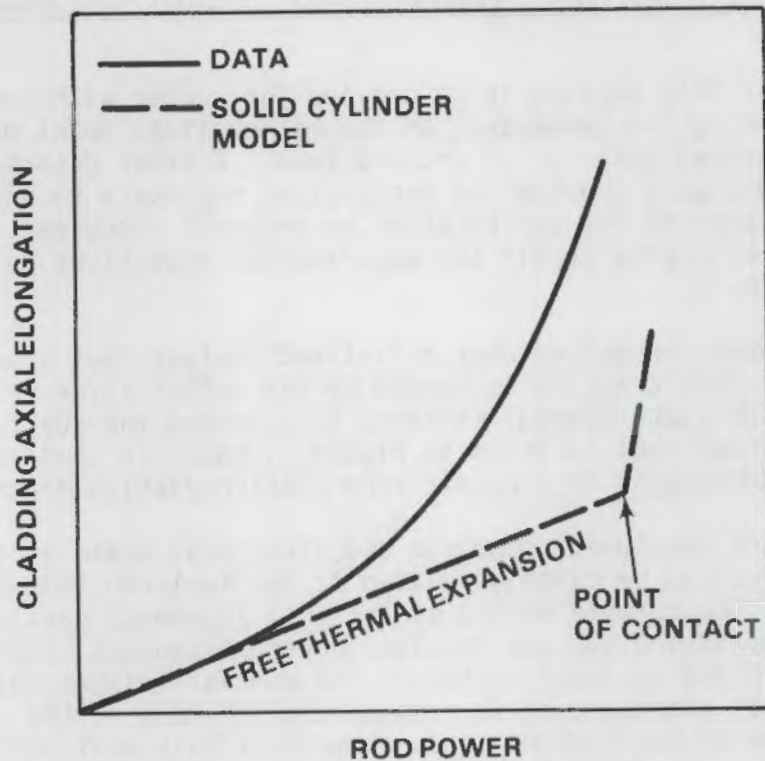
FIGURE 2. Typical Mechanical Behavior of Cracked Fuel Systems

expansion exceeds the cladding inner diameter. However, in-reactor data resembles the continuous curve, which indicates that fuel-cladding contact occurs gradually as the power is increased.

Models describing this behavior are important because the fuel-cladding mechanical interaction (FCMI) is an important contributor to fuel rod failures, with the associated regulatory and economic consequences. However, modelling efforts to date have, in general, not been able to meet the challenge of adequately describing the thermal/mechanical behavior of cracked fuel systems. The model developed in this work has shown some improvement in the predictive capability for cracked fuel models.

The general approach taken was to model the cracked fuel in terms of effective Young's moduli and effective thermal conductivities. In this manner, the results could be implemented in the NRC fuel performance code FRAPCON-2, rather than requiring that a new code be written. The concept of effective properties is not new. Other investigators have modelled effective thermal expansion, effective moduli, and effective conductivities. What is new in this approach is that the fundamental parameters used to describe the effective properties possess three important attributes: 1) conceptual simplicity, 2) physical meaning, and 3) measurability. Measurability also opens the possibility of future standardization of cracked fuel models.

4

The unique geometry of cracked fuel was an important factor in the definition of the modelling parameters. Although the medium is discontinuous, there is still a high degree of ordering—that is, the fragments fit together rather well so that the cracks cause a relatively low "void fraction" to be introduced into the fuel (1 to 5%). This is in contrast to soil mechanics models, which generally assume that the fragments are small spheres, resulting in 10 to 40% void volumes. In addition, the characteristic dimensions of cracked fuel (fragment size versus cladding diameter) violate soil mechanics assumptions. Rock mechanics was also found to be insufficiently developed to model cracked fuel. A new approach was needed.

Because average mechanical properties of the cracked fuel were desired, it was possible to make certain assumptions concerning symmetry. These assumptions resulted in further assumptions such as a hydrostatic state of stress in the transverse (r,θ) plane, and are further discussed in References 1 and 2. For the purposes of this report it is necessary to discuss a most important assumption in detail, as follows.

For U.S. light water reactors (LWR), the fuel temperatures are relatively low ($<1400°C$). Therefore, it was assumed that the thermal-mechanical response of the cracked fuel was dominated by the opening and closing of the cracks, and thus that the fuel fragments behaved as rigid bodies. The qualitative behavior of the model is as follows: changes in rod powers cause changes in fuel temperatures, which cause changes in thermal expansion; changes in thermal expansion cause changes in fuel stresses, which cause changes in crack and gap sizes, which changes the effective Young's moduli and effective thermal conductivity of the cracked fuel. This is shown schematically in Figure 3.

POWER
↓
TEMPERATURE ←
↓
THERMAL EXPANSION
↓
STRESSES
↓
EFFECTIVE MODULI ← CRACK WIDTHS → EFFECTIVE CONDUCTIVITY
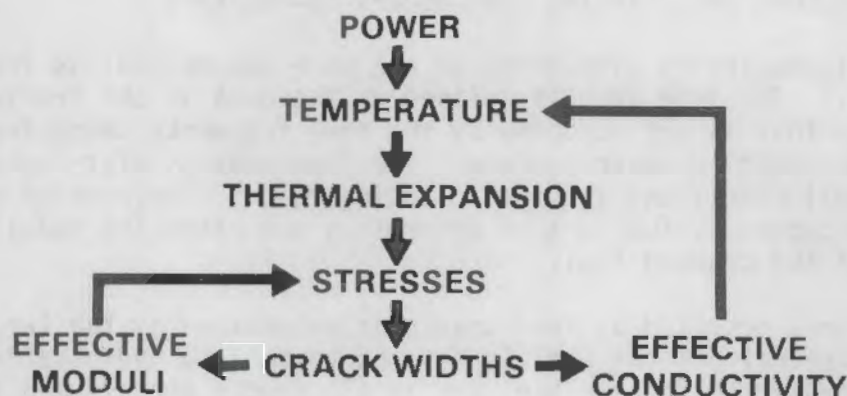
FIGURE 3. Schematic of Cracked Fuel Model Behavior

It was necessary to choose a model to represent the dependence of crack and gap widths on the fuel stresses. The model selected is from the relatively new technology called tribology (friction, lubrication, and wear). It is a fundamental model that describes the normal interaction of two nominally flat,

rough surfaces, and was discussed in a paper concerning contact conductances (heat transfer across solid-solid interfaces)[3]. The mathematical expression is:

$$\frac{1}{2} \, \text{erfc} \left[\frac{d}{R \sqrt{2}} \right] = \frac{\sigma}{\sigma + H} \qquad [1]$$

where erfc = complementary error function = 1-erf
       d = separation between mean surface planes of crack interfaces (crack width)
       R = surface roughness of crack face (one standard deviation of asperity heights)
       σ = stress applied normal to crack
       H = Meyer Hardness of UO_2.

In Reference (3), the surfaces were assumed to be nominally flat. However, fuel crack surfaces are not considered flat, and an effective crack roughness (R_c) is used in the present model. R_c includes the familiar surface microroughness and the surface waviness. This formulation also implies that the maximum actual contact area is one-half of the total apparent contact area, which seems reasonable for "wavy" surfaces.

Because the fuel fragments become slightly misregistered during operation (i.e., relocation is not symmetric), the fuel-cladding interface (gap) also has an effective roughness, Rg. Therefore, the gap was considered as another crack in the model formulation. The error function in the crack compliance model (Equation [1]) is also particularly suited for describing the partial contact between cracked fuel and cladding that occurs in-reactor.

Further discussion is simplified if one more new concept is introduced: the "free area." The free area is defined as the area in the transverse plane of the fuel rod that is not occupied by the fuel fragments themselves, and is enclosed by the cladding inner surface. The free area is distributed between the fuel internal cracks and the fuel-cladding "gap." The portion of the free area that is occupied by fuel cracks determines the effective moduli and conductivity of the cracked fuel.

The free area occupied by fuel cracks is determined by the lengths and widths of the cracks. If the fuel is assumed to be in a hydrostatic stress state in the transverse (r, θ) plane, and if all cracks are assumed to have the same effective roughness (R_c), then the average crack width times the total crack length is the total crack area. Equation [1] relates average crack width to the "hydrostatic" stress, which is the same stress in the radial direction of the gap. Thus, the average gap width is also determined if the effective gap roughness is known.

At this point, we can concisely list the three basic cracked fuel modelling parameters that were mentioned in the above text:

6

- effective crack roughness (R_c)
- effective gap roughness (R_g)
- total crack length (L_{tc}).

It was the purpose of past efforts to deduce values for these three parameters from the NRC/PNL Halden reactor experiments IFA-431 and IFA-432. This was accomplished by devising a simultaneous solution method for the roughnesses that utilized prior thermal solutions as "boundary conditions,"[4] and the in-reactor data for rod powers, center temperatures, and cladding axial elongations.[1,2] The total crack length was inferred from IFA-431 PIE results.[5] It was also possible to deduce effective moduli for both the transverse and the axial directions simultaneously. These methods and results are explained in more detail in References 1 and 2.

Simple laboratory experiments were devised to independently verify the values of the roughnesses and total crack length that were deduced from in-reactor data. Experiments were also conducted to verify the model prediction that the effective Young's Moduli for cracked fuel columns were less than for solid UO_2 pellet columns. This work has been completed, and is described in detail in the following section.

- effective crack roughness (R_c)
- effective gap roughness (R_g)
- total crack length (L_{tc}).

It was the purpose of past efforts to deduce values for these three parameters from the HBO/PR Halden reactor experiments IFA-431 and IFA-432. This was accomplished by devising a simultaneous solution method for the roughnesses that utilized prior thermal solutions as boundary conditions,[4] and the in-reactor data for rod powers, center temperatures, and cladding axial elongations.[1,2] The total crack length was inferred from IFA-431 PIE results.[5] It was also possible to deduce effective elastic moduli for both the transverse and the axial directions simultaneously. These methods and results are explained in more detail in References 1 and 2.

Simple laboratory experiments were devised to independently verify the values of the roughnesses and total crack length that were deduced from in-reactor data. Experiments were also conducted to verify the model prediction that the effective Young's Moduli for cracked fuel columns were less than for solid UO2 pellet columns. This work has been completed, and is described in detail in the following section.

3.0 EXPERIMENTAL VERIFICATION PROGRAM

A series of laboratory experiments were performed in order to independently verify the cracked fuel modelling parameter values and the effective moduli results found from the analysis of in-reactor data. These experiments can be divided into three main classifications: single cracks, crack systems, and cracked fuel-cladding systems.

Load-compliance experiments were performed on single cracks using alumina samples in order to validate the general behavior of the crack compliance model (Equation [1]), and to verify that the values deduced for in-reactor effective crack roughnesses were reasonable.

In order to assess the validity of the effective gap roughness concept, thermally-precracked alumina samples were hydrostatically loaded in a manner such that the outer surface profile of the cracked and relocated pellets could be permanently preserved. This was intended to simulate in-reactor conditions. The standard deviation of the surface asperity distribution (effective gap roughness, R_g) was then compared with R_g deduced from in-reactor data.

The value for total crack length was checked by subjecting 19 PIE transverse photomacrographs to a quantitative optical analysis to determine the mean and standard deviation of total crack length for obviously open and apparently closed cracks.

Mechanical compliance experiments on cracked fuel-cladding systems (fuel rods) were performed in order to verify that the effective Young's moduli for cracked fuel were less than for solid UO_2 pellets, as predicted by the model. These experiments were designed to simulate in-reactor loading systems in a laboratory environment at room temperature. The fuel was in axial compression and the cladding in axial tension. Simultaneous load and deflection measurements on fuel and cladding provided data to calculate effective moduli. Compliance experiments were performed on both unirradiated and irradiated rods.

Table 1 summarizes the experimental program and the general results. Each experiment is discussed in detail in the following sections.

3.1 SINGLE CRACK SYSTEMS (Effective Crack Roughness, R_c)

The objectives of this experiment were to validate the general behavior of the crack compliance model (Equation [1]), and to verify that the values of effective crack roughness deduced from in-reactor data were reasonable. This was accomplished by simple compression tests using alumina samples and an Instron Testing Machine.

The concept for the experiment was relatively simple, as shown in Figure 4. Alumina cylinders (99.9% dense) were cut from commercially available alumina rods. The cylindrical samples were 9.53 mm (0.375 in.) in diameter and 12.70 mm (0.50 in.) long, and were intended to simulate fuel pellets. These

9

TABLE 1. Summary of Experimental Results

EXPERIMENT	PARAMETER	RESULTS
SINGLE CRACKS	CRACK ROUGHNESS	VERIFIED
(Al₂O₃ PELLETS)	CRACK COMPLIANCE MODEL	VERIFIED
CRACK SYSTEMS		
Al₂O₃ PELLETS	GAP ROUGHNESS	LONG TAIL
PIE PHOTOS	TOTAL CRACK LENGTH	VERIFIED
CRACKED-FUEL-CLADDING SYSTEMS (COMPLIANCE TESTS)	EFFECTIVE MODULI	VERIFIED
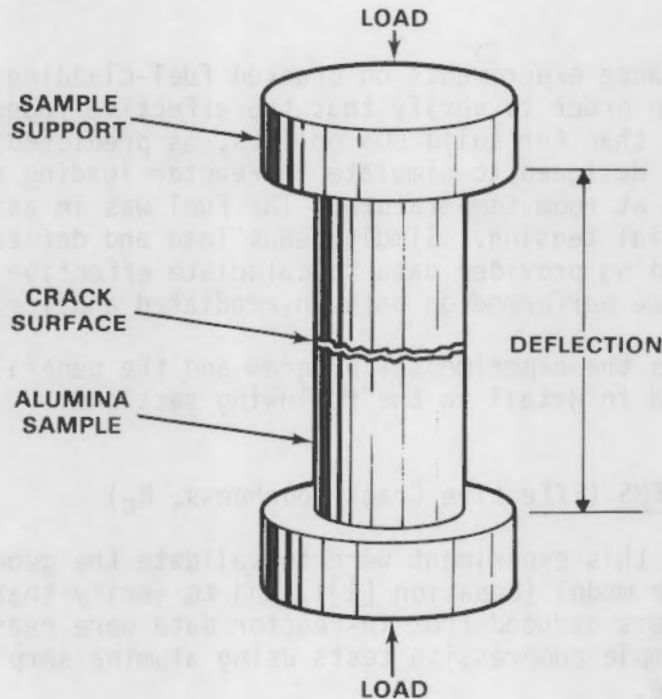
FIGURE 4. Experimental Concept for Crack Compliance Tests

10

cylinders were then fractured across the transverse plane at approximately mid-length to provide the crack surfaces for testing. All fractures were roughly perpendicular to the cylinder axis.

Each two-piece sample was then installed in the support arrangement shown in Figure 5. Each sample half was firmly seated into the 9.53-mm diameter "cups" machined into the sample holders and then cemented into place. The sample holder was installed in the Instron, and two strain gage cantilever "clip" gages were attached to the sample holder across a diagonal (180° apart), as shown in Figure 5. The tips of the clip gages were seated into a 22.86 mm (0.9 in.) diameter groove machined into the sample holder. These clip gages were used to measure the crack compliance during compression to an accuracy of ±0.005 mm (0.0002 in.), and a load cell recorded the applied axial load. Before the load was applied, the sample halves were rotated so that the fracture surfaces appeared to mate. Final transverse alignment was accomplished manually, and was intended to simulate the in-reactor condition of two arbitrary fragments that have undergone slight misregistration during the relocation process. The initial loading condition was about 1 kg (2.2 lb).

The axial load was then applied to the cracked sample. Over a period of about 5 min, the load was increased to about 900 kg while the load-compliance data was recorded on standard charts. A sample of this data is shown in Figure 6. The data is shown up to 454 kg (1000 lb) only, since stresses larger than 69 MPa (10,000 psi) are out of range of most in-reactor data. It is of
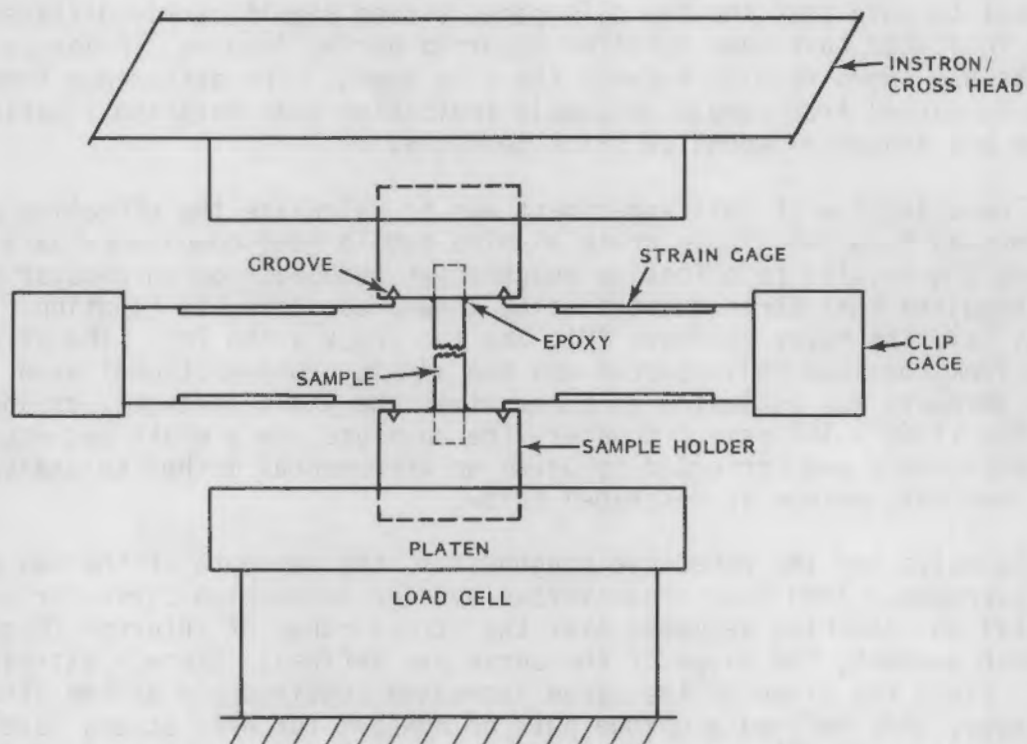
FIGURE 5. Experimental Apparatus for Crack Compliance Tests

11
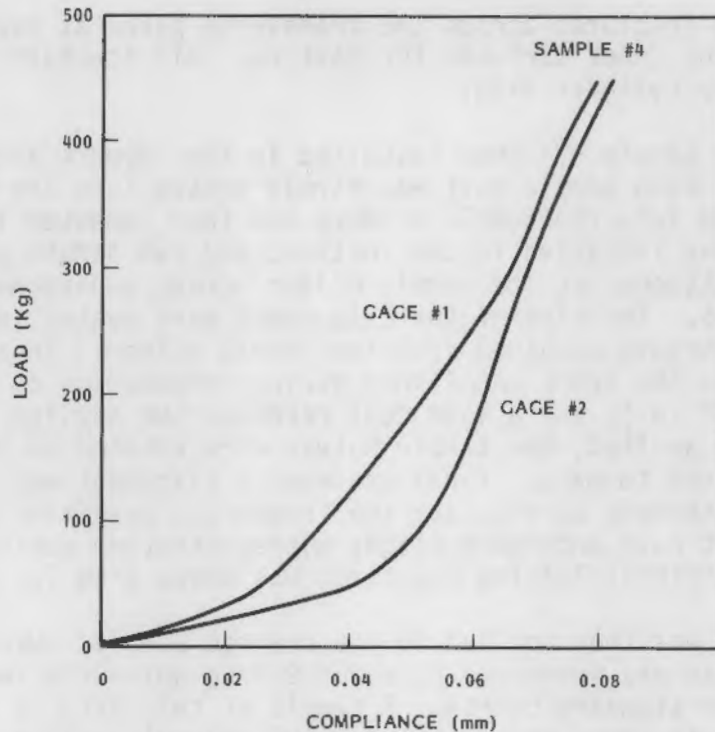
FIGURE 6. Sample Crack Compliance Data

interest to note that the two clip gages showed significantly different outputs, which indicated that some rotation occurred during loading. Prior calibration efforts had shown no bias between the clip gages. The difference between gage readouts varied from sample to sample indicating that rotational motions were random and probably depend on crack geometry.

The objective of this experiment was to calculate the effective crack roughnesses from the single crack alumina sample load-compliance data and then compare the results to effective roughnesses deduced from in-reactor data. This required that three quantities be known, according to Equation [1]: the stress (σ), the Meyer Hardness (H), and the crack width (d). The stress was known from the load cell readout and the sample cross-sectional area. The Meyer Hardness was estimated as three times the yield strength, or about 11.4 GPa (1.65 x 10^6 psi). However, the absolute crack width was not known. This deficiency was corrected by using an incremental method to analyze the data, and this method is described below.

To solve for the effective roughnesses, the readouts of the two clip gages were averaged. Then the stress-versus-average deflection curve for each sample was divided into five segments over the stress range of interest (Figure 7). For each segment, the slope of the curve was defined: slope = Δstress/Δdeflection. Since the slope of the curve increased continuously as the stress increased, this defined a unique pair of numbers for each stress level. For assumed values of effective crack roughness (R_c), another set of unique stress-

12
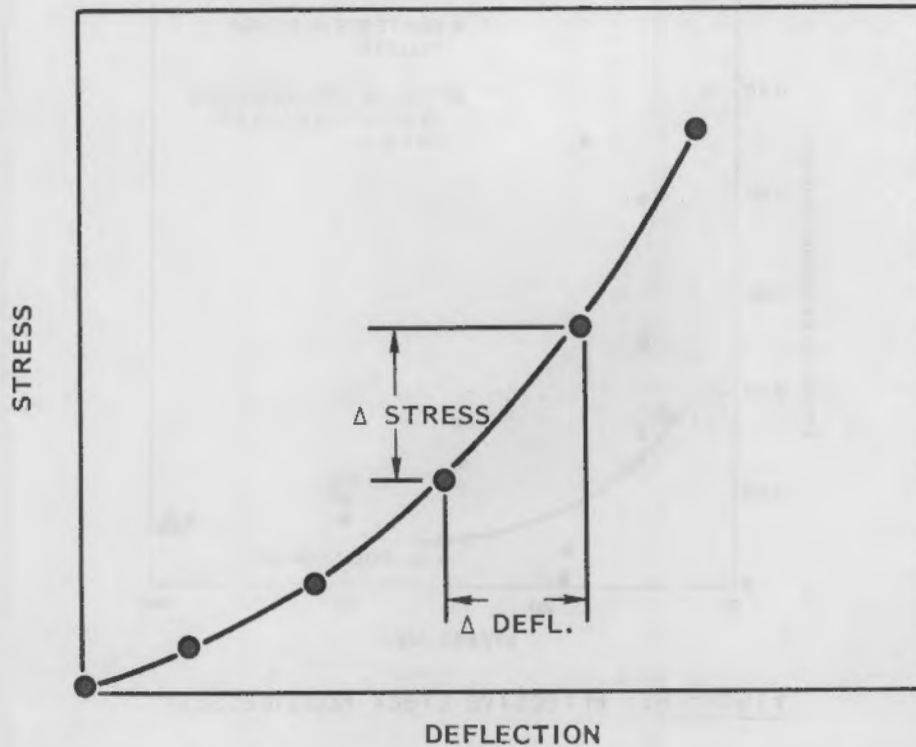
FIGURE 7. Analysis Method for Crack Compliance Data

slope pairs could be generated from Equation [1]. A small computer code was written to compare the two sets of stress-slope pairs, and thus iteratively solve for R_C as a function of stress.

The results of the four samples tested are shown in Figure 8, where the effective roughnesses from IFA-431/432 data are also shown for stress levels corresponding to 30 kW/m. The agreement between the two data sets is reasonably good, considering the different sources of each. The general trend of decreasing effective crack roughness with increasing stress levels is confirmed by the laboratory tests, and indicates that the crack compliance model (Equation [1]) is valid for these analyses.

The magnitudes of the laboratory effective roughnesses also seem reasonable. The microroughnesses of the alumina fracture surfaces were measured with a Talysurf machine and the one standard deviation of the microroughness was found to vary between 0.001 and 0.002 mm (45 to 85 μin.). The waviness of the fracture surfaces was measured with an optical comparator, and varied between 0.7 and 0.8 mm. Thus, the one standard deviation macroroughness was 0.23 to 0.27 mm. The effective crack roughnesses (R_C) deduced from the analysis lie between the microroughness and the waviness, indicating that waviness is an important contributor to R_C.

The converging envelope of the laboratory values for R_C appears to be caused by the relative rotations between sample halves as the load was

13

FIGURE 8. Effective Crack Roughnesses

increased. This is shown in Figure 9 where the changes in angle between mean surface planes are plotted versus stress. These relative angle changes were calculated from the differences in the two clip gage readouts. It appears that the rigid body rotation of fragments as the cracks are closed is an important contributor to the variability in effective roughnesses. This observation supports the assumptions discussed in the Introduction. The importance of rigid body motions of fuel fragments with respect to fuel failure modelling will be discussed in future reports.

The effective crack roughnesses deduced from the laboratory experiments are slightly larger than those deduced from the in-reactor data. There are at least three possible explanations for this behavior, which are discussed as follows.

It is possible that the differences in Meyer Hardness for the room temperature alumina and the in-reactor UO_2 may contribute to the differences in R_c. However, the laboratory results do not appear to be sensitive to Meyer Hardness uncertainties. This is shown in Figure 10, where the data was analyzed for Meyer Hardnesses increased and decreased by factors of ten. The scatter seems to increase at low stresses, but the same asymptote is approached at high stresses. So Meyer Hardness at least does not dominate in producing the laboratory versus in-reactor differences in R_c.

It is possible that the rigid body assumption may not be entirely valid for individual fuel fragments at high stresses, such as for rod 3 in Figure 8. This may influence R_c predictions for small gap rods at high powers and will be further discussed in Section 3.3. Also, the "thermal boundary conditions" used

14

FIGURE 9. Fragment Rotations During Crack Compliance Tests

15

FIGURE 10. Effect of Meyer Hardness on Effective Crack Roughnesses

16

in the in-reactor data analysis (see Introduction) have the highest uncertainty for small gap, helium-filled rods, and it is known that the associated uncertainty distribution for this rod is not Gaussian.[6] It is possible that these uncertainties have propagated through the analysis and influenced the R_c estimates. This condition should be investigated in detail since the high stress condition is usually associated with increased probability for fuel failure.

Finally, it is possible that there is a difference in the fracture surface geometries that could cause the laboratory values for R_c to be slightly greater than the in-reactor values. A difference in fracture surface waviness, or in the initial relative position of adjacent fragments (misregistration via relocation), or in interfragment friction from other adjacent fragments, could all easily cause substantial variability in the rigid body rotation mechanism observed in Figure 9. Although the effects of fracture surface morphology are presently thought to be of lesser importance when compared to the fragment size itself, this important area needs further quantification.

In summary, the laboratory single-crack compliance tests have verified that the crack compliance model is acceptable for modelling in-reactor cracked fuel. The general trend in the R_c versus stress relationship is in good agreement between laboratory and in-reactor results. The magnitude of the laboratory effective roughnesses also appears reasonable and lies between the micro-roughness and the waviness of the fracture surfaces. However, the magnitudes of the laboratory roughnesses appear slightly greater than in-reactor values, probably because of differences in basic fracture surface geometries. The effects of fracture surface geometries are not well understood, and it is recommended that further work be conducted in this area.

3.2 MULTIPLE CRACK SYSTEMS

Two experiments were conducted under this heading to verify that the total crack lengths and the effective gap roughnesses deduced from the analysis of in-reactor data were acceptable. The details of these efforts are explained below.

3.2.1 Effective Gap Roughness

Simple laboratory experiments were conducted in order to measure the effective gap roughness (R_g) for simulated cracked and relocated fuel pellets. During relocation, the fragment ratcheting phenomenon induces a misregistration of fracture surfaces and results in a discontinuous outer surface for the cracked pellet. This geometric feature of the gap has a similar importance for R_g as waviness has for R_c.

The concept of the experiment is simple and is shown in Figure 11. The cracked fuel pellets were simulated by 22.2-mm (0.875-in.) diameter, 28.6-mm (1.125-in.) long alumina samples that had been precracked by thermal shocking, and then the fragments separated by light loading in a bench press. Three such samples were prepared. The number of fragments in each sample ranged from nine to twelve, which roughly approximates cracked fuel. A cracked alumina pellet

CENTRAL HOLE FOR
INDUCING RATCHETING

ALUMINUM SHIM
CONFORMS TO IRREGULAR
SURFACE

HYDROSTATIC STRESS

CRACKS INDUCED BY
THERMAL SHOCKING
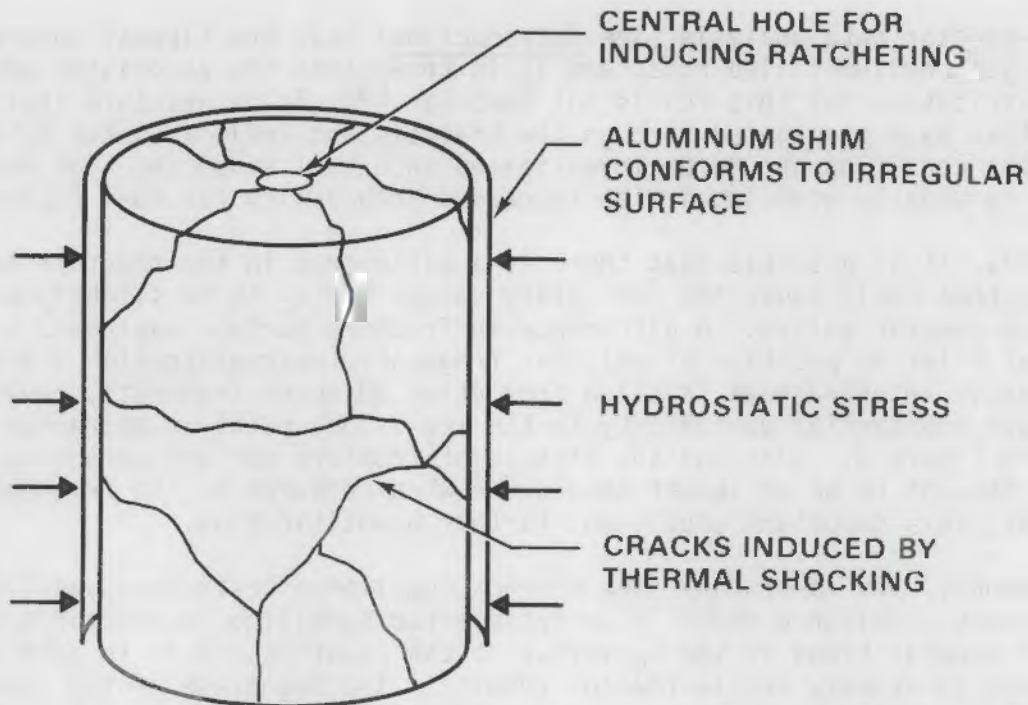
FIGURE 11. Concept for Effective Gap Roughness Experiments

was then reassembled and wrapped in a thin (fully annealed) aluminum shim.
Hydraulic pressure was applied through a rubber tube inserted in the 7.1-mm
(0.28 in.) diameter central hole along the axis of the pellet. This caused
the pellet fragments to be forced outward and simulated the fragment ratchet
phenomenon associated with fuel relocation. The aluminum shim was not deformed
by the relocation simulation process, and merely unwrapped itself slightly as
the pellet expanded.

The relocated sample was then wrapped in a 3.18-mm (0.125-in.) thick sheet
of latex rubber, and inserted into the loading apparatus shown in Figure 12.
The loading apparatus consisted of two brass concentric cones with about a 5°
angle on the lateral surfaces. The inner cone was split into thirds for assem-
bly around the sample. The solid external cone was fitted over the internal
cone-sample assembly, and about 100 kg load was applied as shown in Figure 12.
This caused a relative axial motion of about 9.5 mm (0.375 in.) between the
cones, and decreased the diameter of the inner cone by approximately 1.66 mm
(0.064 in.). During this diametral compression, the alumina fragments were
forced inward by some small amount (unknown), and the approximately hydro-
static pressure on the aluminum shim caused it to conform to the shape of the
pellet outer periphery. The sample was then removed and the aluminum shim
mounted on a lathe spindle, where measurements of the cracked pellet surface
discontinuities were made with a dial indicator accurate to ±0.0013 mm
(0.00005 in.). Seven surface discontinuities were measured on the first
sample and fourteen on each of the following two samples. The accuracy of
these measurements is estimated to be about ±20% of the actual value that
occurred under loading conditions.

18
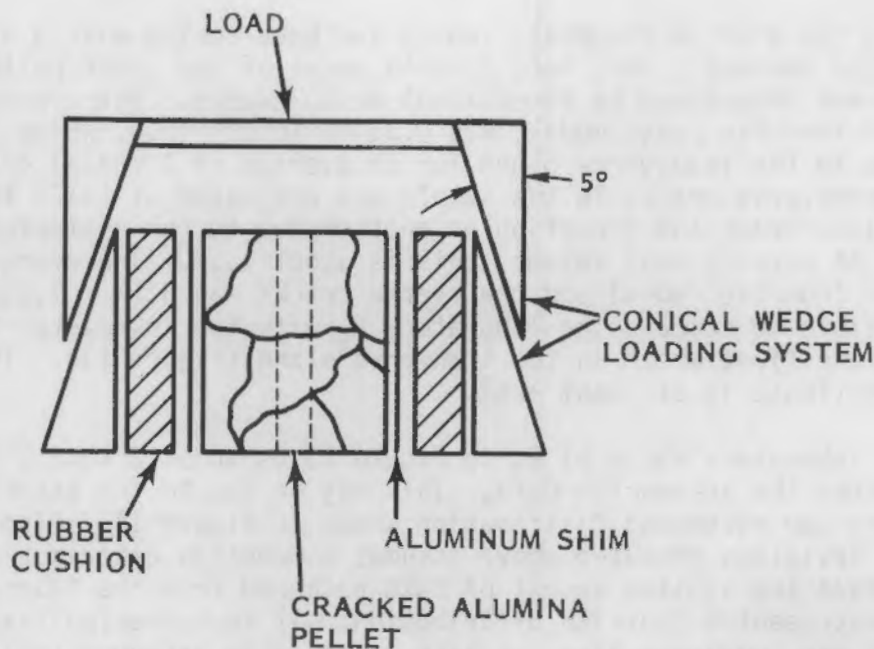
FIGURE 12. Loading Apparatus for Gap Roughness Experiments

Comparison to in-reactor data for effective gap roughness required that the laboratory data be scaled according to the pellet diameters for the two data sources. This means multiplying the laboratory data by factor of 0.4205/0.875 = 0.481. Also, the in-reactor values for R_g were reported in terms of one standard deviation of surface asperity heights, whereas the laboratory data can be assumed to represent the surface asperity height distribution itself. Therefore, the standard deviation of the laboratory-measured gap roughnesses should be compared to the in-reactor values. The scaled mean and standard deviation of gap roughness for the three samples were: $\bar{x}$ = 0.068, 0.051, 0.084 mm; σ = 0.034, 0.035, 0.059 mm. The scaled standard deviation of the total distribution of laboratory measurements for R_g was 0.047 mm (0.0019 in.).

An estimate of the "free area" of the laboratory samples was also required in order to compare these results with the in-reactor data. Because of the difficulties of making dimensional measurements on cracked fuel samples with such a simple experimental apparatus, "free area" estimates for the samples in the hydrostatically-stressed state were not performed. The flexibility of the latex sheet wrapped around the sample precluded making dimensional estimates based on the amount of axial travel by the external cone of the experimental apparatus. Instead, one of the samples was reassembled and inserted into a larger latex tube, and the internal latex tube was pressurized to induce relocation of the fragments and then depressurized so that the cracked pellet assembly was at rest.

The cracked and relocated pellet was then vacuum impregnated with a low viscosity resin that hardened at room temperature. After the resin had

19

hardened, the alumina fragments (which had been coated with a silicon-based spray) were removed. This left a resin model of the crack pattern, the volume of which was determined by dimensional measurements. The average crack width (measured from the resin model) was 0.35 mm (0.014 in.), which gives about 3.1% free area in the transverse plane for an average of 4 radial cracks. The number of transverse cracks in the sample was estimated at 1.125 to 1.250, i.e., one midplane crack and a portion of another due to the asymmetries of cracking. In terms of percent void volume, this is about 1.5%. Therefore, the total percent void from the radial and transverse cracks was 3.1% + 1.5% = 4.6%. It was then possible to compare the laboratory R_g with the in-reactor R_g on the basis of the "free area" in the tranverse plane (Figure 13). The uncertainty of this estimate is at least ±25%.

The laboratory value of R_g in Figure 13 is about 2 to 2.5 times that deduced from the in-reactor data. This may be due to the extended tail in the laboratory gap roughness distribution shown in Figure 14. Also note that the standard deviation computed above assumes a Gaussian distribution, and it appears that the limited amount of data gathered from the laboratory experiments may not represent a Gaussian distribution. It is suspected that the in-reactor effective gap roughness also exhibits a similarly extended tail (Figure 14), which would significantly affect calculations of cladding stress concentrations
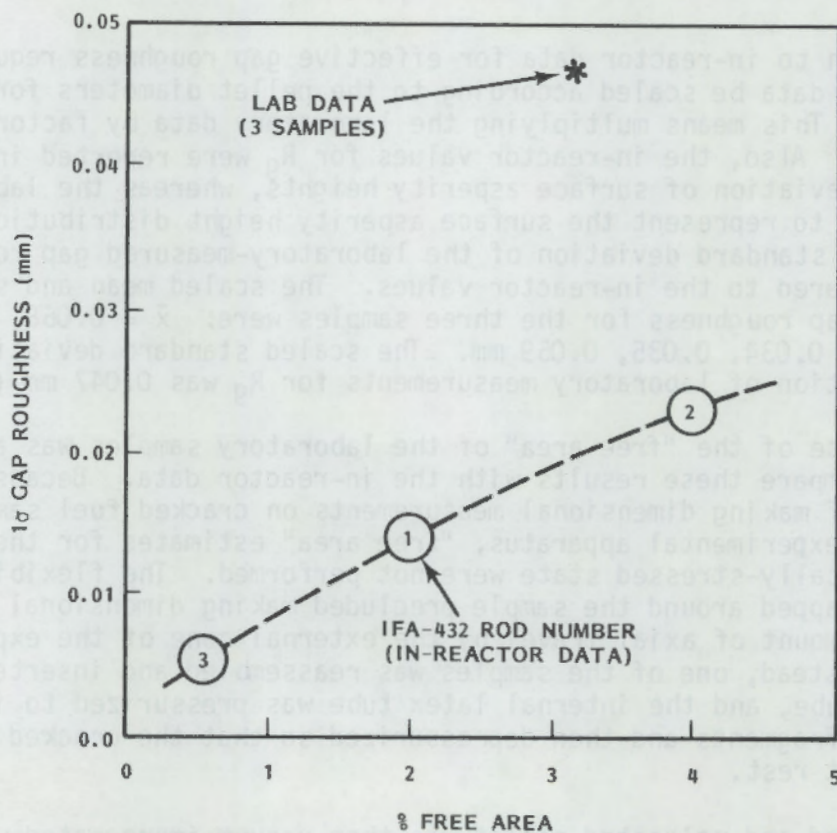
FIGURE 13. Comparison of Laboratory Gap Roughness with In-Reactor Values
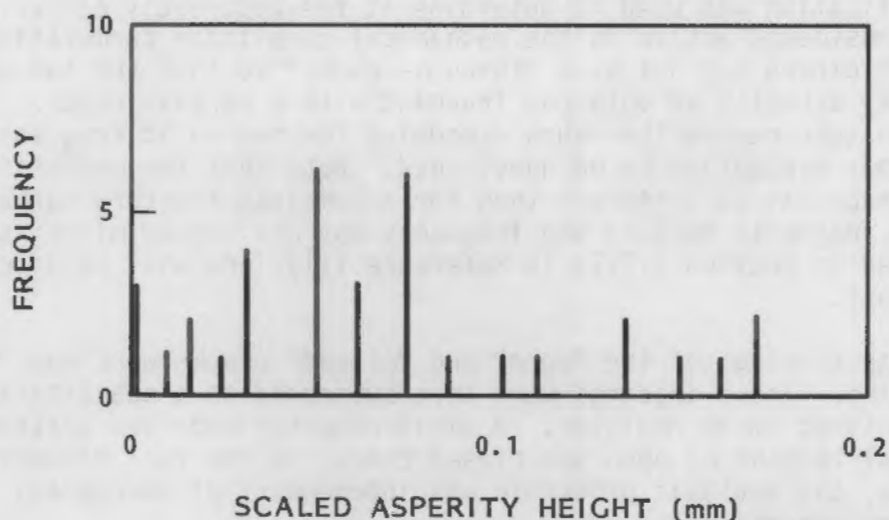
FIGURE 14. Gap Roughness Distribution for Laboratory Samples

for fuel failure models. Variations in cladding localized stress/strain concentrations can cause appreciable uncertainties to be introduced into predicted time-to-failure.[7] It is apparent that more data is needed in this important area, and that future experimental verification efforts should strive for a more typical representation of in-reactor conditions.

The concept of effective gap roughness may also be relatable to other analyses and experiments. There may be a phenomenological relationship between R_g and recently presented analyses that utilized other roughness factors for deducing transient gap conductances,[8] and between R_g and a "constriction factor"[9] or the Hagen number[10] used in axial gas flow analyses and experiments. These possible interrelationships should be investigated further, with at least two objectives in mind: 1) establishing a more unified approach to fuel modelling by relating the thermal performance, mechanical performance, and axial gas flow characteristics via the effective roughness concept, and 2) using these interrelationships to provide further experimental verification data via technology transfer between the thermal, mechanical, and gas flow data bases. All three efforts should expect to benefit from such an analysis.

3.2.2 Total Crack Length

The purpose of this effort was to verify the adequacy of the "total crack length" value used for the analysis of in-reactor data. A value of 3.5 fuel diameters had been assumed, based on PIE results for rod 6 of IFA-431.

To perform this task, 25 transverse photomacrographs were assembled from the literature. Of the original 25, 6 were later discarded because they represented laboratory experiments rather than in-reactor conditions. The crack patterns of the remaining 19 samples (from test reactor fuel rods) were divided into two basic classes: obviously open cracks and apparently closed cracks.

21

This classification was used to determine if the apparently closed cracks should be considered active in the mechanical compliance formulations. A crack that appears closed may not be a "through-crack," so that the two bounding fuel fragments may actually be only one fragment with a partial crack. This partial crack may in turn reduce the Young's modulus for the solid fragment, and cause the rigid body assumption to be questioned. Note that the mechanism of closing a partial crack may be different than for a complete fracture surface that defines two fragments because the fragments may not become misregistered. This was discussed in Section 3.2.1, in Reference (11), and will be discussed later in this report.

Separate tracings of the "open" and "closed" cracks were made for each of the 19 samples. These tracings were then subjected to a quantitative analysis using a Quantimet Image Analyzer. A small computer code was written to normalize the total lengths of open and closed cracks to the fuel diameter in the image. Thus, the analysis procedure was independent of macrograph magnification uncertainties.

The results of this analysis are shown in Table 2. It appears that the assumed 3.5 fuel diameters used for active cracks in the in-reactor analysis

TABLE 2. Crack Pattern Data Base

	Cracks (L/D)*		
Sample	Closed	Open	Reference
1	2.99	2.47	(12) Figure 1.2
2	4.71	1.77	Figure 2.1
3	3.37	3.04	Figure 2.2
4	4.69	3.08	Figure 2.3
5	2.34	3.19	(13) Plate 77L-165
6	4.16	1.07	Figure 11
7	5.03	2.17	Figure 16
8	3.01	2.66	Figure 19
9	3.22	3.92	(14) Plate 77A-108
10	4.37	3.13	Plate 77A-107
11	4.59	2.70	Plate 77A-107A
12	3.49	2.91	Figure 9a
13	2.71	4.55	Figure 10a
14	6.19	2.78	(15) Plate 77N-10
15	3.92	2.66	Plate 77N-9
16	4.14	2.95	Plate 77N-12
17	4.42	4.24	Plate 77N-251
18	3.06	4.01	Plate 77N-434
19	3.65	2.66	Plate 77N-596
mean =	3.90	2.95	
std dev =	0.94	0.83	

*L/D = crack length/pellet diameter

22

compares well with the obviously open normalized total crack length in Table 2
(2.95 diameters, $1\sigma = 0.83$ diameters). In addition, it seems that about 25% of
the apparently closed cracks may either be active or were misclassified to
begin with. However, this uncertainty is about the same as the standard devia-
tion for both crack types, and the results are considered to verify the
original assumption within this uncertainty.

Note that this data base is for test rods only, with generally very low
burnups (<100 MWd/MTM), and with generally the same peak power levels (about
52 kW/m). Samples 1 through 4 range up to 3700 MWd/MTM, but data is too sparse
to infer any burnup dependencies. Instead, Reference (16) is suggested to the
reader for a review of the power and burnup dependencies of fuel cracking; how-
ever, it should be noted that the "number of radial cracks" in Reference (16)
refers to the number of cracks intersecting the fuel outer surface, which is
not the "total crack length" that is discussed in this report. Reference (16)
also contains some power reactor data that should be compared to the test reac-
tor data in this report (Table 2) to identify any possible differences in crack
parameters. The data on "final diametral gap" in Reference (16) should also
be addressed in terms of effective gap roughness, as discussed in Section 3.2.1
of this report. The final gap size may be indicative of the 3σ value for R_g.

3.3 CRACKED FUEL/CLADDING SYSTEMS: EFFECTIVE MODULI FOR CRACKED FUEL

Mechanical compliance experiments on cracked fuel/cladding systems (fuel
rods) have been performed at room temperature in the laboratory with emphasis
on simulating loading systems similar to in-reactor situations. The primary
objective of these tests was to verify the values of the reduced effective
Young's moduli for cracked fuel that were deduced from in-reactor data analyses.

The basic concept of the experiments is shown in Figure 15. The cladding
was supported at the upper end while an axial load was applied to the fuel col-
umn. This put the cladding in axial tension and the fuel column in axial com-
pression, as assumed by many fuel performance modelling codes. As the load was
applied, simultaneous measurements were recorded for the total cladding axial
strain, the fuel column axial strain, the axial load, and the cladding diameter.
Traces of the cladding diameter were recorded as a function of axial and
azimuthal position, similar to some in-reactor experiments.

Two series of experiments were performed. Tests at PNL used 35- to 50-cm-
long simulated fuel rods of PWR dimensions, which were not irradiated. Tests
at AERE-Harwell used IFA-432 BWR design fuel rods which were 60 cm long, one
rod unirradiated and one rod irradiated to about 22 GWd/MTM. These tests have
been designated as "short rod tests" (PNL) and "long rod tests" (Harwell). The
reason for these designations concerns a phenomenon which had been postulated
to occur for this loading system.

It was postulated that the accumulation of cracked fuel-cladding frictional
forces would cause the cladding to exhibit more fuel-induced localized deforma-
tion near the top of the rod (where the load was applied) than at the bottom.

23

AXIAL LOAD AND FUEL COLUMN DEFLECTION

SUPPORT FLANGE

CLADDING DIAMETER

CLADDING ELONGATION
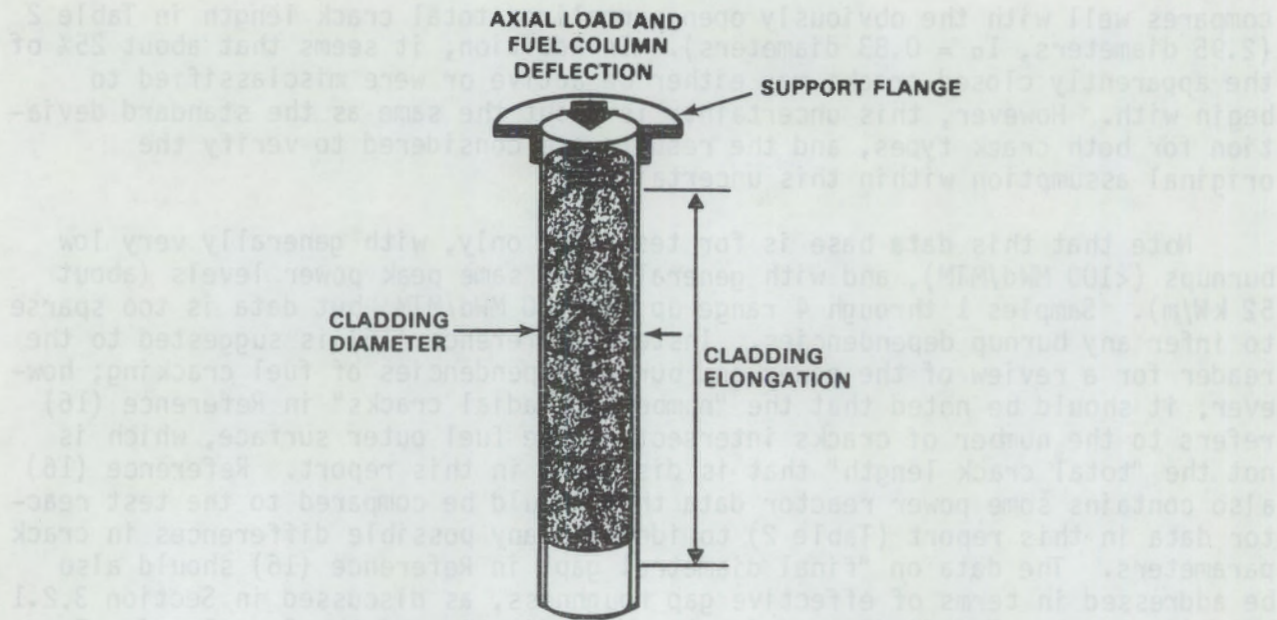
<u>FIGURE 15</u>. Experimental Concept for Compliance Tests

This would, of course, depend on how the cracked fuel transmitted the loads to the cladding, which in turn depends on the fuel geometry, which is determined by the extent of fuel cracking. The quantification of this effect was a second objective of these experiments.

In general, the experiments confirmed the moduli reductions previously predicted from in-reactor data. The quantification of the axial mechanical interaction gradients (discussed above) have yielded strong indications that there are limitations for maximum axial node lengths in fuel performance codes.

The two series of experiments are discussed separately below and are followed by a separate section which summarizes the results.

3.3.1 Short Rod Compliance Experiments

Materials, Apparatus, and Test Sequence

A total of six simulated fuel rods were tested at PNL. The cladding used was of a typical PWR design (Zircaloy-4, 1.092 cm OD x 0.953 cm ID), and cladding lengths varied from 35 to 50 cm. Fuel column lengths varied from 15 to 37 cm; the difference between cladding and fuel column lengths being accounted for by the push rods used to apply the axial loads to the fuel columns. The experimental matrix is shown in Table 3. Both pellet and packed particle (sphere pac) fuel designs were tested.

The pellets used in Rods 1 through 5 were fabricated from steatite (low density electrical porcelain) rather than UO$_2$ because of cost considerations.

24

TABLE 3. Short Rod Compliance Test Matrix

Rod	Clad Length, cm	Pellets Diameter, cm	Pellets Length, cm	Fuel Column Length, cm	Clad Axial GA Length, cm	Dia. Scan Length, cm
1	35.56	0.947	0.947	15.24	27.31	13.02
2	50.80	0.942	1.270	33.02	38.74	30.48
3	40.64	0.942	1.270	27.94	32.07	21.59
4	50.80	0.947	1.270	34.29	38.74	31.12
5	45.72	0.945	1.270	37.47	37.47	23.50
6	45.72	(a)	(a)	35.59	37.47	23.50

(a) 500 μm diameter alumina spheres

Steatite was chosen because its fracture strength and elastic modulus at room temperature (about 7.58×10^7 Pa and 1.72×10^{11} Pa, respectively) provide a better approximation for UO_2 at fuel average operating temperatures (about 750°C) than does alumina (2.6 to 3.1×10^8 Pa and 3.7 to 3.8×10^{11} Pa).

The steatite pellets were precracked by a thermal shocking procedure to predispose them to crack in a manner similar to UO_2 in-reactor. The crack patterns produced by this method were very similar to those shown in Figures 11 and 15. The cracks did not penetrate through the pellet material and fragments did not separate, thus providing a simulation of the partially-cracked UO_2 pellets that occurs during the first ramp to power in an operating fuel rod.

The precracked (but still intact) pellets were then inserted into the cladding, which was equipped with a welded upper support flange and a threaded lower end cap that was removable. Figure 16 shows the Rod 3 components after compliance testing, where the cracked fuel column has been removed from the cladding. The rods were inserted into the compliance testing machine (Figures 17 through 19) and the instrumentation attached (Table 4).

A hydraulic intensifier system (Figure 20) was used to amplify the plant compressed air and thus drive the hydraulic loading system which applied the axial load to the fuel column. The applied load was computed from the hydraulic pressure and the bore area of the hydraulic loading cylinder. The cladding diameter was measured by two precision LVDTs situated 180° apart and mounted on a carriage which traversed along the fuel rod (Figure 19). The tips of these LVDTs were "T"-shaped tungsten carbide cylinders situated with their axes perpendicular to the fuel rod axis so that errors would not be introduced by lateral translations of the fuel rod relative to the LVDT axes (Figure 21).

25
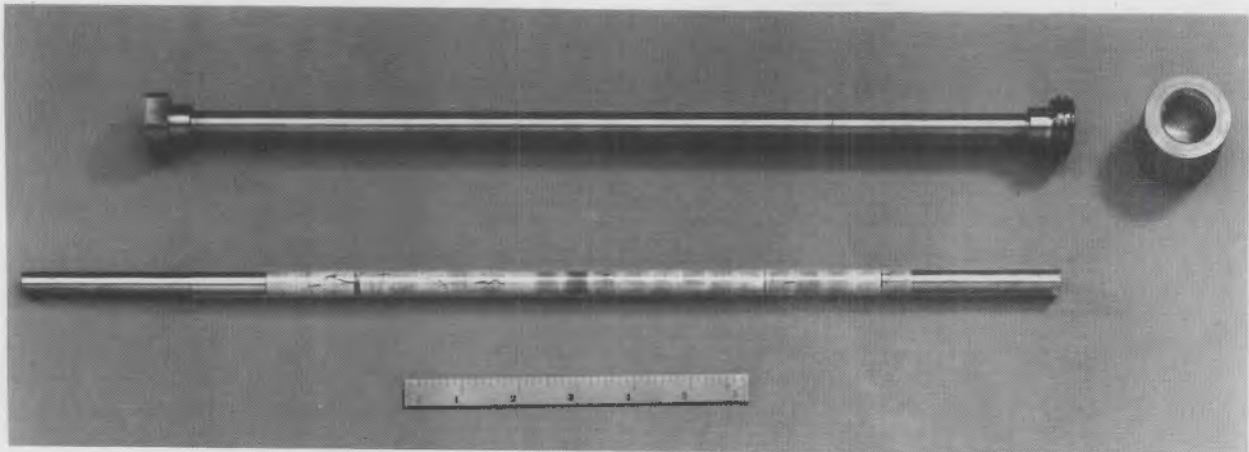
FIGURE 16a. Rod 3 Components: Cladding, End Cap, and Pellet Column (in glass tube)
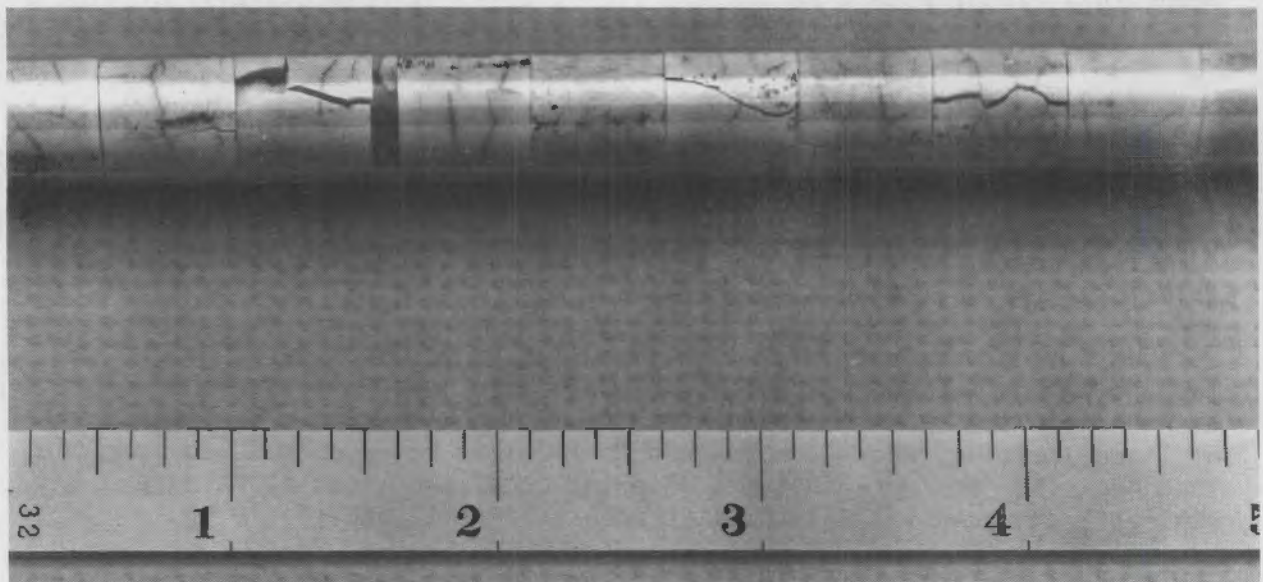
FIGURE 16b. Top of Rod 3 Pellet Column Before Disassembly

Calibration of these instruments was accomplished by inducing known displacements for the LVDTs (feeler gages), and comparing the hydraulic system pressure transducer to a Heise digital readout pressure gage. Tests run with unloaded gage rods showed that repeatability of the installed diameter measurement system was 0.25 to 0.50 μm. This is about 2 to 5 times the LVDT repeatability and is reasonable. The repeatabilities of the axial displacement and pressure measurement systems were comparable to the instrument repeatabilities. However, fuel-induced rod bowing occurred during loading, and probably increased the cladding elongation measurement uncertainty to ±40 μm.

26
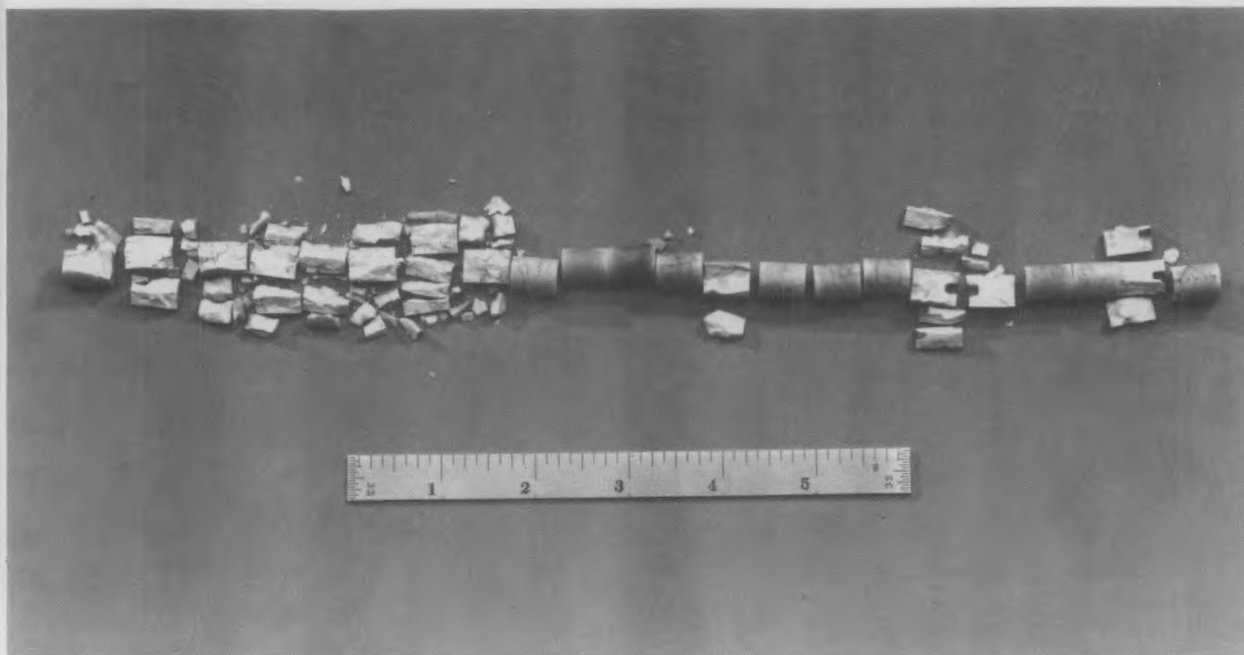
FIGURE 16c. Disassembled Rod 3 Pellet Column, Showing Axial Variation of Cracking

FIGURE 16d. Top of Rod 3 Disassembled Pellet Column

27
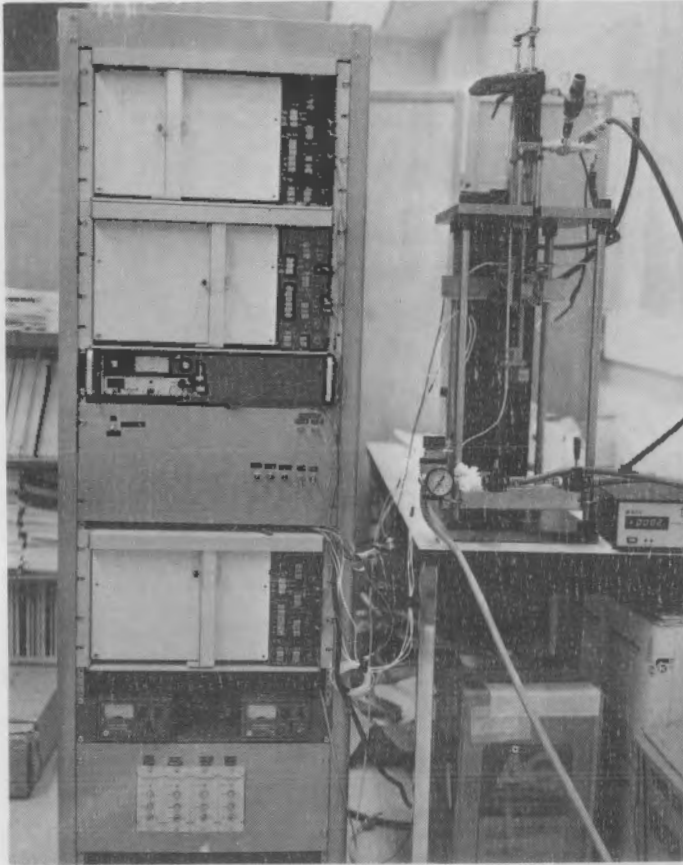
FIGURE 17. Short Rod Compliance Test
Equipment - Overall View
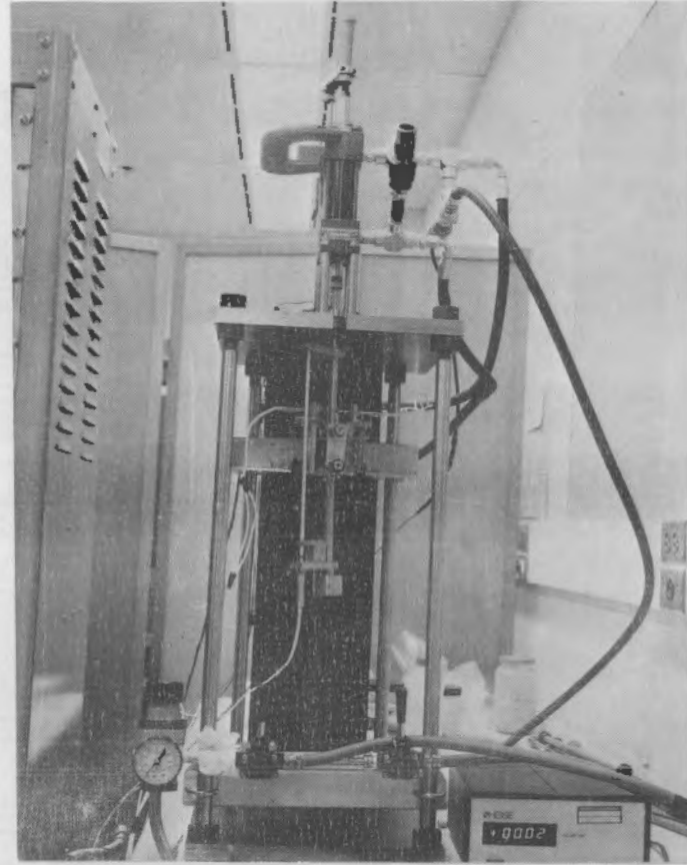
FIGURE 18. Short Rod Compliance Test
Equipment - Load Frame

28
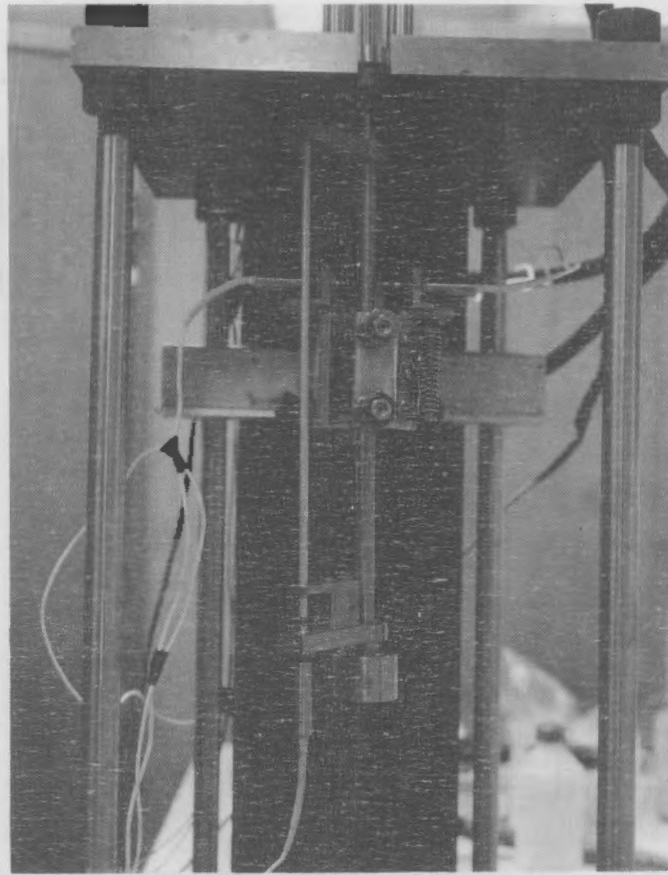
FIGURE 19. Short Rod Compliance Test Equipment,
Diameter Instrument

TABLE 4. Short Rod Compliance Test Instrumentation

Measurement	Instrument	Repeatability
Cladding diameter	2 Schaevitz LVDTs PCA-220-020	± 4 µin. (0.1 µm)
Cladding elongation	Schaevitz LVDT PCA-220-100	± 4 µin. (0.1 µm)
Fuel axial displacement	Schaevitz LVDT GCA-121-050	±25 µin. (0.64 µm)
Fuel axial slipping (friction tests)	Schaevitz LVDT PCA-117-1000	±50 µin. (1.27 µm)
Hydraulic pressure	Schaevitz transducer P701-0001	±0.5%
X-Y recorders	Hewlett Packard HP7015B	--
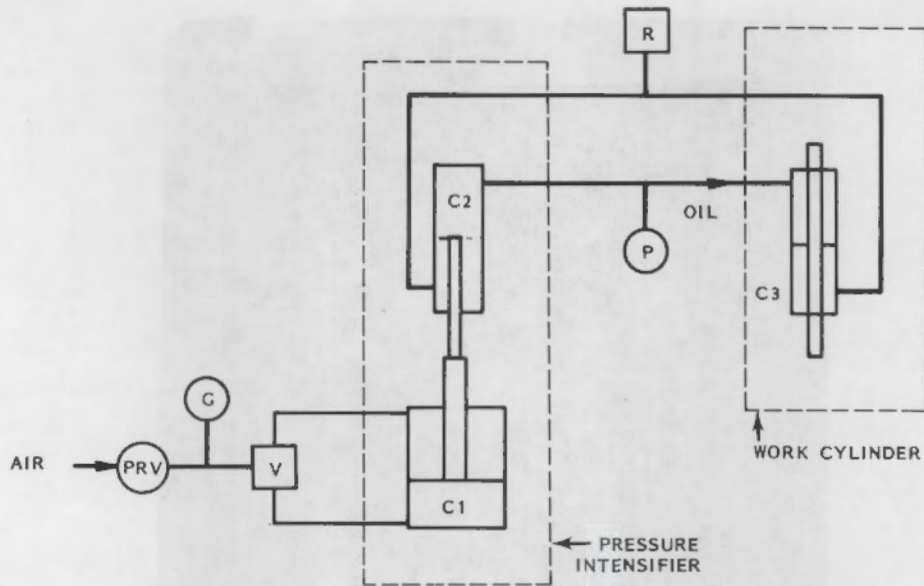
PRV = PRESSURE REDUCING VALVE
G = AIR PRESSURE GAGE
V = DIRECTIONAL CONTROL VALVE
C1 = 6" BORE AIR CYLINDER
C2 = 1 1/8" BORE HYDRAULIC CYLINDER
C3 = 1 1/8" BORE HYDRAULIC CYLINDER
P = PRESSURE TRANSDUCER
R = OIL RESERVOIR

FIGURE 20. Hydraulic Intensifier System for Short Rod Compliance Tests
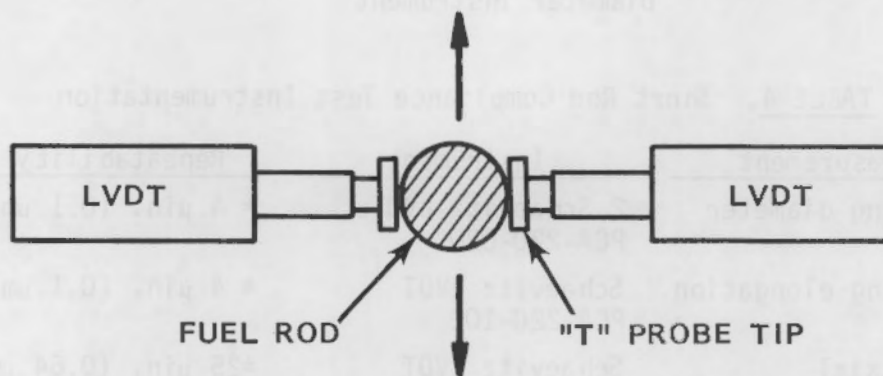
FIGURE 21. Cladding Diameter Measurement System

30

The general test sequence was as follows. The axial load was applied to the top of the fuel column in increments ranging from 130 kg to 200 kg, until a maximum load of about 800 kg was reached. After each load increment, an axial diameter trace was recorded along one generatrix of the cladding. Fuel and cladding axial elongations were recorded continuously. Two such load cycles (ramps) to full load were performed for each rod and the results are discussed below.

Experimental Results

Data from the short rod compliance tests are presented and discussed in the following paragraphs. Subjects covered include: fuel and cladding axial elongations, cladding diameter deformations, deduced effective Young's moduli for the cracked pellets, results of cracked fuel column/cladding friction tests, and results for the sphere pac fuel test.

Fuel and Cladding Axial Strains. The fuel and cladding axial strains for the five pelletized fuel rods are shown in Figures 22 and 23. Note that data for Rod 1 (Ramp 1) are not present because of instrumentation malfunctions. In general, the fuel axial strains were greater than the axial strains predicted for a solid steatite column (free fuel prediction) while the cladding axial strains were less than predicted for an empty tube (free cladding prediction).

The higher than expected axial fuel strains indicate that fuel cracks do have an effect on cracked fuel compliance. Axial strains were generally greater than predicted, even at the lower load ranges, before audible fuel cracking occurred on the first load ramp. This indicates that the pellet-pellet interfaces may also act as cracks and contribute to the reduced effective axial modulus for the fuel column.

An increase in fuel axial strain with load ramp number would indicate that the effects of fuel cracking have reduced the effective modulus, while a decrease in fuel axial strain would indicate that the cracked fuel has become more compacted, partially closing the cracks and increasing the effective axial modulus. Rod 2 shows an increase in axial strain, while Rods 3, 4, and 5 show decreases. Rods 1 and 2 contained flat-ended precracked pellets, while Rods 3, 4, and 5 contained precracked pellets with a small drop of epoxy on one end of each pellet to act as a stress raiser and promote more complete fuel cracking in the first ramp. The results of this procedure are summarized in Table 5, and indicate that the completion of pellet cracking during the first load ramp usually resulted in a decreased fuel axial compliance during the second ramp. Note that no data were recorded for Rod 5 because of attention required for the diameter data (discussed below).

The cladding axial elongation data (Figure 23) also exhibits some Ramp 1 to Ramp 2 effects which are apparently caused by pellet cracking. The Ramp 2 elongations are slightly less than the Ramp 1 elongations for Rods 2, 3, and 4. Rod 5 elongations appear the same for both ramps.

AXIAL LOAD (kg)

200   400   600   800   1000

10^{-2}

10^{-3}

FREE FUEL
PREDICTION

STRAIN

10^{-4}

ROD	RAMP 1	RAMP 2
1	●	●
2	□	■
3	◇	◆
4	△	▲
5	▽	▼

2×10^{-5}

0   1000   2000

AXIAL LOAD (lbs)
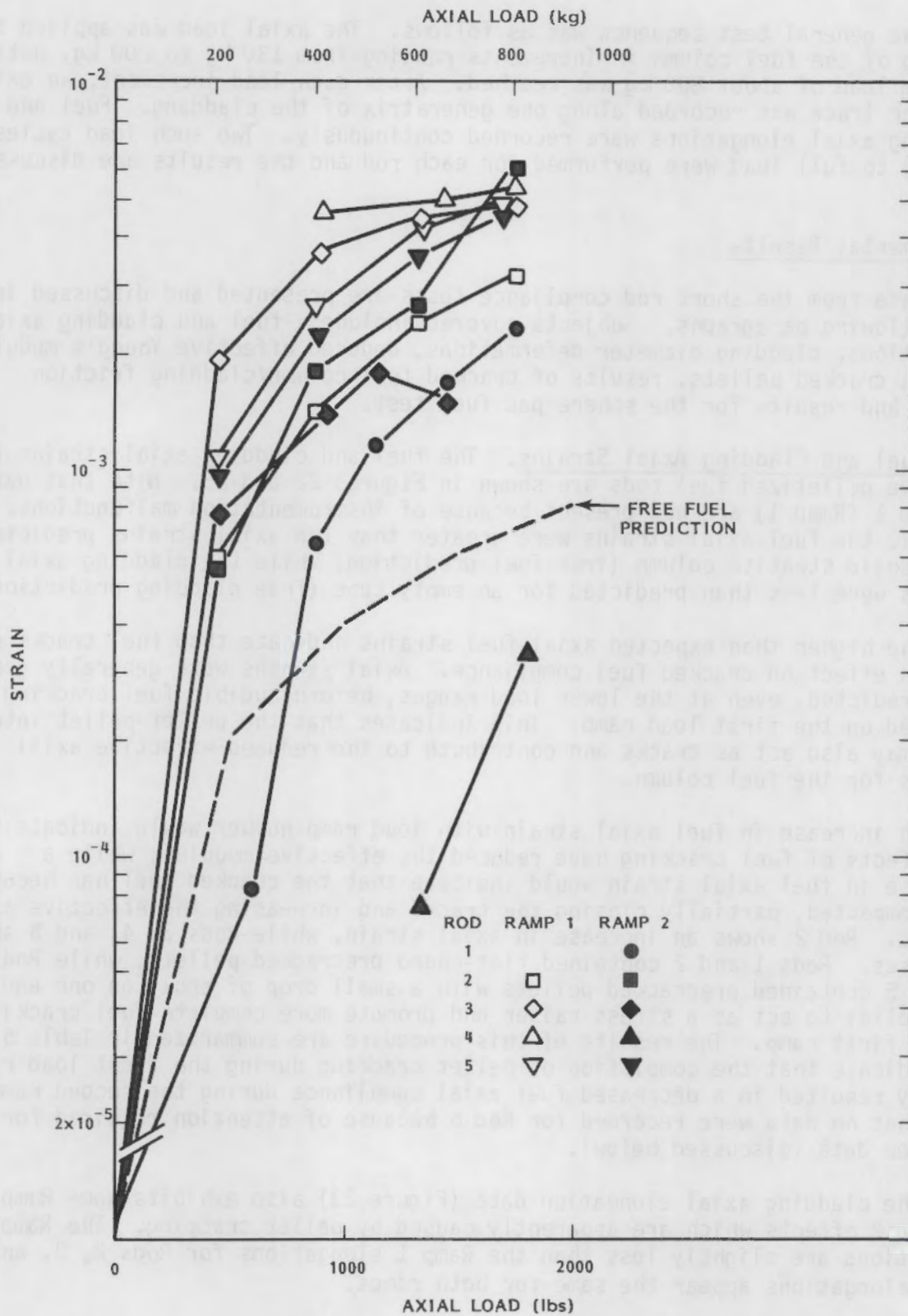
FIGURE 22. Fuel Column Axial Strain for Short Rod Compliance Tests

32
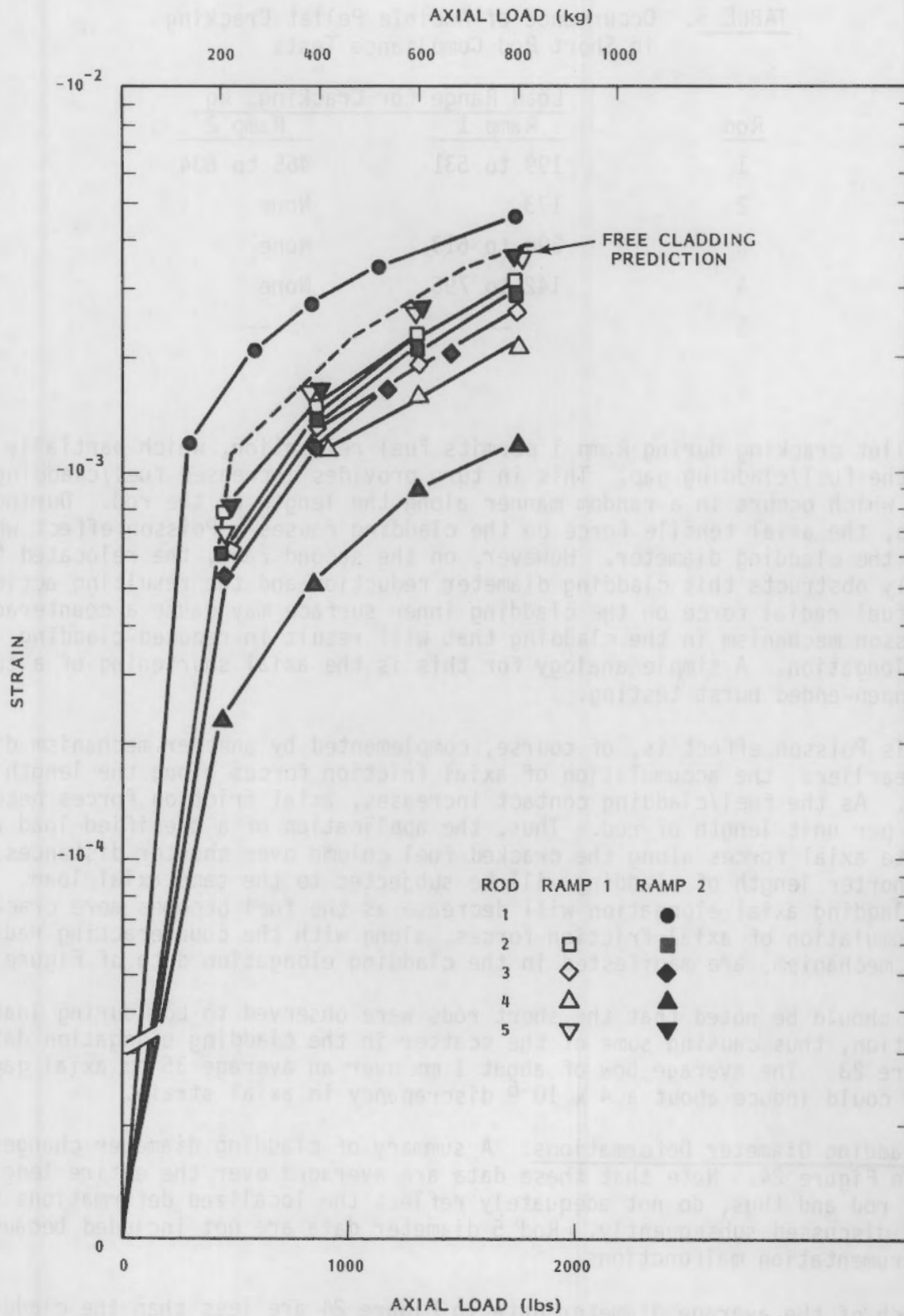
FIGURE 23. Cladding Axial Strain for Short Rod Compliance Tests

TABLE 5. Occurrence of Audible Pellet Cracking
in Short Rod Compliance Tests

	Load Range for Cracking, kg	
Rod	Ramp 1	Ramp 2
1	199 to 531	465 to 604
2	173	None
3	398 to 613	None
4	142 to 796	None
5	--	--

Pellet cracking during Ramp 1 permits fuel relocation, which partially closes the fuel/cladding gap. This in turn provides increased fuel/cladding contact which occurs in a random manner along the length of the rod. During any ramp, the axial tensile force on the cladding causes a Poisson effect which reduces the cladding diameter. However, on the second ramp, the relocated fuel partially obstructs this cladding diameter reduction and the resulting action of the fuel radial force on the cladding inner surface may cause a counteracting Poisson mechanism in the cladding that will result in reduced cladding axial elongation. A simple analogy for this is the axial shortening of a tube during open-ended burst testing.

This Poisson effect is, of course, complemented by another mechanism discussed earlier: the accumulation of axial friction forces along the length of the rod. As the fuel/cladding contact increases, axial friction forces become greater per unit length of rod. Thus, the application of a specified load will propogate axial forces along the cracked fuel column over shorter distances, and a shorter length of cladding will be subjected to the same axial load. The total cladding axial elongation will decrease as the fuel becomes more cracked. The accumulation of axial friction forces, along with the counteracting radial Poisson mechanism, are manifested in the cladding elongation data of Figure 23.

It should be noted that the short rods were observed to bow during load application, thus causing some of the scatter in the cladding elongation data of Figure 23. The average bow of about 1 mm over an average 35 cm axial gage section could induce about a 4×10^{-6} discrepancy in axial strain.

Cladding Diameter Deformations. A summary of cladding diameter changes is shown in Figure 24. Note that these data are averaged over the entire length of each rod and thus, do not adequately reflect the localized deformations that will be discussed subsequently. Rod 5 diameter data are not included because of instrumentation malfunctions.

Much of the average diameter data in Figure 24 are less than the cladding diameter reductions that are predicted for empty cladding subjected to the same

34
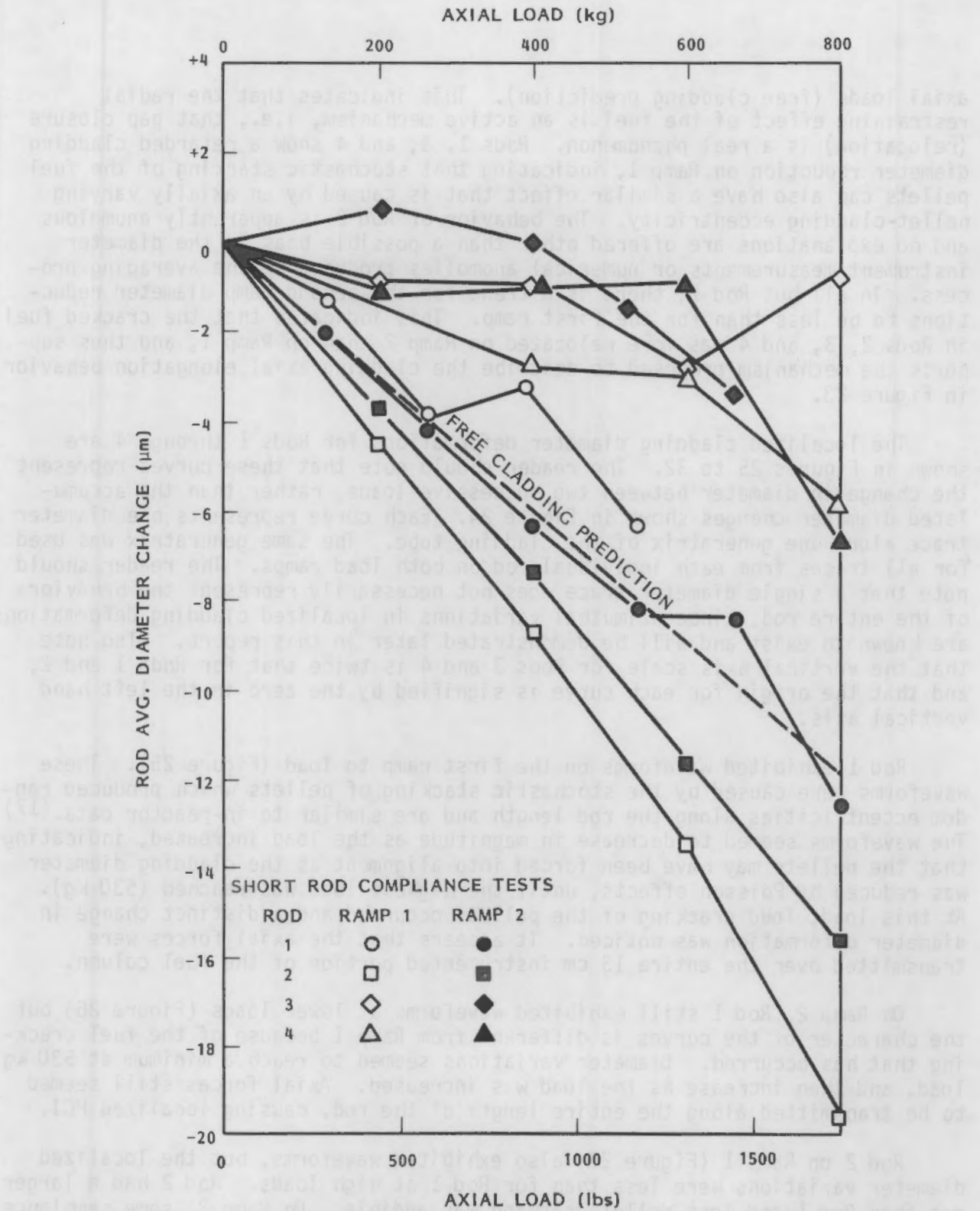
FIGURE 24. Rod Average Diameter Changes for Short Rod Compliance Tests

axial loads (free cladding prediction). This indicates that the radial restraining effect of the fuel is an active mechanism, i.e., that gap closure (relocation) is a real phenomenon. Rods 1, 3, and 4 show a retarded cladding diameter reduction on Ramp 1, indicating that stochastic stacking of the fuel pellets can also have a similar effect that is caused by an axially varying pellet-cladding eccentricity. The behavior of Rod 2 is apparently anomolous and no explanations are offered other than a possible bias in the diameter instrument measurements or numerical anomolies produced by the averaging process. In all but Rod 1, there is a trend for the second ramp diameter reductions to be less than for the first ramp. This indicates that the cracked fuel in Rods 2, 3, and 4 was more relocated on Ramp 2 than on Ramp 1, and thus supports the mechanism proposed to describe the cladding axial elongation behavior in Figure 23.

The localized cladding diameter deformations for Rods 1 through 4 are shown in Figures 25 to 32. The reader should note that these curves represent the change in diameter between two successive loads, rather than the accumulated diameter changes shown in Figure 24. Each curve represents one diameter trace along one generatrix of the cladding tube. The same generatrix was used for all traces from each individual rod on both load ramps. The reader should note that a single diameter trace does not necessarily represent the behavior of the entire rod, since azimuthal variations in localized cladding deformations are known to exist and will be demonstrated later in this report. Also note that the vertical axis scale for Rods 3 and 4 is twice that for Rods 1 and 2, and that the origin for each curve is signified by the zero in the left hand vertical axis.

Rod 1 exhibited waveforms on the first ramp to load (Figure 25). These waveforms were caused by the stochastic stacking of pellets which produced random eccentricities along the rod length and are similar to in-reactor data.[17] The waveforms seemed to decrease in magnitude as the load increased, indicating that the pellets may have been forced into alignment as the cladding diameter was reduced by Poisson effects, until the highest load was reached (530 kg). At this load, loud cracking of the pellets occurred and a distinct change in diameter deformation was noticed. It appears that the axial forces were transmitted over the entire 13 cm instrumented portion of the fuel column.

On Ramp 2, Rod 1 still exhibited waveforms at lower loads (Figure 26) but the character of the curves is different from Ramp 1 because of the fuel cracking that has occurred. Diameter variations seemed to reach a minimum at 530 kg load, and then increase as the load was increased. Axial forces still seemed to be transmitted along the entire length of the rod, causing localized PCI.

Rod 2 on Ramp 1 (Figure 27) also exhibited waveforms, but the localized diameter variations were less than for Rod 1 at high loads. Rod 2 had a larger gap than Rod 1 and less pellet cracking was audible. On Ramp 2, some semblance of waveforms remained at low loads, no further cracking was heard, and the diameter reductions were remarkably uniform (Figure 28). This indicated that the
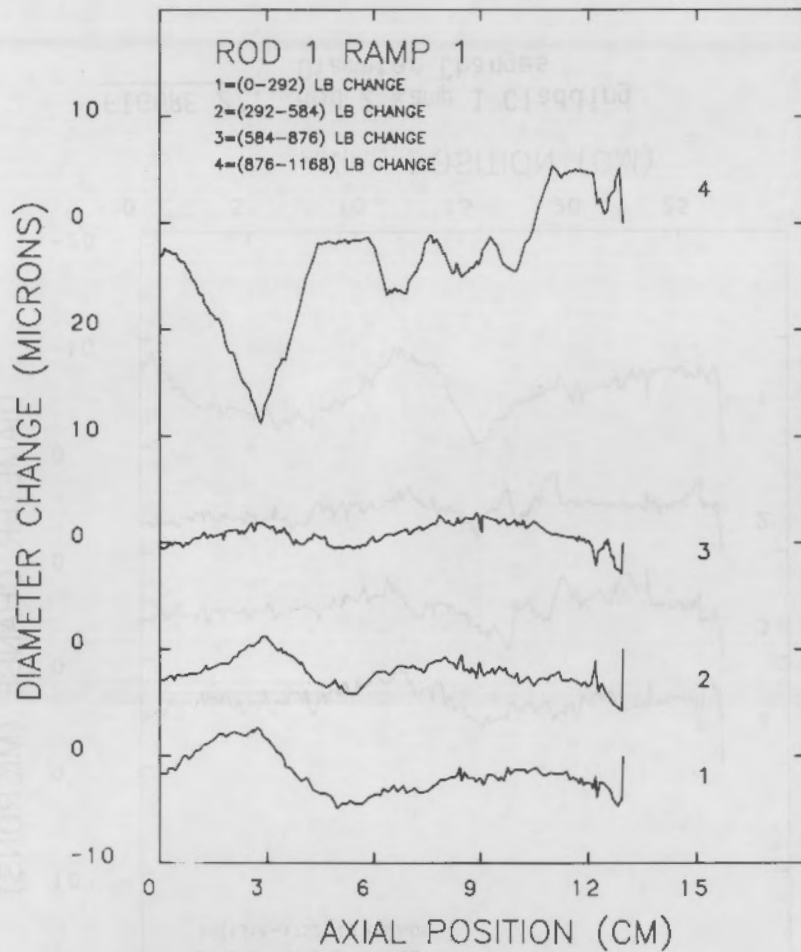
FIGURE 25. Rod 1 Ramp 1 Cladding
Diameter Changes
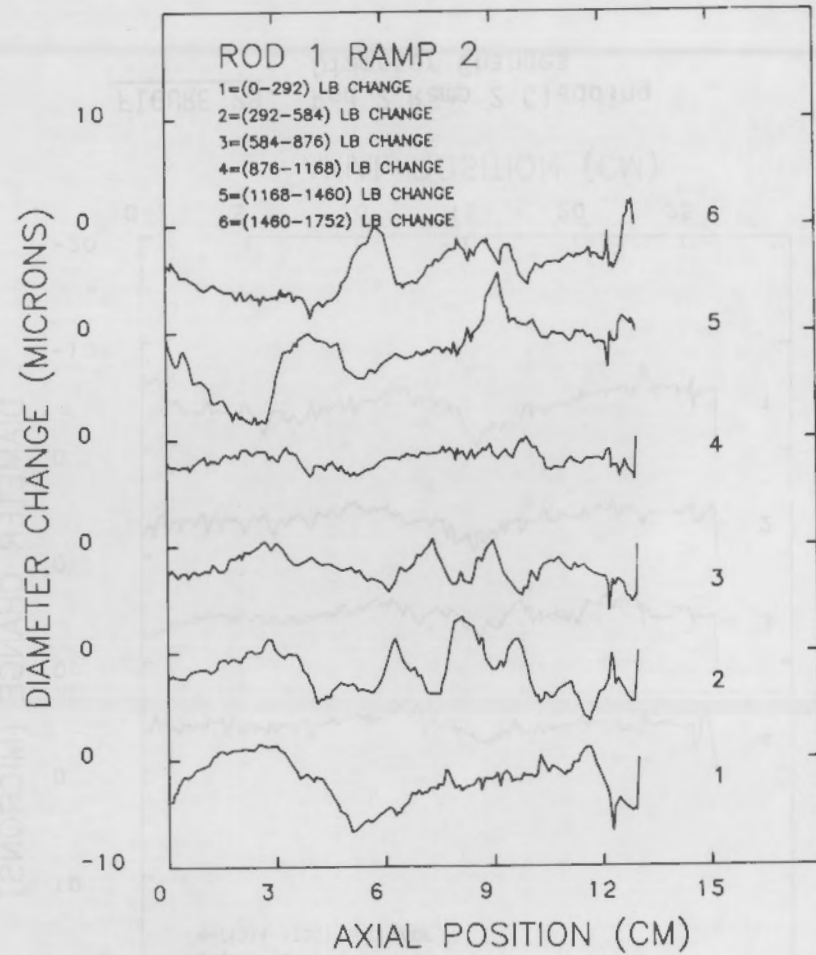
FIGURE 26. Rod 1 Ramp 2 Cladding
Diameter Changes

37
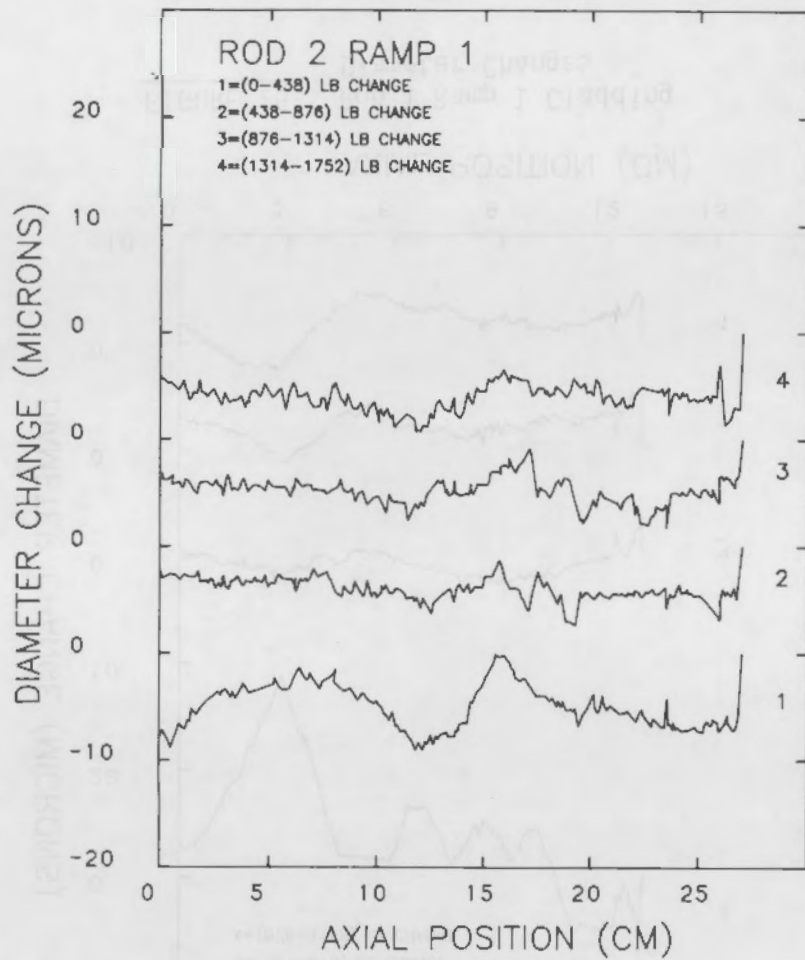
FIGURE 27. Rod 2 Ramp 1 Cladding Diameter Changes
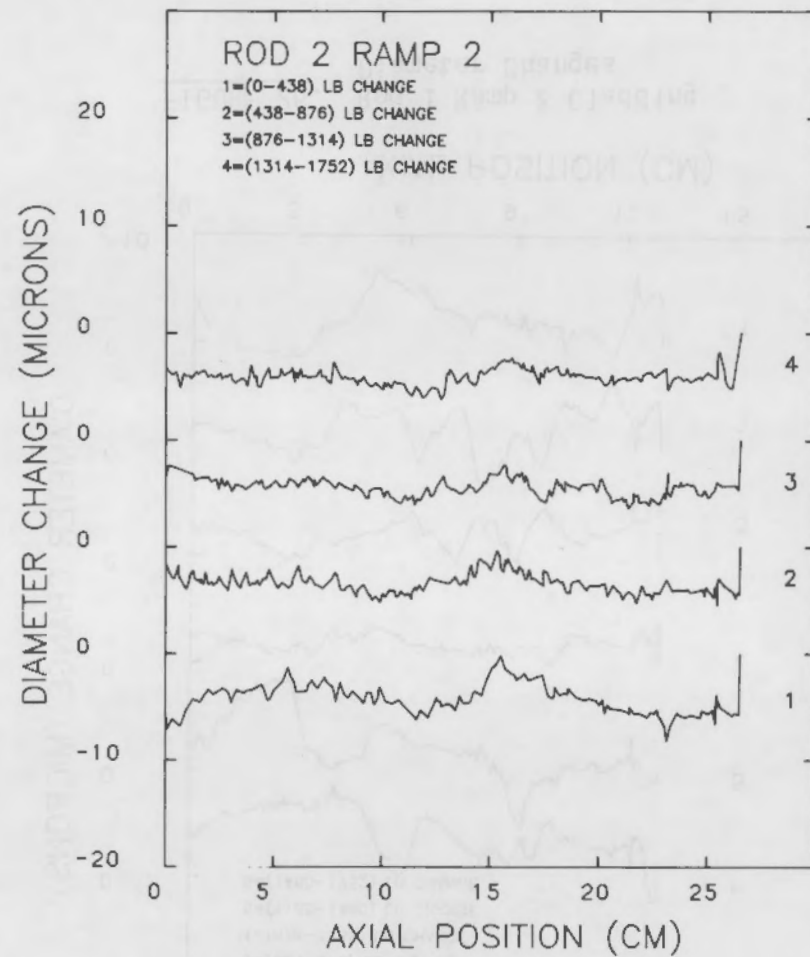
FIGURE 28. Rod 2 Ramp 2 Cladding Diameter Changes

38
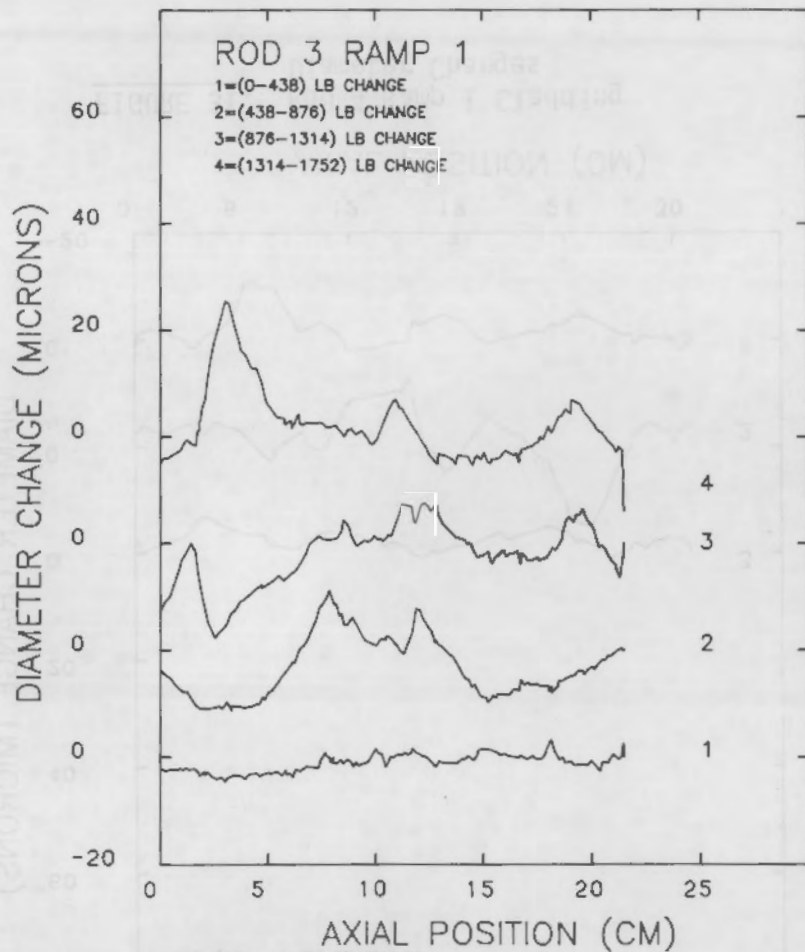
FIGURE 29.   Rod 3 Ramp 1 Cladding
Diameter Changes
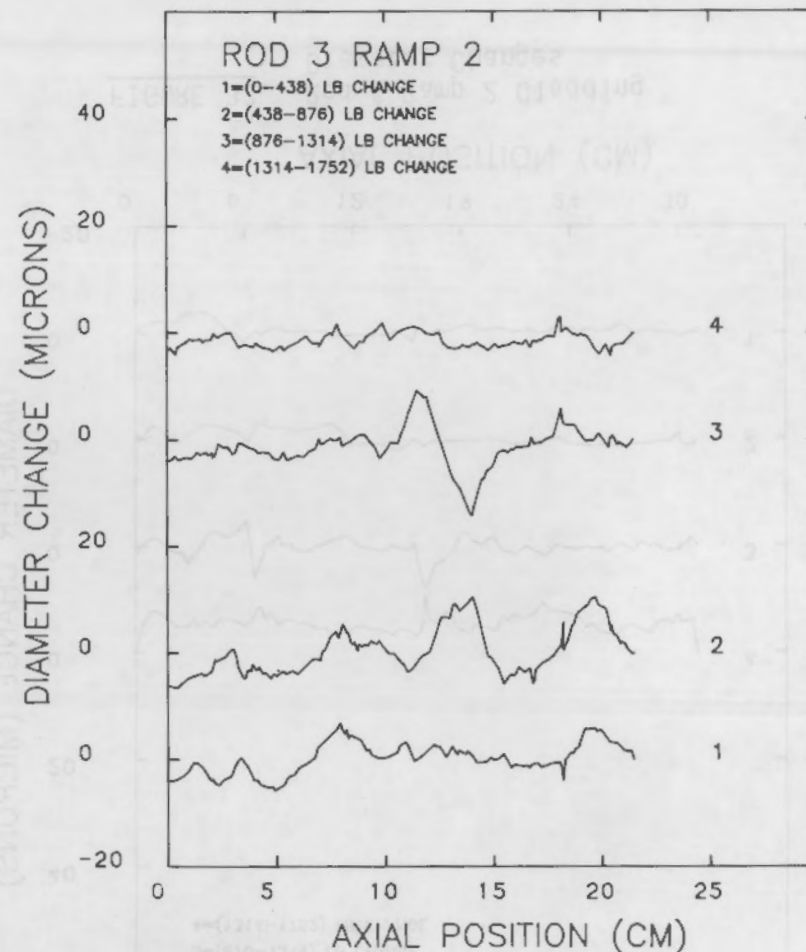
FIGURE 30.   Rod 3 Ramp 2 Cladding
Diameter Changes

39

ROD 4 RAMP 1
1=(0-876) LB CHANGE
2=(876-1314) LB CHANGE
3=(1314-1752) LB CHANGE

ROD 4 RAMP 2
1=(0-438) LB CHANGE
2=(438-876) LB CHANGE
3=(876-1314) LB CHANGE
4=(1314-1752) LB CHANGE

DIAMETER CHANGE (MICRONS)

AXIAL POSITION (CM)
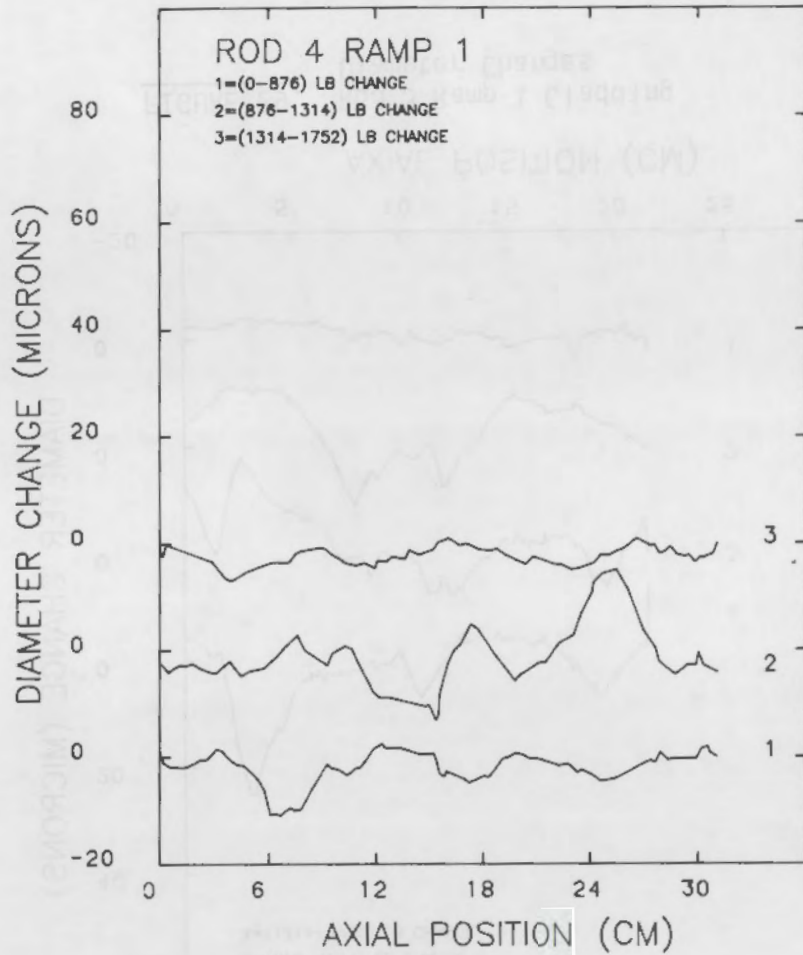
FIGURE 31. Rod 4 Ramp 1 Cladding
Diameter Changes
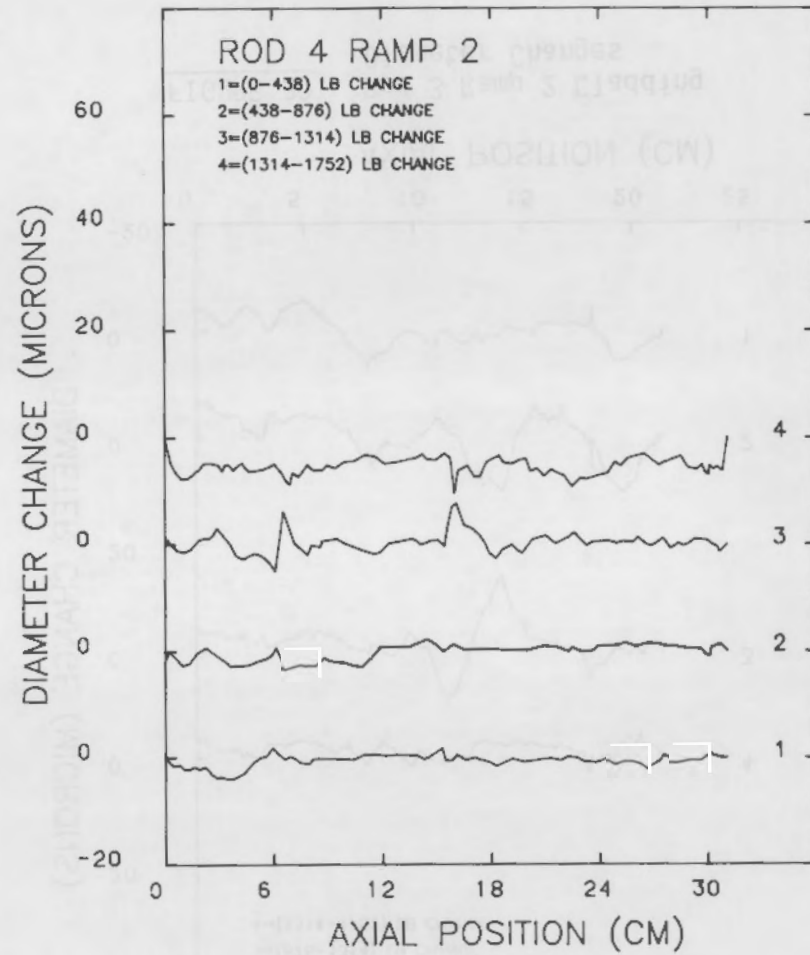
FIGURE 32. Rod 4 Ramp 2 Cladding
Diameter Changes

fuel column had apparently become aligned so that the gap was more uniform than before, and axial forces were tansmitted along the entire length of the mostly uncracked fuel column (~27 cm).

The behavior of Rod 2 showed that some additional measures had to be taken to ensure that the steatite pellets would crack when loaded. A small drop of epoxy resin was placed on one end of each pellet for Rods 3, 4, and 5. This provided a stress riser and was an extreme simulation of pellet hourglassing effects that cause bulged end faces.

The results of this procedure as shown in Figures 29 and 30 for Rod 3, Ramps 1 and 2. Rod 3 had the same gap as Rod 2. Rod 3 pellet cracking was much more pronounced during first ramp loading and did not occur during the second ramp. The first ramp cladding diameter deformations for Rod 3 showed a noticeably different character than Rod 2, with localized deformations increasing with load to significantly larger values than for Rod 2. At higher loads in Ramp 1, Rod 3 seemed to exhibit more dramatic localized PCI (pellet-cladding interaction) near the top of the rod than at the bottom. Although the axial forces still appear to be transmitted over the whole rod length, there was a significant axial gradient of PCI in Rod 3.

On Ramp 2 for Rod 3 (Figure 30), PCI seemed to increase through the mid-range loads, and then decrease at the highest load (796 kg). Axial loads seemed to be transmitted over the whole rod length at lower loads, but were significantly reduced at the higher loads.

Rod 4 used the same diameter pellets as Rod 1, and thus had the same gap size but also had epoxy stress risers as previously described. Rod 4 on Ramp 1 (Figure 31) shows PCI over the whole rod length (31 cm) until the highest load is reached. Cracking occurred throughout most of Ramp 1. On Ramp 2 (Figure 32), no further cracking occurred and localized cladding deformations were significantly less than on Ramp 1. Rod 4 average cladding diameter did not appear to change significantly until the peak load was reached. The uniform diameter reduction with minimal localized PCI at peak load would indicate that axial loads were transmitted over the whole rod length, and is an apparent anomoly considering the fuel/cladding friction accumulation hypothesis discussed above. However, localized PCI seemed to occur more near the top of the rod. No diameter traces were obtained for Rod 5 because of diameter instrument malfunctions.

The variability in the responses of Rods 1 through 4 indicates that PCI is relatively sensitive to changes in gap size and the extent of pellet cracking. It also appears that for these short simulated fuel rods, axial forces were in general transmitted over the entire fuel column length (about 31 cm) on the first load ramp, but PCI was frequently more localized near the top half of the rods on the second ramp when the fuel was totally cracked (Rods 3 and 4).

The Sphere Pac Experiment. A compliance test was also performed on a sphere pac design fuel using 500 μm diameter alumina spheres as in Reference 18. These spheres were loaded into the emptied cladding that had been used for the

41

Rod 5 experiment and was then installed in the compliance testing machine. The spheres were all the same diameter and no special packing procedure was used other than shaking and tapping the rod to settle the sphere pac medium. Thus, the smear density of the sphere pac rod was about the same as the theoretical packing fraction (~65%). Dimensional and weight measurements confirmed this expectation.

Four loading ramps were performed in the sphere pac design (Rod 6). During these ramps the fuel was compressed axially (Figure 33), but there was no significant axial or diametral deformation of the cladding. This would indicate that the fuel itself had totally absorbed the strain energy supplied by the axial load. Some small cracking sounds were audible during the first few ramps, and it is concluded that the crushing of the alumina spheres combined with the low shear strength of the sphere pac system were responsible for the lack of cladding response.

The sphere pac fuel axial deformations are shown in Figure 33. During the first load ramp, there was noticeable axial slipping or relaxation of the fuel column that occurred at constant load while the diameter traces were being recorded. Axial slipping was noticeable only at higher loads during the second ramp, and were not measurable for later ramps.
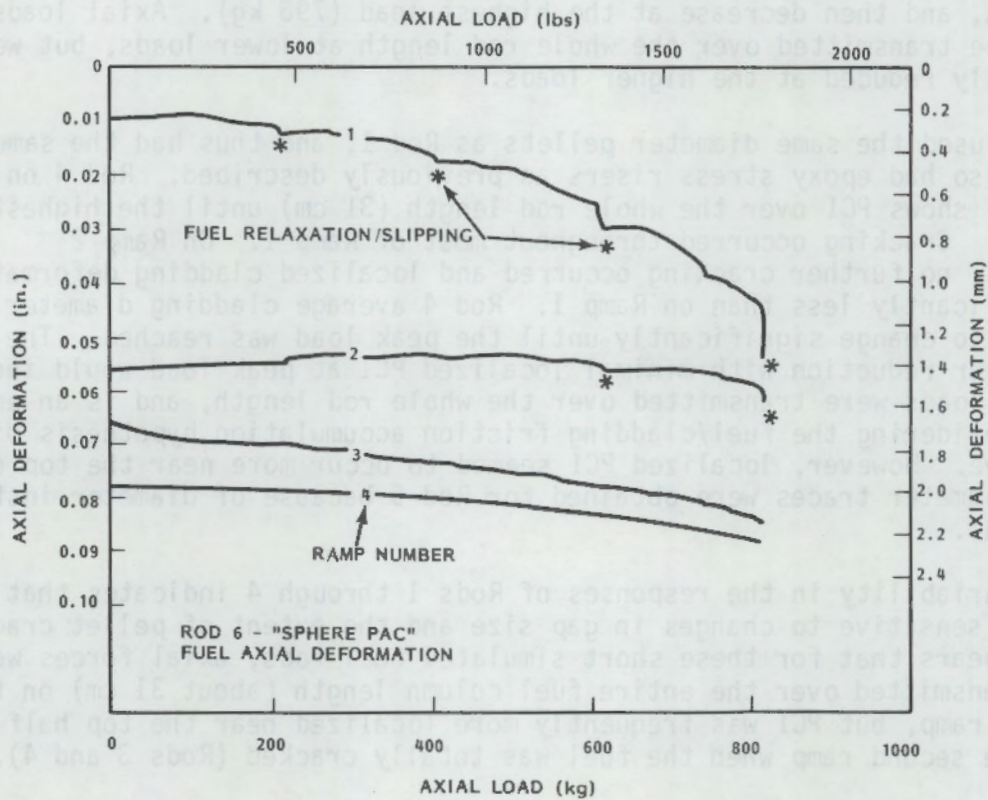
FIGURE 33. Sphere Pac (Rod 6) Axial Elongation

42

When the alumina spheres were removed from the cladding after Ramp 4, it was found that the crushing of the spheres was confined to the top 2 to 3 cm of the fuel column. A fine alumina dust also adhered to the inside of the cladding in this region. The strain energy absorbtion by the sphere pac in this region had apparently been so complete that, if there was any change in cladding diameter, it was uniformly distributed and of such small magnitude that it was not measureable.

The sphere pac design (Rod 6) thus represented an extreme case of cracked fuel, where the "fragments" were so small that all the supplied strain energy was absorbed within the top few centimeters of axial length.

Effective Young's Moduli. The load-deformation data for Rods 1 through 4 were used to deduce the effective Young's moduli for the cracked fuel systems. Since both radial and axial deformation data were needed from each rod, Rod 1 (Ramp 1) and Rod 5 are not included in this analysis. The sphere pac rod will be discussed subsequently. The reader should note that the following analysis is purely elastic and contains no explicit terms to separate either plastic deformations or the viscous axial slipping/relaxation phenomena from the basic elastic response. Thus, the effective moduli deduced from these data include all of these phenomena. The analysis was also intended to infer effective moduli for short (but finite) lengths of fuel columns. Thus, the effective moduli are rod average values for the short rod lengths tested.

For this analysis, the cracked fuel/cladding system was considered as a "solid" system composed of two materials. The cracked fuel was assumed to be a "homogenous" medium in intimate contact with the cladding and axial slipping was ignored. Thus, the concept of the "gap" is not addressed in this analysis. The object of these assumptions was to avoid the necessity of making further assumptions about the effective gap roughness, effective crack roughnesses, and total crack lengths. Thus, the results of the effective moduli deduced from the in-reactor data were tested in as independent a manner as possible.

The fuel cracks were assumed to be primarily radial (confirmed by post-test examination) so that as the fuel expanded (relocated), the fragments moved as rigid bodies. Thus, the radial strain ($\epsilon_r = \partial u/\partial r$) was assumed to be negligible. The hoop and radial stresses for the cracked fuel were assumed to be equal, i.e., a hydrostatic stress state in the transverse plane. Then Hooke's Law for the cracked fuel becomes:

$$0 = \frac{\sigma_r}{E_r} - \frac{\nu\sigma_r}{E_\theta} - \frac{\nu\sigma_z}{E_z} \qquad [1]$$

$$\epsilon_\theta = \frac{\sigma_r}{E_\theta} - \frac{\nu\sigma_r}{E_r} - \frac{\nu\sigma_z}{E_z} \qquad [2]$$

43

$$\varepsilon_z = \frac{\sigma_z}{E_z} - \frac{\nu \sigma_r}{E_r} - \frac{\nu \sigma_r}{E_\theta} \qquad [3]$$

where it was assumed that Poisson's ratio was the same for all three principal directions and equal to 0.25.[2] With three equations and three unknowns (E_r, E_θ, E_z), we can solve for the effective moduli for the cracked fuel:

$$E_r = \frac{\sigma_r (1+\nu)(1-2\nu)}{\nu(\varepsilon_\theta + \varepsilon_z)} \qquad [4]$$

$$E_\theta = \frac{\sigma_r (1+\nu)(1-2\nu)}{(1-\nu)\varepsilon_\theta + \nu\varepsilon_z} \qquad [5]$$

$$E_z = \frac{\sigma_z (1+\nu)(1-2\nu)}{\nu\varepsilon_\theta + (1-\nu)\varepsilon_z} \qquad [6]$$

The stresses and strains were deduced from the measured load/deformation data. The axial strain for the cracked fuel column (ε_z) was found by subtracting the cladding axial elongation (corrected for gage length versus total length) from the total axial deflection (fuel compression plus cladding elongation) measured at the top of the fuel column. Since the fuel and cladding were assumed to be in contact, the fuel hoop strain (ε_θ) was assumed to be equal to the measured cladding hoop strain.

The rod average cladding axial stress was computed from the plane stress equation:

$$\sigma_{zc} = \frac{E_c}{1 - \nu^2} (\varepsilon_{zc} + \nu\varepsilon_{\theta c}) \qquad [7]$$

where $\varepsilon_{\theta c}$ and ε_{zc} were determined from cladding average diameter and axial deformation measurements, and ν is taken as 0.3. The rod average axial stress for the cracked fuel column (σ_z) was computed from the rod average axial stress for the cladding by a simple ratio of cross-sectional areas in the transverse plane. This approach was taken rather than using the load applied at the top of the fuel column because the accumulation of axial friction forces via fuel/cladding contact reduces fuel axial stresses along the length of the fuel rod.

44

The fuel radial stress (σ_r) was determined by assuming that the cladding acts as a thin shell in plane stress ($\sigma_{rclad} = 0$), and that the fuel radial stress acted as an "internal pressurization" that prevented the cladding diameter from being reduced to its theoretical value by Poisson mechanisms associated with the cladding axial deformation. If the cladding was empty (no fuel), then the "theoretical" cladding diameter reduction caused by the measured axial cladding strain would be:

$$\epsilon_{\theta Tc} = -\nu \epsilon_{zc} \qquad [8]$$

However, because the cracked fuel is present and in contact with the cladding, it prevents the cladding diameter from being reduced by its full theoretical amount. The difference between actual and theoretical cladding hoop strains is:

$$\epsilon_{\theta D} = \epsilon_{\theta c} - \epsilon_{\theta Tc} \qquad [9]$$

If the thin wall formula is used to describe this cladding hoop strain discrepancy, we have:

$$\sigma_{\theta c} = \frac{Pr}{t} = E_c \epsilon_{\theta D} \qquad [10]$$

where $\sigma_{\theta c}$ = cladding hoop stress discrepancy
  P = internal pressurization and is equal to the compressive radial stress on the fuel, σ_r
  r = shell radius
  t = shell thickness
  E_c = cladding Young's Modulus.
Thus, the rod average fuel radial stress is given by:

$$\sigma_r = \frac{t}{r} E_c \epsilon_{\theta D} \qquad [11]$$

The above method was used to deduce effective elastic moduli for the cracked fuel samples from the load/deformation data. This was performed in an incremental manner—that is, the changes in stresses and strains from one load level to the next were used to calculate the secant moduli along the nonlinear stress/strain curve for the cracked fuel. This method yields a better representation of the nonlinearity of the effective moduli. The results are plotted in Figure 34 versus the average stresses over the load ranges noted in Figures 25 through 32.

45
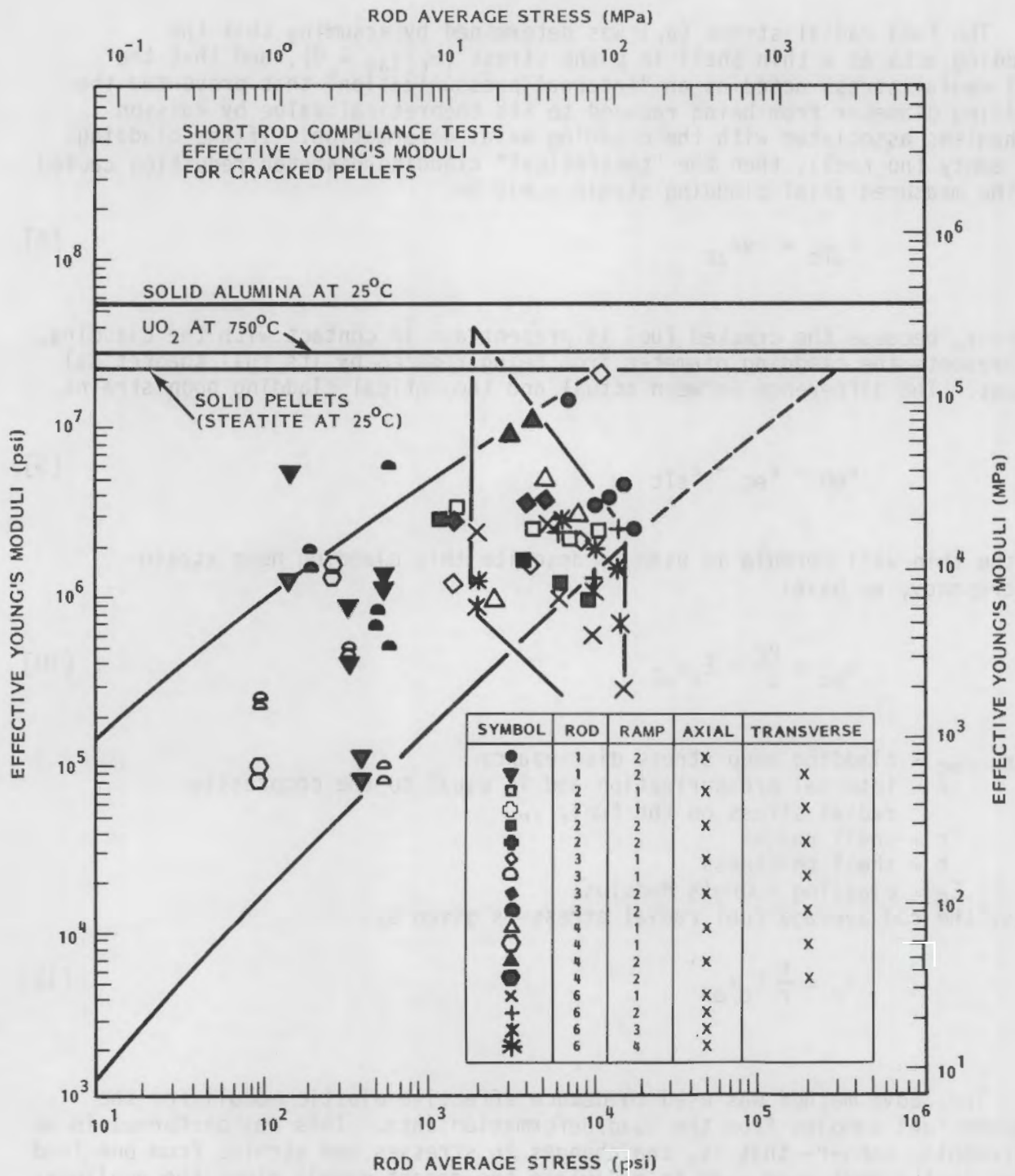
FIGURE 34. Effective Moduli for Short Rod Compliance Tests

The effective moduli for the sphere pac design (Rod 6) are also shown in Figure 34. These were computed from the simplest form of Hooke's Law ($\sigma = E\epsilon$), and no account is made for Poisson effects, plastic deformations, or axial slipping between fuel and cladding that were apparent in Figure 33. Rod 6 effective moduli are included for the purpose of comparison. Because of the negligible cladding deformation response for Rod 6, the axial gage length used to calculate effective moduli in Figure 34 was taken as the 3-cm alumina crushing distance observed during post-test examination. Rod 6 data are shown outlined by the diamond-shaped boundary in Figure 34, the reason for which will become clear in the next few paragraphs.

Certain general characteristics should be noted in Figure 34. In general, the data appear scattered, but all effective moduli are less than the corresponding solid pellet moduli shown by the bold horizontal lines. The effective moduli approach the solid moduli as rod average stresses increase, which is consistent with the crack closure model discussed earlier. Thus the reduction in effective moduli caused by pellet cracking was confirmed. These data compare well with the in-reactor data which will be discussed in the next section.

Also in Figure 34, there is a grouping of transverse moduli of lower stresses and axial moduli at higher stresses. This was expected because of the loading system utilized. In-reactor transverse or axial stress states can conceivably vary anywhere along the horizontal axis. However, the consistent upward trend of the short rod test data indicates that radial and axial cracks behave similarly, and thus that the data base as a whole is adequate for estimating in-reactor effective moduli for cracked fuel systems.

Although the data are scattered, some indications of ramp-dependent trends may have occurred. There may be a tendency for the transverse moduli to increase with loading ramp for Rods 3 and 4, where more complete cracking occurred on the first ramp. Thus ramp 2 data indicates that the fuel was becoming more compacted, and is consistent with the crack closure hypothesis presented earlier. The same trend appears for the Rod 3 axial data. Rod 2 had no stress risers on the pellet ends, and thus did not complete the cracking sequence on Ramp 1.

The sphere pac design (Rod 6) also indicates a slightly increasing effective axial modulus as the ramp number increases due to compaction (closure of many small "cracks"). Also for Rod 6, there is a trend for the axial modulus to decrease as the load increases. This is shown by the diamond shaped outline around Rod 6 data. This decreasing trend indicates that sphere crushing/shear/slipping mechanisms are important for the limiting "small fragment" case. The pelletized designs also show similar trends, indicating that axial slipping/relaxation were important for these tests. Also note that the cracked/solid modulus ratio was less for the sphere pac design (alumina) than for the pelletized design (steatite), indicating that the more the "cracks," the less the effective modulus.

Acknowledging the axial slipping/decreasing modulus trend allows certain hypotheses to be proposed from Figure 34. If we assume that the upper edge of the data base envelope represents the maximum effective modulus, and the lower

47

edge of the envelope represents the minimum, then the passage from maximum to minimum represents the effects of axial slipping/relaxation/etc. From the scattered data available, a first approximation to this modulus reduction path may be taken as approximately perpendicular to the maximum/minimum envelope lines. Unfortunately, the time required to traverse this path was not recorded in these experiments, so no comparison to in-reactor fuel rod relaxation data can be made. However, these times were recorded for the long rod tests performed at AERE Harwell, and will be discussed in the following section. The only data available from the short rod tests for evaluating the viscous axial slipping effect was in the form of "push-through" friction tests, which are discussed below.

Friction Tests

The data collected from the Rod 4 axial "push-through" friction tests are shown in Figures 35 to 37. This experiment was conducted after the standard load ramps were performed by removing the lower end cap and inserting a loose fitting tissue plug into the lower end of the cladding to prevent pellet fragments from falling out. The tissue plug provided no resistance to axial slipping between fuel and cladding.

The object of this experiment was to determine the friction characteristics of a cracked fuel column, and to investigate any possible difference in static/dynamic friction coefficients. The data are also useful for evaluating the stress level at which axial slipping becomes a factor in the effective modulus calculations which were discussed in the preceeding paragraphs.

From Figures 35, 36, and 37, the axial loads and cladding axial strains at which gross fuel cladding axial slipping occurred are as follows (Table 6):

TABLE 6. Axial Friction Tests

Test	Axial load (lb)	(kg)	Clad axial strain
1	675	307	1.44×10^{-4}
2	900	409	1.47×10^{-4}
3	1090	495	2.72×10^{-4}

Each test began from zero load and axial slipping began where it had stopped on the previous friction test. Note that the "breakaway" load seems to increase slightly with friction test number, and that there was a residual cladding axial elongation that remained after load removal at the end of each test. This indicates that the fuel column was becoming more intimately locked to the cladding as the tests proceeded. On the last test, the cladding elongation exhibited a dramatic reduction as axial slipping began, and returned to a

48
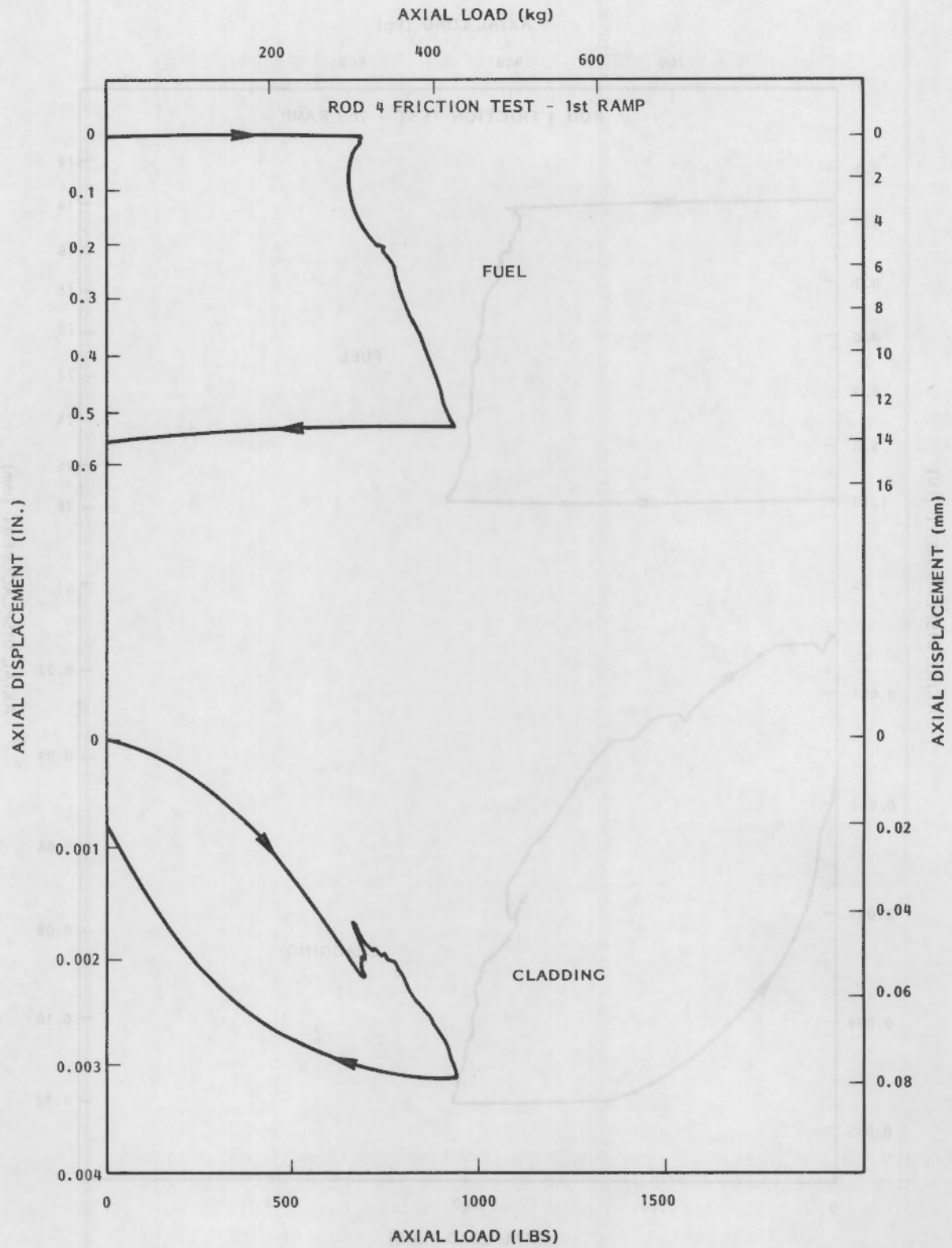
FIGURE 35. Axial Friction Test No. 1 for Rod 4

49
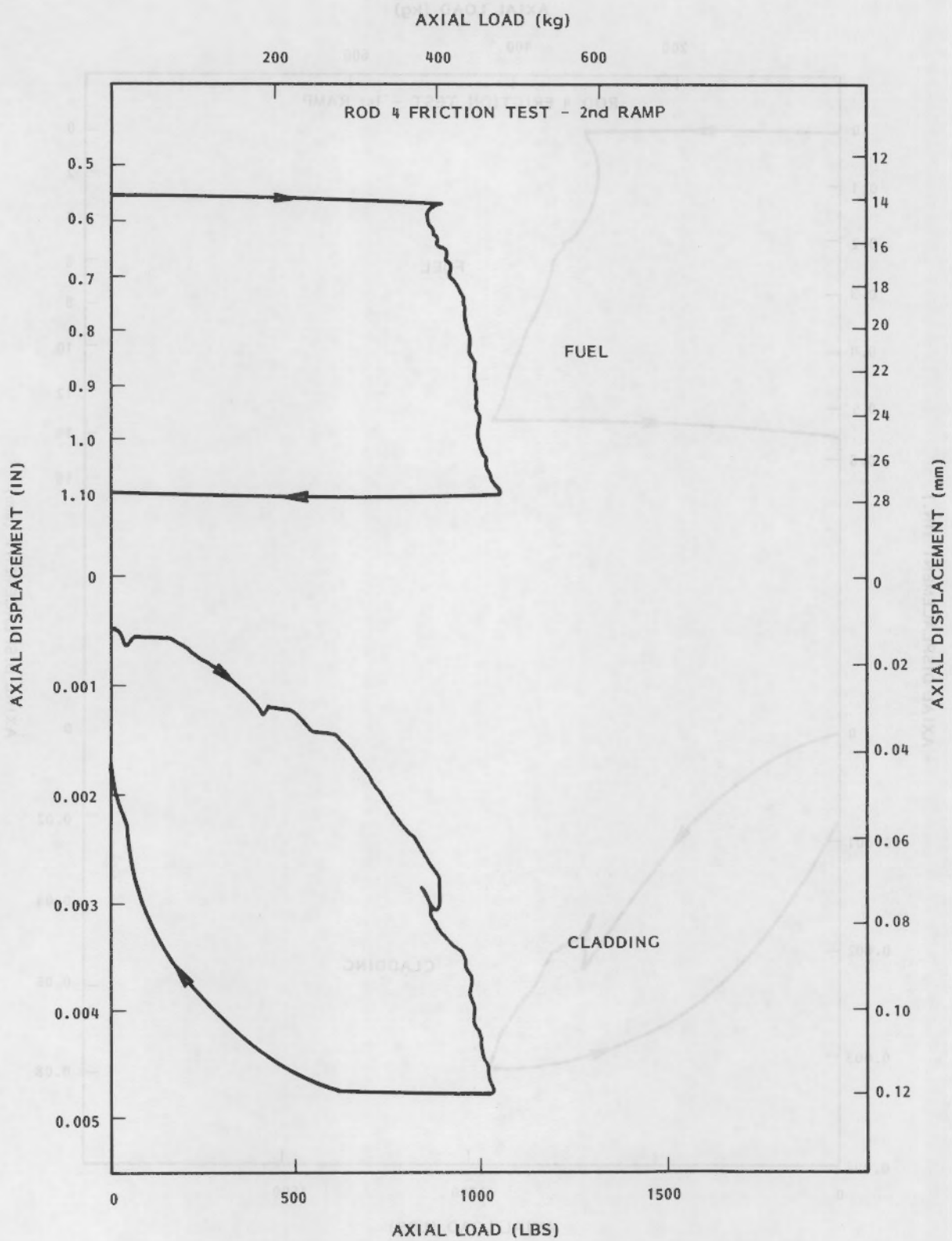
FIGURE 36. Axial Friction Test No. 2 for Rod 4

50

200   400   600

ROD AND FRICTION TEST - 3rd RAMP

FUEL

CLADDING

AXIAL DISPLACEMENT (IN)

AXIAL DISPLACEMENT (mm)

1.0 24
1.1 26 28
1.2 30 32
1.3 34

0   0

0.001 0.02 0.04
0.002 0.06
0.003 0.08
0.004 0.10 0.12
0.005 0.14
0.006 0.16

0   500   1000   1500

AXIAL LOAD (LBS)
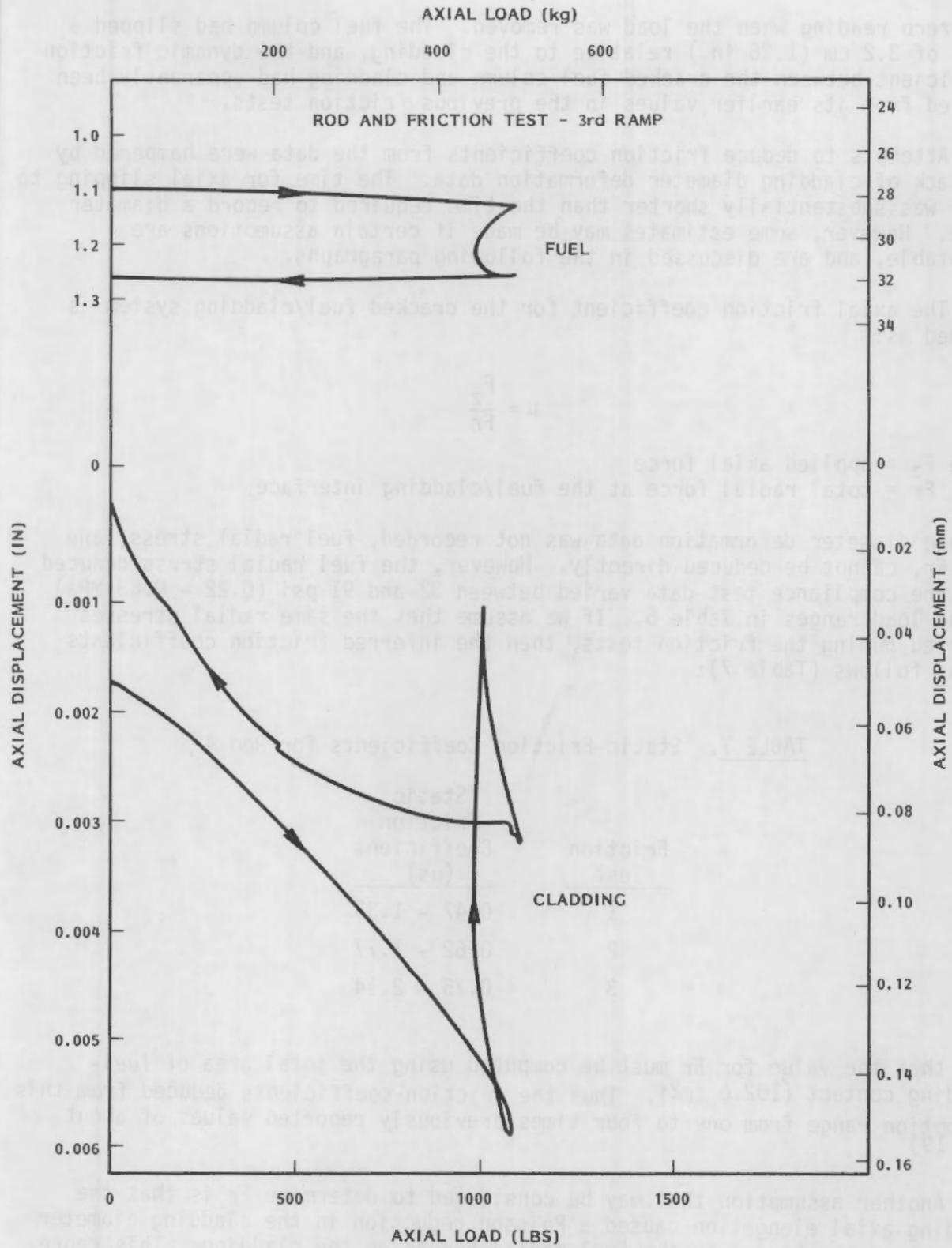
FIGURE 37. Axial Friction Test No. 3 for Rod 4

51

near zero reading when the load was removed. The fuel column had slipped a total of 3.2 cm (1.26 in.) relative to the cladding, and the dynamic friction coefficient between the cracked fuel column and cladding had apparently been reduced from its earlier values in the previous friction tests.

Attempts to deduce friction coefficients from the data were hampered by the lack of cladding diameter deformation data. The time for axial slipping to occur was substantially shorter than the time required to record a diameter trace. However, some estimates may be made if certain assumptions are acceptable, and are discussed in the following paragraphs.

The axial friction coefficient for the cracked fuel/cladding system is defined as:

$$\mu = \frac{F_z}{Fr}$$

where F_z = applied axial force
Fr = total radial force at the fuel/cladding interface

Because diameter deformation data was not recorded, fuel radial stress, and thus Fr, cannot be deduced directly. However, the fuel radial stress deduced from the compliance test data varied between 32 and 91 psi (0.22 - 0.63 MPa) at the load ranges in Table 6. If we assume that the same radial stresses occurred during the friction tests, then the inferred friction coefficients are as follows (Table 7):

TABLE 7. Static Friction Coefficients for Rod 4

Friction Test	Static Friction Coefficient (μs)
1	0.47 - 1.33
2	0.62 - 1.77
3	0.75 - 2.14

Note that the value for Fr must be computed using the total area of fuel-cladding contact (102.6 cm²). Thus the friction coefficients deduced from this assumption range from one to four times previously reported values of about 0.5.[19]

Another assumption that may be considered to determine Fr is that the cladding axial elongation caused a Poisson reduction in the cladding diameter which was not retarded by the fuel radial forces on the cladding. This represents an extreme case compared to the compliance data analysis. We also may assume that the fuel hoop strain is equal to this "theoretical" cladding hoop strain, and that the fuel radial modulus is in the range of those deduced from

the compliance data analysis (about 3540 Mpa from Figure 34). The radial
stress on the fuel is computed from Hooke's law in its simplest form:

$$\sigma_{rF} = E_F \; \varepsilon_{rF}$$

$$\text{where } \varepsilon_{rF} = -\nu_C \; \varepsilon_{zC}$$

These gross assumptions yield estimates for friction coefficients of 1.97, 2.57,
and 1.68 for friction tests 1, 2, and 3, respectively, and are similar to the
higher values noted in Table 7.

The larger values for the deduced cracked fuel column/cladding friction
coefficient may be caused by the fragments gouging the cladding inner surface
as sliding proceeded. Although the fuel column used for the friction tests
(Rod 4) could not be removed from the cladding, post test inspection of
previous rods showed that the cladding was galled during fuel column removal.

Large friction coefficients may also indicate that the radial force (Fr)
was underestimated. This is consistent with the failure to remove the Rod 4
fuel column, and with the residual cladding axial elongation remaining after
the friction tests (Figures 35 and 36). Higher than expected radial forces
would also support the conclusion that the fuel strain energy (supplied by the
axial load) was being dissipated in the radial direction, as discussed in an
earlier section of this report.

In summary, it appears that the static friction coefficient for the
cracked fuel column/cladding system may vary between 0.5 and 2.0, and may
increase slightly with sliding distance.

At the point of breakaway (when sliding starts), the cladding axial elon-
gation exhibits an abrupt decrease. During friction tests 1 and 2, the cladd-
ing elongation curves seemed to re-establish their original slopes, as the fuel
column continued sliding, indicating that the static and dynamic friction coef-
ficients are approximately equal (i.e., the force systems are about the same).
Note that the load must still increase to maintain sliding. However, the
required load (F_z) decreases as complete breakaway occurs during the third fric-
tion test (Figure 37), and the cladding elongation reduction is much more dra-
matic. It appears that the dynamic friction coefficient can be significantly
reduced under certain conditions.

Another objective of the friction experiments was to determine if axial
slipping was indeed a factor that was implicitly included in the deduced
effective moduli (Figure 34). Recall that a purely elastic analysis was used
to calculate effective moduli, and that inelastic effects were expected to be
included. A comparison with calculations performed during the effective moduli
analyses show that the "breakaway" loads in Table 6 are associated with rod
average fuel axial stresses of 1500-2600 psi (10.3 - 17.9 MPa). Since almost

53

all axial moduli in Figure 34 are above this stress level, it seems that those
effective moduli must include some effects due to axial slipping. Recall an
earlier argument (Page 48) that curves bisecting the envelope boundaries in
Figure 34 were suggested as being first order approximations for the effects
of axial slipping. These effects were also implicit in the long-rod compliance
experiments, but were better quantified by recording the elapsed time. The
long-rod compliance experiments are discussed in the next section.

3.3.2 Long Rod Compliance Experiments

Three long rod compliance tests were conducted at AERE Harwell. The rods
were of BWR design, and the cladding dimensions were 1.279 cm OD x 1.091 cm ID.
The test matrix and other dimensions are shown in Table 8.

The first test used steatite pellets and zircaloy cladding. The objec-
tives of this test were to proof test the specially designed compliance test
equipment, and to establish a relationship between the short rod tests and the
long rod tests. Both objectives were accomplished successfully.

The other two long rods tested were from the NRC/PNL Halden experiment
IFA-432. The IFA-432 6-Rod BWR assembly had been irradiated in the Halden
Boiling Water Reactor in Norway. The non-instrumented Rod 8 was taken from
this assembly at about 22 GWD/MTM for the compliance test. Rod 7 was identical
in design to Rod 8, but had not been irradiated, having been held as a replace-
ment should any other rod fail during irradiation. The purposes of compliance
testing Rods 7 and 8 were 1) to compare UO_2 to the steatite results, 2) to
compare unirradiated (uncracked) UO_2 to irradiated (fully cracked) UO_2, and
3) to compare the long rod results with the short rod results so that the
extent of axial coupling would be determined according to the hypothesis dis-
cussed in section 3.3. (Recall that it was postulated that the frictional

TABLE 8. Long Rod Compliance Test Matrix

Rod	Clad lgt. (cm)	Pellets Dia (cm)	Pellets lgt. (cm)	Fuel Col. lgt. (cm)	Clad Ax. Ga. lgt. (cm)	Dia scan lgt. (cm)
Zr-steatite	69.8	1.080	1.28	49 cm + 18.3 cm steel rod	57.6	52
Rod 7 (unirrad)	62.0	1.068	1.27	57.23	56.4	50
Rod 8 (irrad)	62.0	1.068	1.27	57.73	58.2	49

54

effects of increased fuel cracking would be expected to decrease the distance of axial force transmission along the fuel rod via radial dissipation of strain energy in a more uniform and localized manner.)

The UO_2-steatite comparison showed that both materials behaved similarly and thus showed that the entire data base could be used to evaluate the effective moduli for cracked fuels. The unirradiated-irradiated comparison showed that increased fuel cracking causes a localization of PCI according to the above hypothesis. The short-long rod comparison defined the extent of axial interaction effects according to the same hypothesis.

The compliance testing machine used for these tests (Figures 38, 39, 40) was designed and built by AERE Harwell according to PNL specifications. The basic principle of the machine was the same as for the short rod tests, but with a number of improvements. Along with the ability to simultaneously measure axial load, fuel and cladding axial elongations, and cladding diameters, the long rod testing machine was capable of:

- Azimuthal rotation of the rod at load so that more than one diameter trace could be recorded at each load level.

- Simultaneous recording of the fuel rod bowing caused by the axial load application to the cracked fuel column.

- Recording of the axial position of the diameter gage along the rod length.

- Recording of the elapsed time for each phase of the test on strip charts.

- Improved accuracy and repeatibility of all dimensional measurements.

- The ability to test irradiated rods in a hot cell.

A more complete description of the long rod compliance testing machine is included in Appendix A.

The basic test scheme was similar to the short rod tests, except that data density was significantly greater. The axial load was applied to the top of the fuel column via a push rod in 500 lb (227 kg) increments ranging from about 100 lb (45 kg) to 2000 lb (909 kg). After each load step, five diameter traces were recorded over about 50 cm of rod length at 72° azimuthal increments. This is shown schematically in Figure 41. The data were recorded on strip charts and forwarded to PNL, where the charts were digitized by computer for subsequent analysis, which is discussed below.

Experimental Results

The long rod compliance test results will be discussed in two segments. The first discussion will concern the zircaloy-steatite experiment, so that the
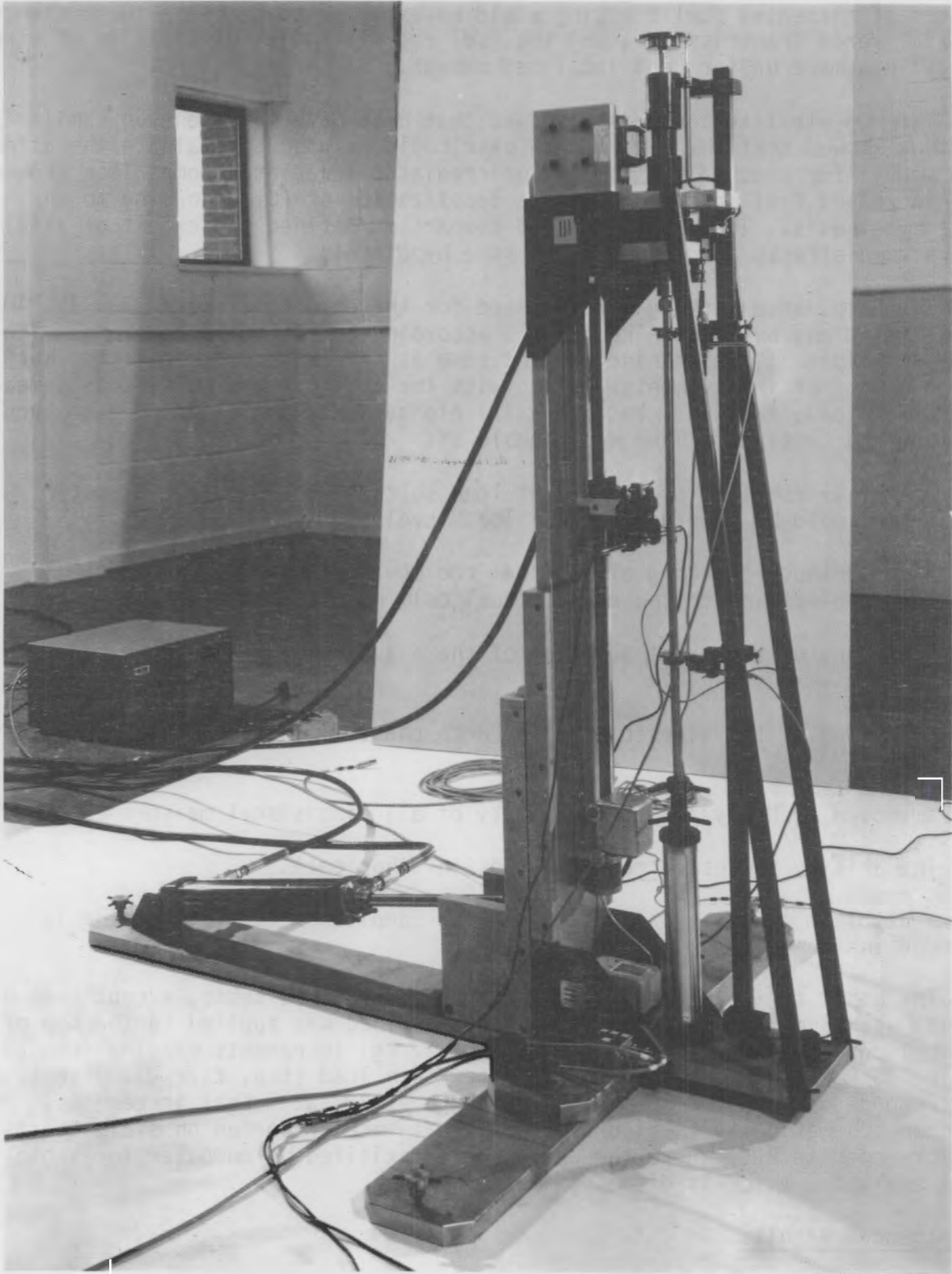
FIGURE 38. Long Rod Compliance Testing Machine – Overall View
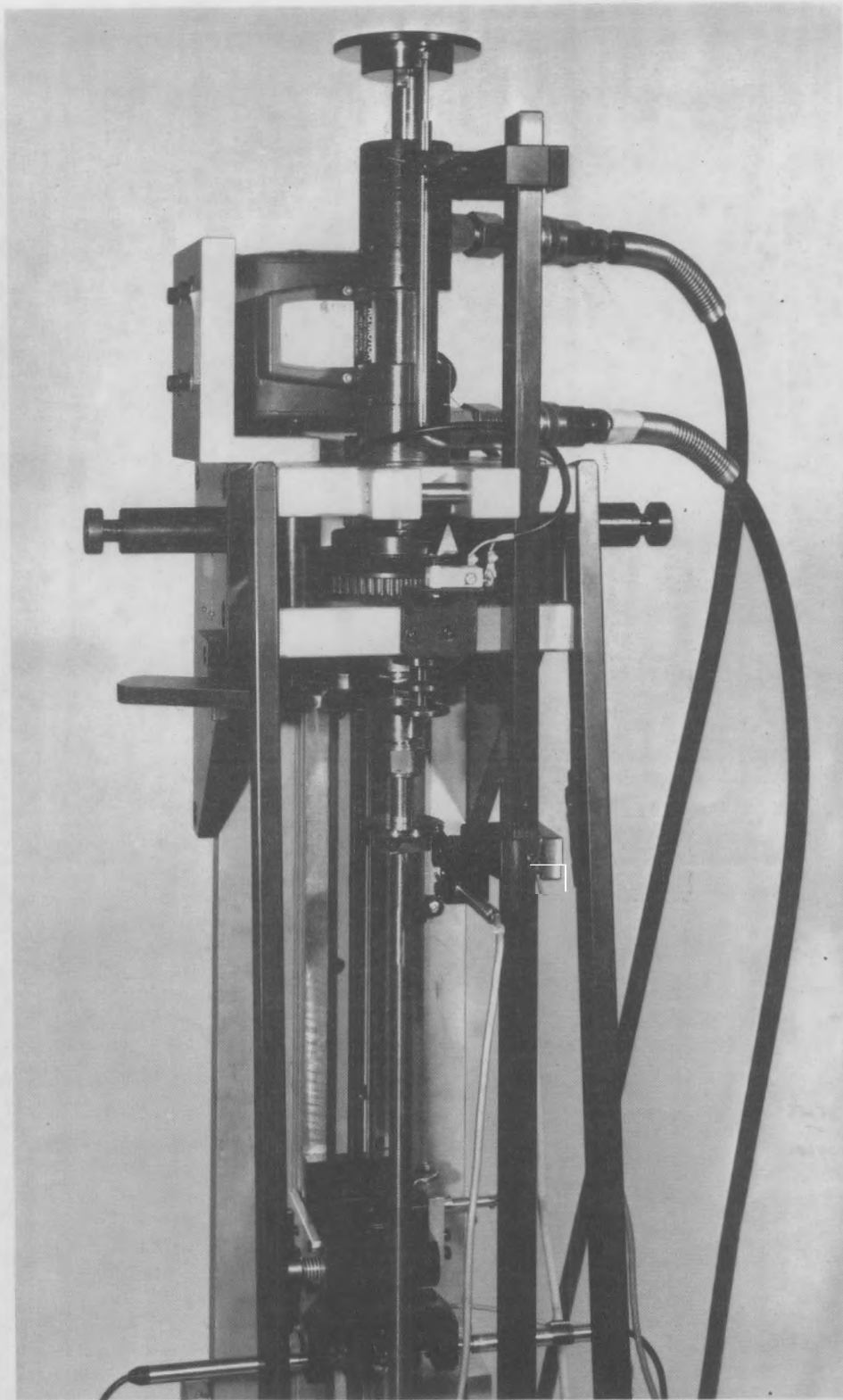
FIGURE 39. Long Rod Compliance Testing Machine — Rod Rotation Mechanism
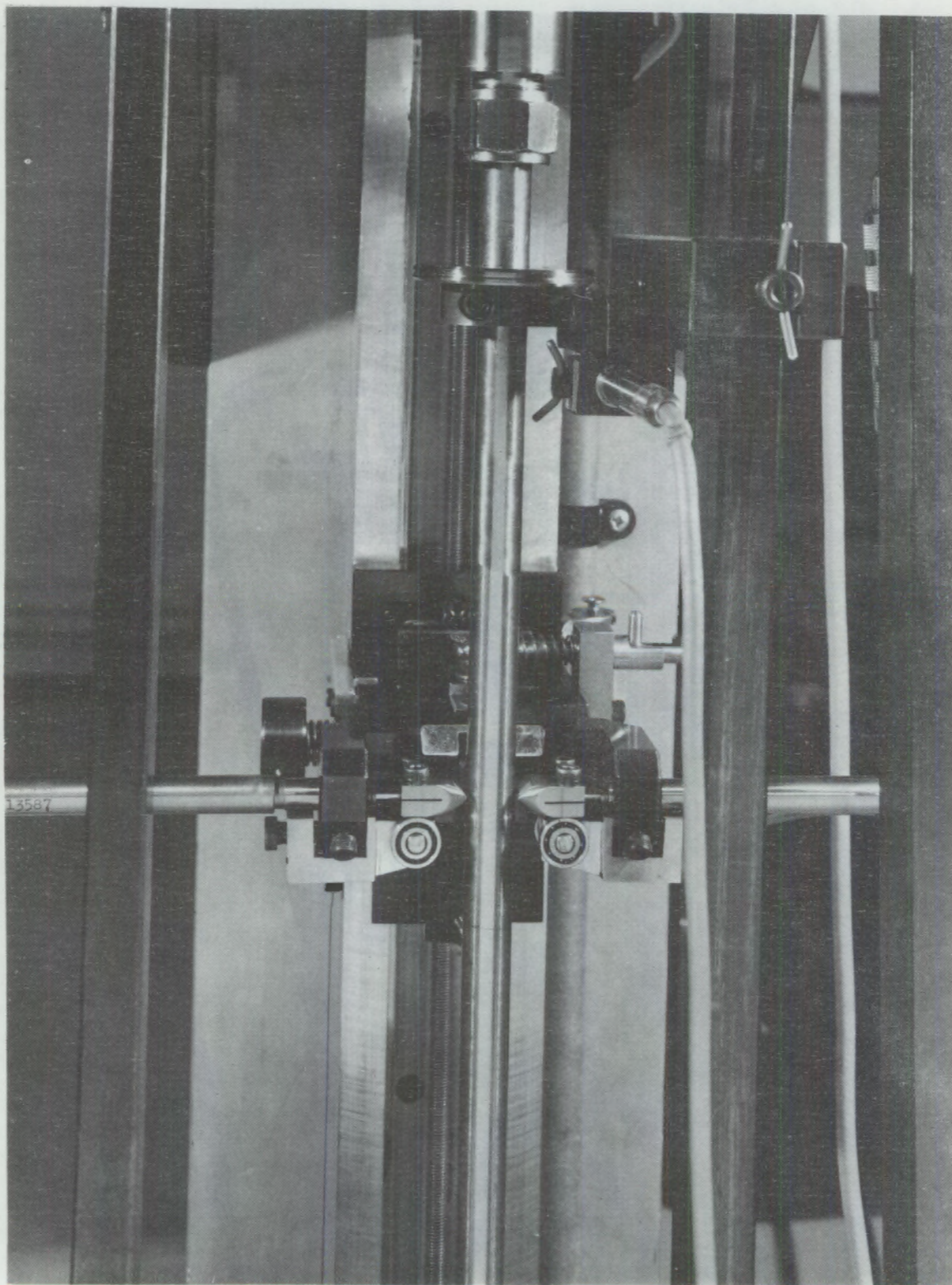
FIGURE 40. Long Rod Compliance Testing Machine - Diameter Instrument

58
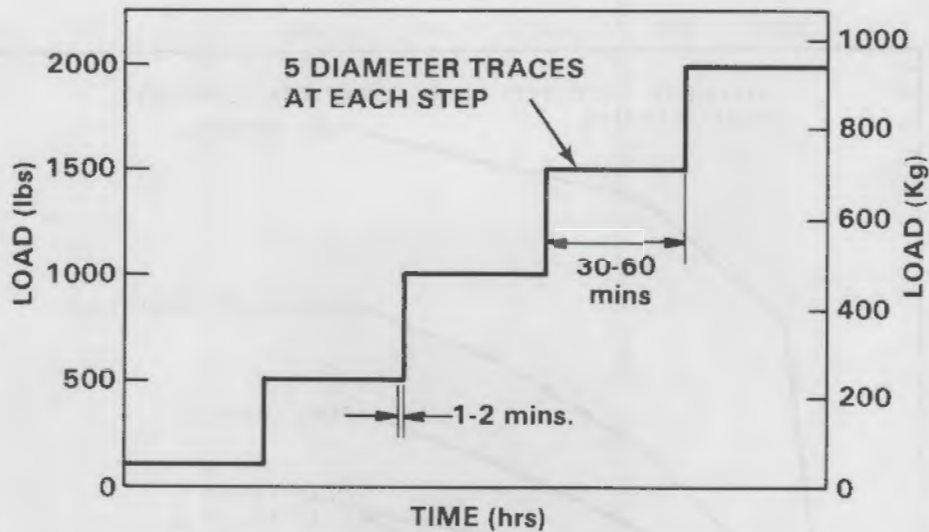
FIGURE 41. Long Rod Compliance Test Sequence

relationship to the short rod tests may be established. This will be followed by the Rods 7 and 8 analysis so that the effects of irradiation (cracking) can be clarified.

The Long-Rod Zircaloy-Steatite Experiment

The pellets for this rod had been prepared by the thermal precracking process previously discussed. The pellets were also equipped with a stress raiser (epoxy with 220 grit boron carbide; 0.1 mm high x 1 mm dia) on one end of each pellet to promote pellet cracking during load application.

The fuel and cladding axial strains for the long rod steatite test are shown in Figure 42. Comparison with Figures 22 and 23 for the short rod tests shows that the long rod fuel axial strains appear to bound those for the short rods. The long rod on Ramp 1 exhibited fuel axial strains that were comparable to the short rod Ramp 1 results where stress raisers on the pellets were also used (Rods 3 and 4). On the second load ramp, the long rod fuel axial strains were significantly reduced, indicating that the fuel had cracked and had been axially compressed as expected. Fuel cracking was audible during the last half of the first loading ramp.

In general, it appears that the long rod steatite fuel axial strains behaved as expected, decreasing with increasing loading ramp numbers, but remaining greater than the free fuel prediction. It also appears that the long rod fuel axial strains compare well with those of the short rods previously discussed.

The cladding axial elongations in Figure 42 behaved as expected regarding the free cladding prediction (for empty cladding). The cladding elongation decreased slightly from Ramp 1 to Ramp 2, as expected, indicating that fuel
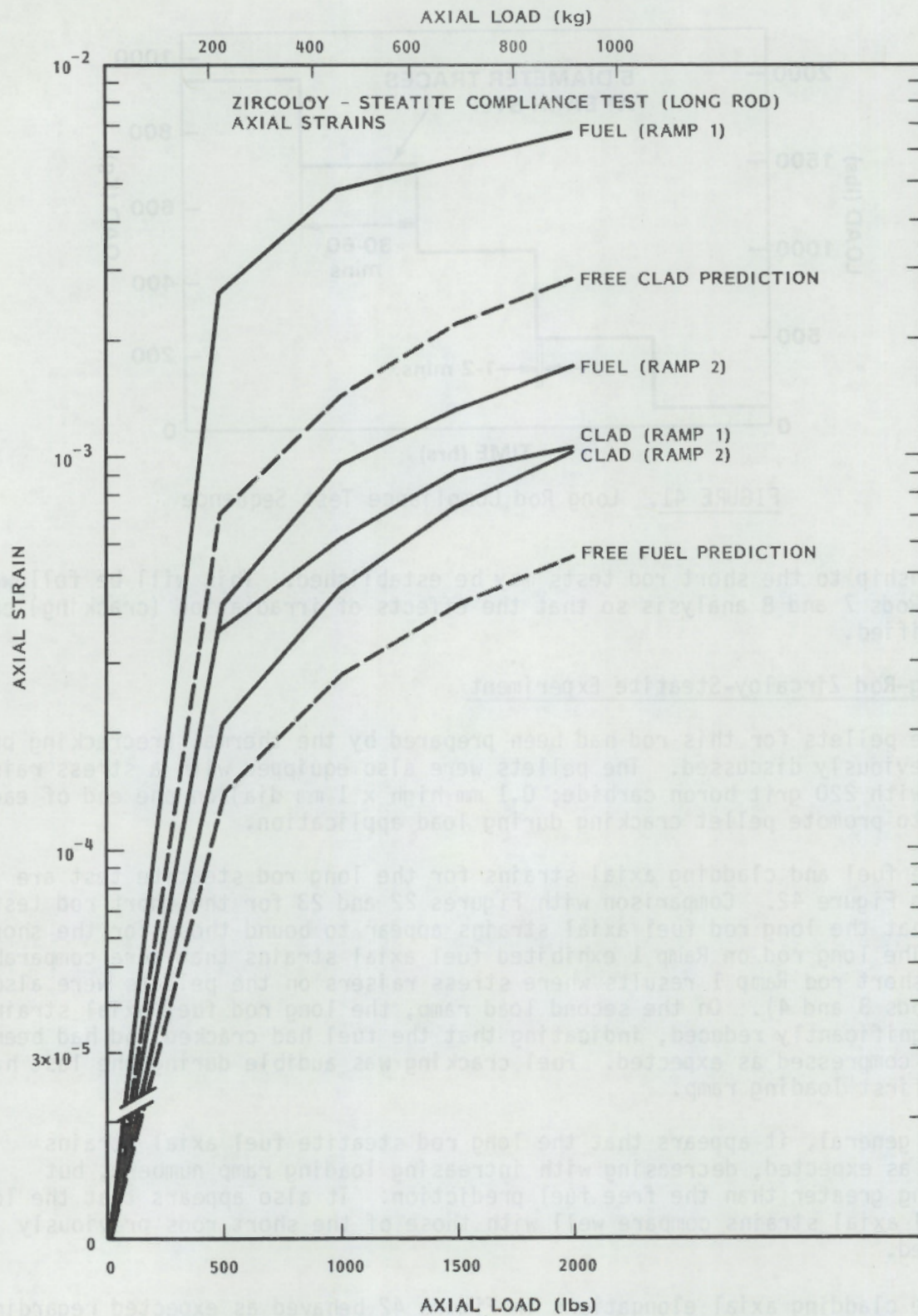
FIGURE 42. Zircaloy-Steatite Long Rod Test - Axial Strains

cladding contact was increasing as the fuel cracked and relocated. The permanent axial elongations for fuel and cladding were 467 μm compression of the fuel and 134 μm extension of the cladding on Ramp 1. On Ramp 2, the fuel and cladding permanent elongations were 477 μm and 167μm, respectively.

The rod averaged cladding diameter deformations for the steatite long rod are shown in Figure 43. These results are the opposite of expectations since the rod averaged diameter reductions increased with fuel cracking. It is possible that numerical anomolies caused by averaging the diameter changes for the entire rod could be contributing to the behavior of the diameter reductions in Figure 43. However, it seems more likely that pellet eccentricities on Ramp 1 probably had a greater effect on diameter reductions than the cracking did on Ramp 2.

The expected behavior for the zircaloy-steatite long rod diameters is demonstrated by the 1000 lb (454 kg) load trace in Figure B.1 of Appendix B where the most dramatic cladding ridges are localized near the top of the rod. The other diameter traces in Appendix B show that PCI was more random as the test continued. This is thought to be due to the partially cracked state of the fuel column, shown in Figure 44. The incomplete cracking left some pellets intact and able to transmit axial forces with a minimum of fuel – cladding friction.

Also included in Appendix B are traces of the fuel rod bowing which occurred during the test. Bowing was defined as positive if the tube became convex in the direction of measurment, i.e., if the tube centerline was displaced outward in the azimuthal plane of measurement. It should be noted that the bottom of the fuel rod was free to move axially, thus eliminating any column buckling effects. The bowing was produced by the path of load transmission through the partially cracked steatite pellets, and not by any compliance test machine restraint.

When those rod bowing measurements are correlated versus the rod average diameter changes from Figure 43, another possible contributor to diameter deformations may be assessed. When an empty hollow tube is subjectd to lateral bending, it flattens (ovalizes) in the plane of bending, and the diameter in that plane is reduced. [This assumes that the tube was already slightly bowed in the direction of lateral bending (bowing). If the tube was initially bowed opposite to the direction of bowing, the diameter will increase in the plane of bowing.[20]]

Figure 45 shows the diameter changes plotted versus bowing at all azimuthal positions for both ramps, along with the diameter decrease to be expected from theoretical bow-induced ovalization. The zircaloy-steatite long rod data
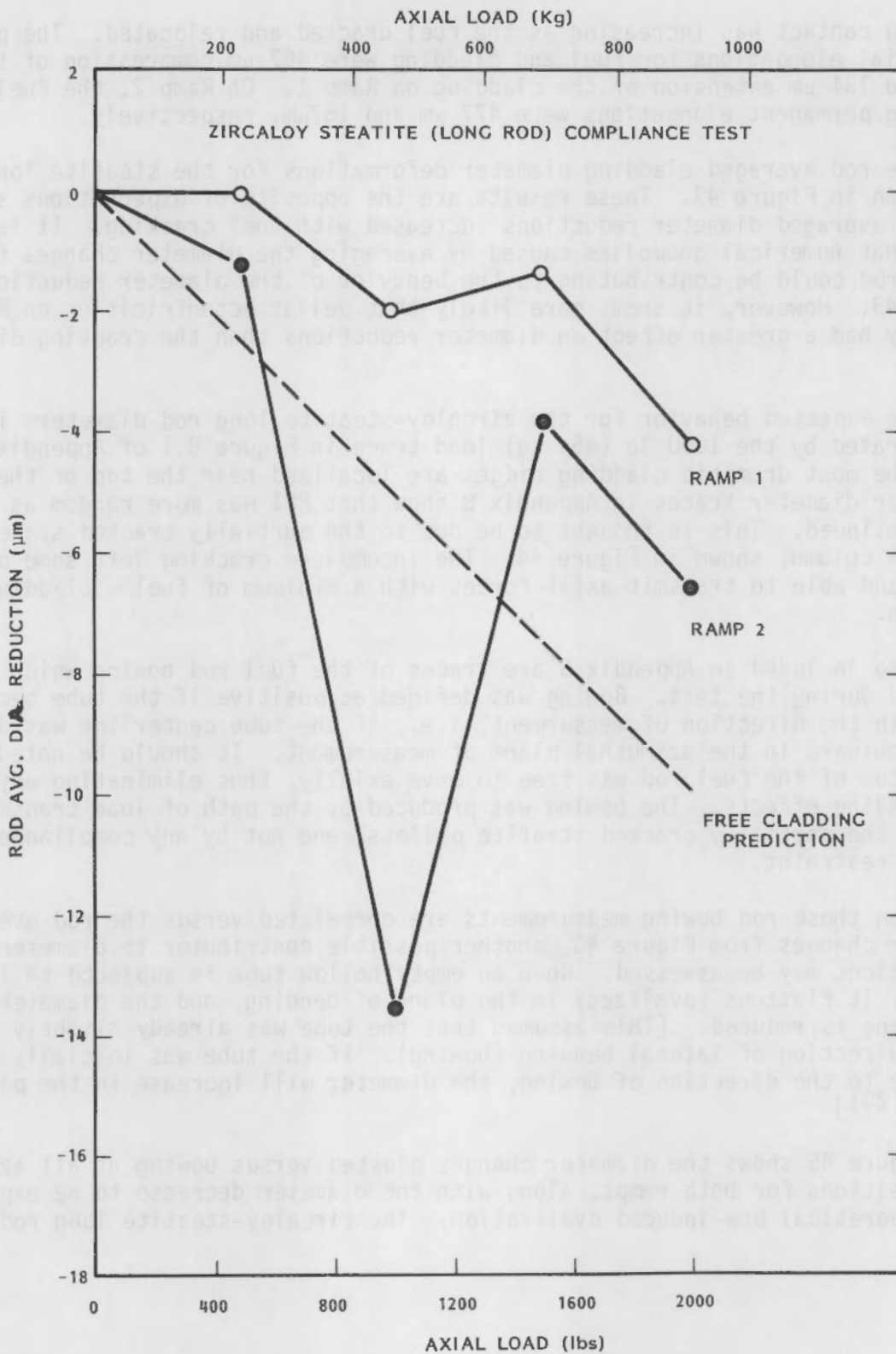
FIGURE 43. Zircaloy-Steatite Long Rod Test – Rod Average Diameter Changes

CRACKED FUEL COLUMN FORM
LABORATORY COMPLIANCE
EXPERIMENTS
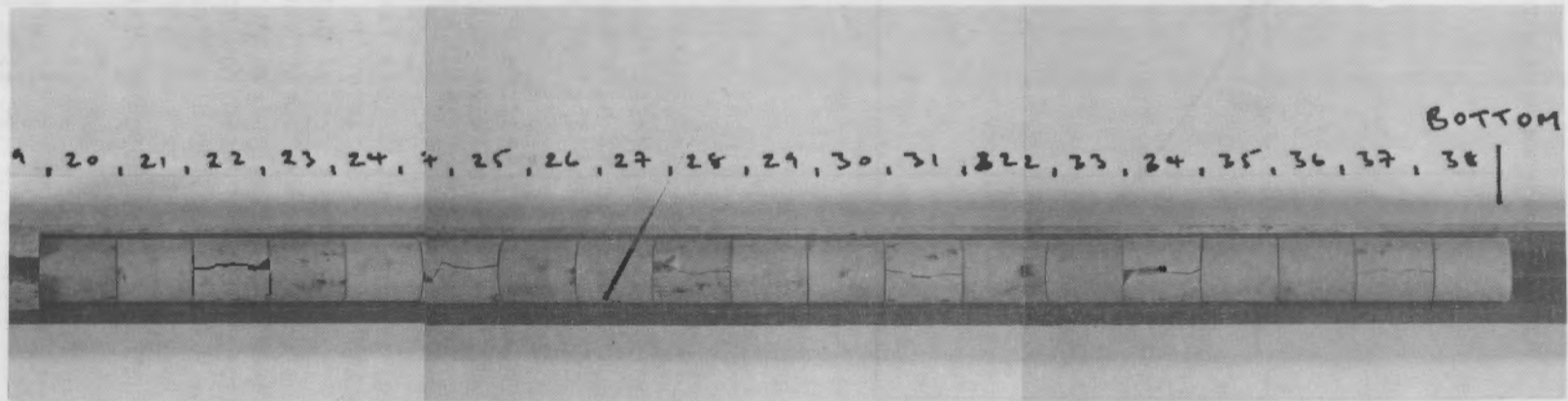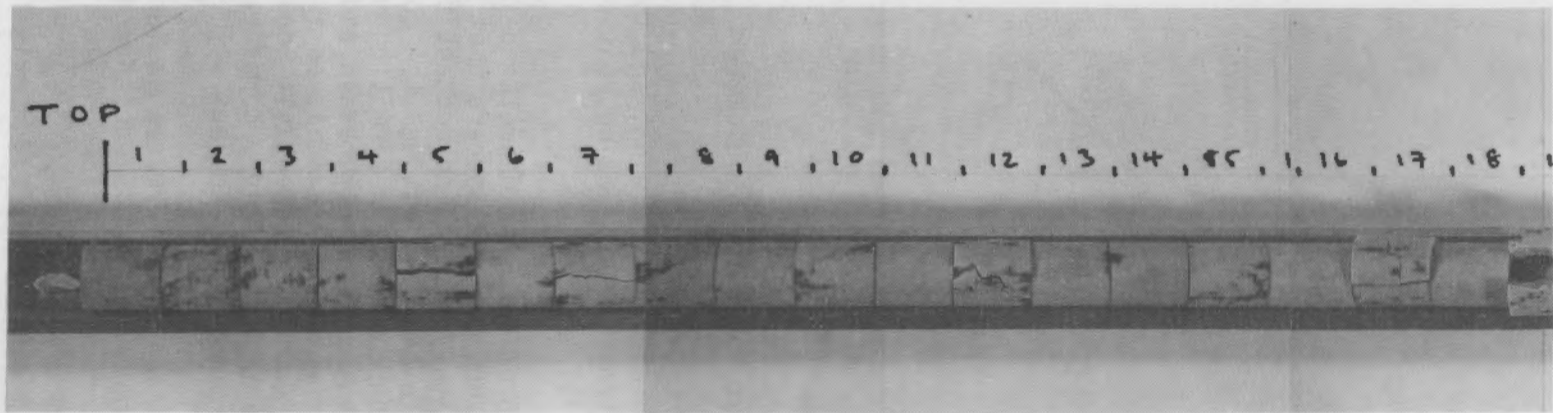
FIGURE 44. Zircaloy-Steatite Long Rod Test - Fuel Column
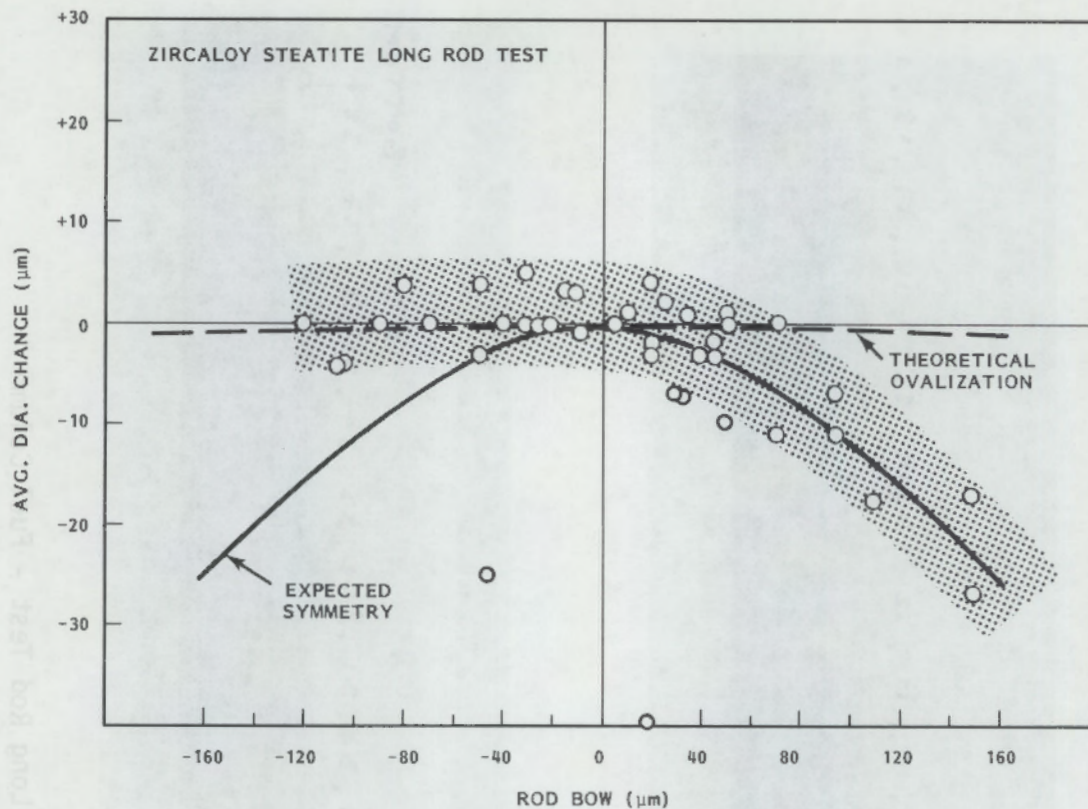
FIGURE 45. Zircaloy-Steatite Test - Bow Versus Diameter

show greater diameter decreases than could be caused by bowing, and thus the diameter reductions seem to have been dominated by the cladding Poisson mechanism activated by the applied axial loads.

Another interesting feature of Figure 45 is that the diameter deformations were not symmetric for positive and negative bowing. It appears that negative bowing (the concave side of the tube) caused the cladding to contact the fuel and prevent further diameter reductions, while positive bowing (the convex side of the tube) somehow caused less fuel-cladding contact and permitted more diameter reduction. (This behavior is also illustrated in Figures 46 and 47. Note that Figure 46 shows radial deformations which were calculated from the diametral deformations by a matrix method.) By this argument, it would seem that the internal stress systems of the cracked fuel are very complicated, and the mechanics of fuel-induced rod bow is not immediately obvious. The asymmetry in Figure 45 could also have been slightly enhanced by the bow-affected cladding stresses on either side of the tube, or by differences in local initial tube geometry. It appears that the mechanism of fuel-induced rod bow is in need of further study.

Attempts were also made to correlate cladding radial ridge heights over the length of a single pellet (see Figure 46) with the bowing behavior. This

64
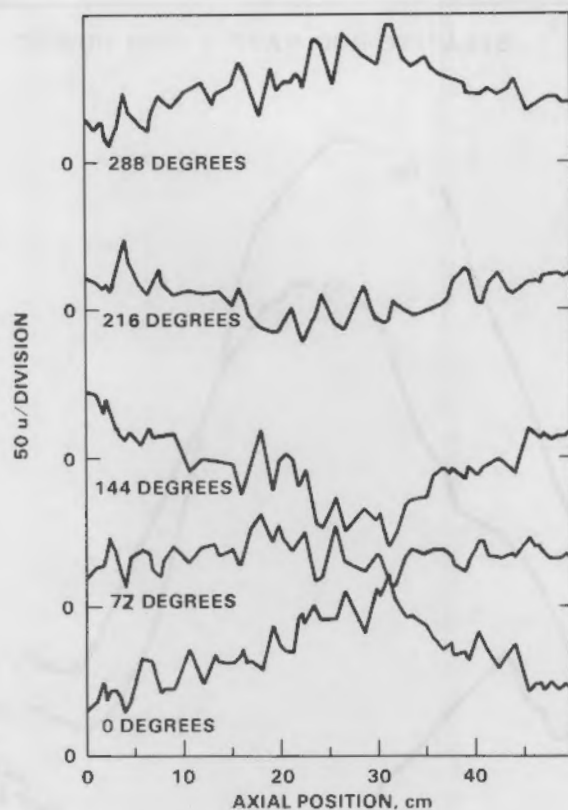
FIGURE 46. Zircaloy-Steatite Test - Radial Deflections

attempt was made because previous analyses[21] had revealed a relationship between axial creep deformation gradients and fuel rod failures, and because ridges are also associated with failures. However, the results showed no clear indications of such a correlation for these data. It is recommended that a ridge bow relation be attempted for internally heated fuel rods, where the ridges are usually more uniform, and the data not as scattered.

The methods described in section 3.3.1 were used to calculate the effective Young's moduli for the zircaloy-steatite long rod test. The results are shown in Figure 48 and compare well with the short rod tests, thus establishing that any possible bias between short and long rod experimental facilities was negligible.

A push-through friction test was also performed for the steatite long·rod to determine the effects of length on the friction coefficient between cracked fuel and zircaloy. The results are shown in Figure 49, where it is seen that the breakaway loads were 160, 225, and 125 kg for these successive tests. The general increasing trend until more complete breakaway on the third test is similar to the short rod test results, but the breakaway loads were substantially less. This was probably caused by the difference in diametial gap sizes

65
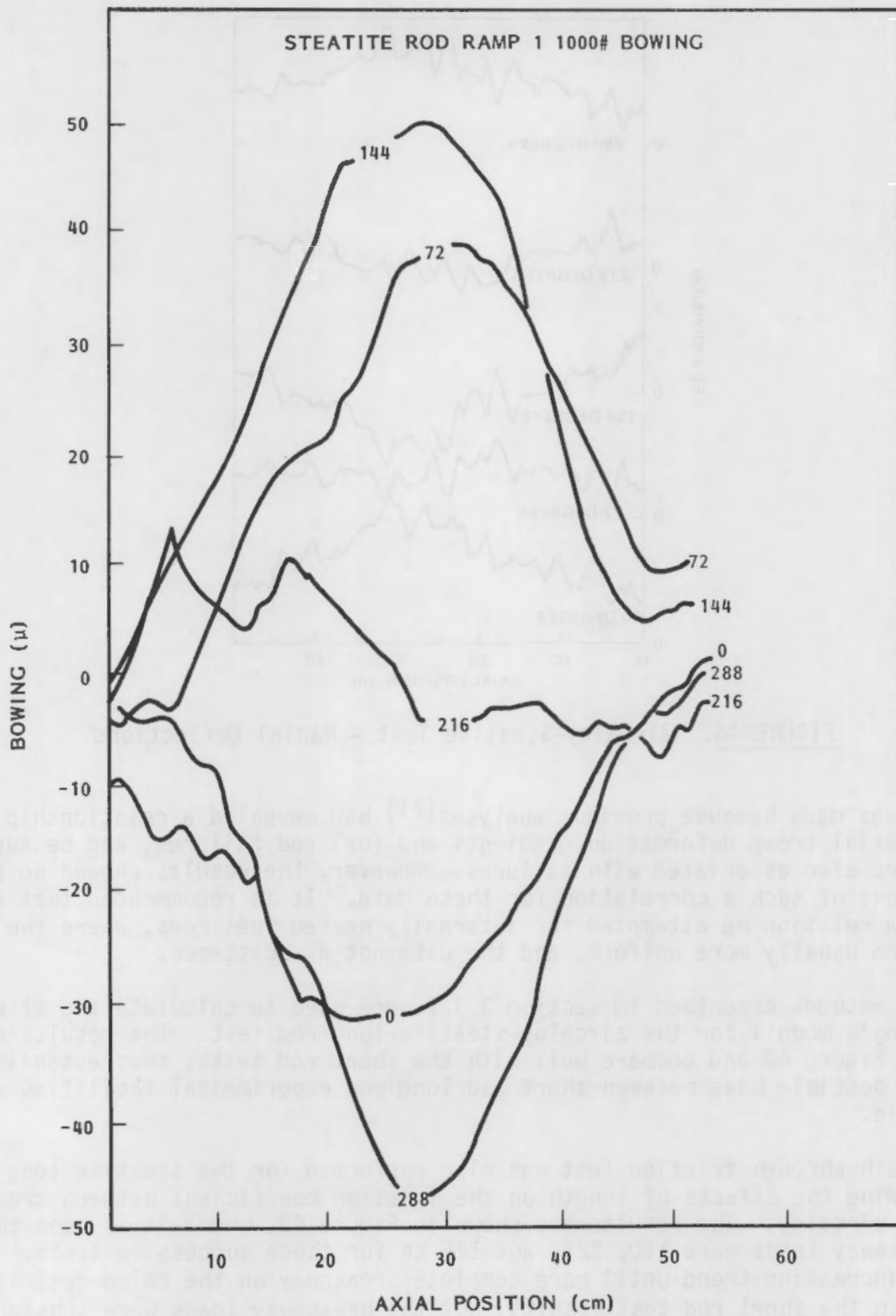
FIGURE 47. Zircaloy-Steatite Test - Bow at 1000 lb Load

66
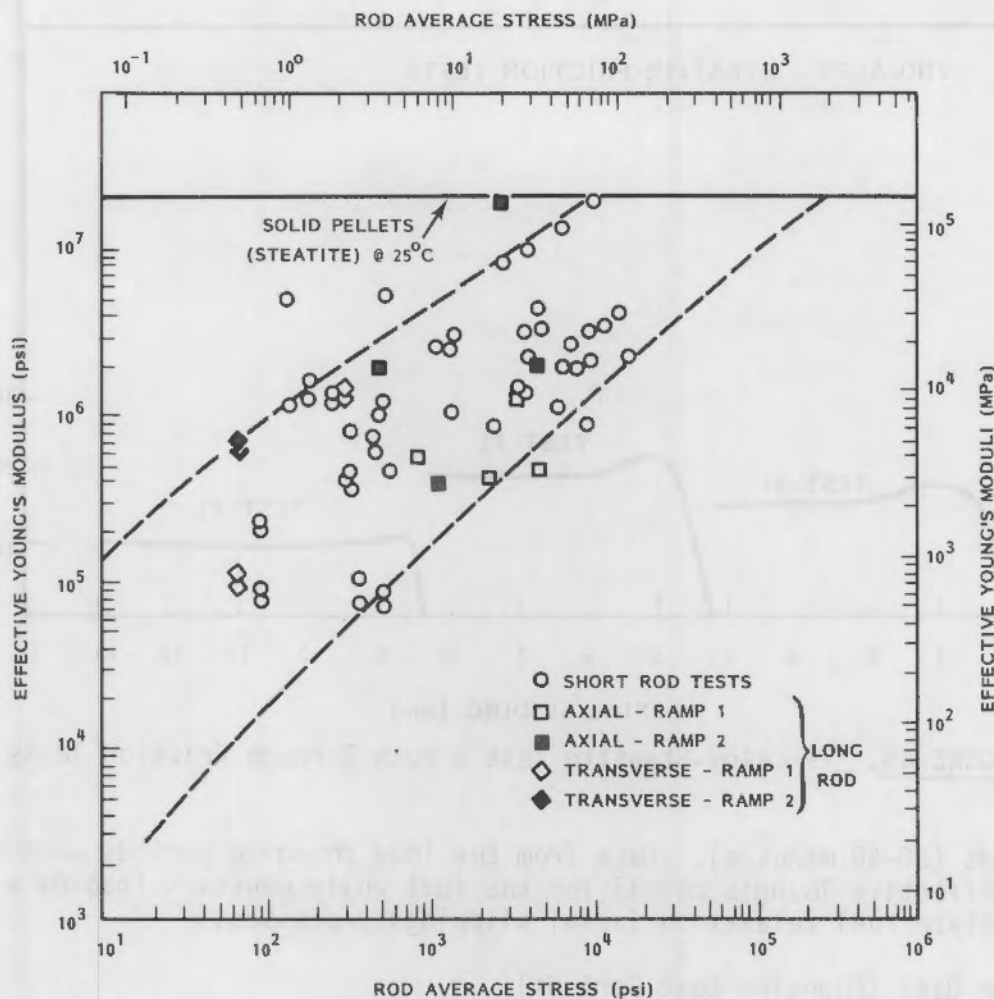
FIGURE 48. Zircaloy-Steatite Test - Effective Moduli

between the short rod and long rod friction tests (0.051 mm and 0.114 mm diameter gaps, respectively.) The breakaway loads to overcome the static friction coefficient seem to be roughly inversely proportional to gap size.

The Long Rod Zircaloy-UO$_2$ Compliance Experiments

Two rods from the IFA-432 experimental assembly were tested on the Harwell compliance testing machine. Rod 7 was unirradiated, and Rod 8 had been irradiated to about 22 GWD/MTM. These rods were the same design as the long rod zircaloy-steatite test, but the fuel was UO$_2$ and the initial diametral gap was 0.229 mm.

The data were separated into two categories for analysis: 1) changing loads over short-time periods (1-2 minutes), and 2) constant loads over longer
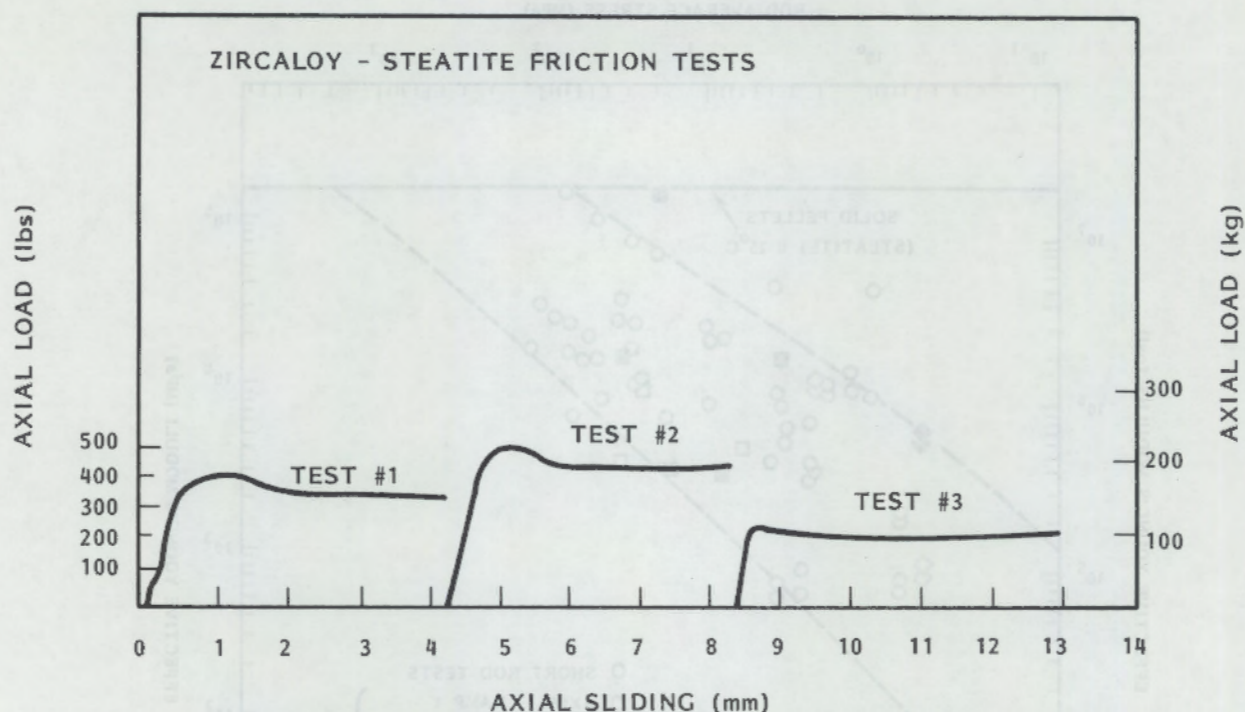
FIGURE 49. Zircaloy-Steatite Test - Push Through Friction Tests

time periods (30-60 minutes). Data from the load changing periods were used to calculate effective Young's moduli for the fuel while constant load data were used to analyze fuel relaxation (axial slipping) processes.

Deformation Data (Changing Load Periods)

The fuel and cladding axial deformations during the load changing periods only are shown in Figure 50. Also plotted are predictions for "free" fuel and cladding elongations, assuming that no fuel-cladding contact occured and that the axial load was transmitted over the entire lengths of a solid fuel column (compression) and the cladding (tension). Rod average diameter changes for the same load changing periods are shown in Figure 51.

The fuel column axial compressions were generally greater than the free fuel prediction, while the cladding elongations were less than the free cladding prediction. Fuel and cladding deformations generally decreased with loading cycle (ramp) for both rods.

Fuel axial deformations during the first load ramp indicate that the loosely stacked unirradiated fuel (Rod 7) behaved similarly to the irradiated fuel (Rod 8). The 18 axial gaps averaging 0.004 in. wide (0.1 mm) found during PIE gamma scans of Rod 8 (see Appendix C) correspond to 0.0015 in. (0.04 mm) gaps between all 47 pellet-pellet interfaces in Rod 7. This is equivalent to

68
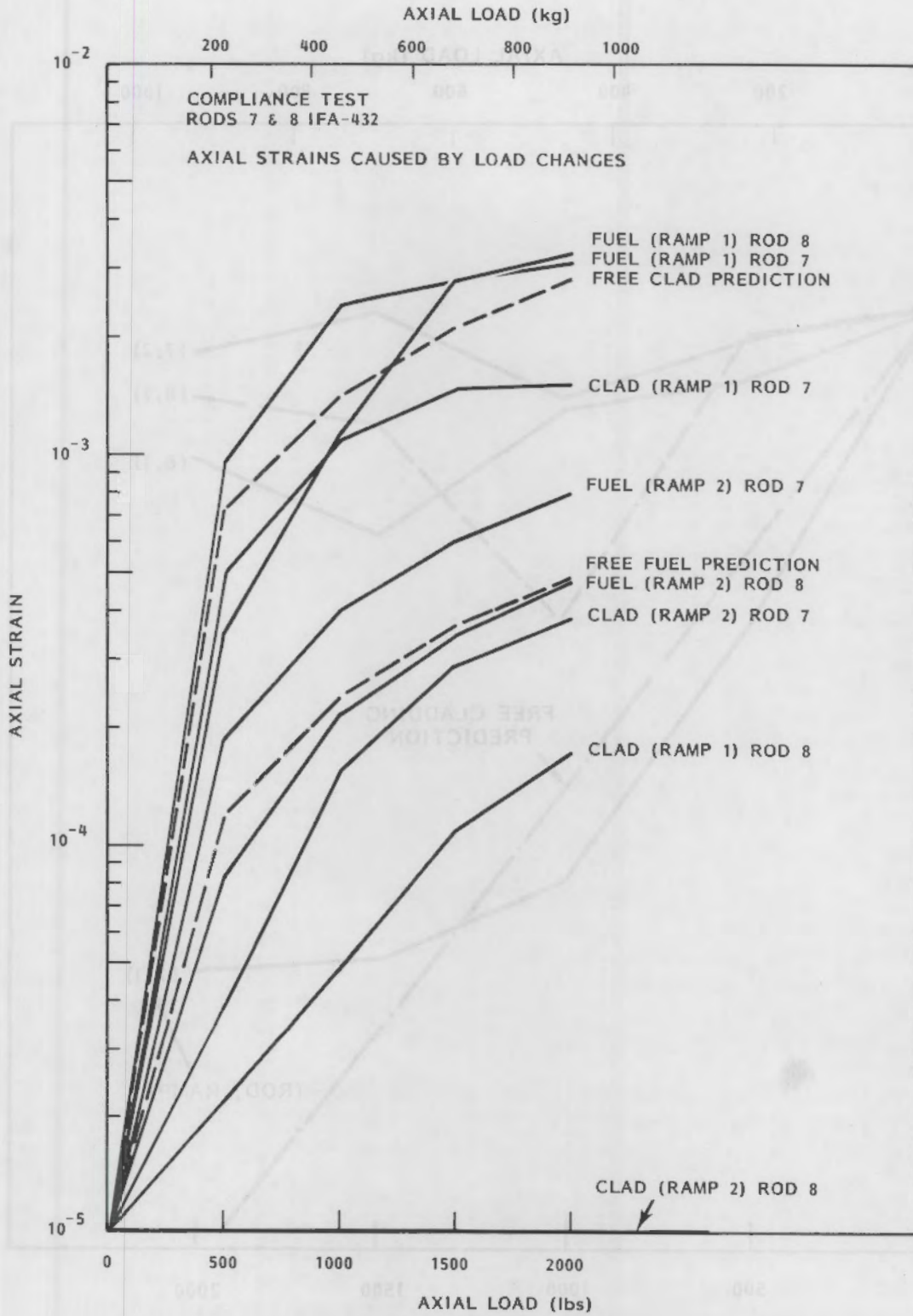
FIGURE 50. Fuel and Cladding Axial Strains for UO$_2$ Long Rod Compliance Tests

69
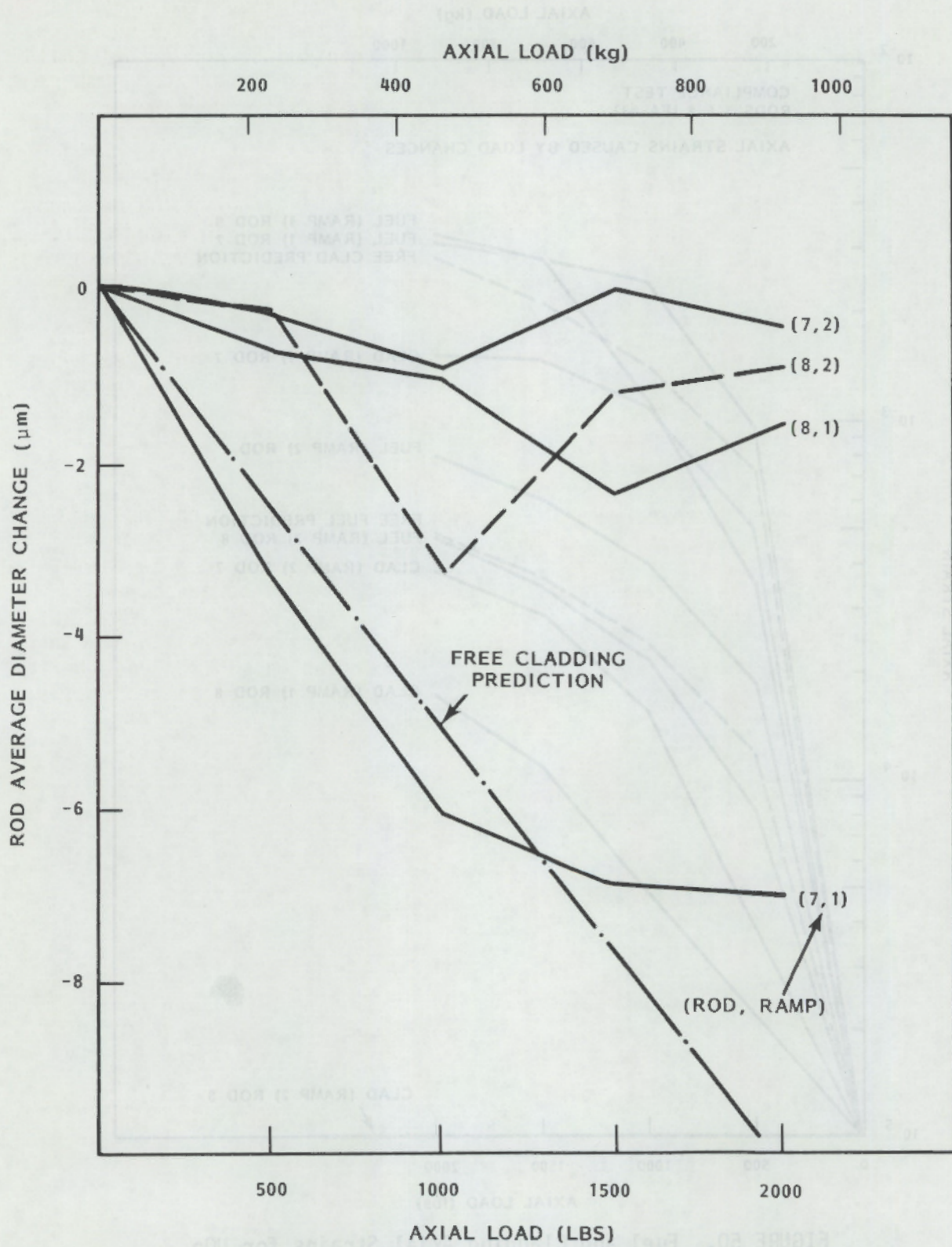
FIGURE 51. Average Diameter Changes for UO₂ Long Rod Compliance Tests

70

a 1σ surface roughness of 0.005 in. (0.01 mm) at zero load and, from previous discussion, is consistent with in-reactor data. Since the previously uncracked Rod 7 fuel had less intimate fuel-cladding contact than Rod 8, Rod 7 fuel could transmit axial loads over greater distances, thus activating a greater number of axial cracks. This is shown by the Ramp 1 cladding axial and diametral deformations in Figures 50 and 51.

On the second load ramp, fuel axial response approached the solid free fuel predictions, while cladding response decreased even further. Rod 8 cladding axial elongation was actually slightly negative (not shown in Figure 50), indicating that a radial force/Poisson mechanism was probably active somewhere in the rod. Total permanent axial deformations are shown in Table 9.

A mechanism that would contribute to Rod 8 Ramp 2 behavior in Figure 50 was noticed during the short rod compliance experiments on different fuel types (uncracked, cracked, sphere-pac). The smaller the fragments, the more strain energy was dissipated uniformly in the radial direction over progressively shorter axial distances. This can occur via a shear mechanism where a fuel diameter increase conserves the volume of a fuel length decrease.

The diameter deformation data for Rods 7 and 8 are shown in Appendix D. Note that Ramp 1 data show incremental deformations between successive load levels, while Ramp 2 data (prepared at a later date) are referenced to diameter traces at near-zero loads recorded before Ramp 2 loads were increased.

Rod 7 on Ramp 1 shows PCI all along the rod length, with some significant ridges appearing near the bottom of the rod. As the load was increased, the axial interaction distance decreased, and localized PCI produced ridges mostly

TABLE 9. Permanent Axial Deformations: Rods 7 & 8
IFA-432 Compliance Tests

		Fuel (mm)	Cladding (mm)
Rod 7 (unirrad)	Ramp 1	2.44	0.30
	Ramp 2	0.49	0.09
	Total	2.93	0.39
Rod 8 (Irrad)	Ramp 1	2.28	0.08
	Ramp 2	0.19	-0.03
	Total	2.47	0.05

71

near the top of the rod at high loads. This indicates that fuel-cladding contact was increasing as the load increased, causing axial friction forces to accumulate and retarding the axial transmission of the applied load. Most fuel cracking was completed during Ramp 1.

Very similar behavior was repeated for Rod 7 on Ramp 2, and axial PCI was limited to the top 20 cm of rod length. Localized PCI is much less apparent for Rod 8 on Ramp 1, and appeared limited to the top 25 cm of rod length. The same general behavior was noticed on Ramp 2, with localized PCI and axial interaction distances reduced even further.

For purposes of comparison, Figures 52 and 53 show the incremental diameter deformations for the 1000 to 1500-lb (454-681 kg) load change for Rods 7 and 8 during Ramp 1. The five azimuthal positions of measurement are shown in each figure. It can be easily seen from these two figures that the distance for transmission of axial forces was much greater in the unirradiated Rod 7 (previously uncracked fuel) than in the irradiated Rod 8 (fully cracked fuel). This again supports the hypothesis that greater fuel cracking permits more complete absorption of the fuel strain energy, and tends to radially dissipate this strain energy (via shear mechanisms) over shorter axial distances. Axial PCI coupling appears to extend over about 20-25 cm at beginning of life (Rod 7). The distance for axial PCI coupling in the high burnup Rod 8 was about 3-4 cm, and is shown in Figure 54. This trace was taken from the top 10 cm of Rod 8 at high load after Ramp 2, and required removal of some of the axial elongation measurement equipment (the upper "disc" on the rod in Figures 38, 39, and 40. See Appendix A.) The top of the compressed fuel column of Rod 8 coincided approximately with the 1 cm axial distance in Figure 54, while the start of the diameter scan in Figure 53 coincided approximately with the 2.5 cm axial distance in Figure 54.

These data indicate that there may be a maximum allowable axial node length in fuel performance codes. Longer axial node lengths could result in errors in axial stress estimates. This allowable axial node length also seems to be burnup dependent, decreasing from about 20-25 cm at beginning-of-life to about 3-4 cm at 22 GWD/MTM. The importance of calculational economy in fuel performance codes is apparent.

Rod bowing data recorded from the Rod 7 and Rod 8 compliance tests are shown in Appendix E. Note that the bowing for these rods was substantially greater than for the zircaloy-steatite long rod test. This was probably caused by the larger initial diametral gap size (0.229 mm for Rods 7 and 8, 0.114 mm for the zircaloy-steatite rod), which permitted more asymmetric cracked fuel load transfer systems via fragment rotation mechanisms.

Figures 55 and 56 show maximum rod bow plotted versus rod average diameter deformations at all azimuthal measurement positions for both ramps of Rods 7 and 8. Rod 7 (Ramp 1) showed a similar pattern to the long rod zircaloy-steatite test (see Figure 45). Rod average diameter reductions were greater

72
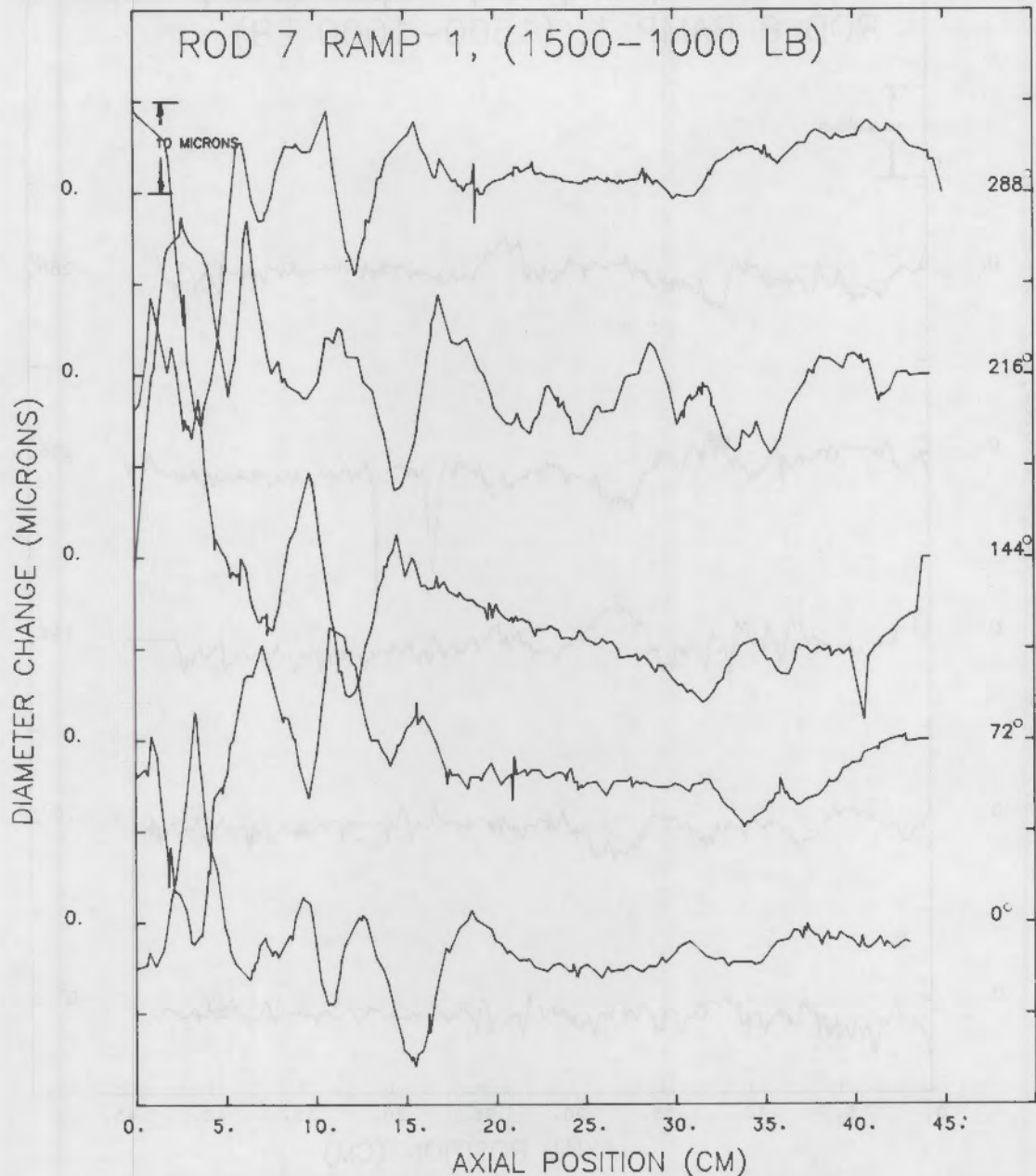
FIGURE 52. Rod 7 Diameter Deformations

for postive rod bow (convex tube), and were also greater than predictions of
theoretical ovalization, indicating domination by the axial force/Poisson
mechanism of the cladding. However, for negative rod bow (concave tube), the
Rod 7 Ramp 1 diameter reductions still occurred, indicating that the larger
gap size may not have been totally closed by bowing/ovalization/fuel relocation
mechanisms previously discussed. On Ramp 2, Rod 7 showed a slight diameter
increase with positive bowing (Figure 55). This is the trend that would be
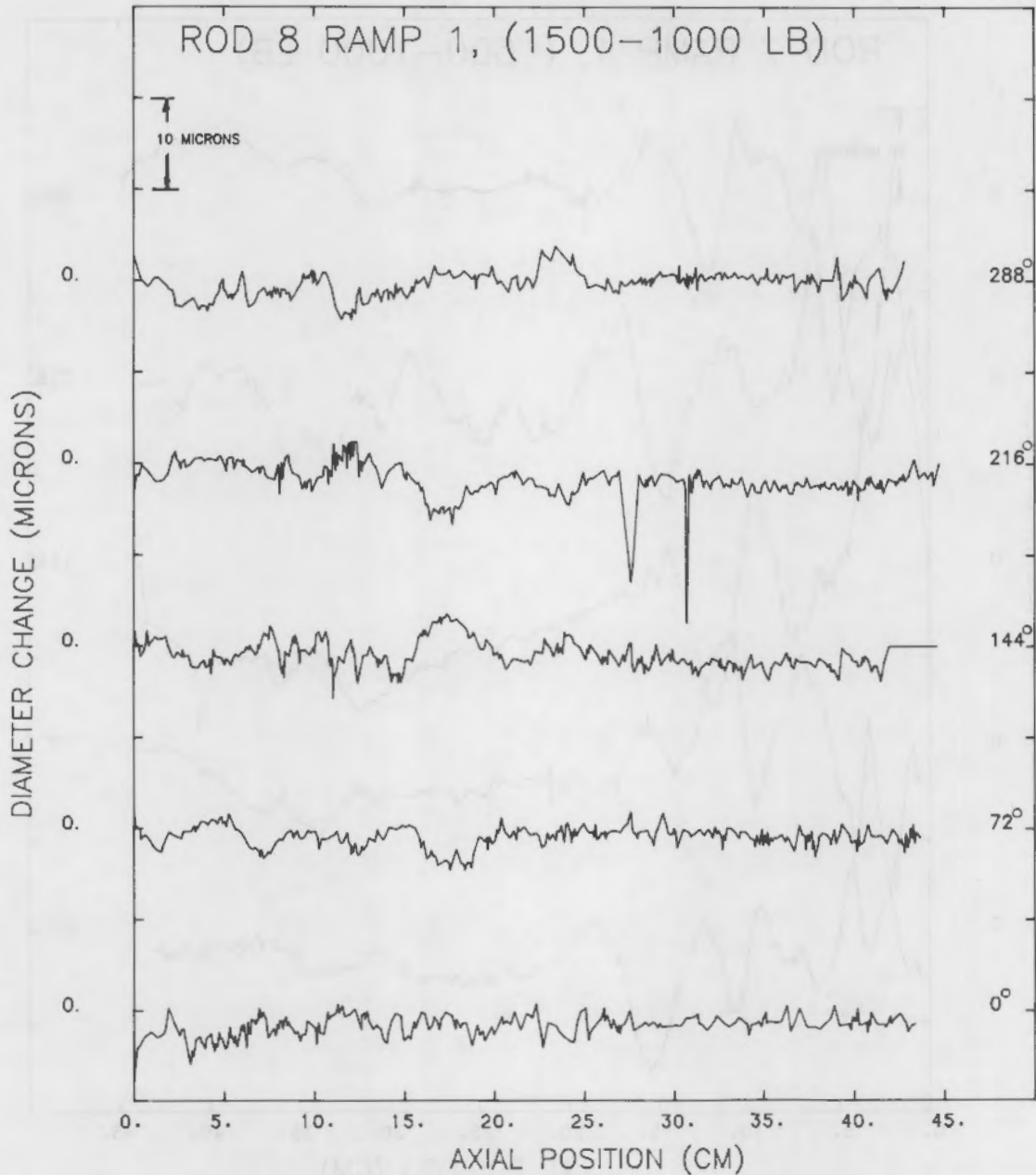
FIGURE 53. Rod 8 Diameter Deformations

expected for fuel-induced rod bowing, where the fuel pushes outward radially
on the cladding to cause tube bending, while the concave side of the tube
(negative bowing) shows the effects of bending-induced ovalization. Recall
that Rod 7 unirradiated UO₂ fuel cracking was completed primarily during
Ramp 1.

The irradiated Rod 8 bow-diameter data (Figure 56) show that the fully
cracked fuel column induced about half the maximum bow that occurred in Rod 7.

74

ROD 8, TOP 10 CENTIMETERS

20 MICRONS

DIAMETER (MICRONS)

0.
0.
0.
0.
0.

288.
216.
144.
72
0

0.   1.   2.   3.   4.   5.   6.   7.   8.   9.

AXIAL POSITION (CM)
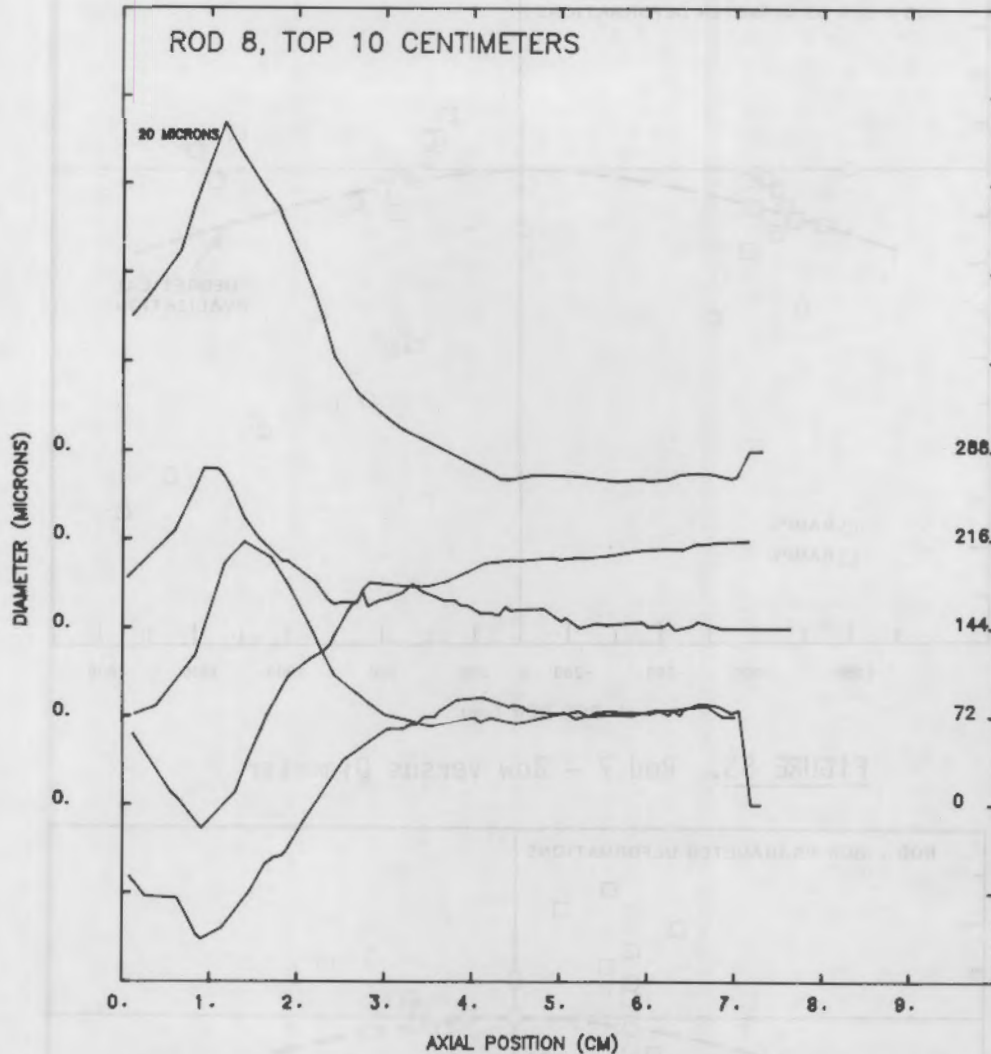
FIGURE 54.   Top 10 cm of Rod 8 - Diameter Deformations

This probably occurred because the smaller fuel fragments in Rod 8 could trans-
mit less moments, fuel deformations being dominated more by shear-type mechan-
isms which tended to close any remaining gap.   Thus the maximum bow of Rod 8
lies between the zircaloy-steatite rod and Rod 7 values for maximum rod bow.
Rod 8 data appears dispersed around zero diameter reduction except for the
familar grouping in the lower right hand quadrant of the plot.   The patterns of
the bow-diameter data for the three long rod tests are shown in Figure 57.   A
most interesting feature is that cladding diameter reductions appear to occur
frequently when bowing is positive; that is, on the convex side of the rod.
This seems anomolous when the mechanism for fuel-induced rod bowing is con-
sidered, and the subject should be investigated further since it probably
influences cladding localized stress distributions, and thus fuel failure.

75
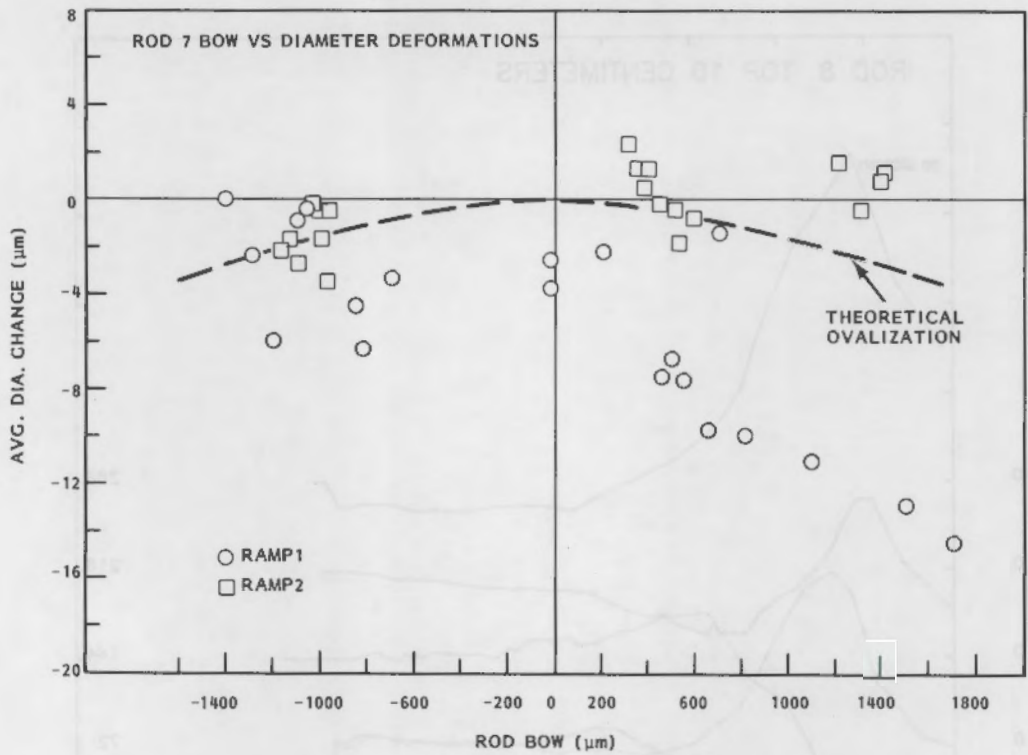
FIGURE 55. Rod 7 – Bow Versus Diameter
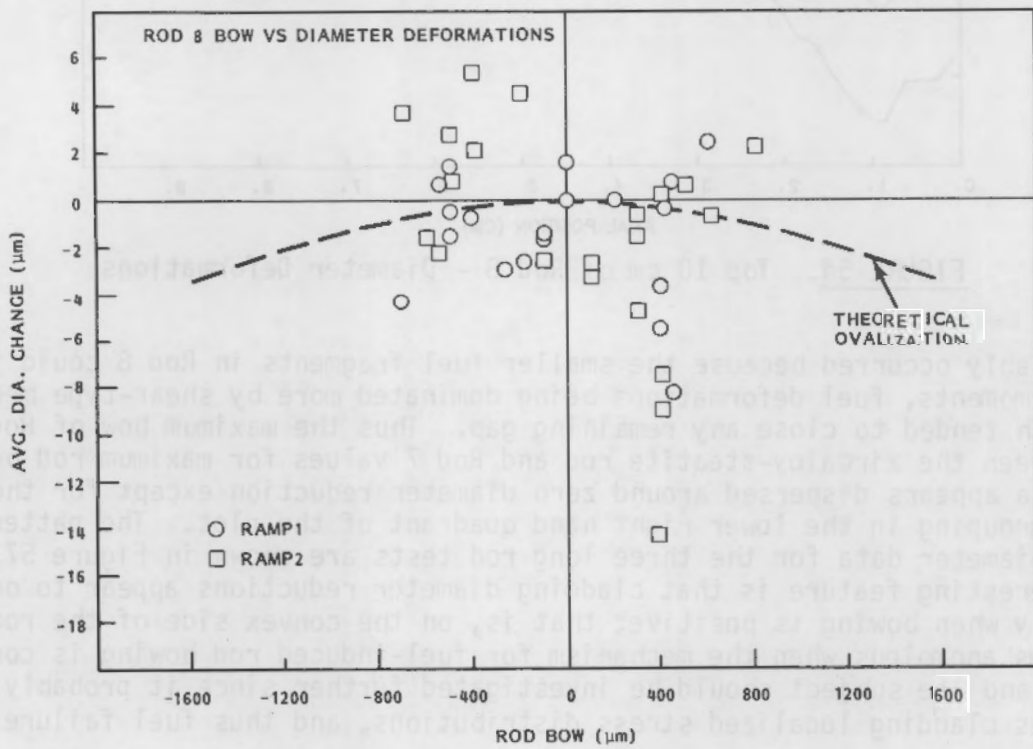
FIGURE 56. Rod 8 – Bow Versus Diameter

76
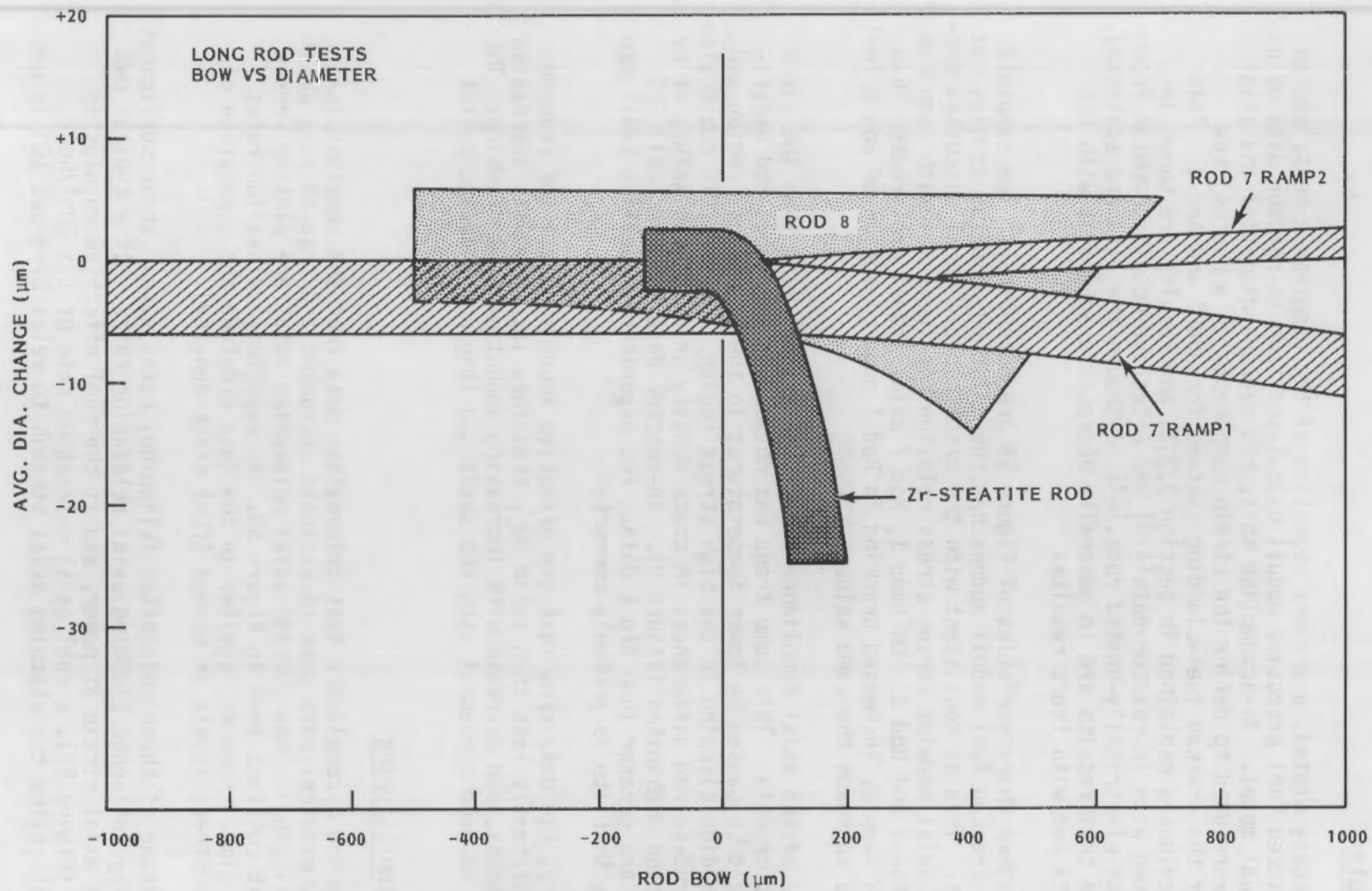
FIGURE 57. Bow Versus Diameter for the Long Rod Tests

77

Effective Moduli

As previously stated, a primary objective of the compliance tests was to verify the cracked fuel effective moduli calculated from in-reactor data using the cracked fuel model. To accomplish this, rod average diametral and axial deformations were used to define the strain components in a Hookes' Law description of the cracked fuel-cladding systems for Rod 7 and Rod 8. This method was previously explained in section 3.3.1, and results are shown in Figure 58, along with in-reactor data[1,2] and effective moduli computed from Ito's work with electrically-heated rods.[22] Although the data are scattered, the compliance test results are in generally acceptable agreement with the in-reactor data and with Ito's results.

Certain other characteristics of Figure 58 are noteworthy. The complete data base for cracked fuel moduli approaches the solid UO_2 modulus at high rod average stress. This is consistent with the crack closure model discussed previously. The axial modulus versus stress relationship increases with ramp number for both Rod 7 and Rod 8. On Ramp 1, Rod 7 axial moduli are greater than for Rod 8. On Ramp 2, increased cracking in Rod 7 and compaction of Rod 8 fuel causes both to approach the same value.

The slope of the axial compliance data appears to be less than the slope of the in-reactor data. This same trend was noticed in the short rod experiments, and could be caused by lower temperatures in the low stress region and axial fuel-cladding slipping in the high stress region. However, it could also be caused by rod-to-rod differences in crack density or roughness values or by fragment rotation mechanisms (Figure 9). In-reactor data for the small G/D (0.007) Rod 3 are greater than Ito's data. PNL experience modelling small gap rods indicates that Ito is probably correct.

In summary, the data show that the effective Young's moduli for cracked fuel are significantly less than solid UO_2, that they increase with increasing rod average stress, and decrease with increasing amount of fuel cracking. The data are also in good agreement with the short and long rod steatite pellet experiments.

Axial Relaxation/Slipping

Rod 7 and Rod 8 compliance test deformation data from the constant load periods (30-60 minutes) were used to evaluate uncracked and cracked fuel axial relaxation (slipping). Rod average axial relaxation rates are plotted versus elapsed time at constant load in Figure 59. As expected, relaxation rates decrease with time. However, scatter in the data preclude the separation of effects due to stress levels or burnup (fuel crack density).

The magnitude of these relaxation (slipping) rates appear to be sufficient to significantly influence cladding axial relaxation rates. If a typical BWR rod shows 0.1% axial strain at power, and if the fuel effective modulus is 7.5×10^5 psi (Figure 58), a fuel axial relaxation rate of 1×10^{-4}/hour (Figure 59) will allow the cladding axial strains to relax by about 10% in one
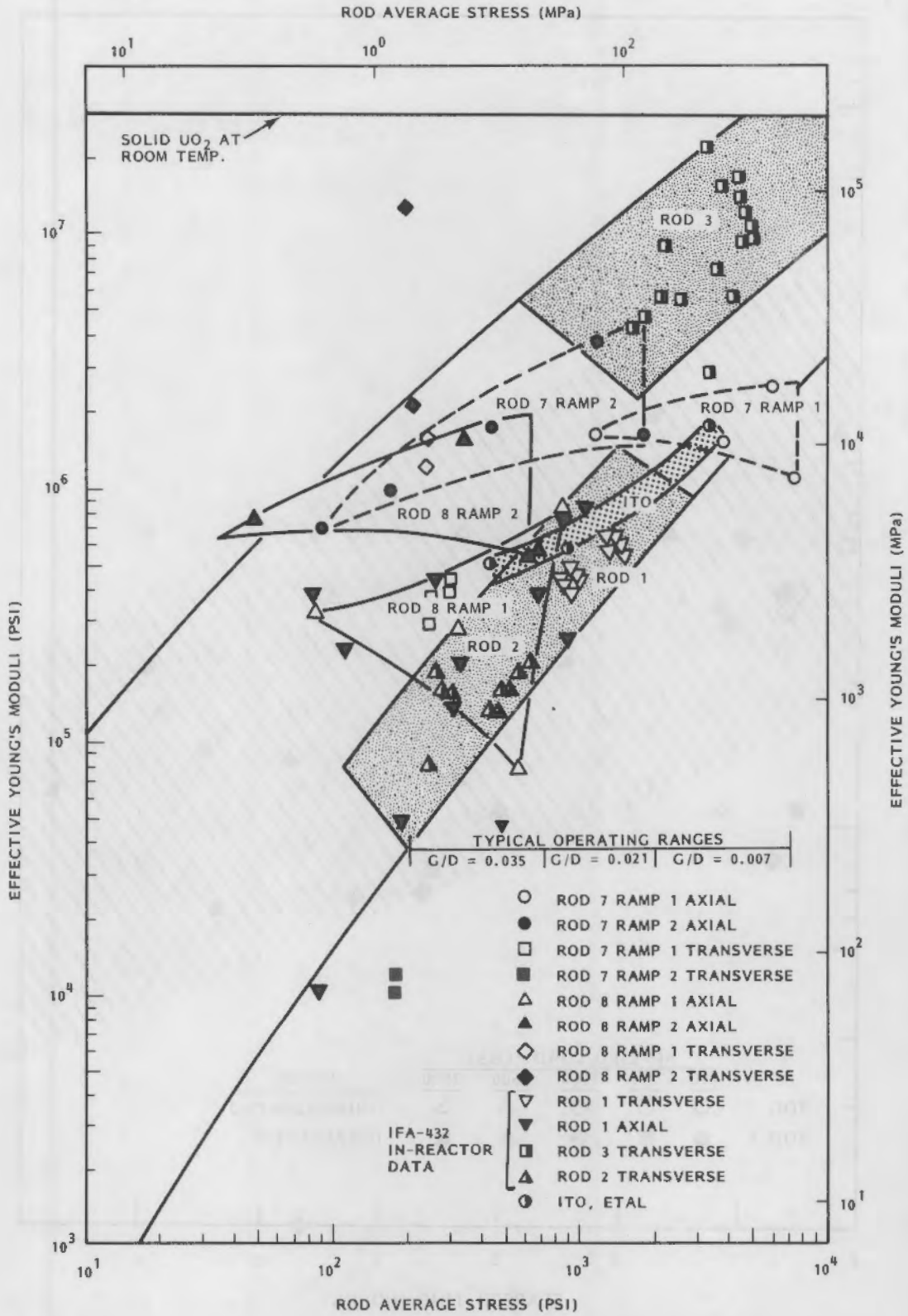
FIGURE 58. Effective Moduli for Long Rod UO₂ Compliance Tests
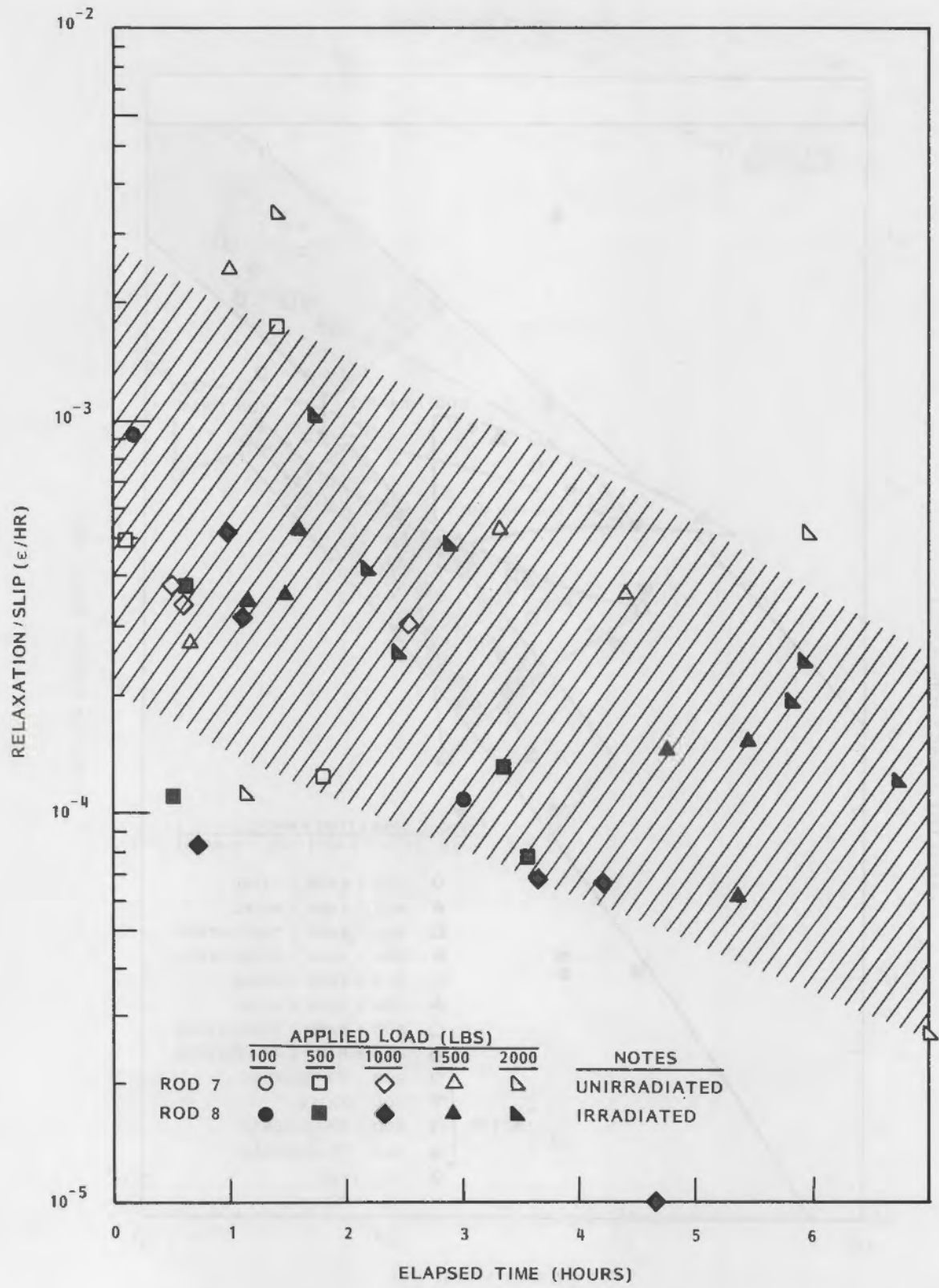
FIGURE 59. Rod 7 and Rod 8 Axial Slipping Rates

80

hour to a value of 0.09%. This is consistent with in-reactor fuel rod axial relaxation behavior. It seems that the viscous nature of axial fuel compliance (slipping) may be an important factor to consider when modelling fuel relaxation behavior, especially when rod power exceeds the previously conditioned power.

3.3.3 Summary of Compliance Test Results

A laboratory simulation of the internal stress systems for fuel rods with cracked and uncracked pellets has verified the model predictions for significant reductions in effective Young's moduli for cracked fuel. The laboratory and in-reactor results show good agreement except in the case of very small gap rods, where the model predictions were slightly greater (Figure 58). The data are also in reasonably good agreement with the results of other investigators. There was no apparent bias between results obtained for short rods (35-50 cm long) or long rods (60 cm long) tested at two sites using low density electrical porcelain (steatite) as a fuel substitute (Figure 48). There was also no apparent bias between results obtained for the steatite and UO_2 pellet systems.

Since a purely elastic formulation was used to analyze these data, the effects of axial fuel/cladding slipping are implicit in the estimates for the effective moduli of cracked fuel. It was found that the viscous nature of fuel/cladding slipping was of sufficient magnitude to affect the analysis of in-reactor fuel rod axial relaxation behavior. A very approximate method of accounting for slipping was proposed: as the fuel slips axially, the effective modulus follows a path from the upper boundary of the data envelope to the lower boundary, roughly perpendicular to both boundaries. It should be recognized that stresses increase along this path, so that fuel rods held at constant power in-reactor may experience even greater reductions in effective moduli.

It was found that fuel and cladding axial strains decreased with successive applications of axial loads to the top of the fuel column. This indicated that fuel/cladding contact was becoming more intimate with loading cycle (ramp), and that axial friction forces between fuel and cladding were increasing. This was caused by fuel cracking, which permitted the fuel to move outward toward the cladding (relocation). In the extreme cases for fully cracked pellet fuel (the irradiated Rod 8) and the sphere pac fuel design, the fuel/cladding contact was so intimate that significant axial friction forces accumulated over very short distances (3-4 cm). These accumulated friction forces were of sufficient magnitude to prevent the transmission of an axial forces further down the fuel column (see Figures 52 to 54). Instead, the strain energy applied to the top of the fuel column was absorbed by a shear mechanism within the cracked fuel, and dissipated in the radial direction by deforming the cladding locally. This implies that there may be limitations to the maximum allowable axial node length in fuel performance codes for the adequate prediction of axial stresses in the cladding. This may be especially important if axial gaps are suspected of occurring randomly in the fuel column.

81

Friction coefficients between cracked fuel columns and the cladding were found to vary between 0.5 and 2.0. The occurrence of fuel fragments gouging or galling the cladding may case the higher values of friction coefficient for long sliding distances. The axial load required to cause "breakaway" between fuel and cladding (suddenly reduced friction coefficients) seemed to decrease as the initial gap size increased.

Fuel-induced rod bowing seemed to increase with initial gap size and decrease with the amount of fuel cracking. When rod bow was plotted versus rod average diameter deformations at five azimuthal locations, unexpected behavior was found (Figure 57). Cladding diameter reductions were frequently greater on the convex side of the rod than on the concave side. The fuel would normally be expected to push radially outward on the convex side, and retard diameter reductions at that azimuthal location. It appears that the mechanics of load transfer within the cracked fuel column are not well understood.

4.0 CONCLUSIONS AND RECOMMENDATIONS

A series of laboratory experiments was conducted in order to verify a model describing the mechanical behavior of cracked UO_2 fuel columns. This effort consisted of verifying the general behavior and numerical values for the model's three primary independent parameters (effective crack roughness, effective gap roughness, and total crack length), and verifying the model's results that the effective Young's moduli for cracked fuel were substantially less than for solid UO_2. The following conclusions were reached during the course of this work. Recommendations for future work are included.

- The effective crack roughness (R_c) was verified. Reasonably good agreement was found between data from simple laboratory experiments (using alumina samples) and roughnesses deduced from the analysis of in-reactor data. R_c was found to decrease with increasing stress (or decreasing crack width), which verified the behavior of the crack compliance model. Laboratory values of R_c were between the measured crack surface microroughnesses and macroroughnesses (waviness), confirming that crack morphology (waviness) was an important contributor to the effective crack roughnesses. The scatter in the laboratory results for R_c decreased as stresses increased, implying that fragment rotations were also important. Since fragment rotations are probably controlled by crack surface morphology (waviness), this is an area recommended for further work.

- Laboratory values for the effective gap roughness (R_g) were found to be 2.0-2.5 times the values deduced from in-reactor data. These data were obtained by simulating the fuel relocation/fragment ratcheting mechanism for cracked pellets. The resulting fuel surface asperity distribution (caused by fragment misregistration) exhibited an extended tail for large asperities. In-reactor R_g distributions are suspected of having similar characteristics, and this parameter should be studied further since it affects cladding stress concentrations and fuel failure analyses.

- The total crack length (L_{tc}) in the transverse plane was verified. Nineteen PIE photomacrographs from test reactor rods were quantitatively analyzed for the total crack lengths of obviously open and apparently closed cracks. The results compared well with the L_{tc} assumed for the in-reactor analysis (3.5 fuel diameters). Although it was found that about 25% of the apparently closed cracks may be active in reducing the effective moduli for cracked fuel, the results were within the uncertainties in the analysis. The data analyzed were from test reactor rods at low burnups and relatively high powers, and it is recommended that the data base be extended to power reactor rods at high burnups.

- The reductions in effective Young's moduli caused by fuel cracking were verified with a series of fuel rod compliance experiments designed to simulate in-reactor stress systems at room temperature

83

in the laboratory. Good agreement was found between the laboratory data, in-reactor data, and the results of other investigations, except in the case of very small initial gap sizes, where uncertainties in in-reactor data or total crack length may have influenced the results.

- The purely elastic formulation used in the laboratory data analysis implied that the effects of axial fuel/cladding slipping are included in the effective modulus estimates. Since the viscous nature of axial slipping was found to be of sufficient magnitude to affect the analysis of in-reactor axial relaxation data, an approximate method was suggested for estimating the effects of axial slipping on effective modulus.

- Increased fuel cracking was found to cause the strain energy in the cracked fuel to be dissipated radially over progressively shorter axial distances by increased fuel/cladding friction and fuel shearing mechanisms. The maximum axial node lengths acceptable for estimating fuel and cladding stresses were found to be 20-25 cm at beginning-of-life and 3-4 cm at 22 GWD/MTM. It is recommended that further compliance experiments be conducted to determine axial interaction distances for intermediate burnups, alternate fuel designs, and lower-power operation.

- The friction coefficients for cracked fuel columns in zircaloy cladding were found to range between 0.5 and 2.0, depending on the distance of axial sliding. The axial load required to cause low-restraint sliding (breakaway) decreased as gap size increased.

- Fuel-induced rod bowing increased with initial gap size and decreased with the amount of fuel cracking. Plots of rod bow versus rod average diameter reduction at five azimuthal locations revealed an apparently anomolous mechanism: the cladding diameter frequently decreased at the position where the fuel was expected to be pushing radially outward on the cladding. Thus the mechanics of load and moment transfer within the cracked fuel column are in need of greater understanding.

- In general, it was found that the formulation of the cracked fuel model using independent parameters that were experimentally measurable was of great advantage in verifying the model, and it is recommended that future modelling efforts continue this approach.

- In general, it appears that cracked fuel mechanics is not well understood. The effects of fragment geometries on interfragment load, moment, and frictional mechanisms yielded some surprises during this work. It is recommended that cracked fuel mechanics continue to be studied both experimentally and theoretically, with the objective of improving estimates of localized cladding stress concentrations so that adequate fuel failure models may be developed. Some of this work is presently in process at PNL, under support from the Fuel Behavior Branch of the USNRC.

84

5.0 ACKNOWLEDGMENTS

6.0 REFERENCES

1. R. E. Williford, et al., February 1982. "A Model for the Effective Thermal and Mechanical Properties of Cracked UO_2 Pellets," Nuclear Technology Vol. 56 pp. 340-350.

2. R. E. Williford, et al., April 1980. The Analysis of Fuel Relocation for the NRC/PNL Halden Assemblies IFA-431, IFA-432, and IFA-513, NUREG/CR-0588, PNL-2709, Pacific Northwest Laboratory, Richland, Washington.

3. B. B. Mikic, 1974. "Thermal Contact Conductance: Theoretical Considerations," Int. J. Heat Mass Transfer, 17, 205.

4. D. D. Lanning et al., October 1979. A Procedure for the Interpretation of Transient Fuel Centerline Thermocouple Data, NUREG/CR-1012, PNL-3096, Pacific Northwest Laboratory, Richland, Washington.

5. C. Nealley, et al., October 1979. Post-Irradiation Data Analysis for NRC/PNL Halden Assembly IFA-431, NUREG/CR-0797, PNL-2975, Pacific Northwest Laboratory, Richland, Washington.

6. C. R. Hann., et al., February 1977. A Method for Determining the Uncertainty of Gap Conductance Deduced from Measured Fuel Centerline Temperatures, BNWL-2091, Pacific Northwest Laboratory, Richland, Washington.

7. R. E. Williford, and D. D. Lanning, March 1982. "Cracked Fuel Mechanics," presented at the IAEA Fuel Modellers Conference, PNL-SA-10168, Preston UK, March 15-19, 1982.

8. F. Pazdera and K. Lassman, March 1982. "URGAP: A Gap-Conductance Model for Transient Conditions," presented at the IAEA Fuel Modellers Conference, Preston, UK, March 15-19, 1982.

9. N. Kjaer-Pedersen, March 1982. "The Effect of Axial Diffusional Delays on the Overall Fission Gas Release," presented at the IAEA Fuel Modellers Conference, Preston UK, March 15-19, 1982.

10. D. S. Rowe and R. N. Oehlberg, August 1981. "An Analytical Model for Transient Gas Flow in Nuclear Fuel Rods", Nuclear Technology Vol 54, pp 174-179.

11. H. Blank, et al., March 1982. "Characterization of the Mechanical Properties of UO_2 Pellets," presented at the IAEA Fuel Modellers Conference, Preston, UK, March 15-19, 1982.

12. K. P. Galbraith, 1973. "Pellet-to-Cladding Gap Closure from Pellet Cracking." XN-73-17.

13. D. K. Kerwin, 1978. "Postirradiation Examination Data Report for Gap Conductance Test Series Test GC2-2." NUREG/CR-0211.

14. B. A. Murdock, 1977. "Experimental Data Report: Gap Conductance Test Series GC1-3 Postirradiation Examination." TREE-NUREG-1088.

15. B. A. Cook, 1978. "Postirradiation Data Report for Gap Conductance Test Series GC2-3." NUREG/CR-0253.

16. L.A. Walton and D. L. Husser, March 1982. "Fuel Pellet Fracture and Relocation," presented at the IAEA Fuel Modeller's Conference, Preston, UK, March 15-19, 1982.

17. M. Uchida and M. Ichikawa, 1980. "In-Pile Diameter Measurement of Light Water Reactor Test Fuel Rods for Assessment of Pellet-Cladding Mechanical Interaction" Nuclear Technology 51:33-44.

18. Montgomery, et al., 1980, "Axial Shear of Simulated Sphere Pac Fuel", Trans Am. Nucl. Soc. 35:205.

19. M. Nakatsuka, 1977. The Atomic Energy Society of Japan Annual Meeting, paper G39.

20. S. P. Timoshenko, 1955. Strength of Materials, Vol 1, page 405, Van-Nostran Company, Inc.

21. R. Christensen, March 1980. SPEAR Fuel Reliability Code System, EPRI-NP-1378, Electric Power Research Institute, Palo Alto, California.

22. K. Ito, et al, 1980. "Pellet Compliance Model Based on Out-of-Pile Simulation," Nuclear Engineering and Design 56:117-122.

APPENDIX A

THE HARWELL LONG ROD COMPLIANCE TESTING MACHINE

APPENDIX A - THE HARWELL LONG ROD COMPLIANCE TESTING MACHINE

MACHINE DESCRIPTION

General

The machine consists of a rigid steel and aluminum alloy frame approximately 60 in. (152 mm) high which is mounted on a tee shaped base plate. For ease of remote operation the whole unit is attached to a hydraulically actuated tilting platform which allows the machine to be rotated from the vertical to the horizontal plane (Figure A.1).

A rigid two level platform is attached at right angles to the upper end of the main vertical member of the frame. This platform carries the fuel rod cladding anchorage device and its associated rotation mechanism, the hydraulic fuel column loading cylinder and the fuel column axial deflection measuring transducer (Figure 39).

A motorized precision slide assembly which carries the cladding radial deflection measuring transducers, is also attached to the main vertical member of the frame (Figure A.2).

A rectangular section steel bar fixed parallel to the slide assembly carries the transducers which measure clad axial deflection.

Cladding Tube Anchoring System

The cladding anchorage system utilizes a 316 stainless steel Gyrolok 1/2-in. pipe connector type 8 COS-316. Preliminary tests had proved that, when used in conjunction with a specially developed internal support sleeve and tightened to 90-100 lb ft (12-14 kg-m) torque, a reliable joint capable of supporting a load in excess of 2D00 lbs (909 kg) could be made.

The pipe connector is screwed to a hollow steel arbour utilizing the standard integral male thread. The arbour passes through a hardened steel bush which is press fitted into the main frame top platform lower plate. This bush has a thrust face machined on its upper end, and the arbour is free to rotate in the bush thus permitting azimuthal rotation of the fuel rod. A matching thrust face on the arbour transfers axial loads to the machine frame via the bush.

The arbour is rotated by an electric motor-gear unit via an external gear train.

Fuel Column Loading System

The axial load is applied to the fuel column by means of a double acting hydraulic ram. The ram body is bolted to the upper plate of the top platform, an extension piece attached to the piston rod passes through the hollow center
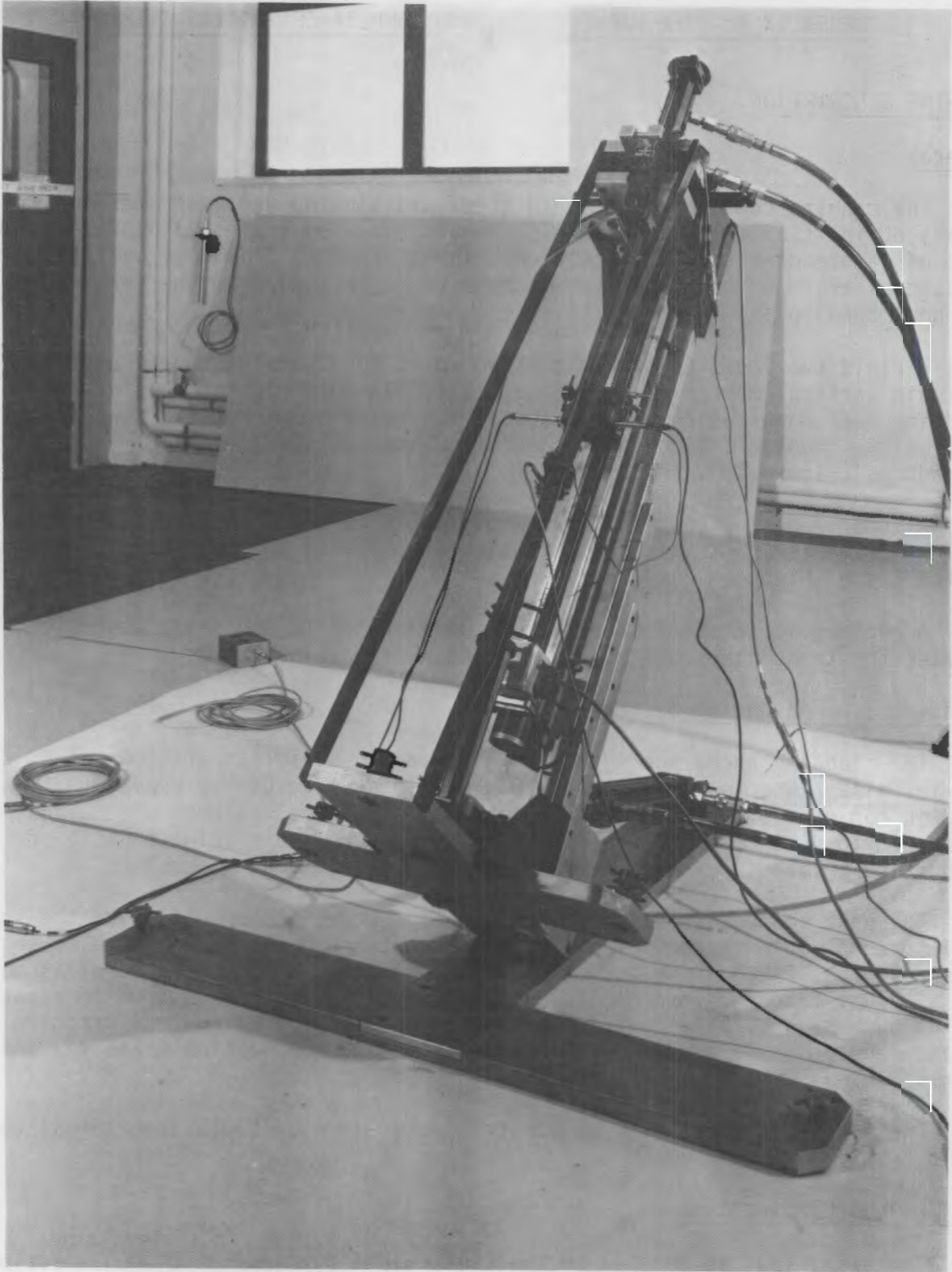
FIGURE A.1. The Harwell Compliance Testing Machine Being Rotated to Upright Position

A.2
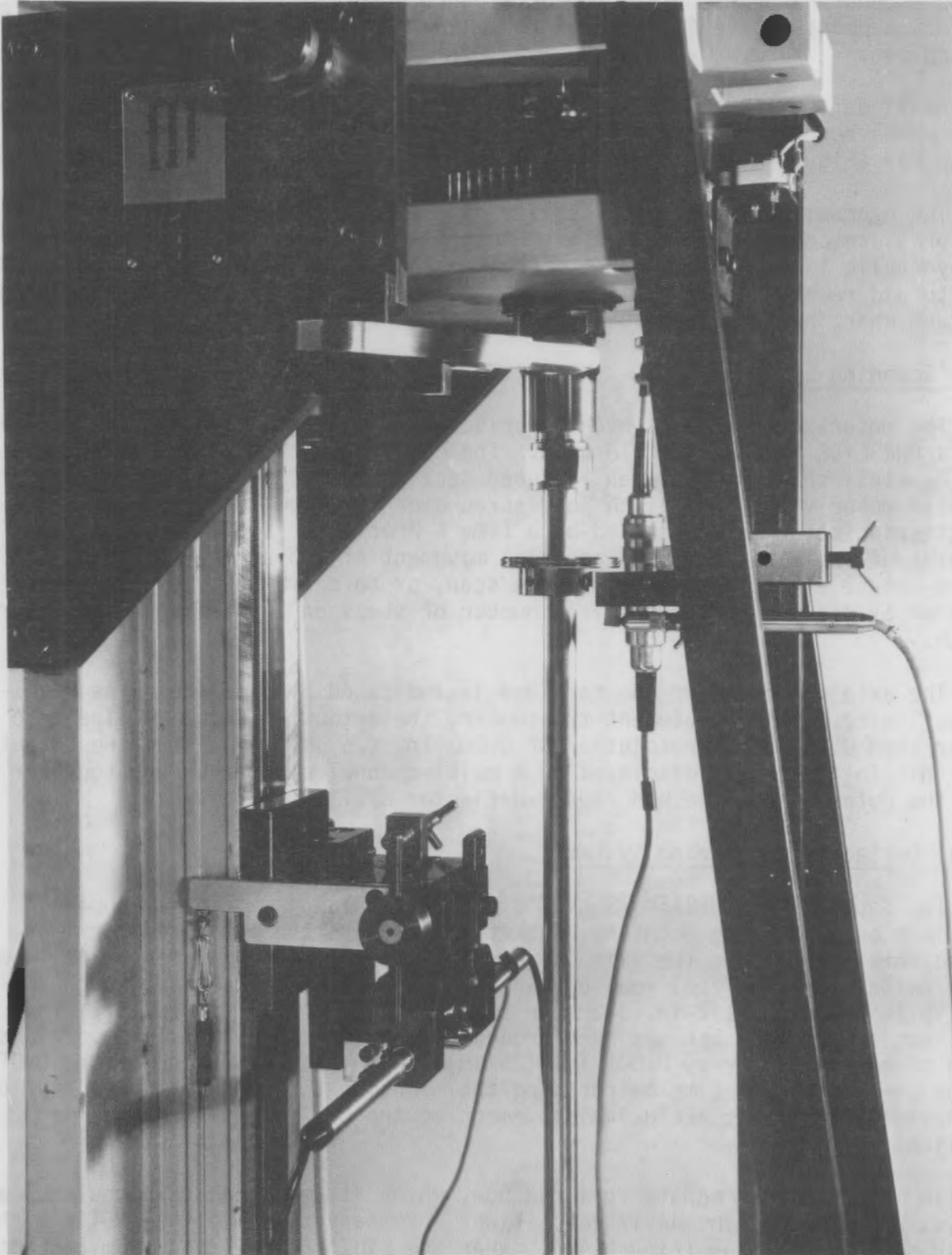
<u>FIGURE A.2.</u> The Cladding Radial Deflection Instrument (Standby Position)

of the arbour and bears on the end of a punch. This in burn passes through the internal support sleeve in the fuel rod plenum and bears on the top face of the fuel column.

Axial deflection of the fuel column is measured by a ±10 mm stroke transducer which bears on a disc attached to the upper end of the hydraulic ram piston rod (Figure A.2).

The hydraulic pressure is supplied by a pump unit equipped with a motorized pressure control valve, a 10 in. test gauge and a pressure transducer. The hydraulic lines are attached to the machine via self-sealed couplings modified to aid remote handling. The hydraulic system is filled with fluid using a vacuum charging technique to minimize the entrapment of air.

Axial Scanning System

The motorized carriage which comprises the axial scanning system is basically a UNISLIDE Type B25-30 Q1J unit. The carriage, which slides in a precision dovetail shaped slot in an extruded section bed, is driven by an electric stepping motor via a 1 mm pitch lead screw over an effective length of 66 cm. The stepping motor is controlled by a Time & Precision Indexer Type 2B 7403. One step of the motor produces an axial movement of 2.5 μm. The indexer can be pre-set to effect a suitable length scan, or to drive to a pre-determined position by dialing up the required number of steps on a thumb wheel selector switch.

The axial position of the carriage is indicated by a Celesco Type PT101-50A pull wire type displacement transducer, the output of which is linear to better than 0.1% with a resolution of 0.001 in. (25 μm). The analogue output from this instrument is displayed on a multi-channel chart recorder together with the outputs from the rod radial deflector LVDT's (Figure 40).

Radial Deflection Measuring System

Two Sangamo Type NBR/5mm/S LVDT's are fitted in diametrically opposed positions on a pivoting mounting bracket attached to the motorized carriage. In the working position the axis of the LVDT's passes through the nominal longitudinal axis of the fuel rod, but when the mounting is rotated through 90° the LVDT's bear on a 1/2-in. diameter standard gauge bar (Figure A.2). The outer surface of this bar has been ground to provide two cylindrical portions whose diameters differ by 0.001 in. (25 μm), thus the calibration of the LVDT's can be checked at any time by rotating the mounting through 90°. A safety lock is provided to prevent accidental movement of the LVDT's from the working position.

In order to accommodate fuel rod bow, which it had been shown could be as much as 2 mm center line deviation, it was necessary to equip the LVDT's with tee shaped contact tips (Figure 40). When the LVDT's were moved from contact with the fuel rod to the standard gauge and vice verse, unacceptably high rotational loads were applied to the peg and slot of the LVDT's integral shaft

A.4

anti-rotation system. To overcome this problem twin ball races are fitted to the LVDT mounting bracket which effectively prevent rotary movement of the LVDT shaft but which have a minimal effect on linear movement.

Length Datum Disc Position Determination

All axial position measurements are made relative to the machine frame length datum point. This point is close to the upper limit of travel of the motorized carriage. A micro-switch fixed to the machine frame is activated by an arm attached to the carriage. The carriage is driven upwards until the micro-switch is activated completing a circuit containing a signal lamp. The carriage is then inched downward until the signal lamp is extinguished. The carriage is then set at the datum position.

The carriage is then driven downwards until the diameter LVDT's reach the center of the fuel rod lower fiducial groove. The distance traveled can be determined by counting the number of pulses delivered to the stepping motor. Thus the position of the fuel rod datum relative to the machine datum at the start of the test sequence is established.

The positions of the axial deflection length datum discs relative to the machine datum are measured by a similar method. In this case an electrical contact fixed to the diameter LVDT mounting bracket is brought into contact with the lower face of the discs in turn thus completing a circuit through the fuel rod to ground illuminating a signal lamp.

Cladding Axial Deflection Measuring System

A rectangular section steel pillar, attached to the machine base plate and the upper platforms, and parallel to the fuel rod axis carries the two LVDT's which measure clad axial deflection. These LVDT's are attached to mounting blocks which slide on the pillar and are locked in place when correctly positioned. The LVDT's bear via 90° bell cranks onto the faces of the two length datum discs which are fitted to the fuel rod prior to setting up on the machine. The discs are subsequently lightly clamped in position, one close to the top of the rod, the second at least 80 mm below the first.

The difference between the LVDT outputs indicates the deflection of the cladding between the length datum discs while the deflection indicated by the top LVDT is the summation of slippage in the anchoring system, machine component settling, and deflection in that portion of the clad above the datum disc.

Fuel Column Deflection Measuring System

The fuel column deflection is measured by a ±10 mm stroke LVDT which bears directly on the underside of a disc attached to the outboard end of the hydraulic ram piston rod. The LVDT is held in a mounting block which is attached to the upper end of the same rectangular bar which carries the cladding axial deflection LVDT's (Figure 39).

Compression of the fuel column plus cladding axial deflection results in downward movement of the punch. Piston rod extension and piston rod are all constrained to move axially only. Thus the deflection of the fuel column can be determined by subtracting the axial clad deflection from the deflection of the piston rod assembly.

TABLE A.1. Transducers

Transducer	Manufacturer	Type	Stroke	Accuracy
LVDT A	Sangamo Weston	NBR	±5 mm	<0.3%
LVDT B	Sangamo WEston	NBR		
LVDT F	Novibra	QET/002	±10 mm	0.1%
LVDT C1	Novibra	QET/122	±1 mm	<0.2%
LVDT C2	Novibra	QET/122	±1 mm	
Position	Celesco	PT 101-50A	0-50"	<*0.1%
Pressure	Bell & Howell	BHL 4100-06 -05 MO	0-250 BAR	0.7%

APPENDIX B

ZIRCALOY-STEATITE DIAMETER AND BOW DATA
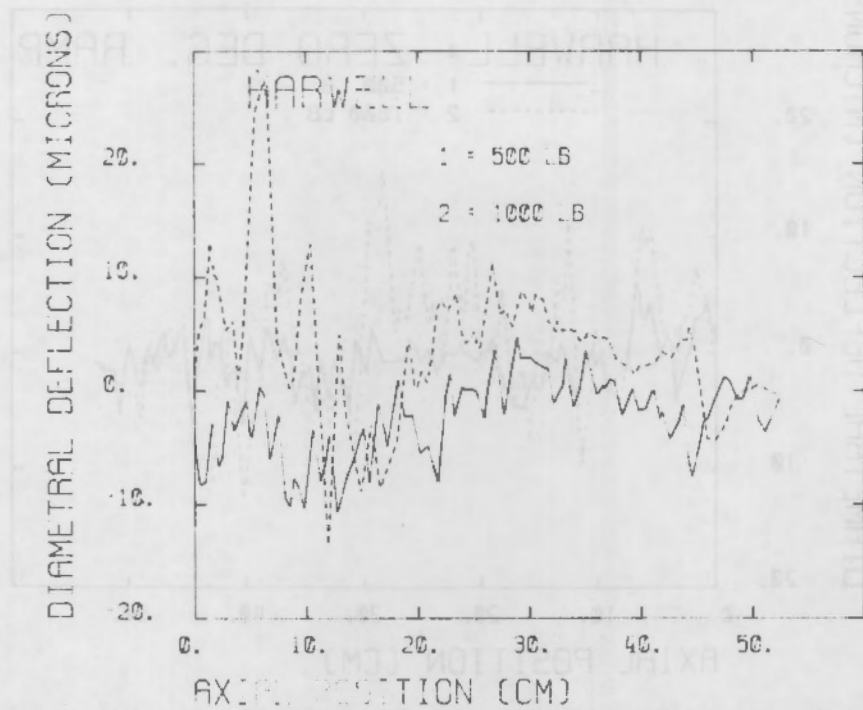
FIGURE B.1. Diameter Deformations for Zircaloy-Steatite Long Rod: Ramp 1, 0 Degrees, 500 and 1000 lb loads
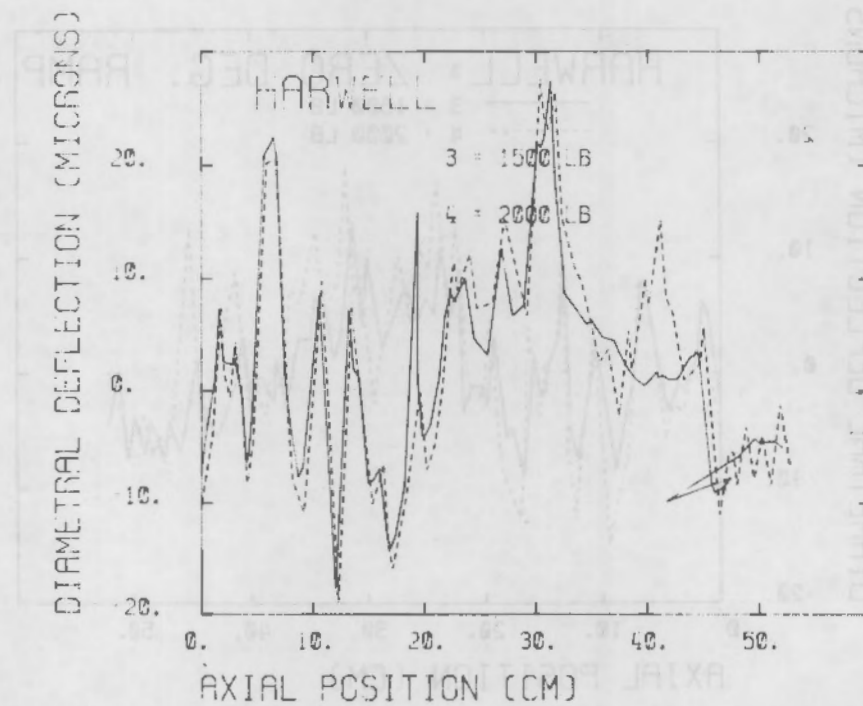
FIGURE B.2. Diameter Deformations for Zircaloy-Steatite Long Rod: Ramp 1, 0 Degrees, 1500 and 2000 lb loads

B.1
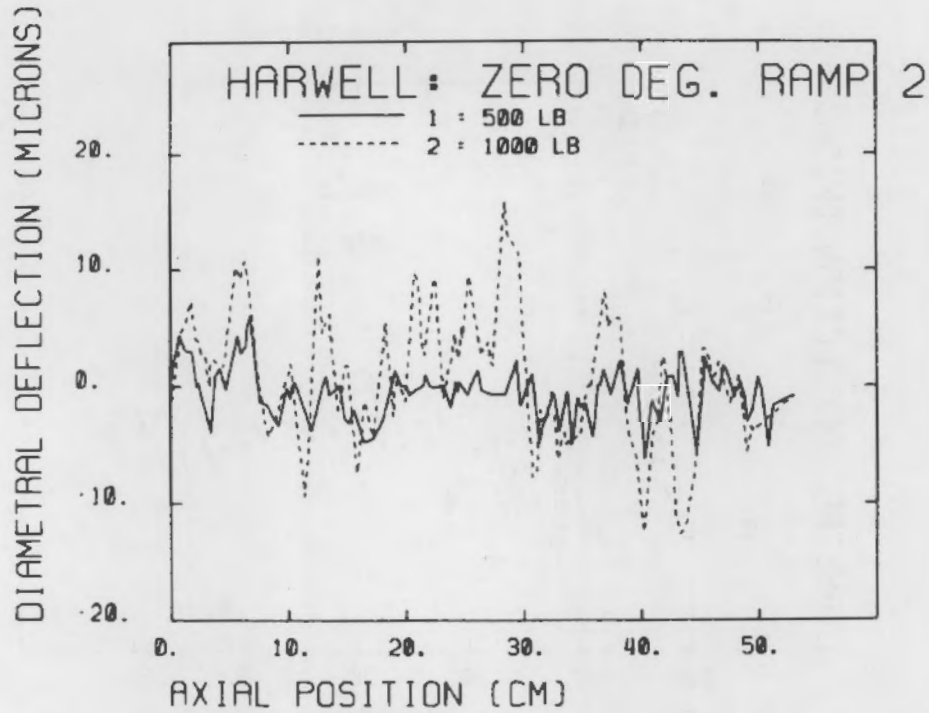
FIGURE B.3. Diameter Deformations for Zircaloy–Steatite Long Rod:
Ramp 2, 0 Degrees, 500 and 1000 lb loads
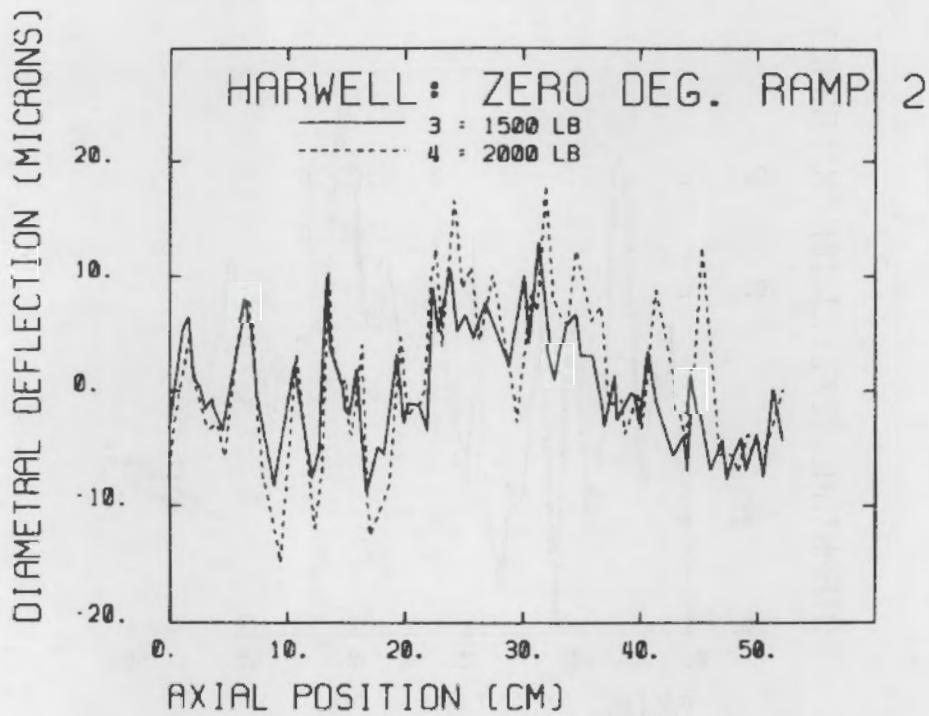
FIGURE B.4. Diameter Deformations for Zircaloy–Steatite Long Rod:
Ramp 2, 0 Degrees, 1500 and 2000 lb loads

B.2
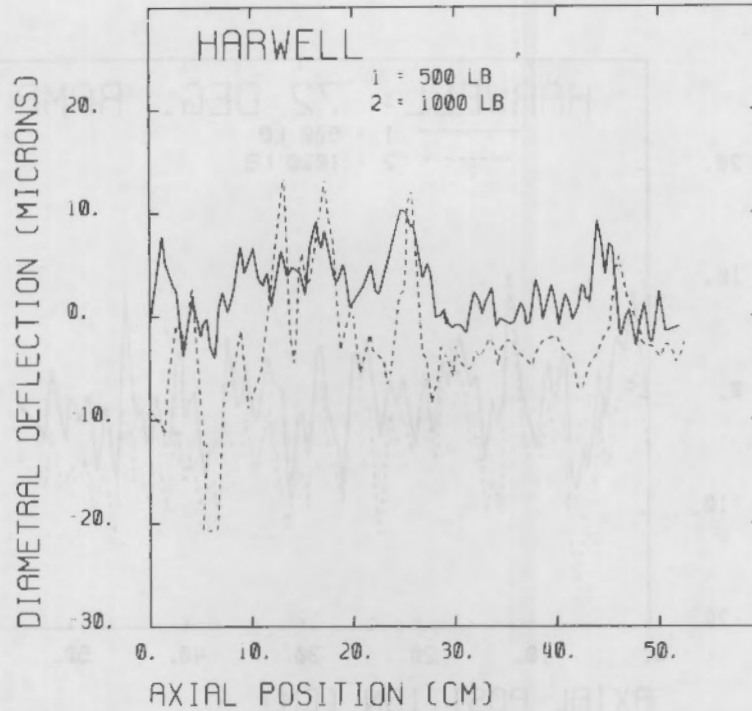
FIGURE B.5. Diameter Deformations for Zircaloy-Steatite Long Rod:
Ramp 1, 72 Degrees, 500 and 1000 lb loads
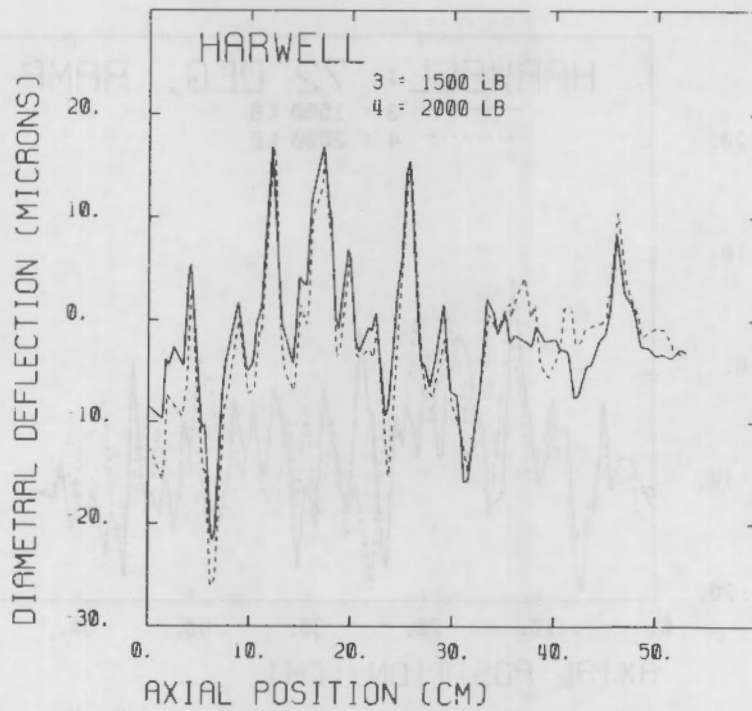
FIGURE B.6. Diameter Deformations for Zircaloy-Steatite Long Rod:
Ramp 1, 72 Degrees, 1500 and 2000 lb loads

B.3
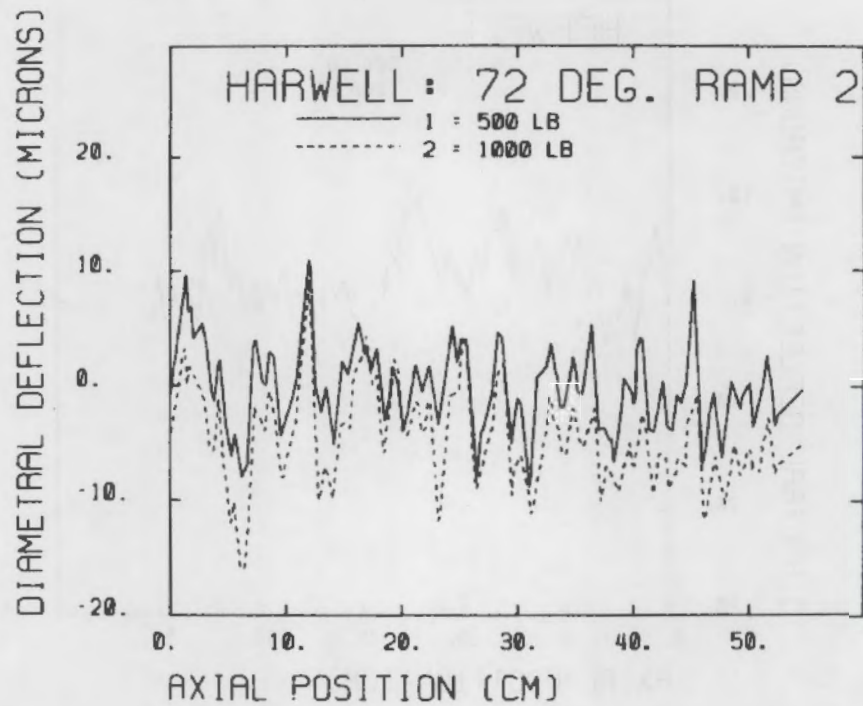
FIGURE B.7. Diameter Deformations for Zircaloy-Steatite Long Rod: Ramp 2, 72 Degrees, 500 and 1000 lb loads
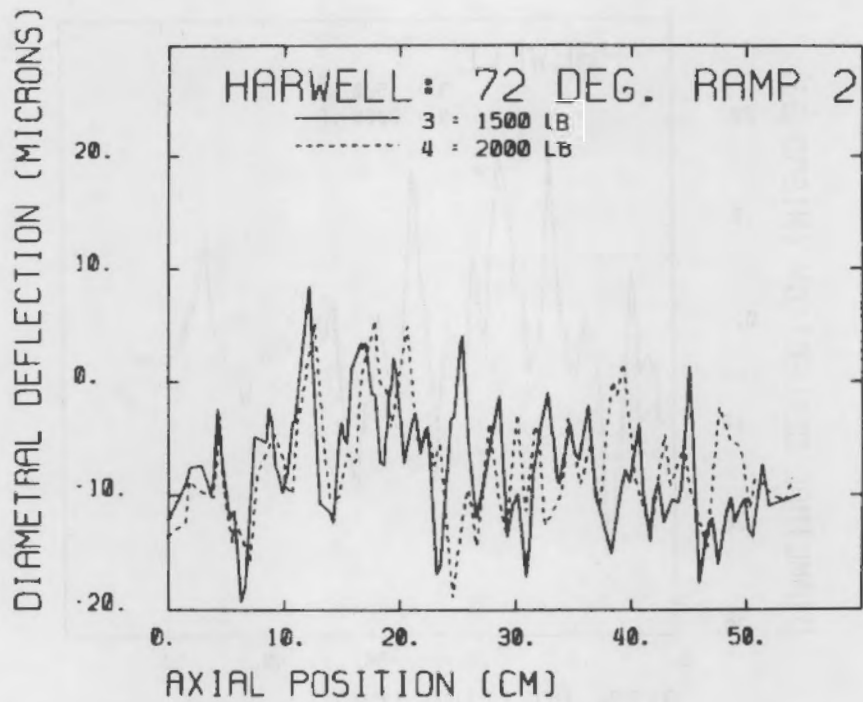
FIGURE B.8. Diameter Deformations for Zircaloy-Steatite Long Rod: Ramp 2, 72 Degrees, 1500 and 2000 lb loads

B.4
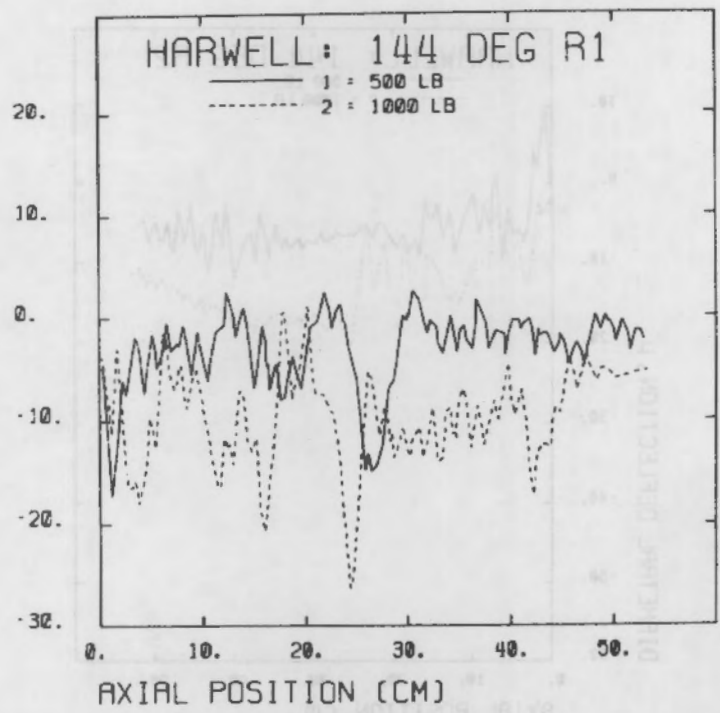
FIGURE B.9. Diameter Deformations for Zircaloy-Steatite Long Rod: Ramp 1, 144 Degrees, 500 and 1000 lb loads
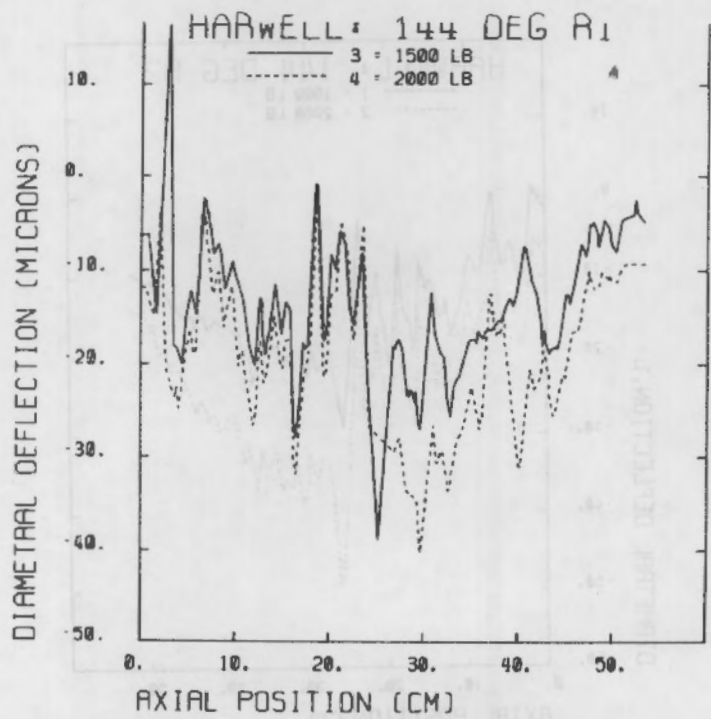
FIGURE B.10. Diameter Deformations for Zircaloy-Steatite Long Rod: Ramp 1, 144 Degrees, 1500 and 2000 lb loads
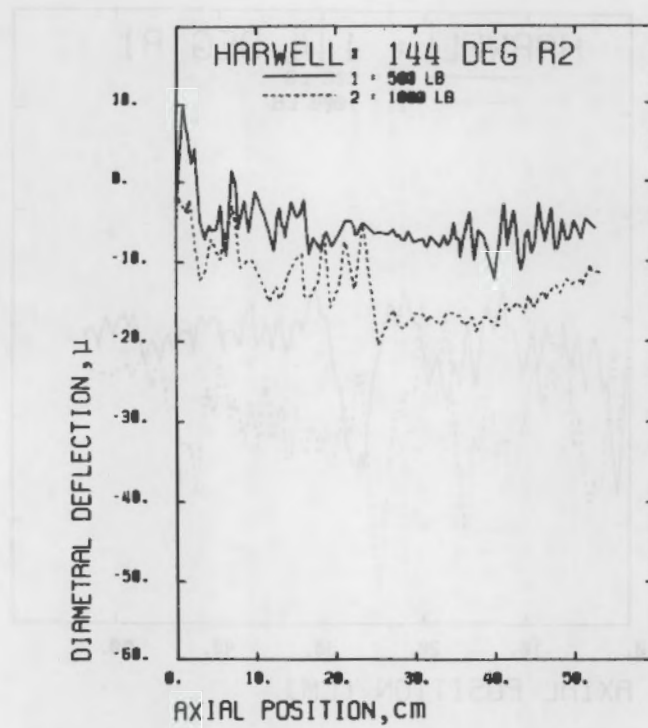
FIGURE B.11. Diameter Deformations for Zircaloy-Steatite Long Rod:
Ramp 2, 144 Degrees, 500 and 1000 lb loads
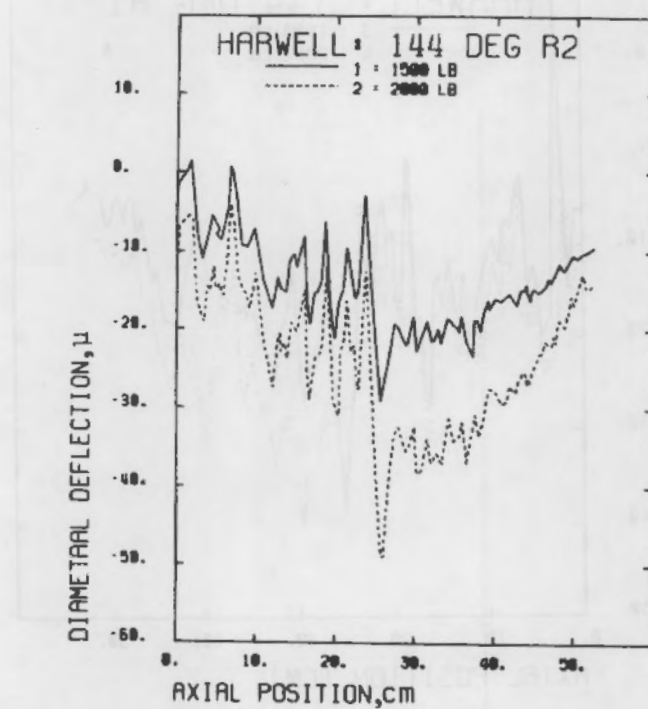
FIGURE B.12. Diameter Deformations for Zircaloy-Steatite Long Rod:
Ramp 2, 144 Degrees, 1500 and 2000 lb loads

B.6
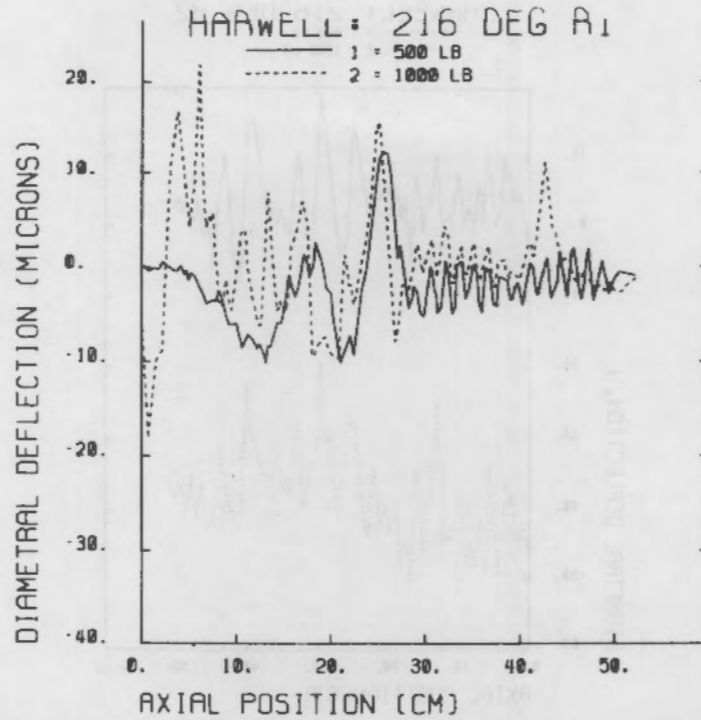
FIGURE B.13. Diameter Deformations for Zircaloy-Steatite Long Rod: Ramp 1, 216 Degrees, 500 and 1000 lb loads
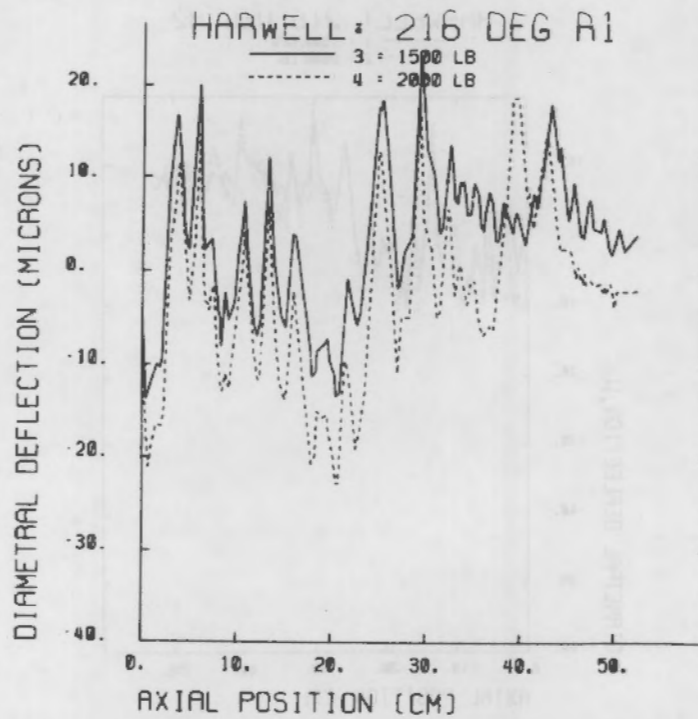
FIGURE B.14. Diameter Deformations for Zircaloy-Steatite Long Rod: Ramp 1, 216 Degrees, 1500 and 2000 lb loads
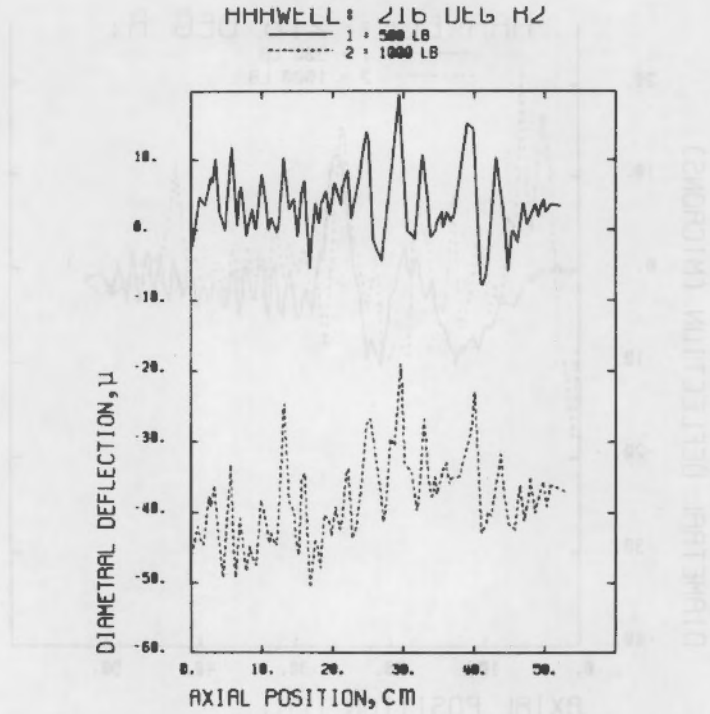
FIGURE B.15. Diameter Deformations for Zircaloy-Steatite Long Rod: Ramp 2, 216 Degrees, 500 and 1000 lb loads
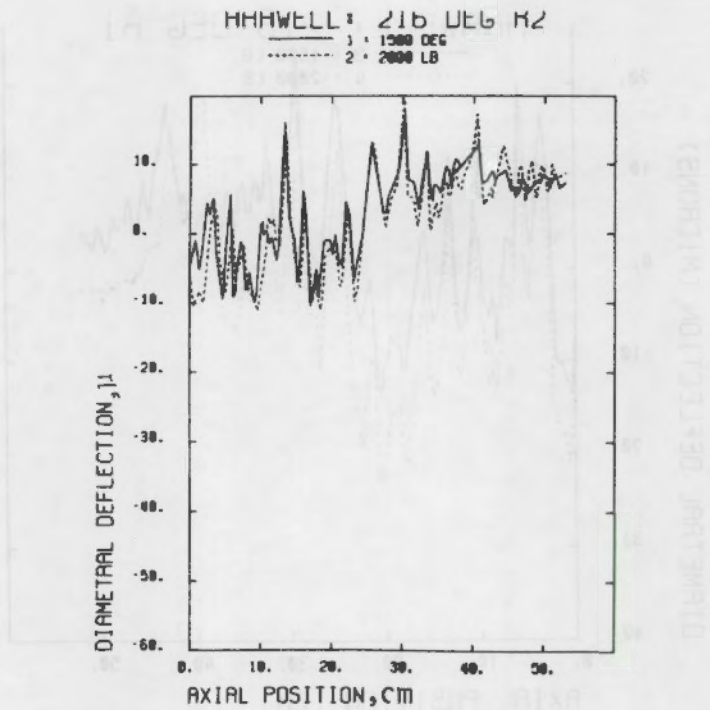
FIGURE B.16. Diameter Deformations for Zircaloy-Steatite Long Rod: Ramp 2, 216 Degrees, 1500 and 2000 lb loads
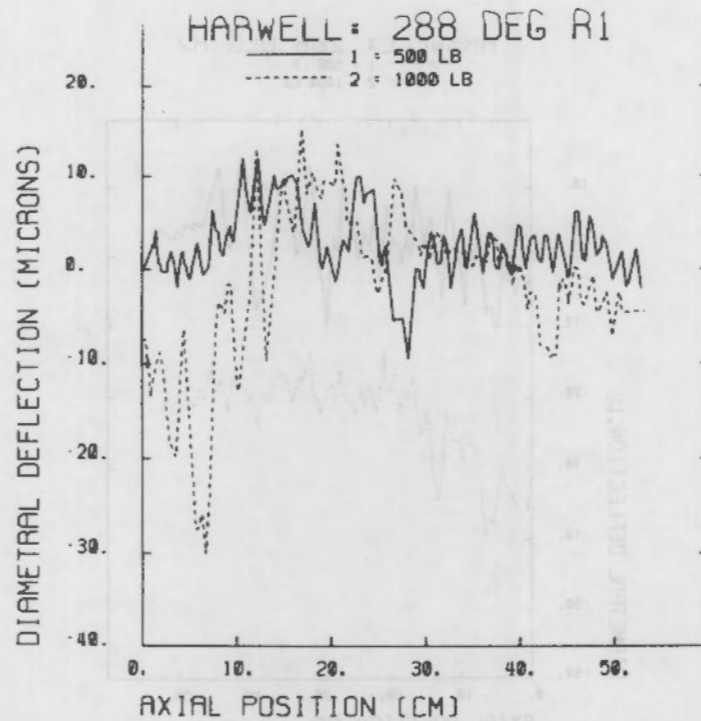
FIGURE B.17. Diameter Deformations for Zircaloy-Steatite Long Rod: Ramp 1, 288 Degrees, 500 and 1000 lb loads
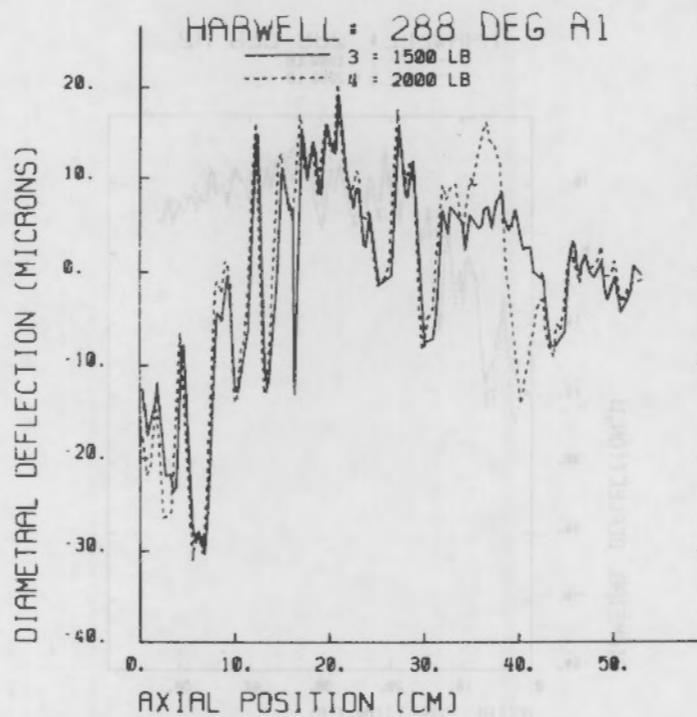
FIGURE B.18. Diameter Deformations for Zircaloy-Steatite Long Rod: Ramp 1, 288 Degrees, 1500 and 2000 lb loads
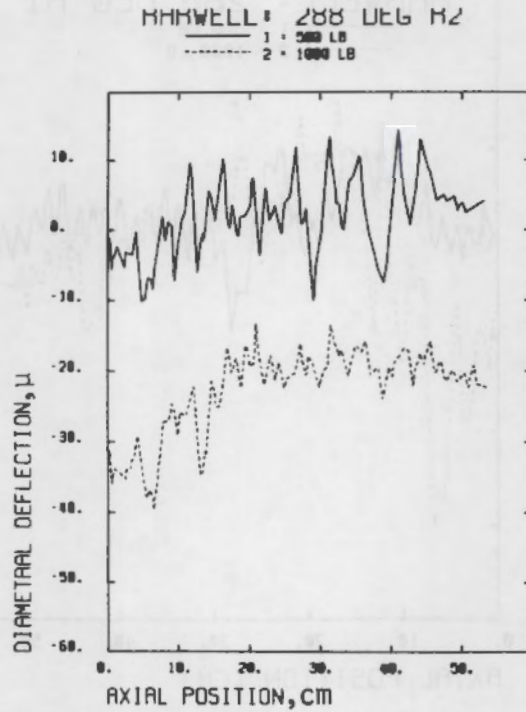
FIGURE B.19.   Diameter Deformations for Zircaloy-Steatite Long Rod:
                Ramp 2, 288 Degrees, 500 and 1000 lb loads
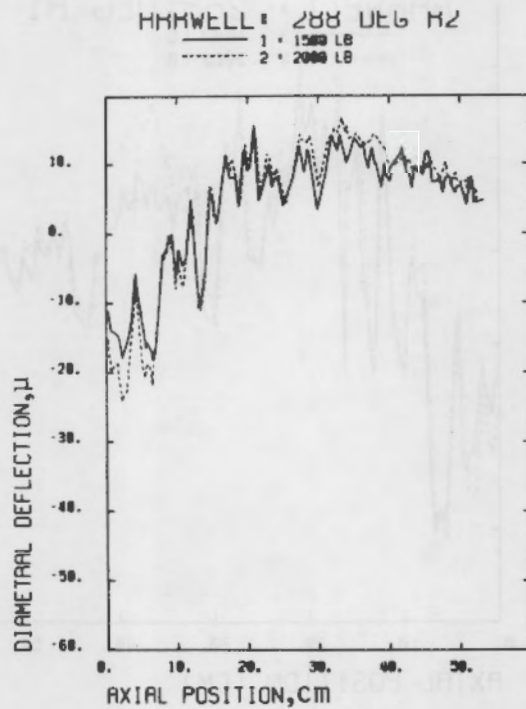
FIGURE B.20.   Diameter Deformations for Zircaloy-Steatite Long Rod:
                Ramp 2, 288 Degrees, 1500 and 2000 lb loads
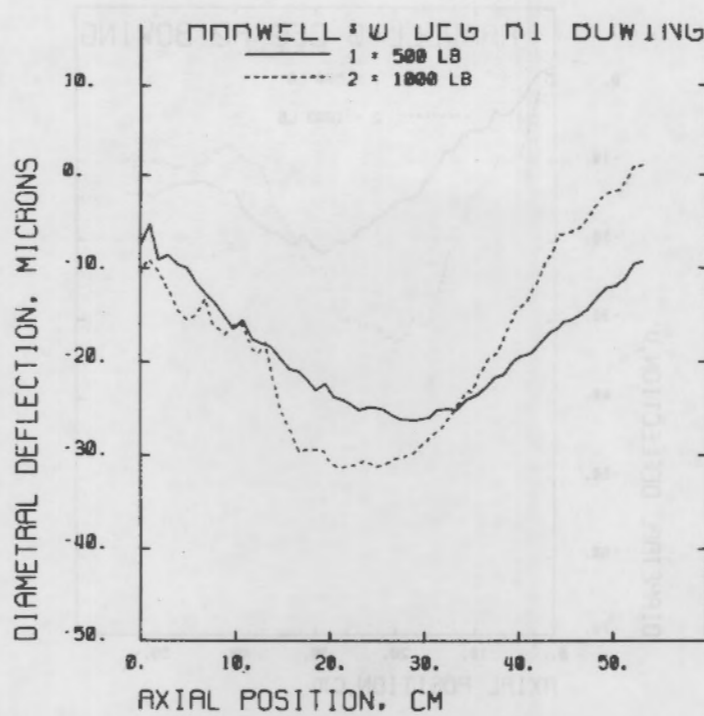
FIGURE B.21.   Rod Bowing for Zircaloy-Steatite Long Rod: Ramp 1, 0 Degrees, 500 and 1000 lb loads
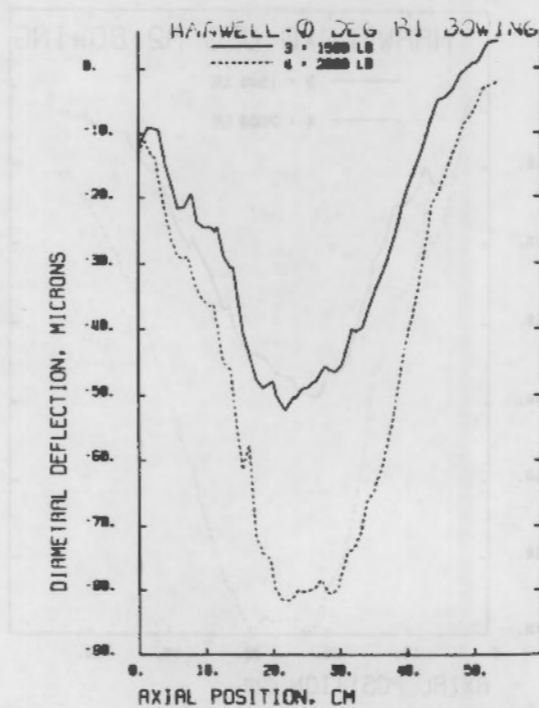
FIGURE B.22.   Rod Bowing for Zircaloy-Steatite Long Rod: Ramp 1, 0 Degrees, 1500 and 2000 lb loads

B.11
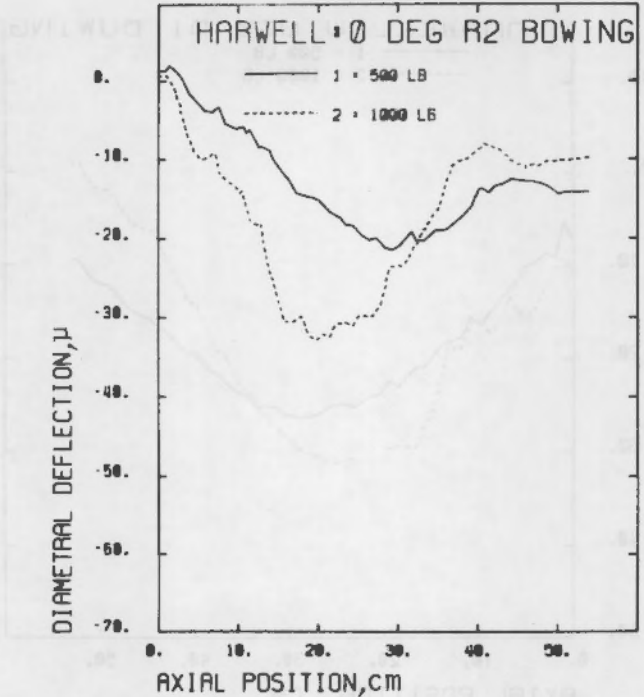
FIGURE B.23. Rod Bowing for Zircaloy-Steatite Long Rod: Ramp 2,
0 Degrees, 500 and 1000 lb loads
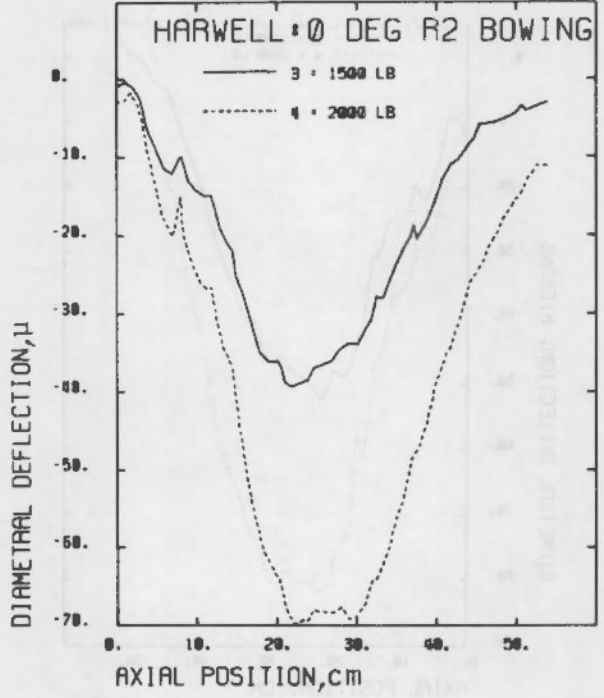
FIGURE B.24. Rod Bowing for Zircaloy-Steatite Long Rod: Ramp 2,
0 Degrees, 1500 and 2000 lb loads
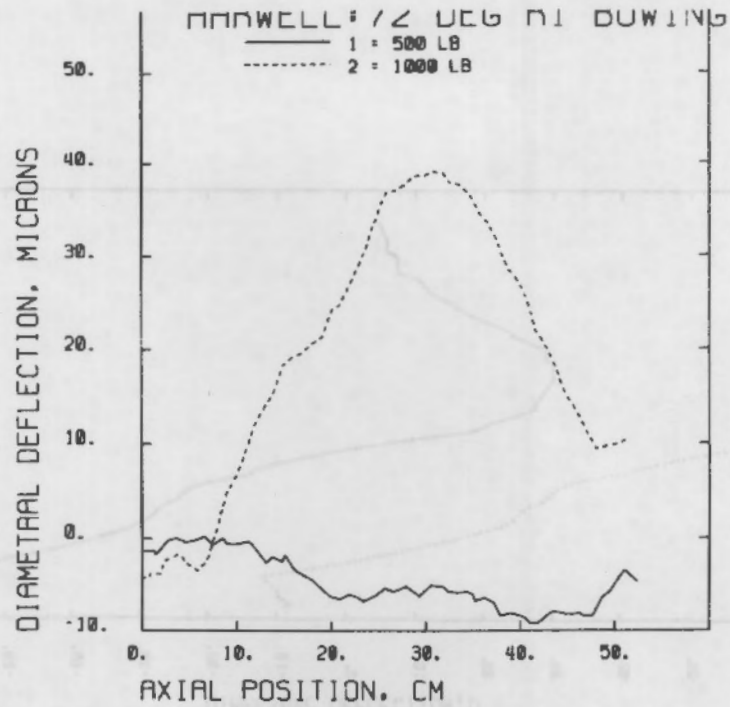
FIGURE B.25. Rod Bowing for Zircaloy-Steatite Long Rod: Ramp 1,
72 Degrees, 500 and 1000 lb loads
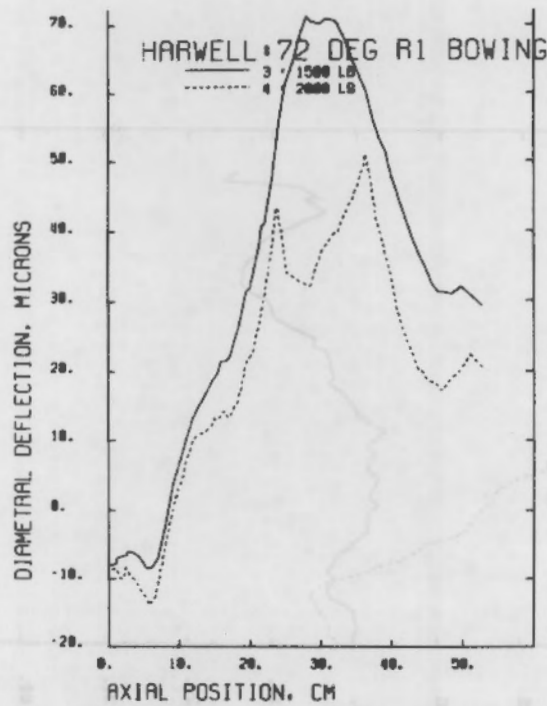
FIGURE B.26. Rod Bowing for Zircaloy-Steatite Long Rod: Ramp 1,
72 Degrees, 1500 and 2000 lb loads
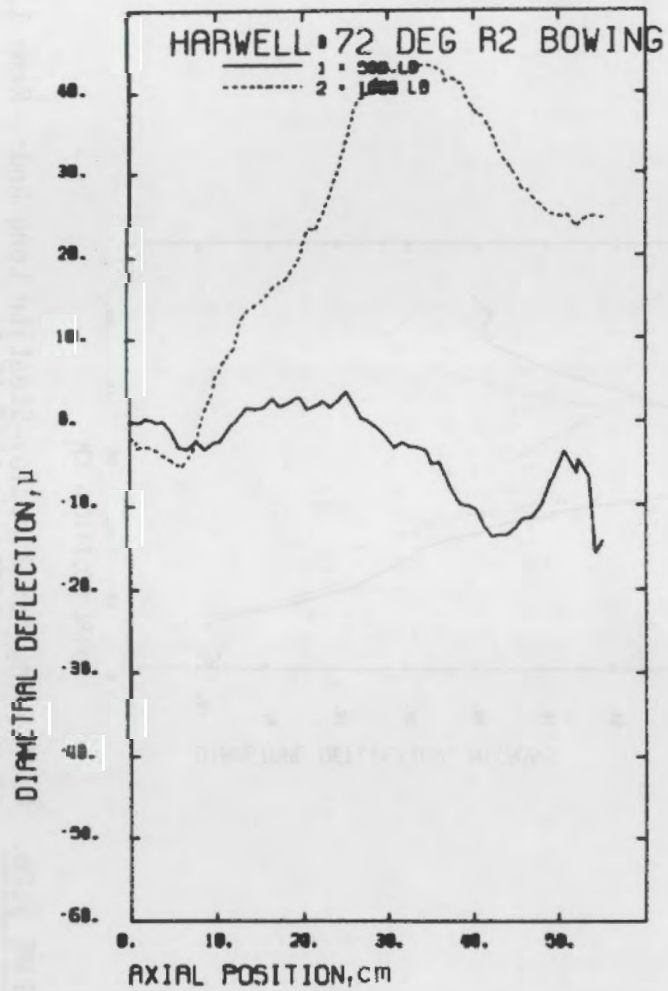
FIGURE B.27. Rod Bowing for Zircaloy-Steatite Long Rod: Ramp 2, 72 Degrees, 500 and 1000 Tb loads
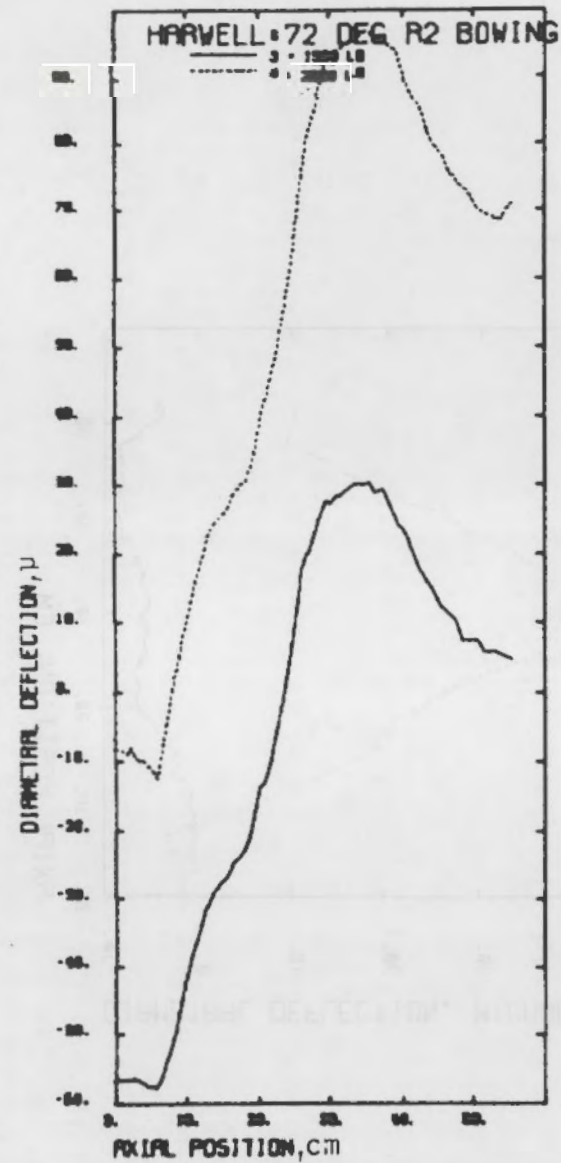
FIGURE B.28. Rod Bowing for Zircaloy-Steatite Long Rod: Ramp 2, 72 Degrees, 1500 and 2000 Tb loads
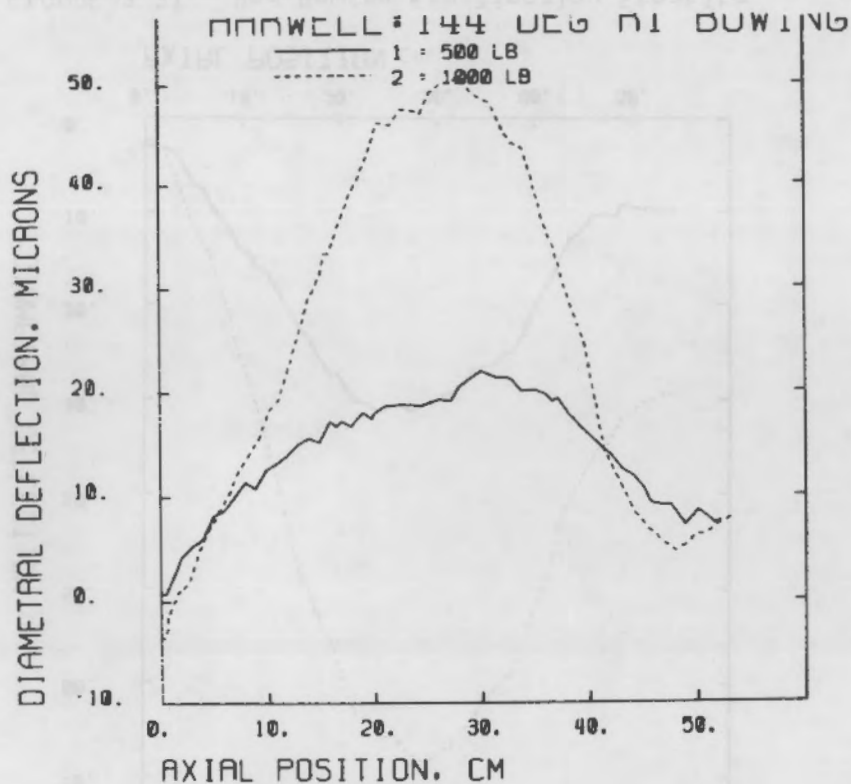
FIGURE B.29. Rod Bowing for Zircaloy-Steatite Long Rod: Ramp 1, 144 Degrees, 500 and 1000 lb loads
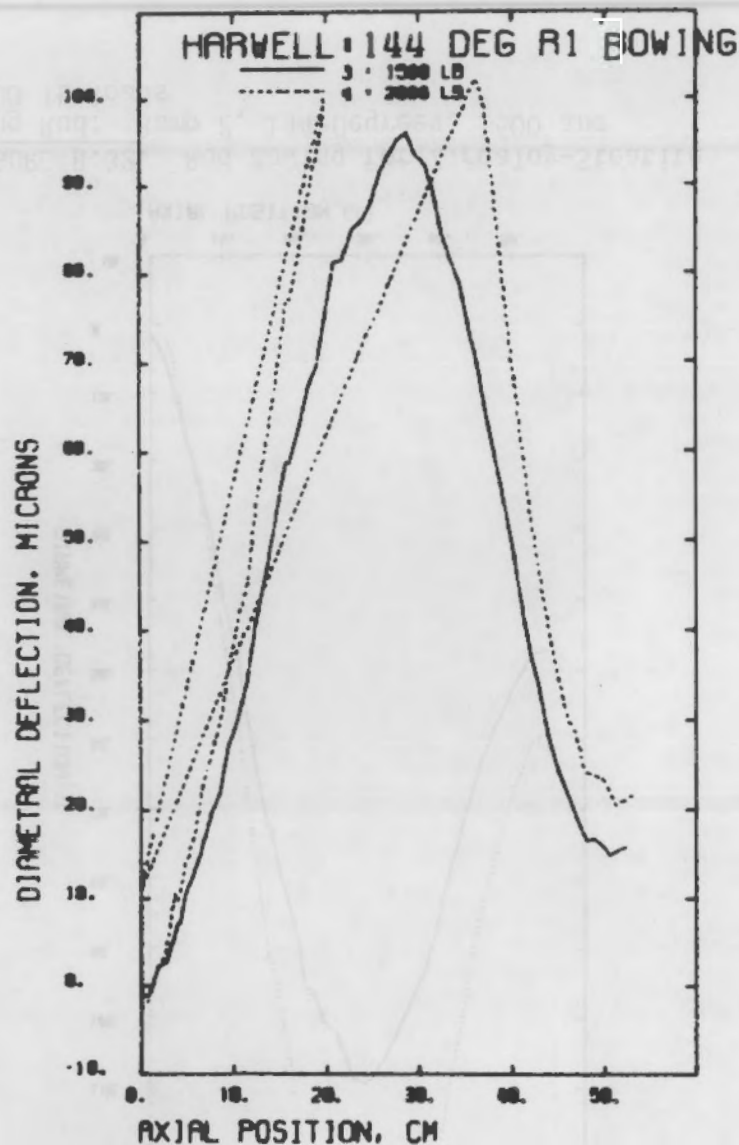
FIGURE B.30. Rod Bowing for Zircaloy-Steatite Long Rod: Ramp 1, 144 Degrees, 1500 and 2000 lb loads

HARWELL • 144 DEG R2 BOWING
1 = 500 LB
2 = 1000 LB

DIAMETRAL DEFLECTION μ MICRONS

AXIAL POSITION cm
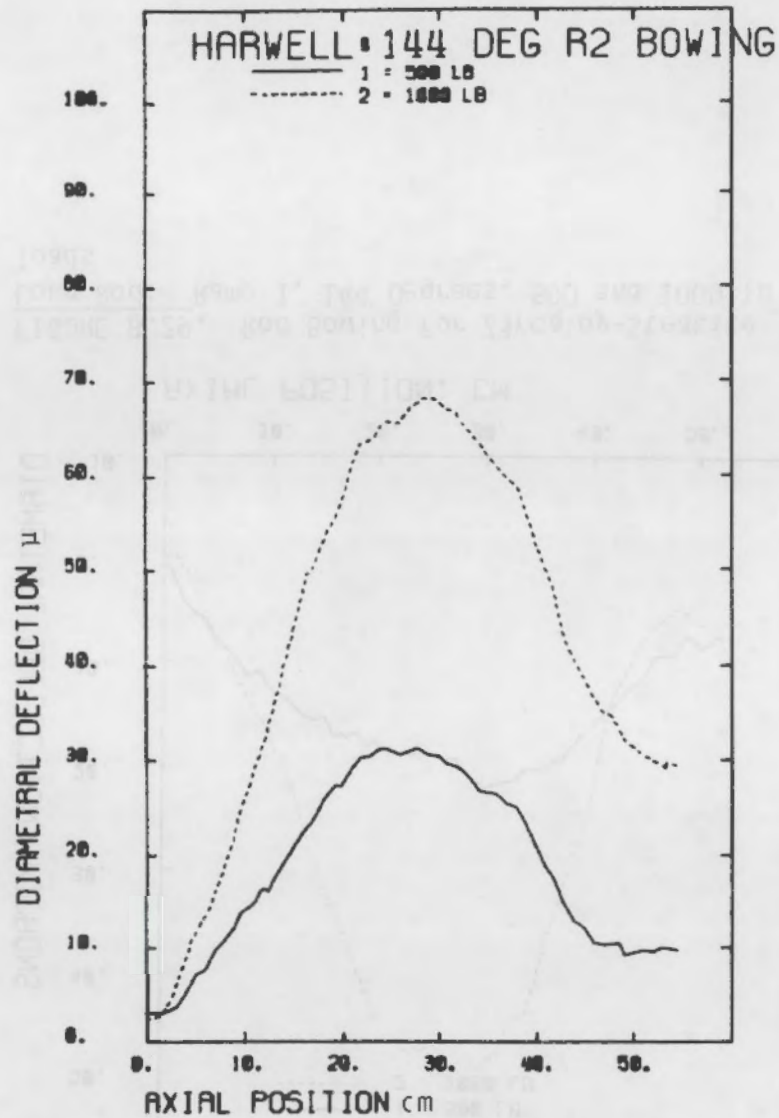
FIGURE B.31. Rod Bowing for Zircaloy-Steatite
Long Rod: Ramp 2, 144 Degrees, 500 and
1000 lb loads

HARWELL • 144 DEG R2 BOWING
3 = 1500 LB
4 = 2000 LB

DIAMETRAL DEFLECTION, U MICRONS

AXIAL POSITION, CM
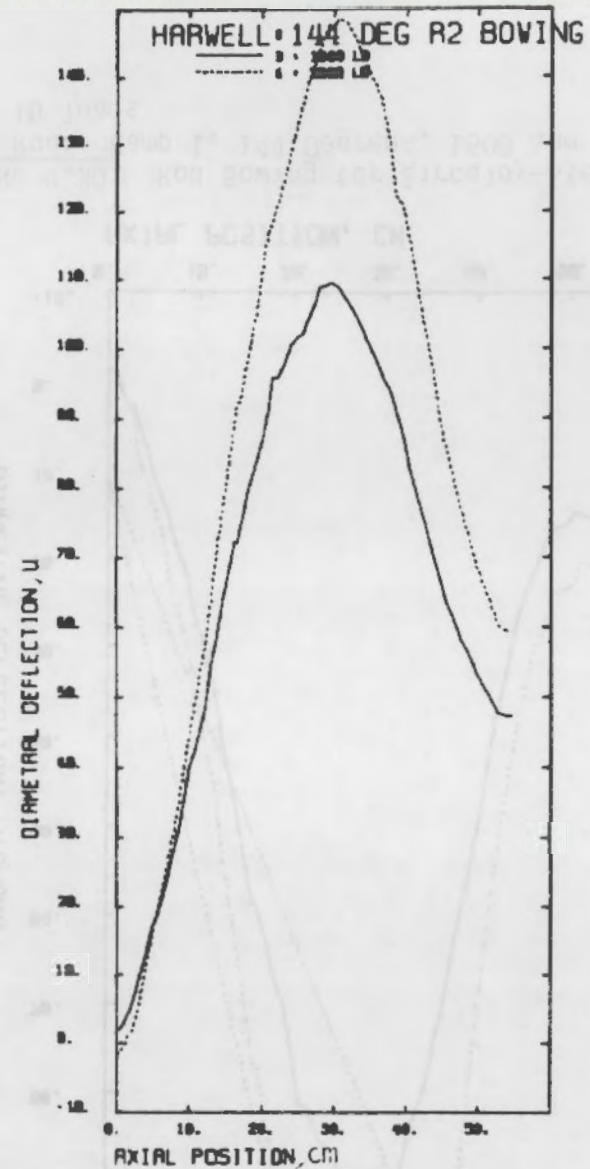
FIGURE B.32. Rod Bowing for Zircaloy-Steatite
Long Rod: Ramp 2, 144 Degrees, 1500 and
2000 lb loads
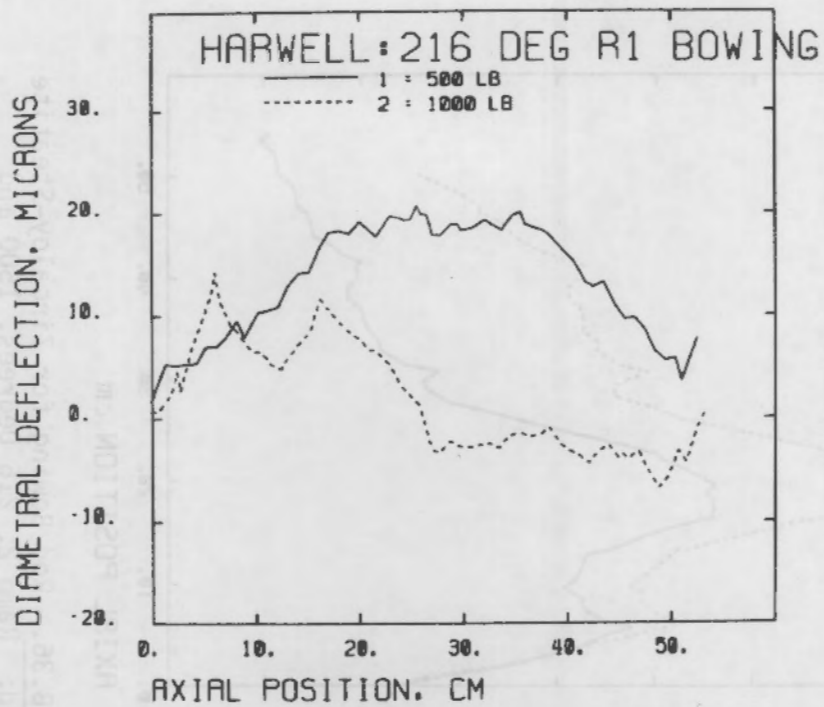
FIGURE B.33. Rod Bowing for Zircaloy-Steatite Long Rod: Ramp 1, 216 Degrees, 500 and 1000 lb loads
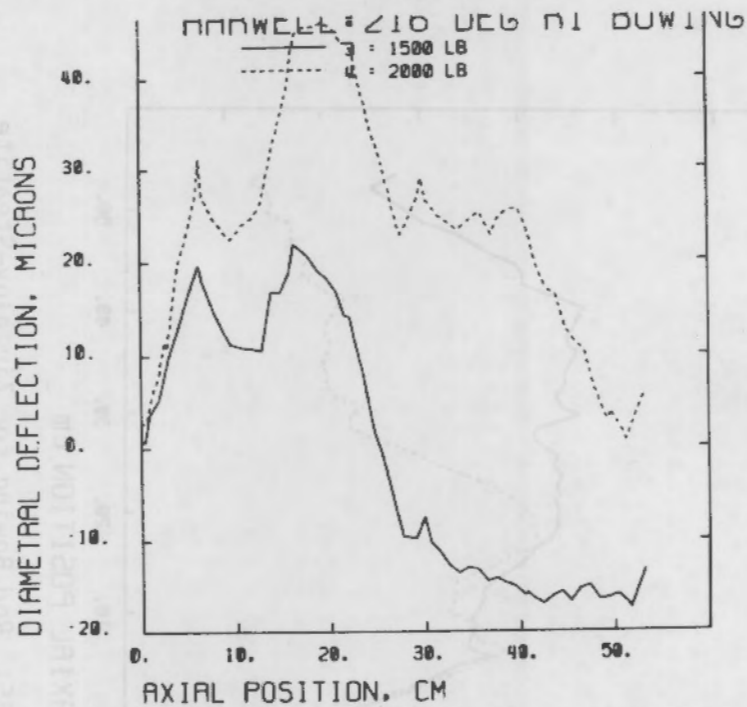
FIGURE B.34. Rod Bowing for Zircaloy-Steatite Long Rod: Ramp 1, 216 Degrees, 1500 and 2000 lb loads
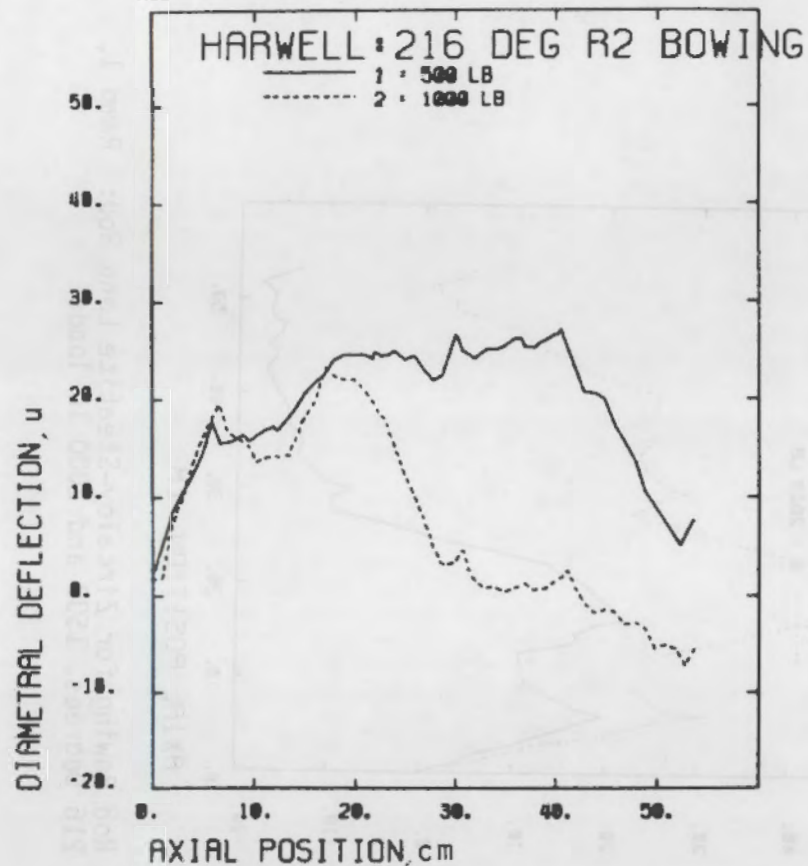
FIGURE B.35. Rod Bowing for Zircaloy-Steatite Long Rod: Ramp 2, 216 Degrees, 500 and 1000 lb loads
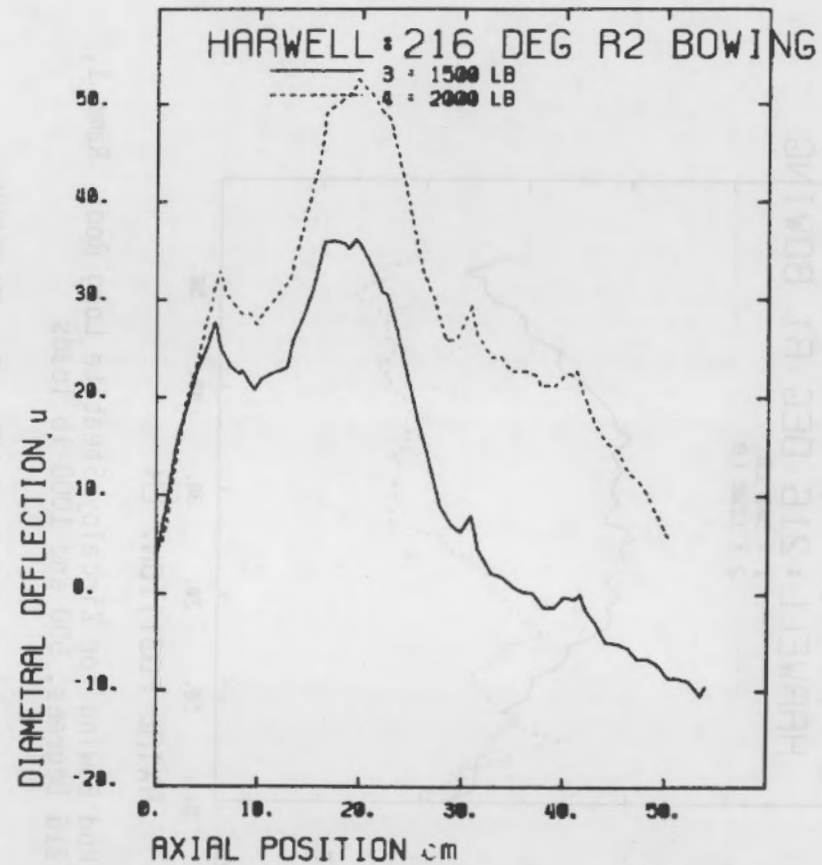
FIGURE B.36. Rod Bowing for Zircaloy-Steatite Long Rod: Ramp 2, 216 Degrees, 1500 and 2000 lb loads

HARWELL:288 DEG R1 BOWING

DIAMETRAL DEFLECTION, MICRONS

AXIAL POSITION, CM
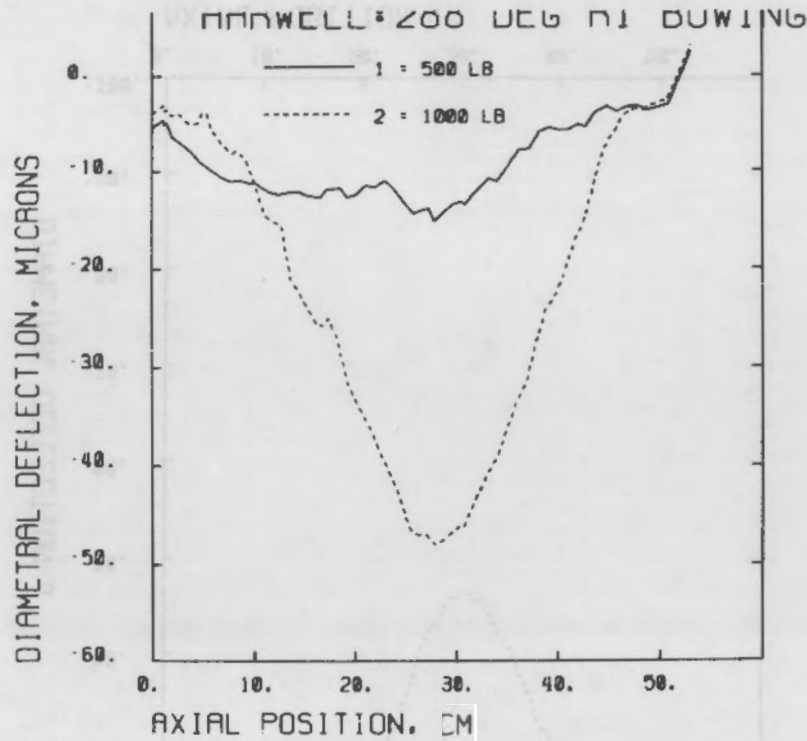
FIGURE B.37. Rod Bowing for Zircaloy-Steatite
Long Rod: Ramp 1, 288 Degrees, 500 and
1000 lb loads

HARWELL:288 DEG R1 BOWING

3 : 1500 LB
4 : 2000 LB

DIAMETRAL DEFLECTION, MICRONS

AXIAL POSITION, CM
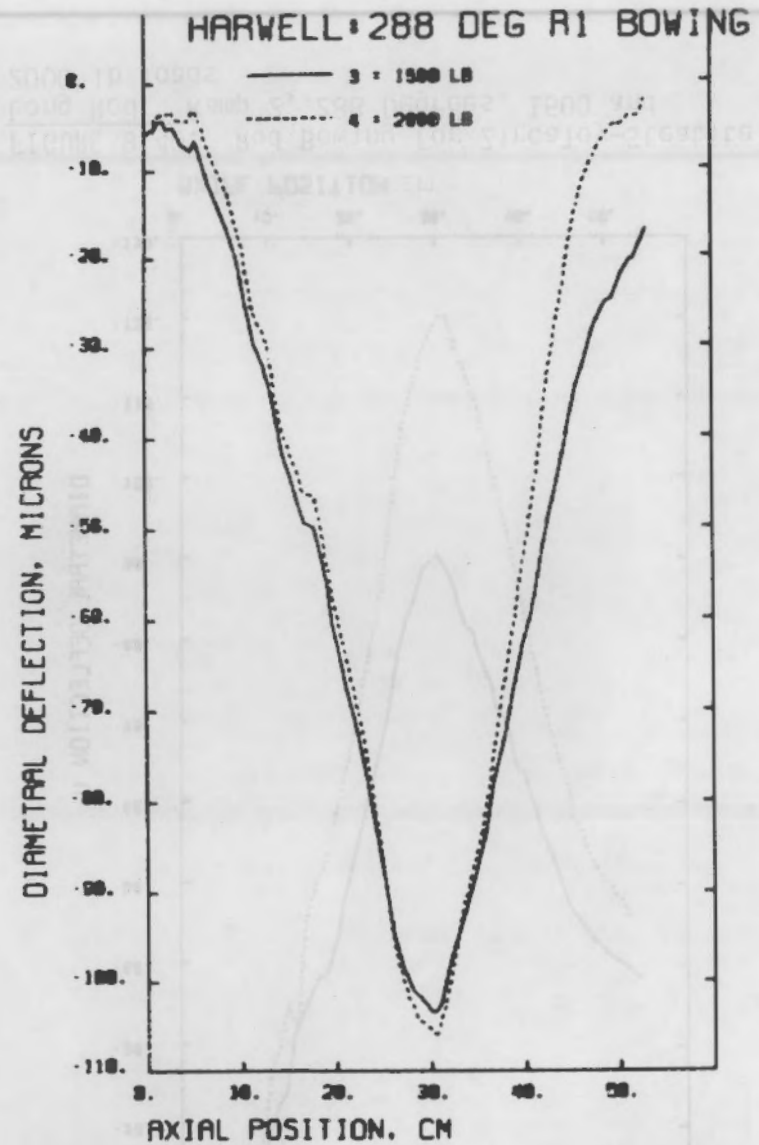
FIGURE B.38. Rod Bowing for Zircaloy-Steatite
Long Rod: Ramp 1, 288 Degrees, 1500 and
2000 lb loads
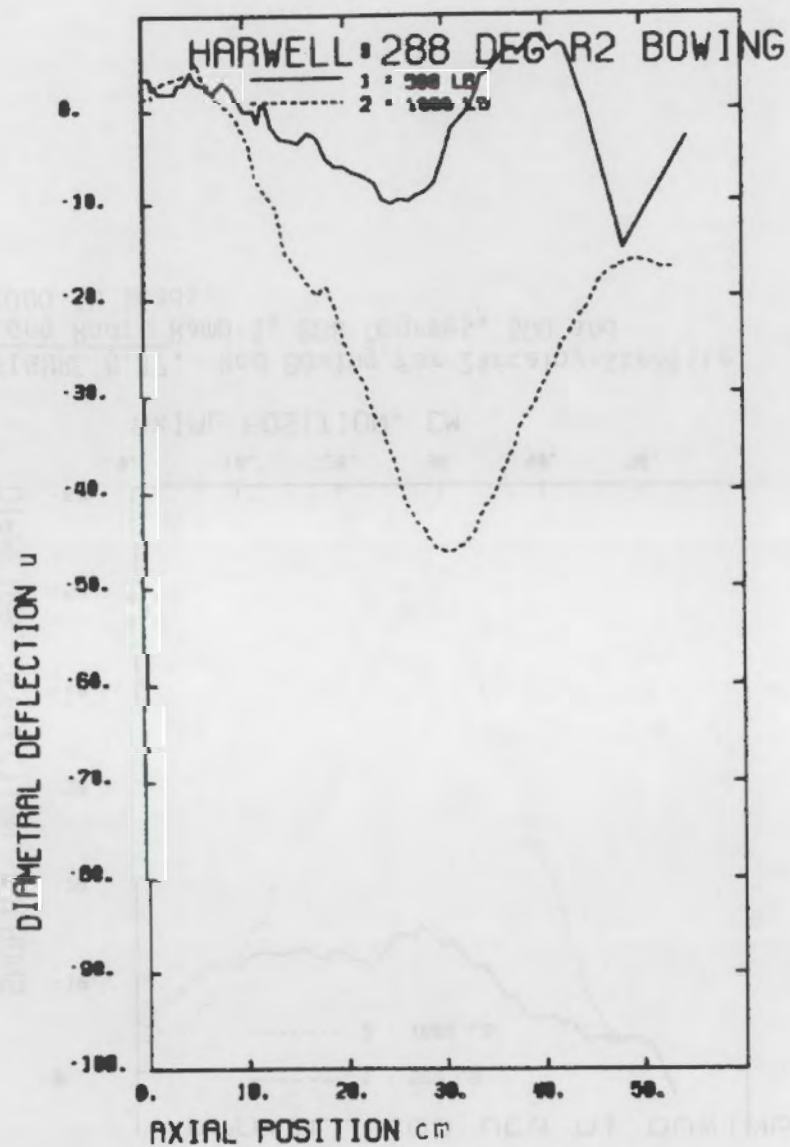
FIGURE B.39. Rod Bowing for Zircaloy-Steatite
Long Rod: Ramp 2, 288 Degrees, 500 and
1000 lb loads
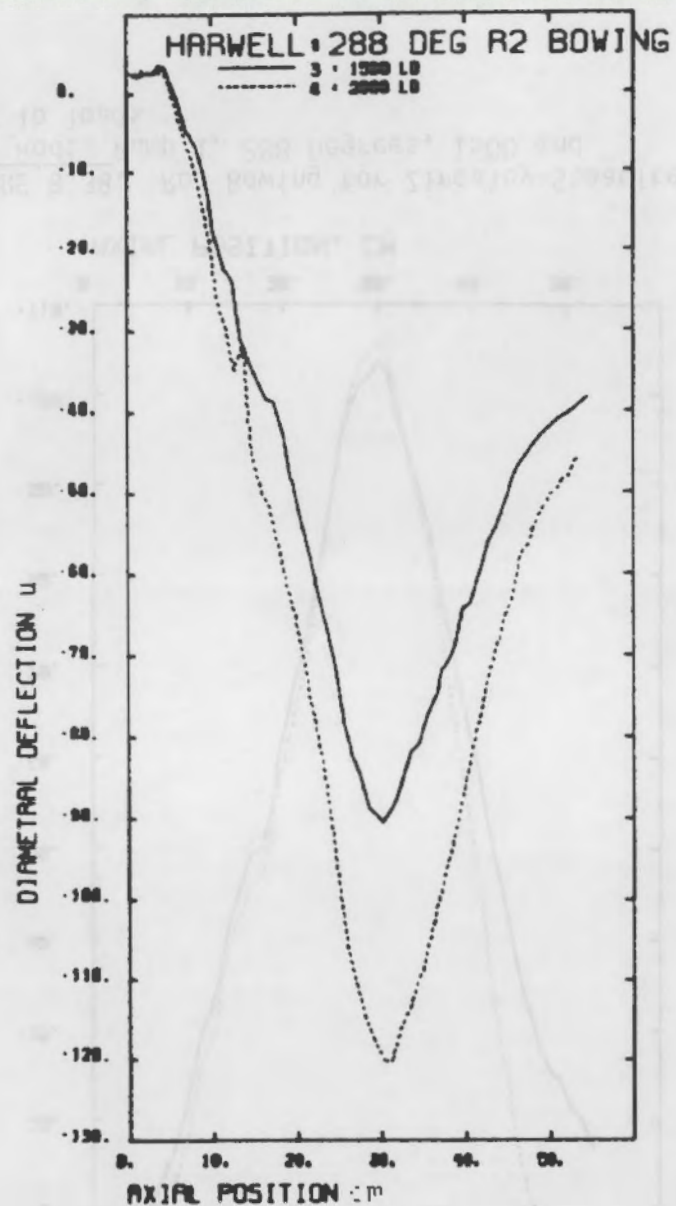
FIGURE 8.40. Rod Bowing for Zircaloy-Steatite
Long Rod: Ramp 2, 288 Degrees, 1500 and
2000 lb loads

APPENDIX C

GAMMA SCAN OF ROD 8

FIGURE C.1.   Gamma Scan of Rod 8

C.1
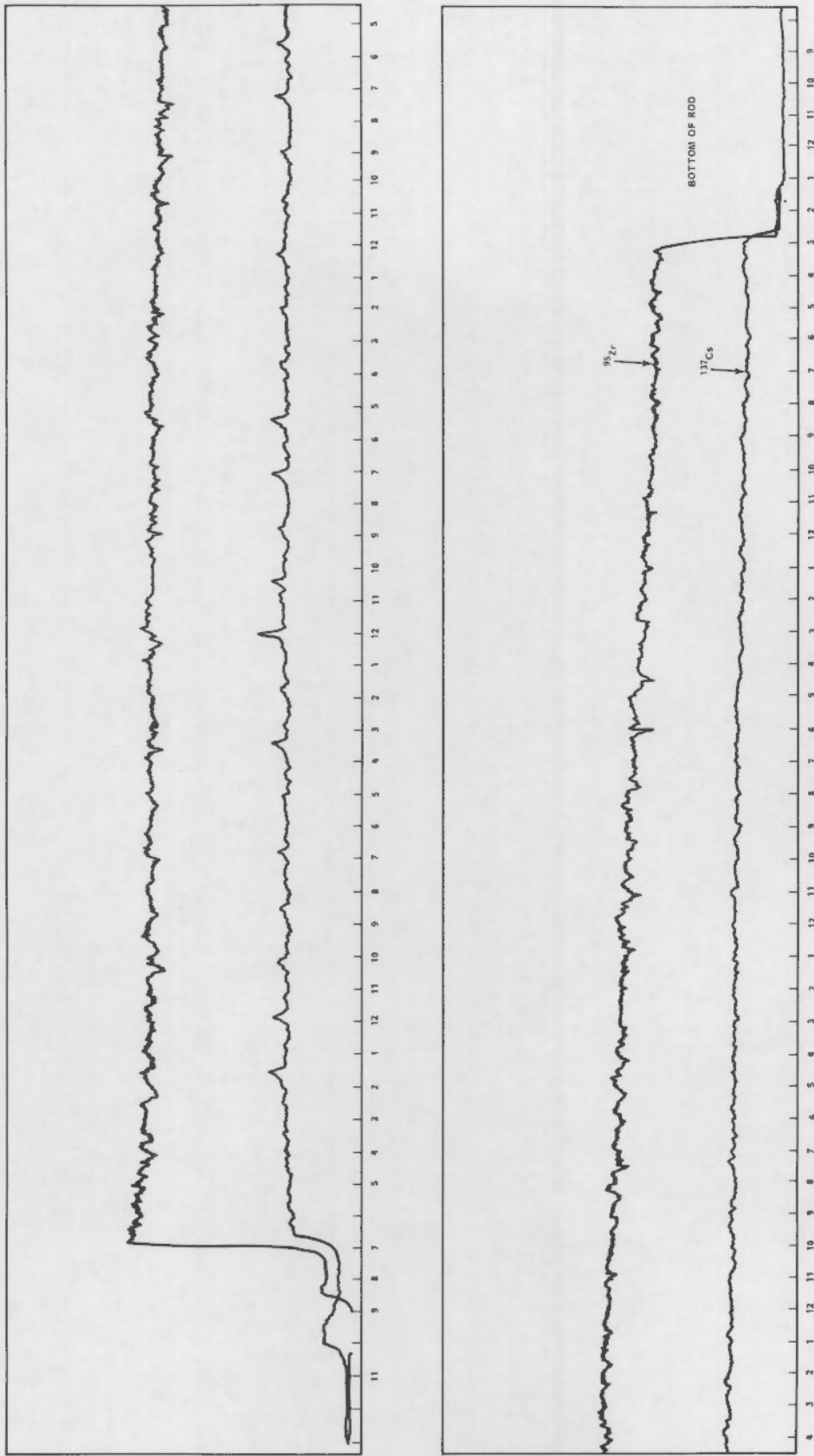
FIGURE C.1. Gamma Scan of Rod B.

APPENDIX D

ROD 7 AND 8 DIAMETER DATA
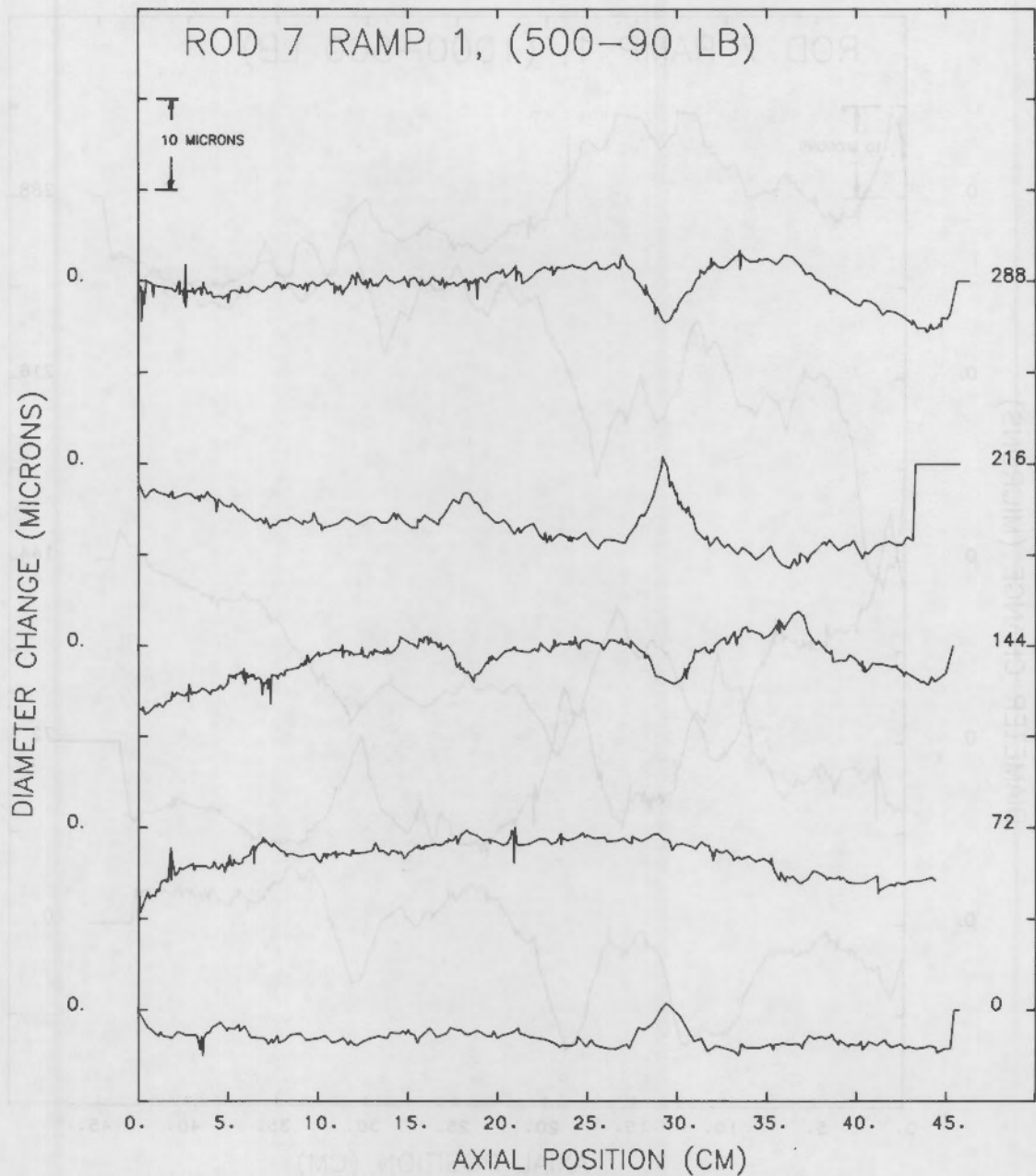
FIGURE D.1. Rod 7 Incremental Diameter Deformations:
Ramp 1, 90 to 500 lb load
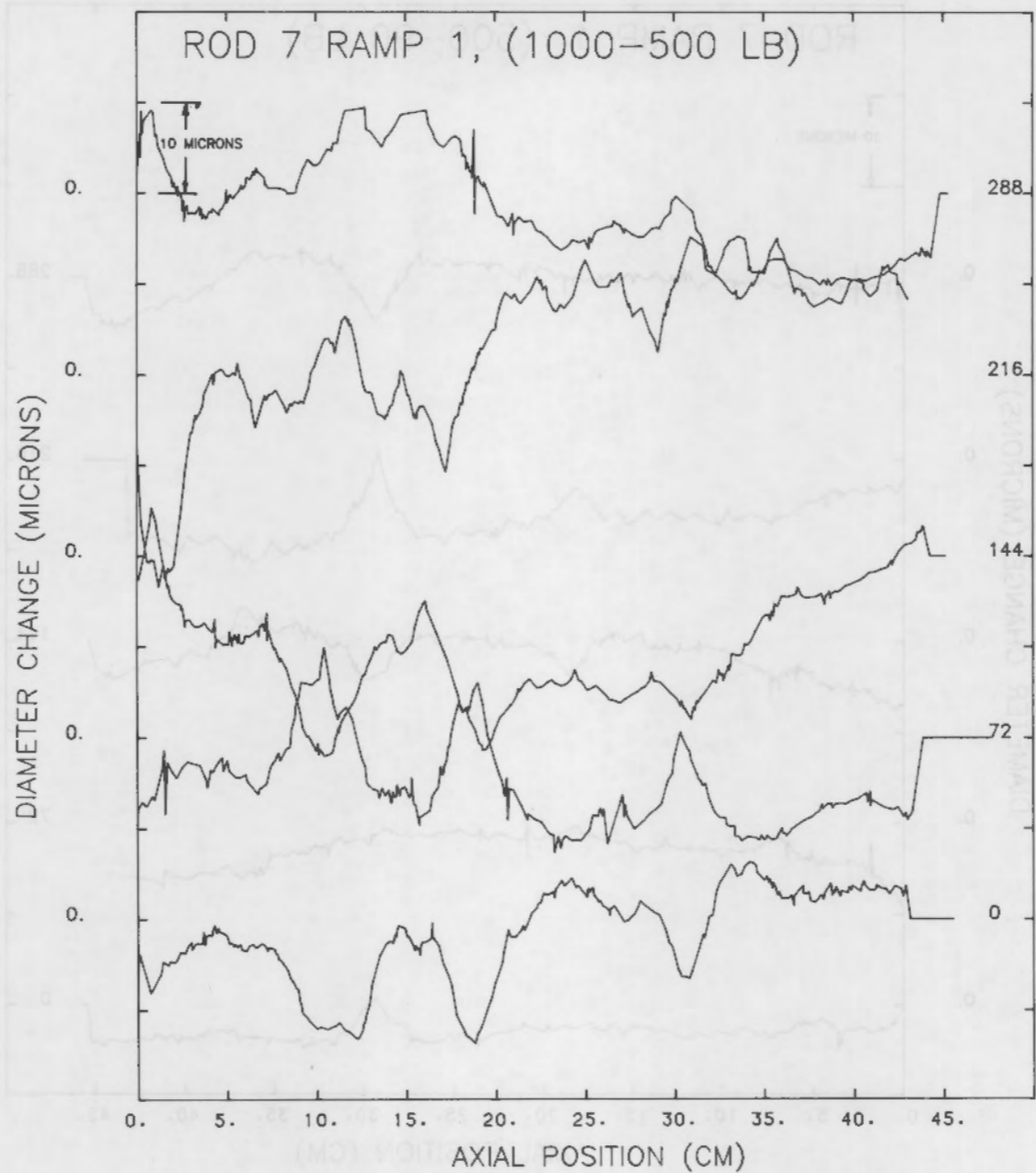
FIGURE D.2. Rod 7 Incremental Diameter Deformations: Ramp 1, 500 to 1000 lb load

D.2
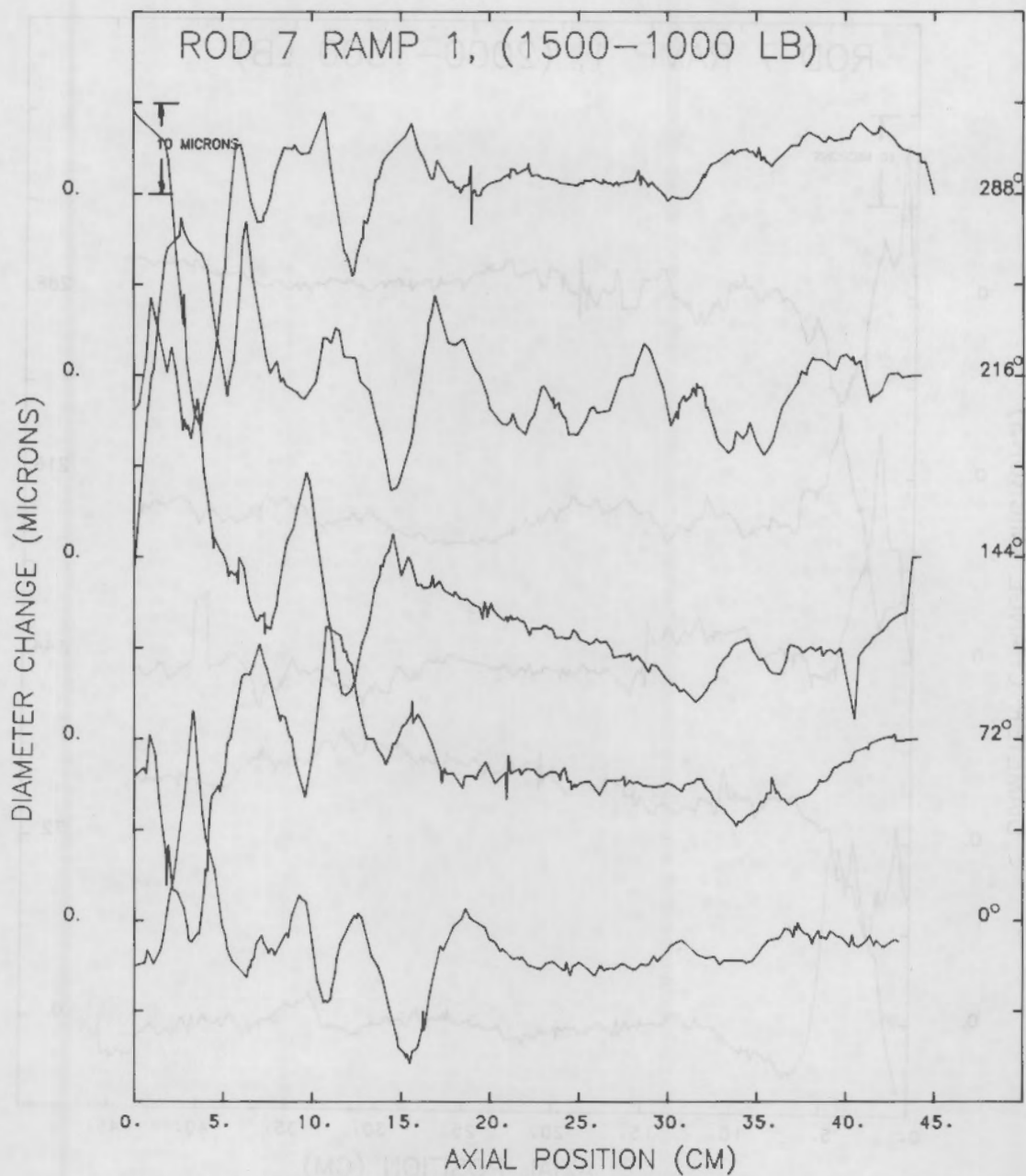
FIGURE D.3. Rod 7 Incremental Diameter Deformations:
Ramp 1, 1000 to 1500 lb load
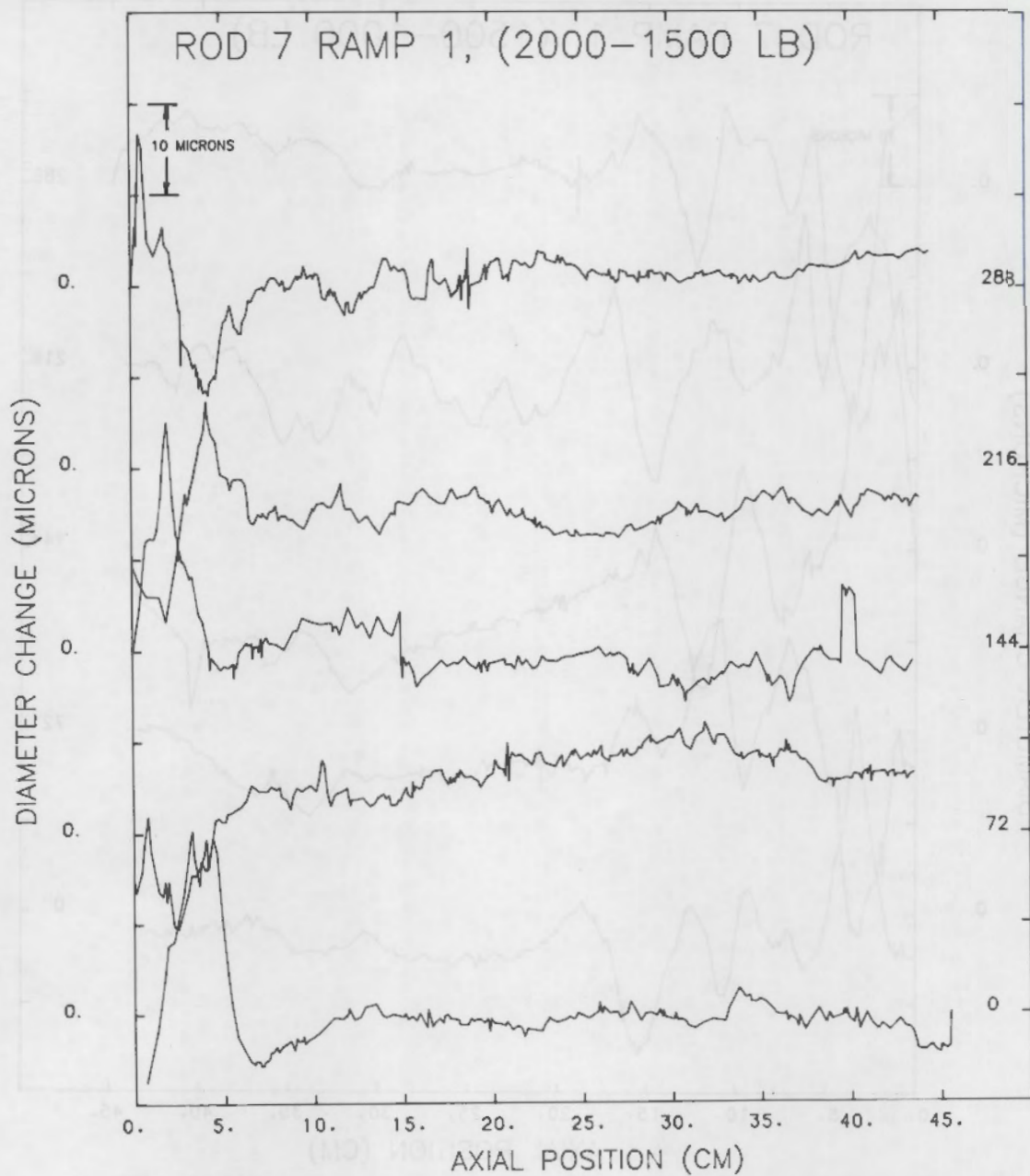
FIGURE D.4. Rod 7 Incremental Diameter Deformations: Ramp 1, 1500 to 2000 lb load

D.4
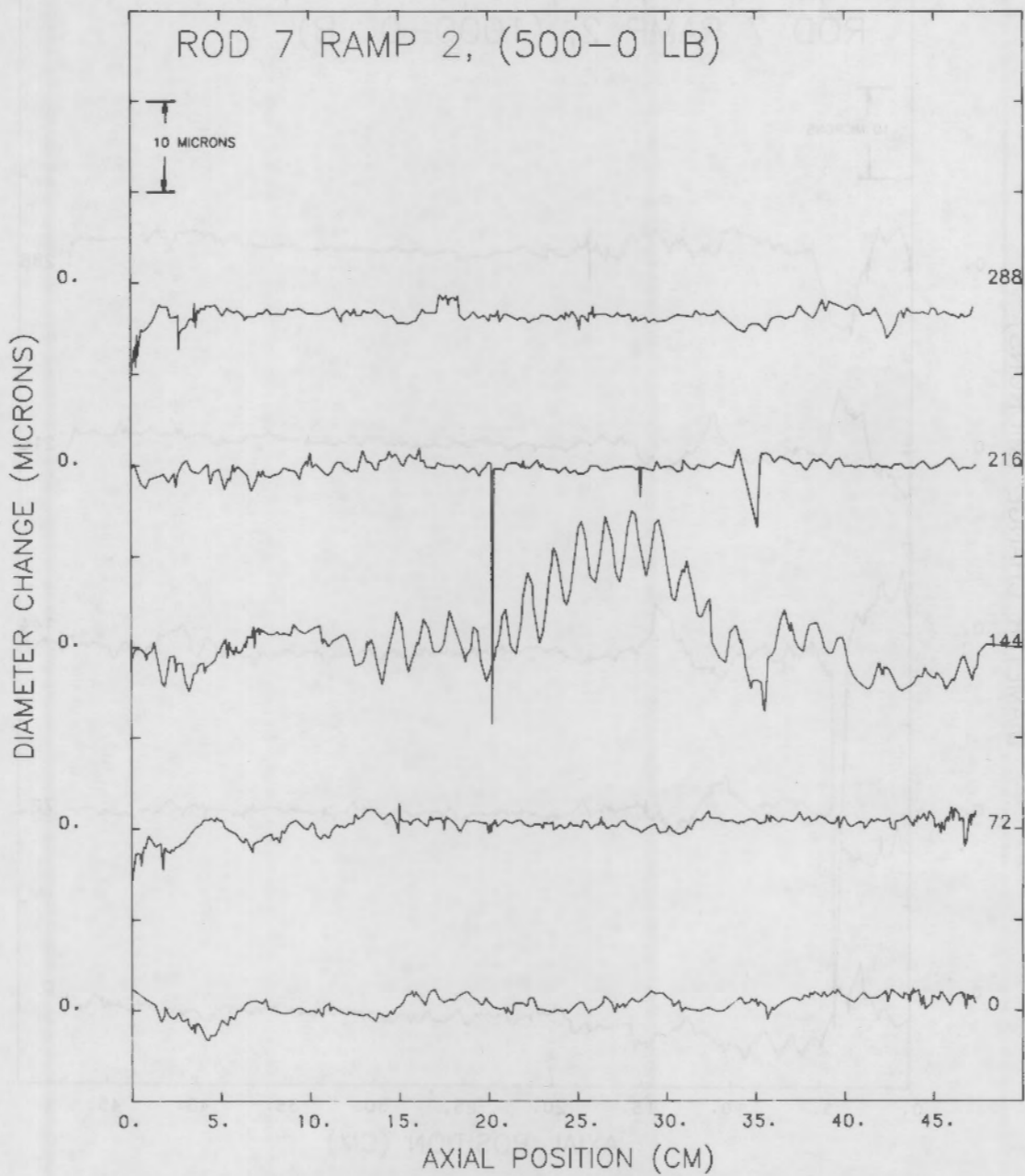
FIGURE D.5. Rod 7 Incremental Diameter Deformations:
Ramp 2, 500 lb load
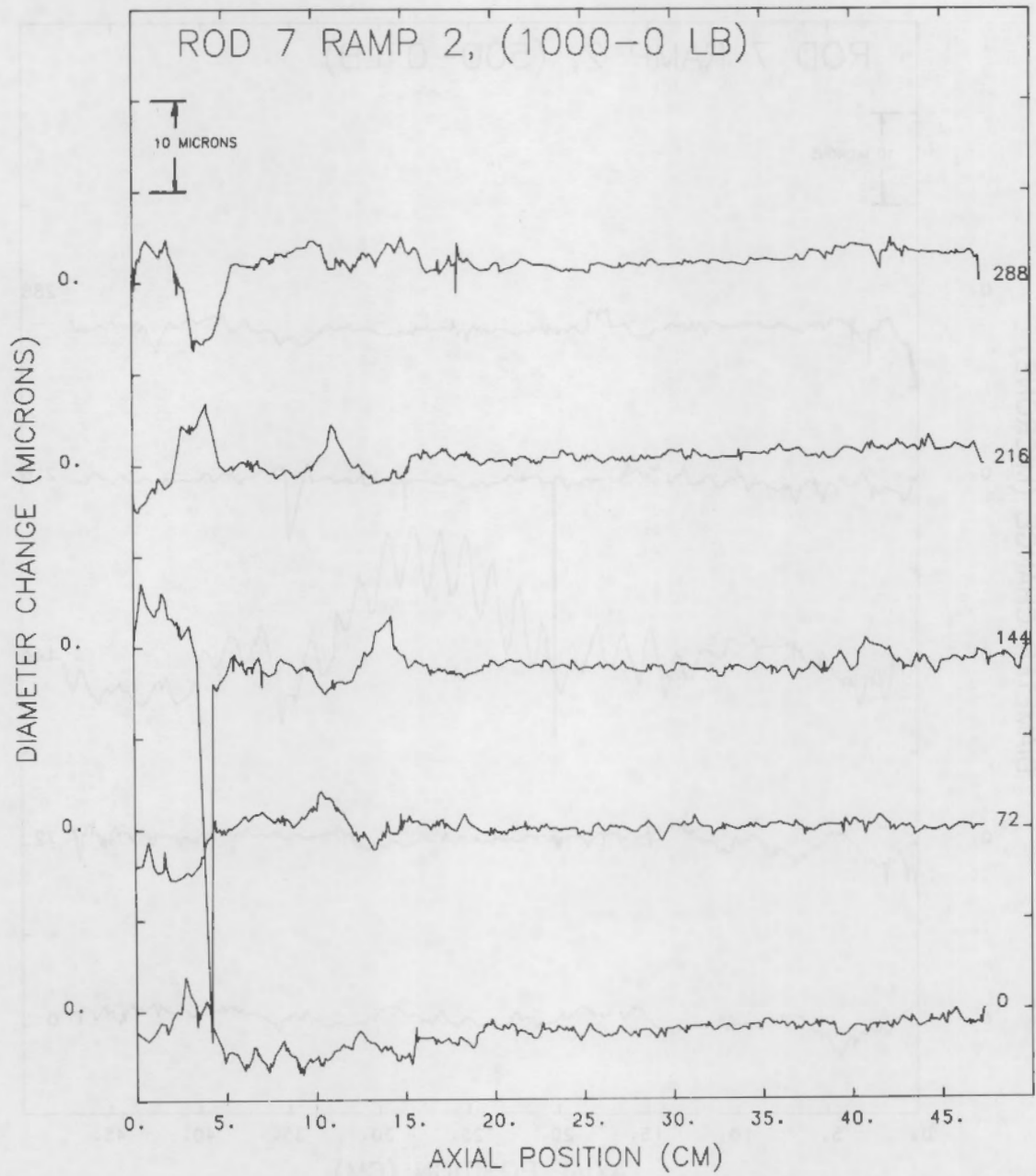
FIGURE D.6. Rod 7 Incremental Diameter Deformations:
Ramp 2, 1000 lb load
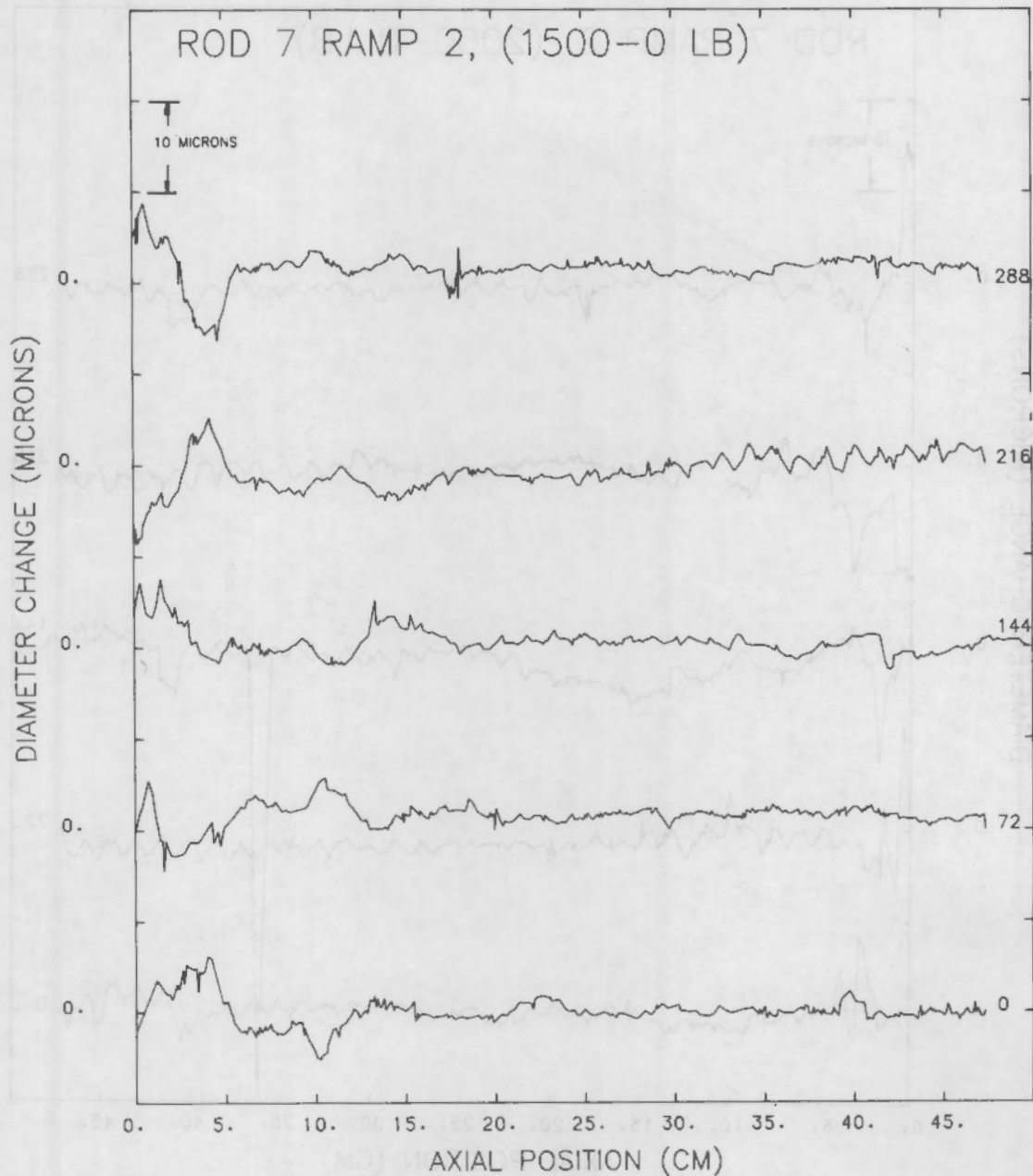
FIGURE D.7. Rod 7 Incremental Diameter Deformations:
Ramp 2, 1500 lb load
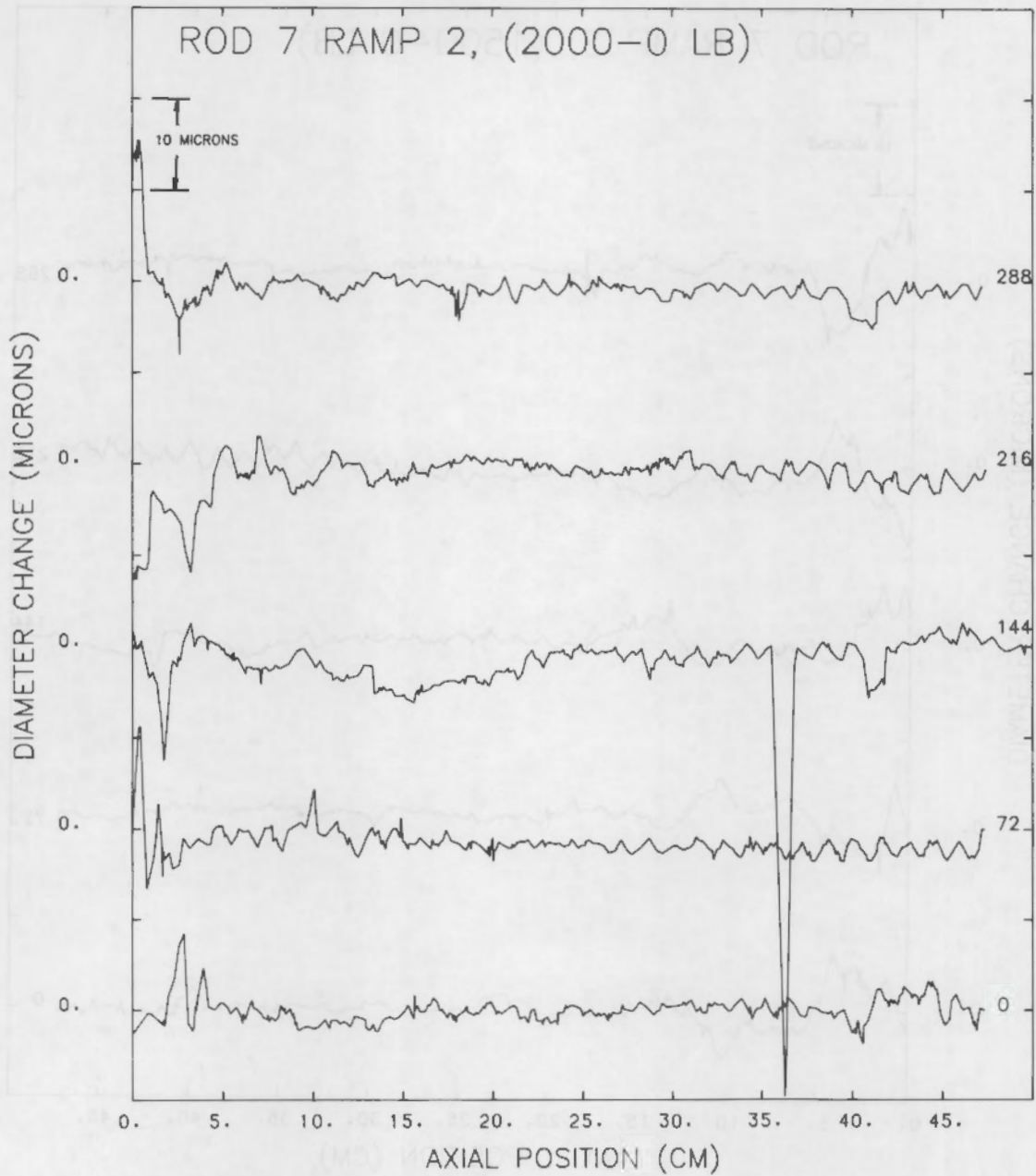
FIGURE D.8. Rod 7 Incremental Diameter Deformations: Ramp 2, 2000 lb load

D.8
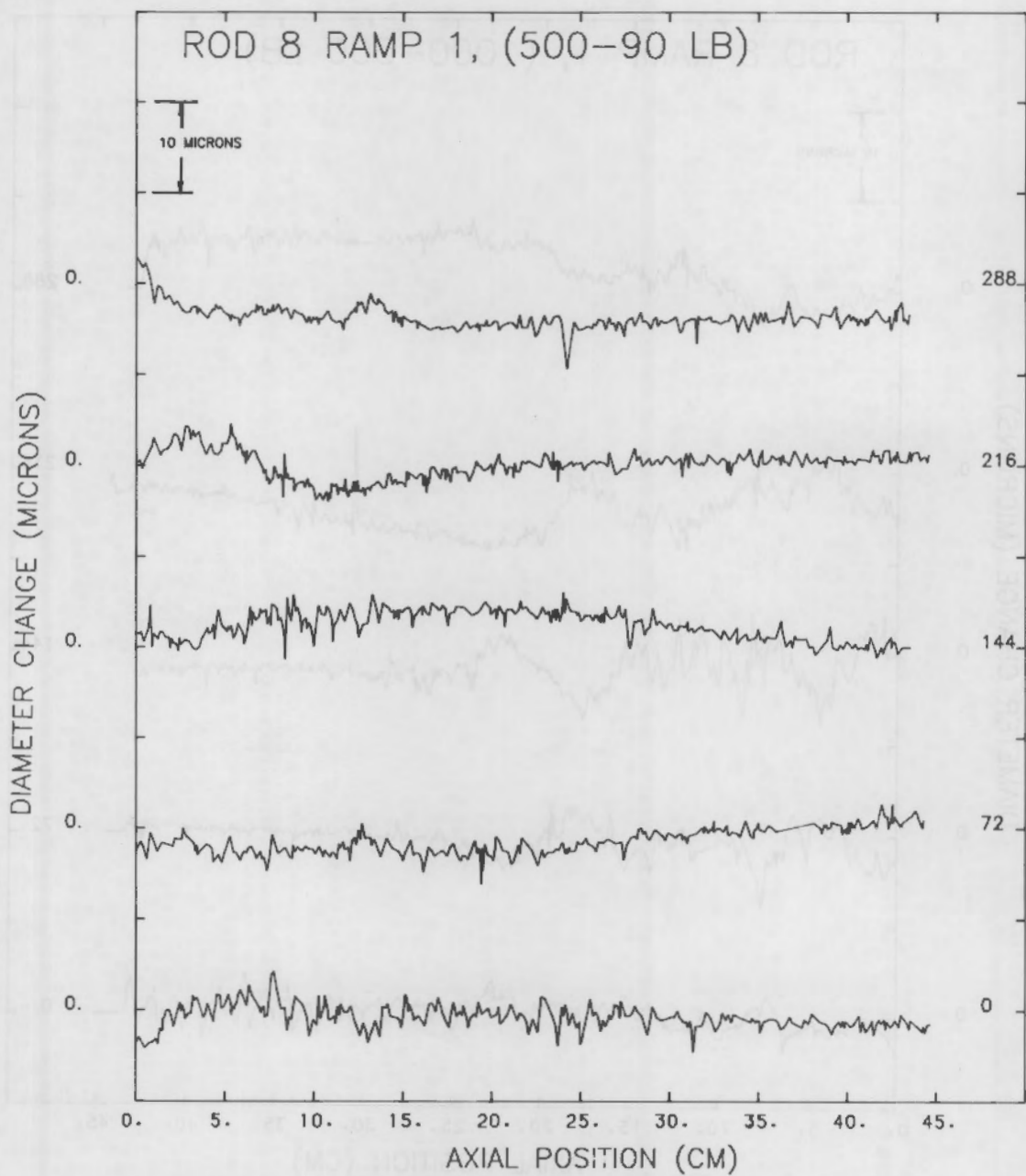
FIGURE D.9. Rod 8 Incremental Diameter Deformations: Ramp 1, 90 to 500 lb load

D.9
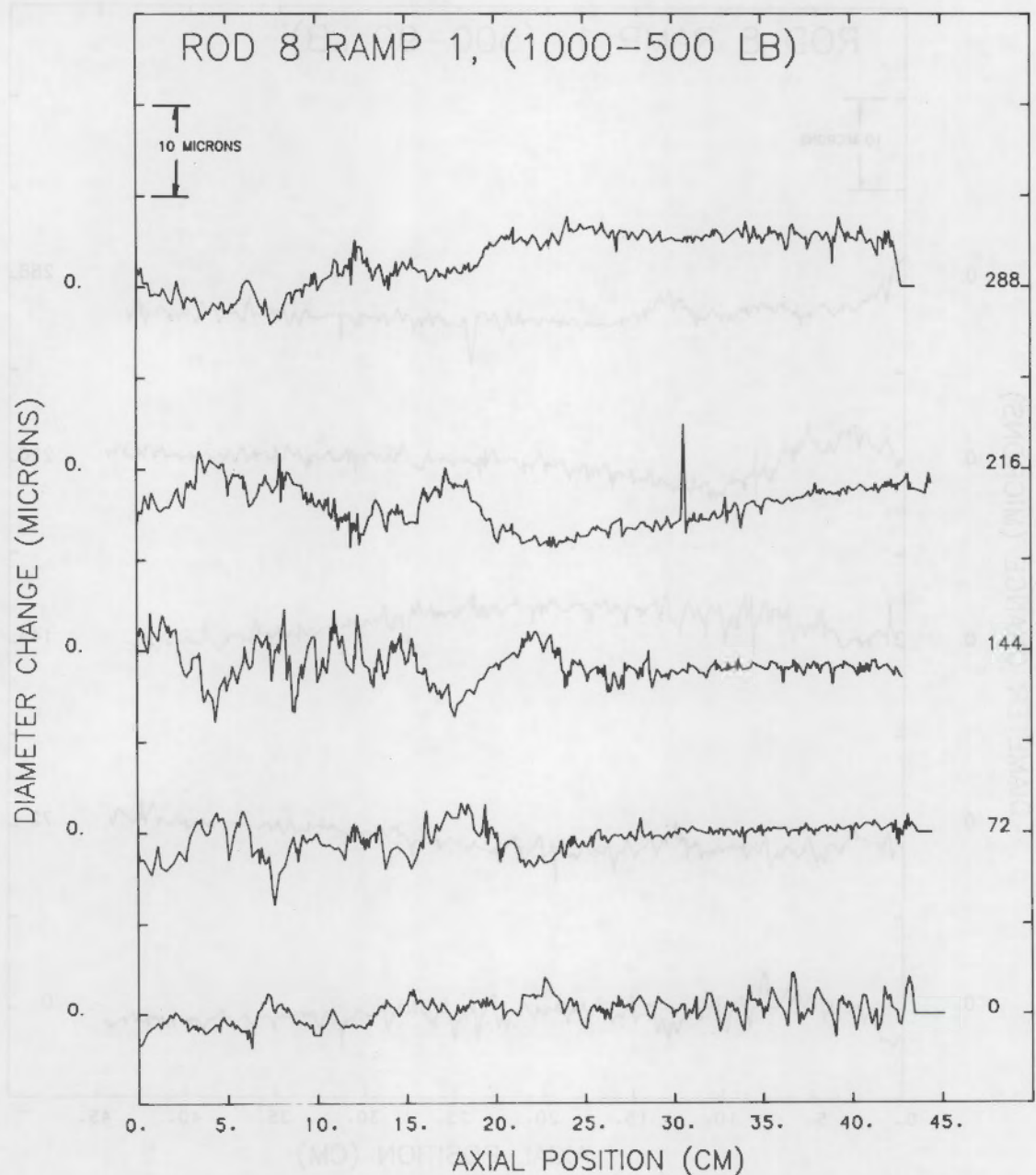
FIGURE D.10. Rod 8 Incremental Diameter Deformations: Ramp 1, 500 to 1000 lb load

D.10
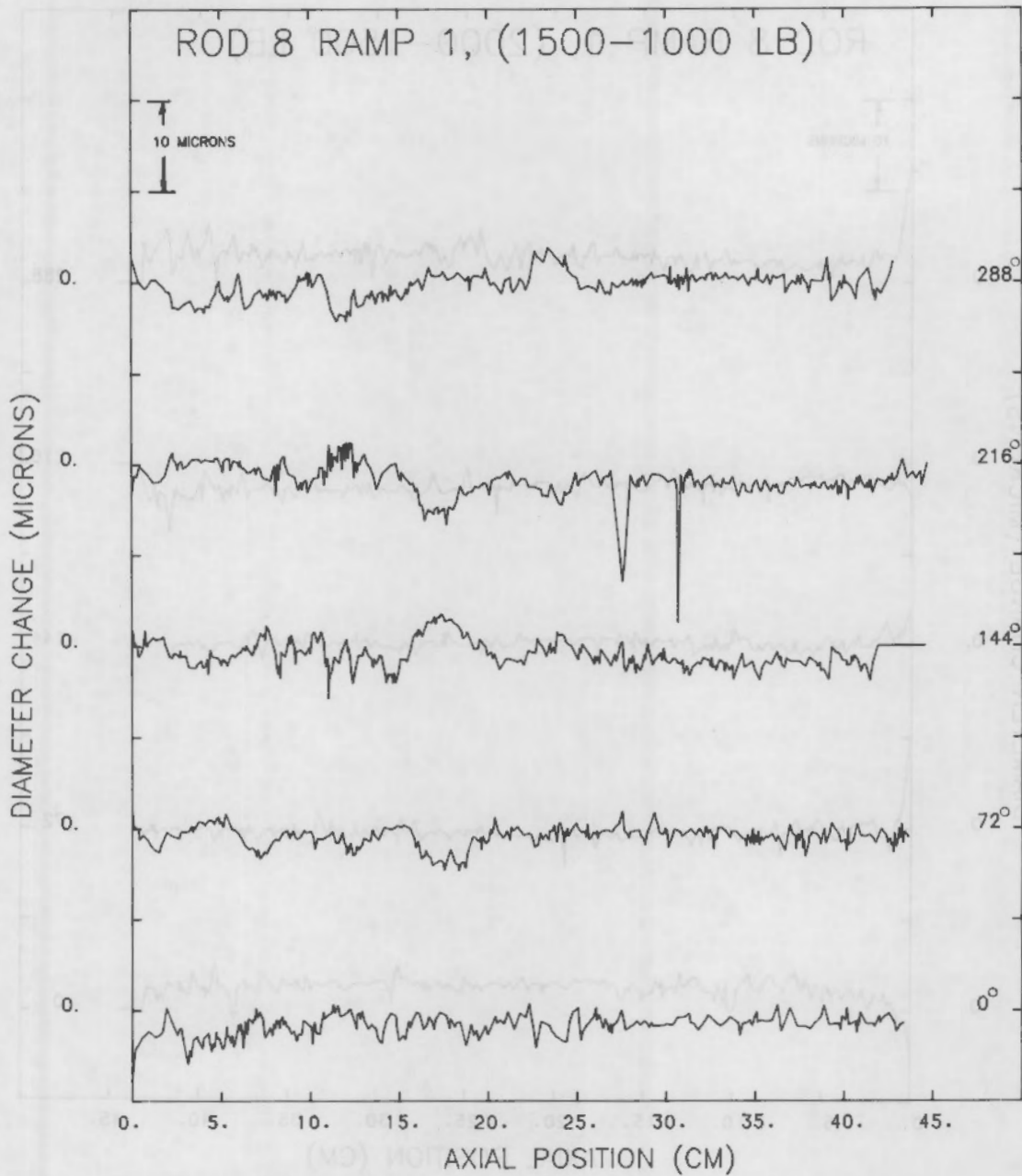
FIGURE D.11. Rod 8 Incremental Diameter Deformations:
Ramp 1, 1000 to 1500 lb load
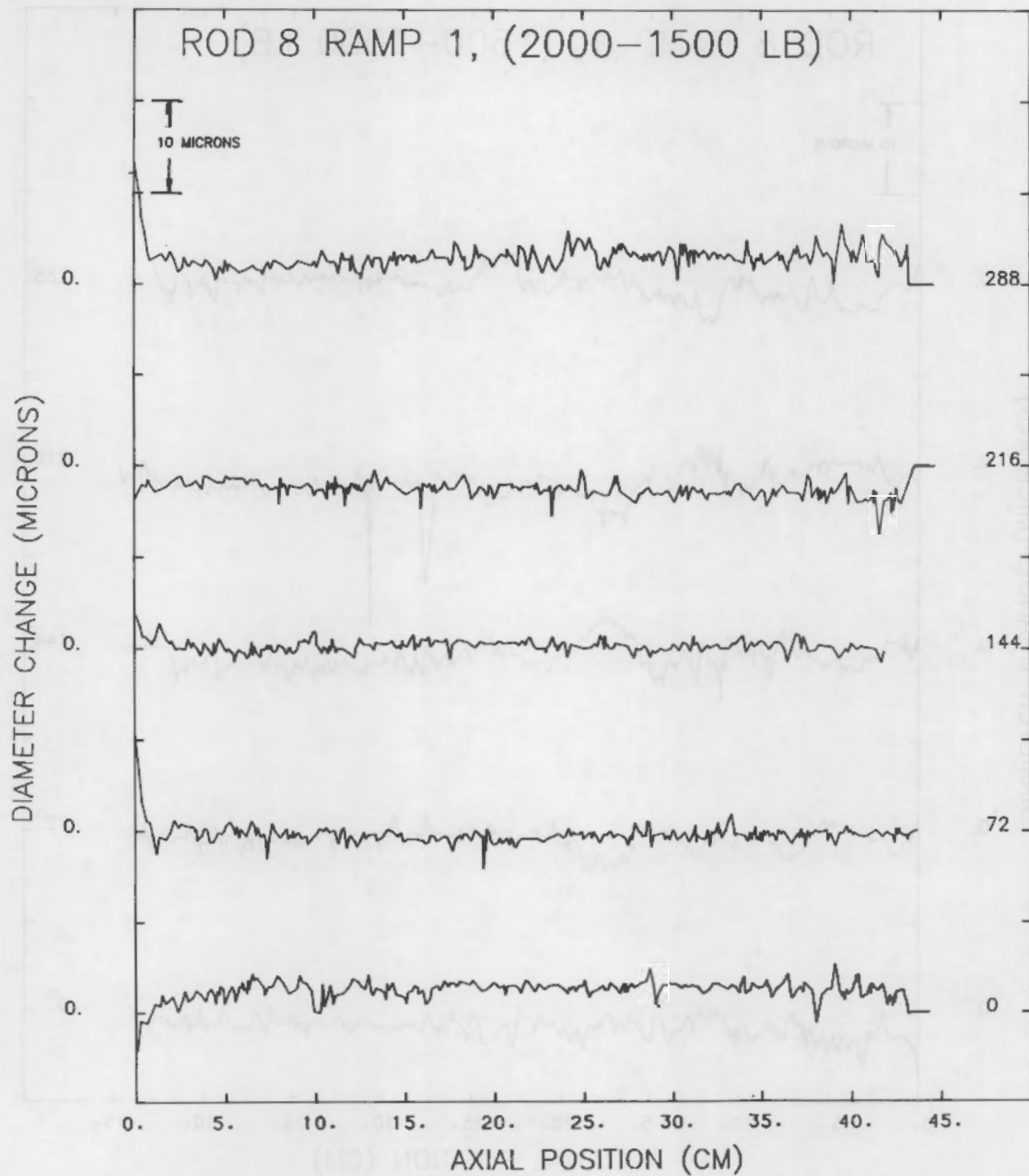
FIGURE D.12. Rod 8 Incremental Diameter Deformations: Ramp 1, 1500 to 2000 lb load
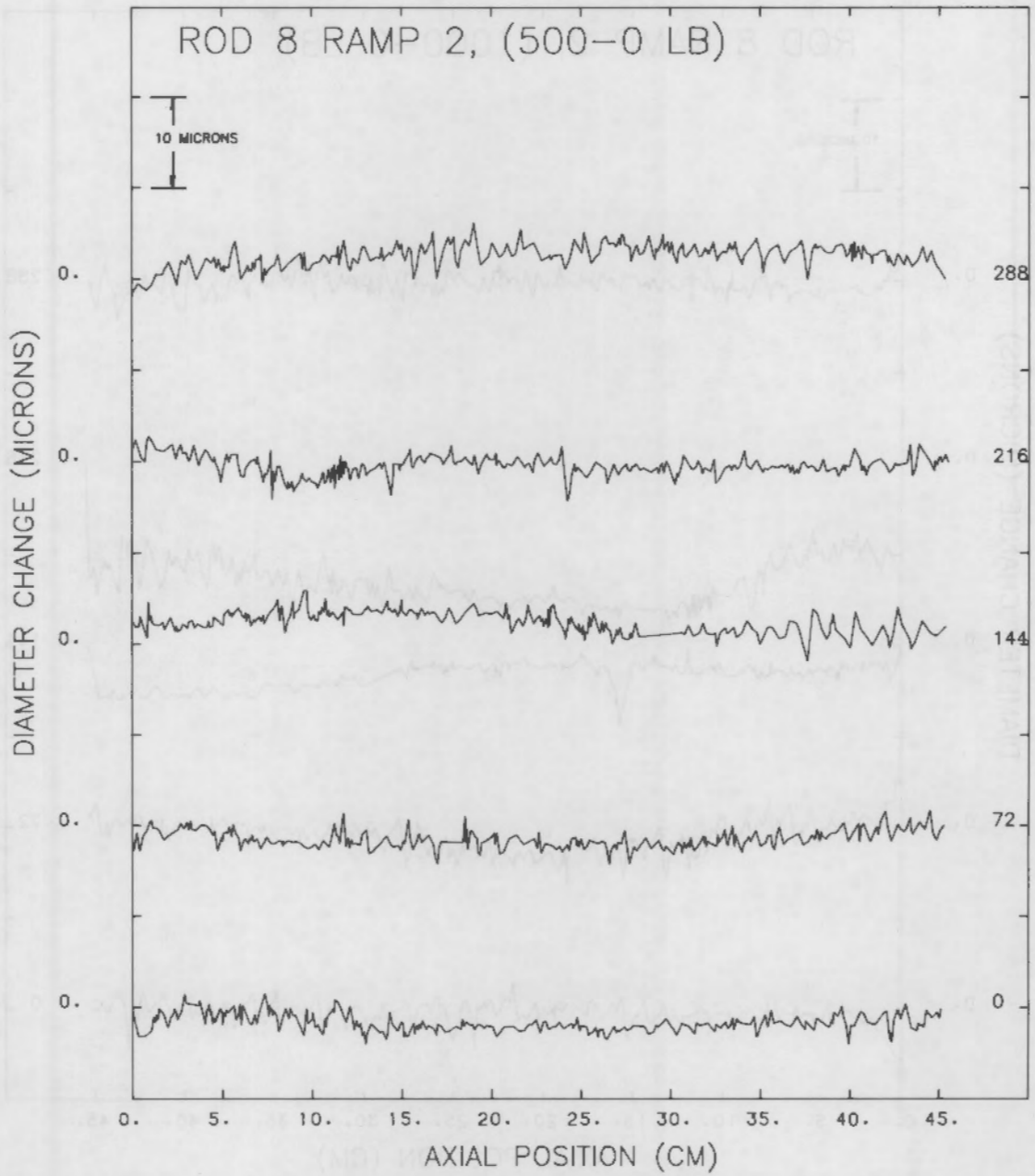
FIGURE D.13. Rod 8 Incremental Diameter Deformations: Ramp 2, 500 lb load
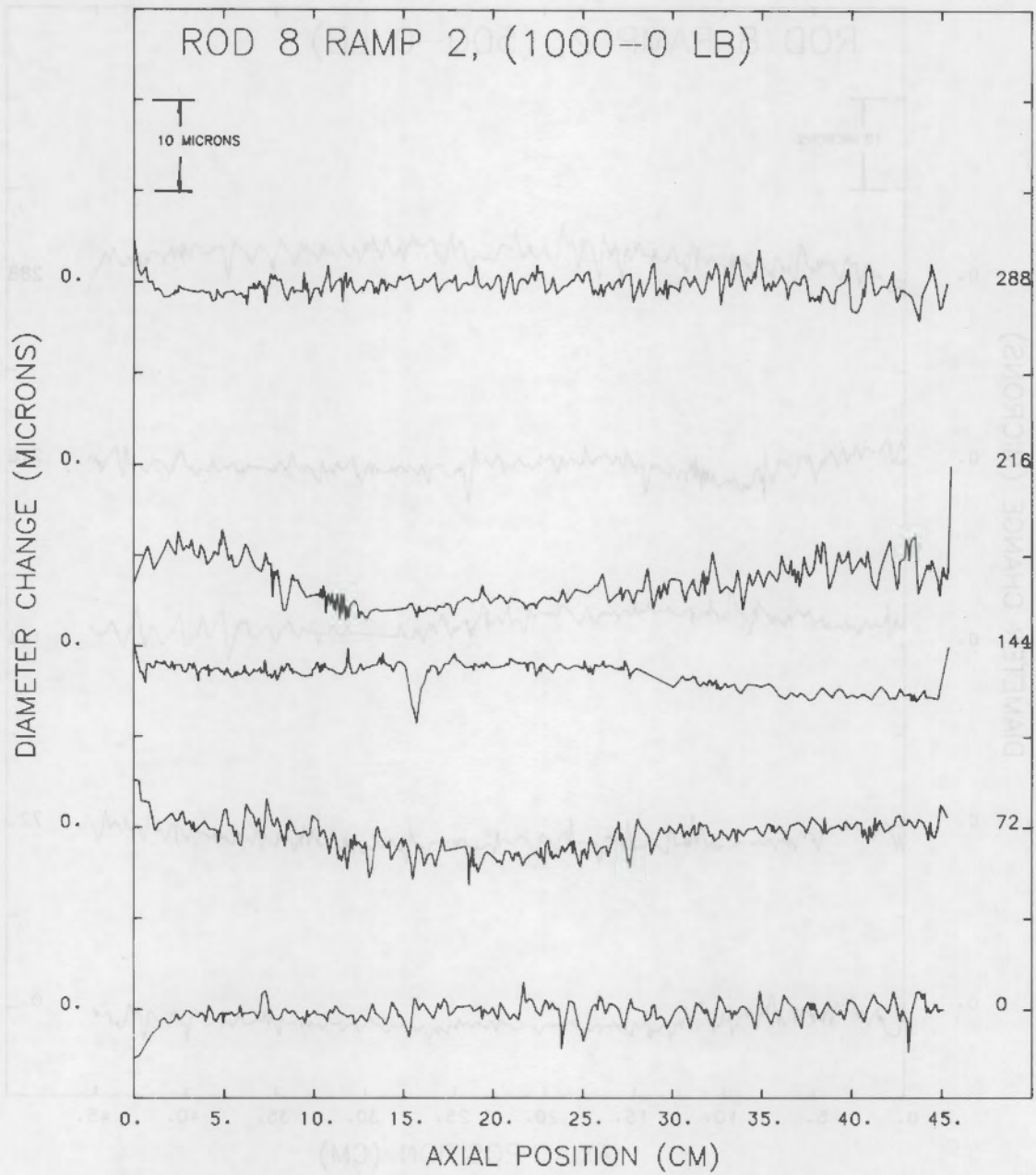
FIGURE D.14. Rod 8 Incremental Diameter Deformations: Ramp 2, 1000 lb load
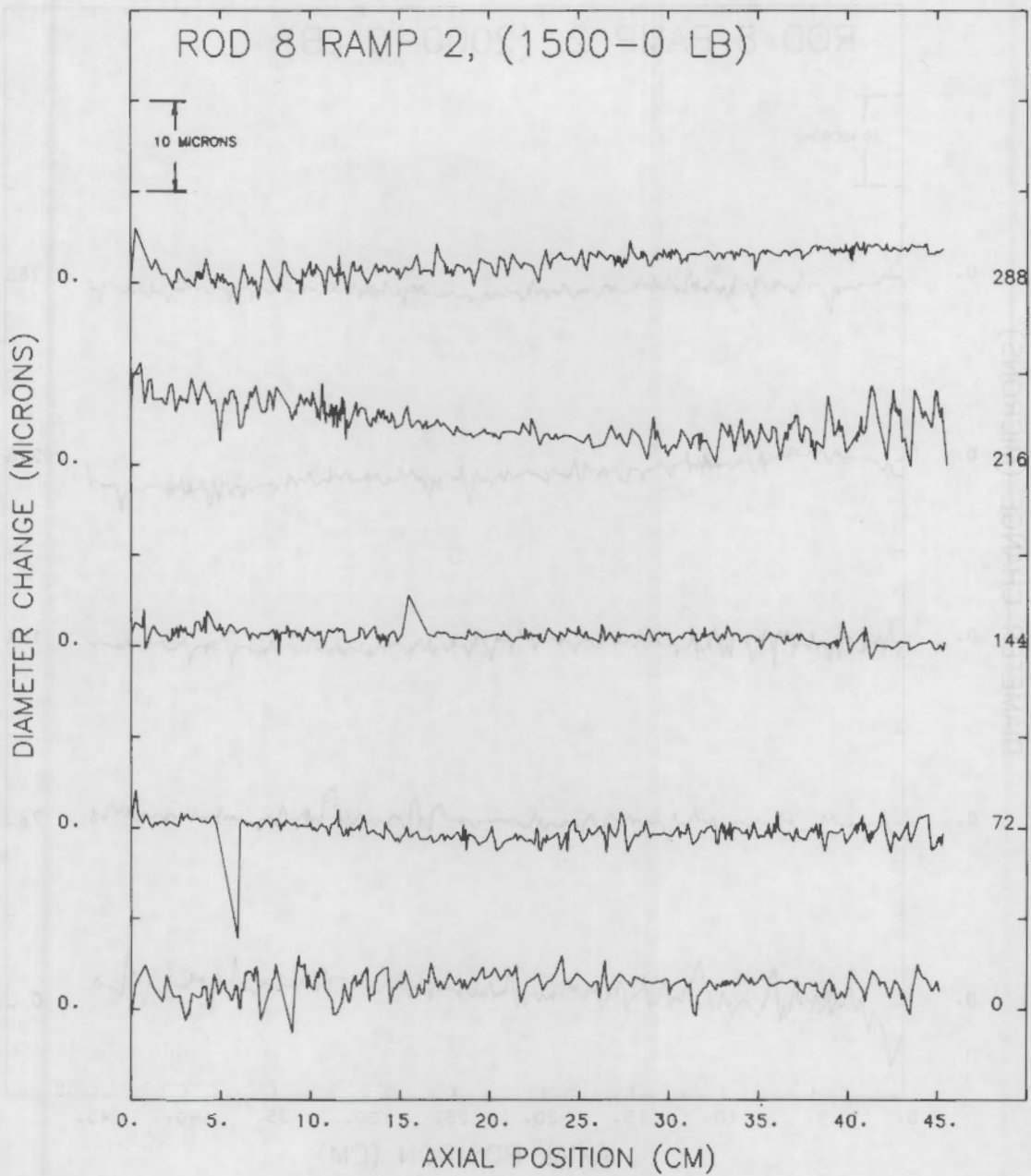
FIGURE D.15. Rod 8 Incremental Diameter Deformations: Ramp 2, 1500 lb load
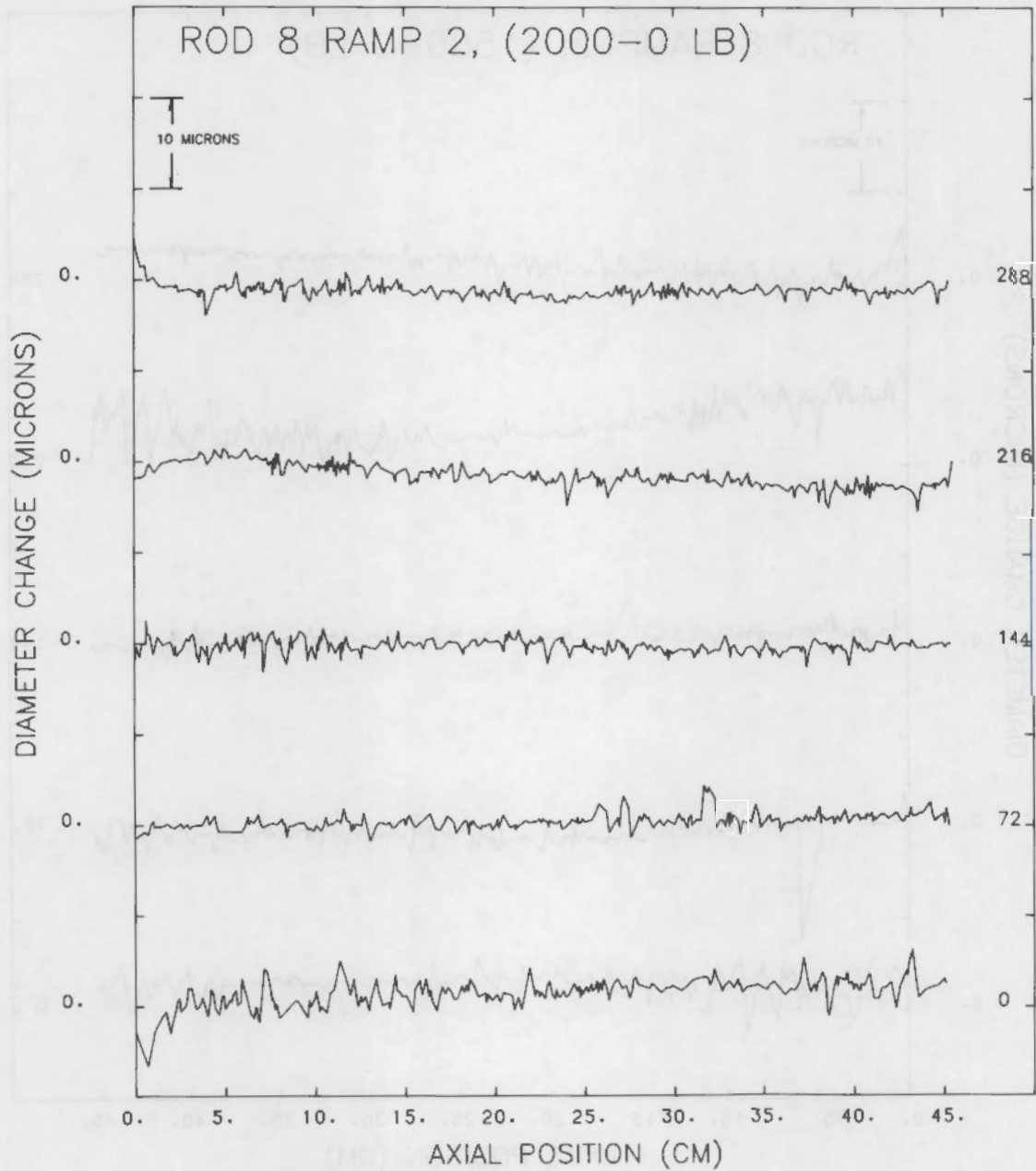
FIGURE D.16. Rod 8 Incremental Diameter Deformations: Ramp 2, 2000 lb load

APPENDIX E

ROD 7 AND 8 BOW DATA
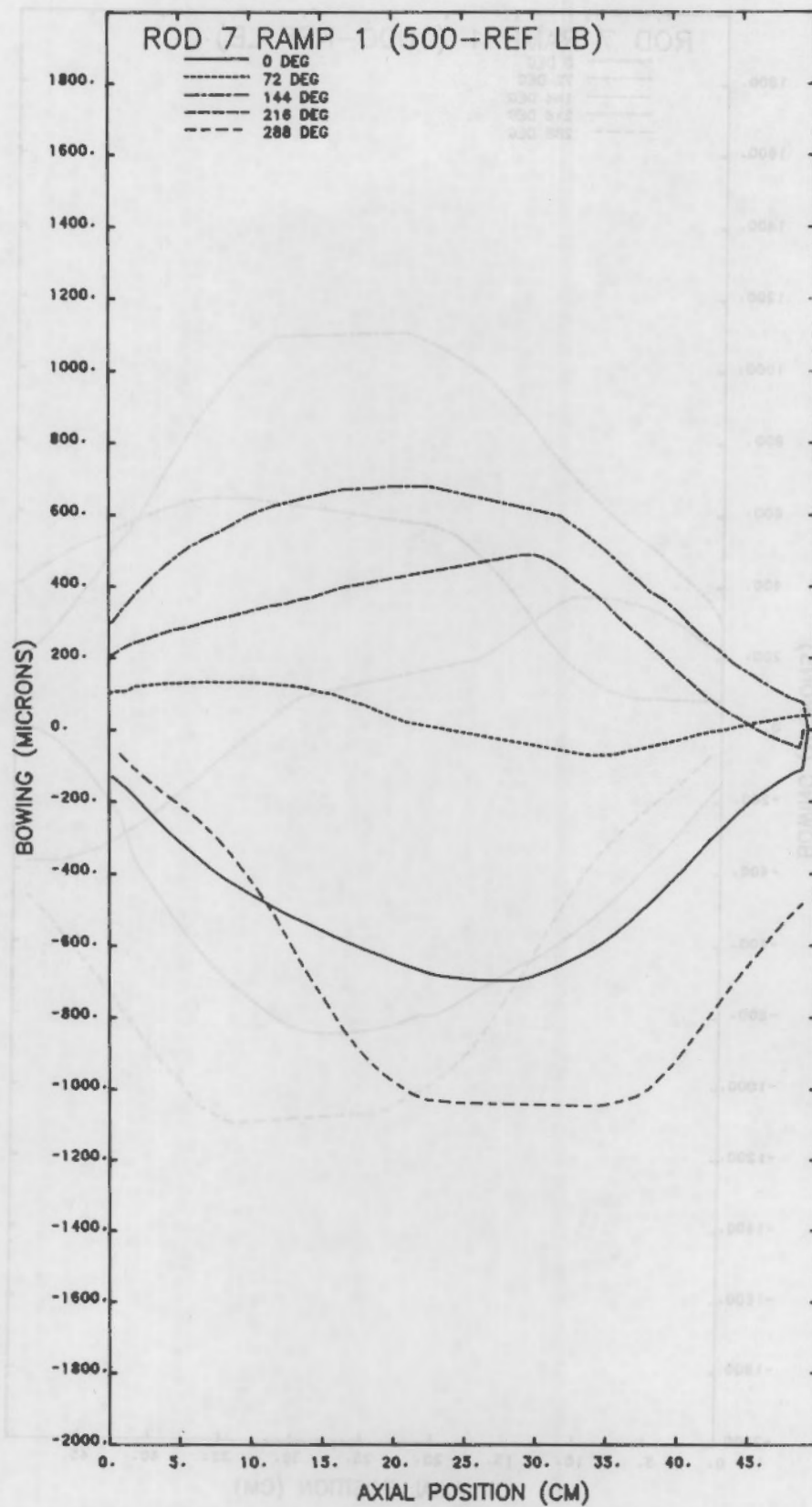
FIGURE E.1. Rod 7 Bowing: Ramp 1, 500 lb load

E.1
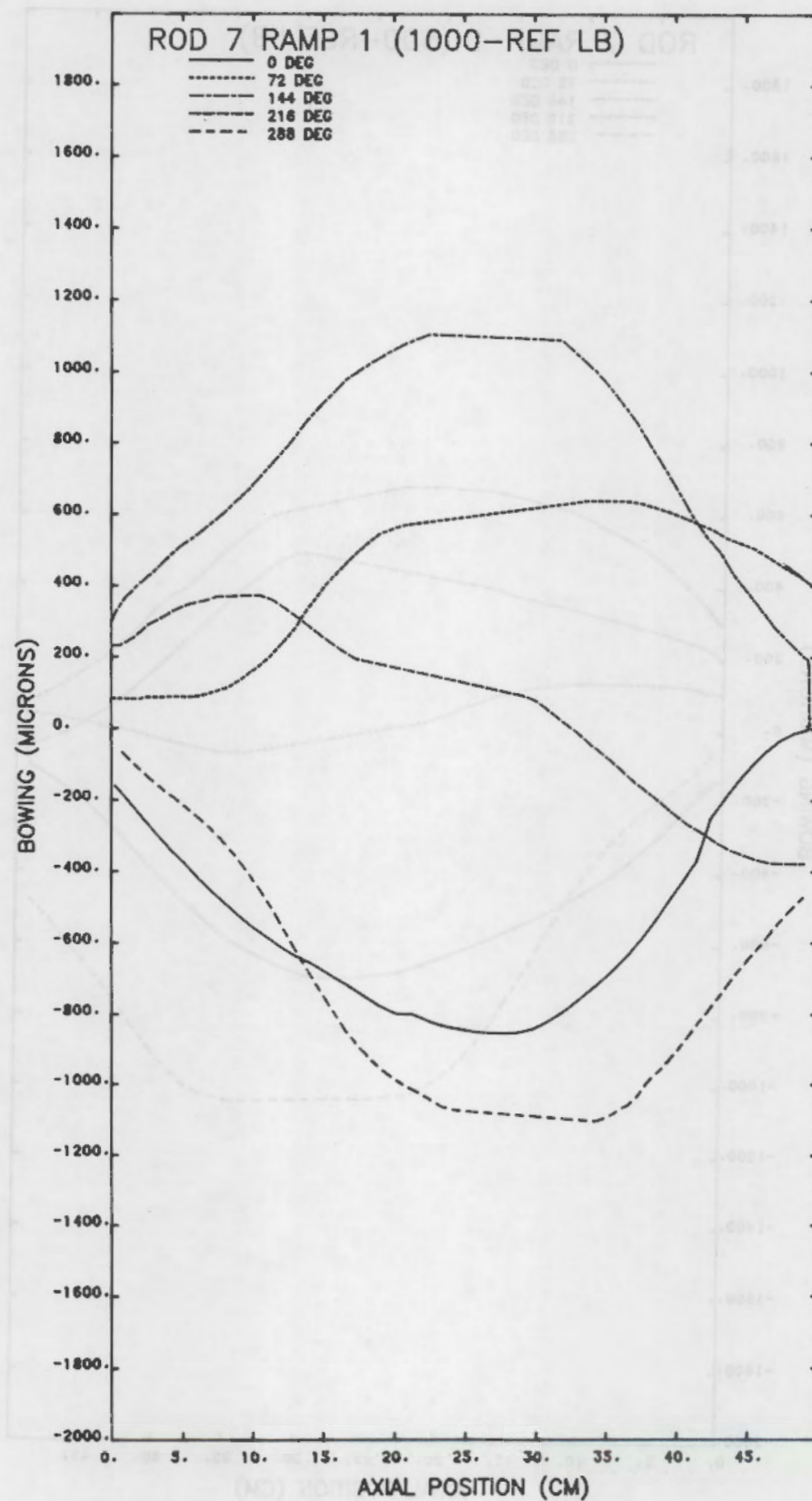
FIGURE E.2. Rod 7 Bowing: Ramp 1, 1000 lb load

E.2
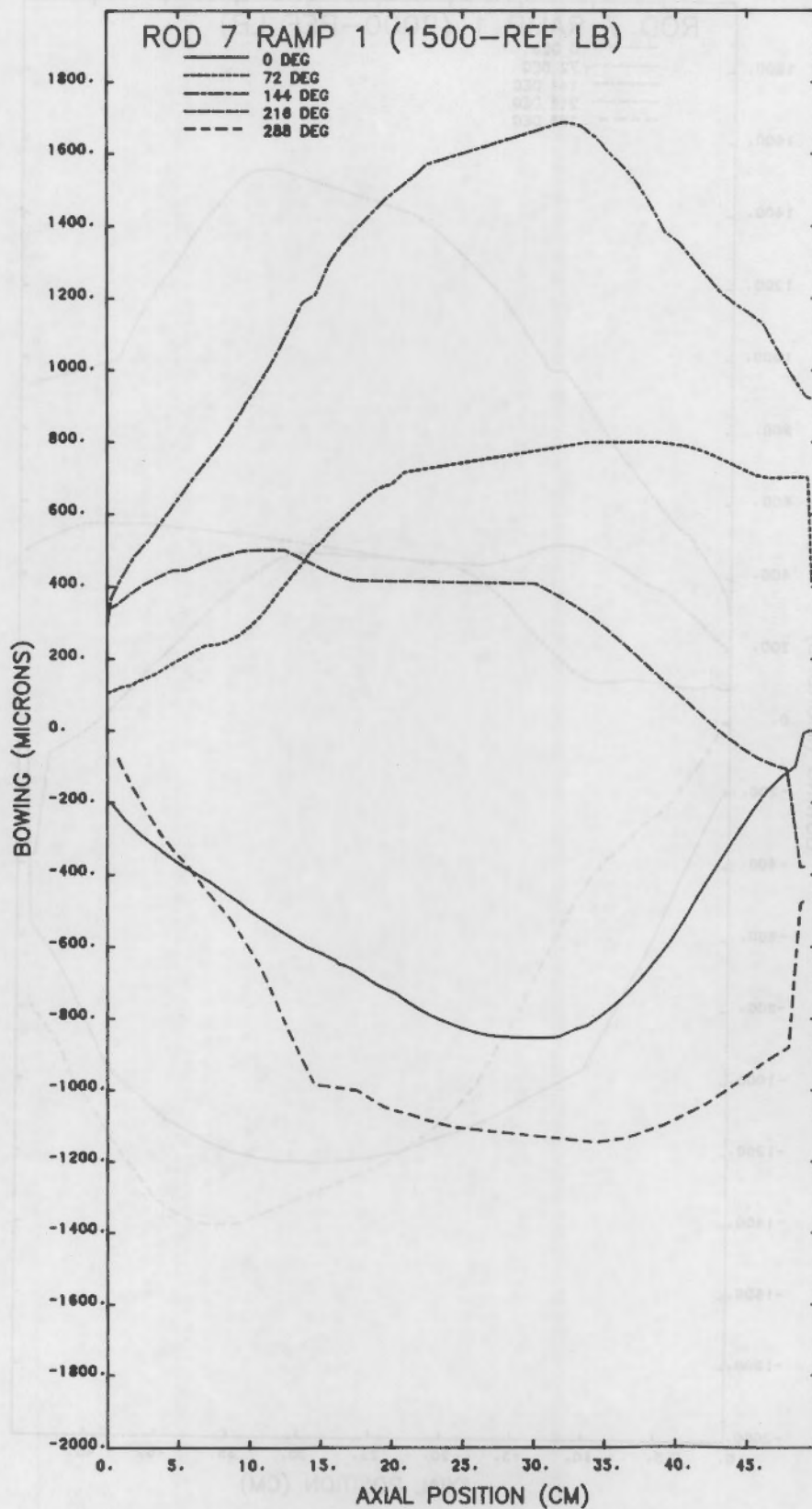
FIGURE E.3. Rod 7 Bowing: Ramp 1, 1500 lb load

E.3
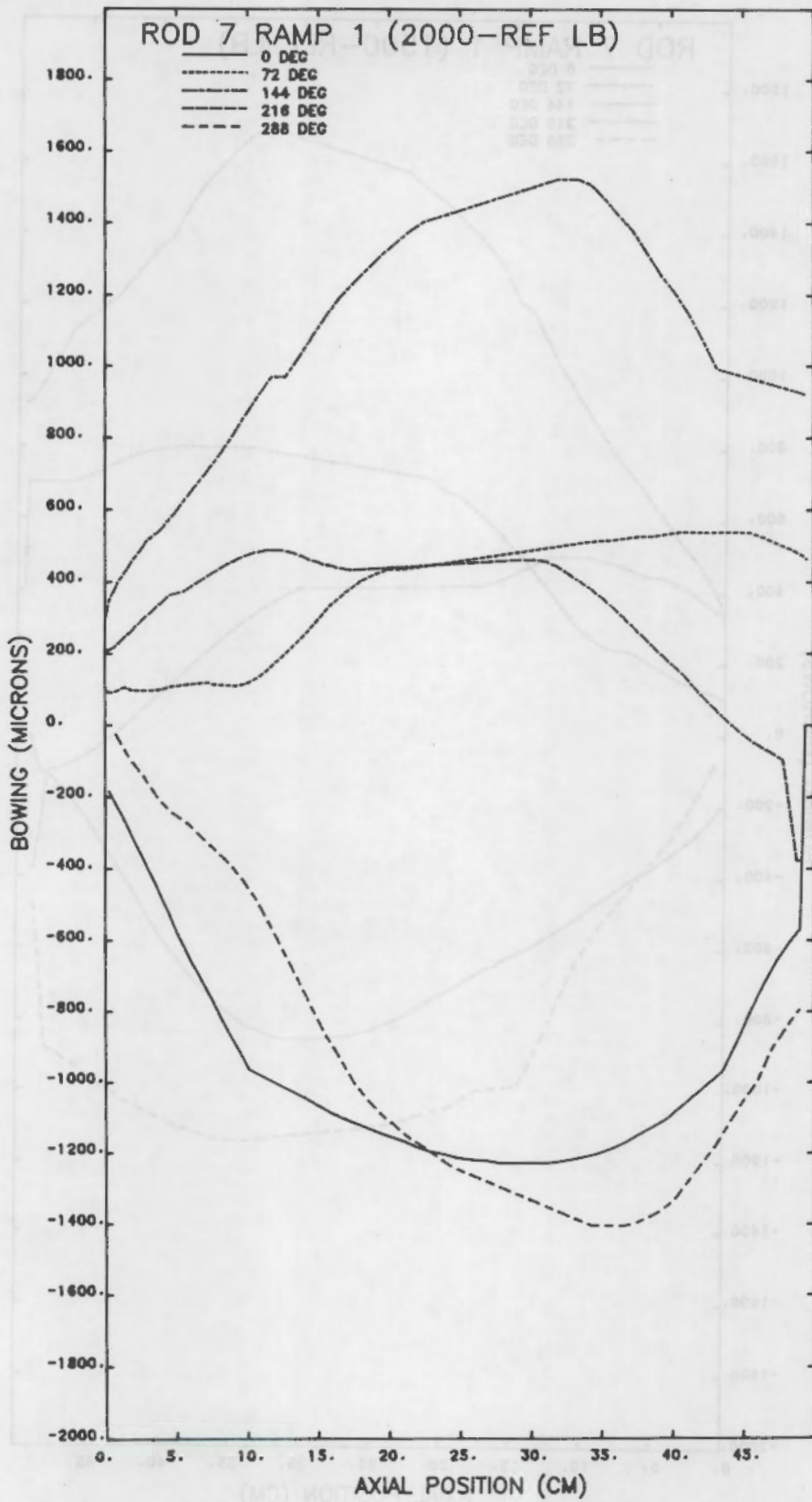
FIGURE E.4. Rod 7 Bowing: Ramp 1, 2000 lb load

E.4
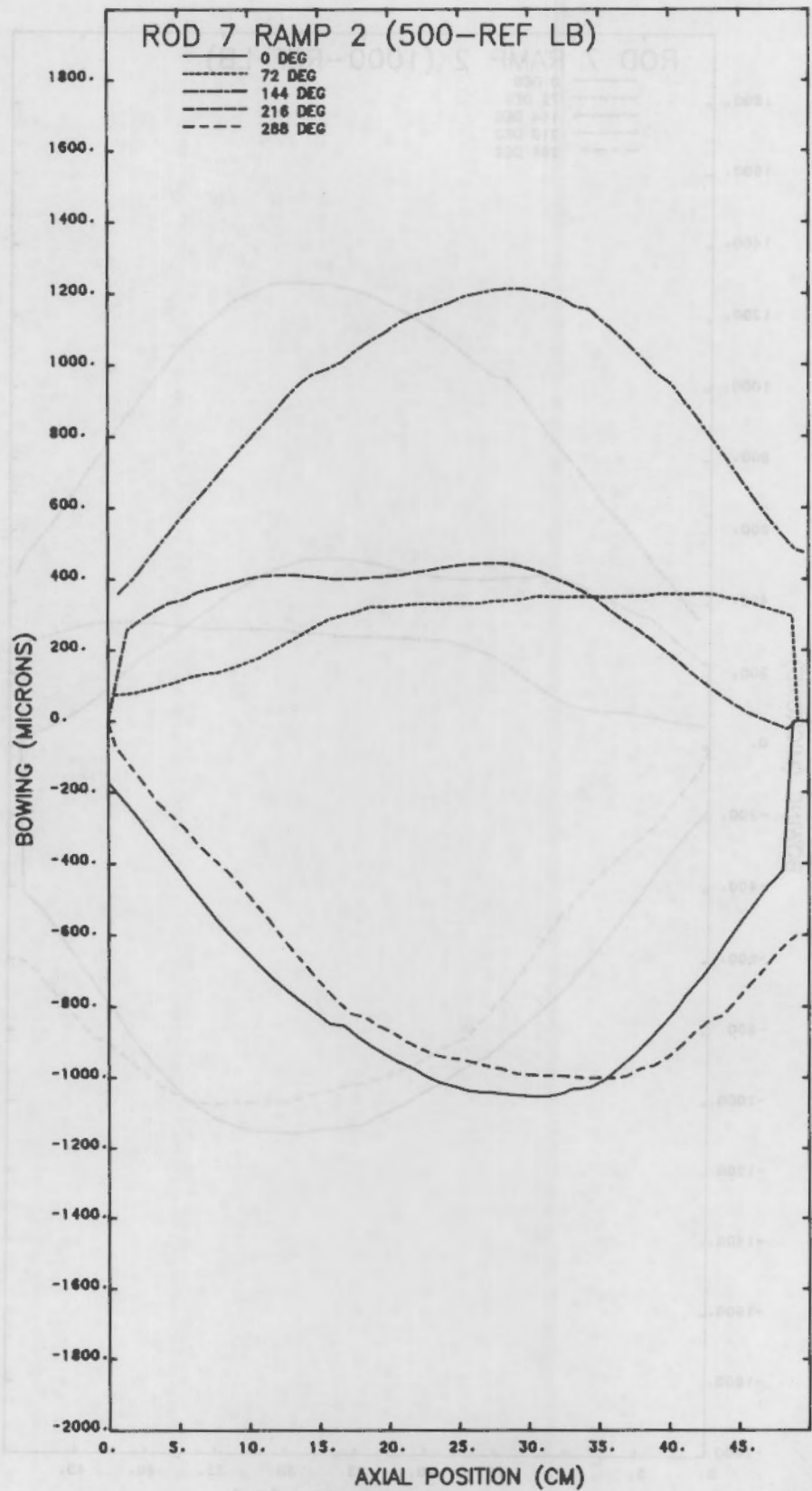
FIGURE E.5. Rod 7 Bowing: Ramp 2, 500 lb load

E.5
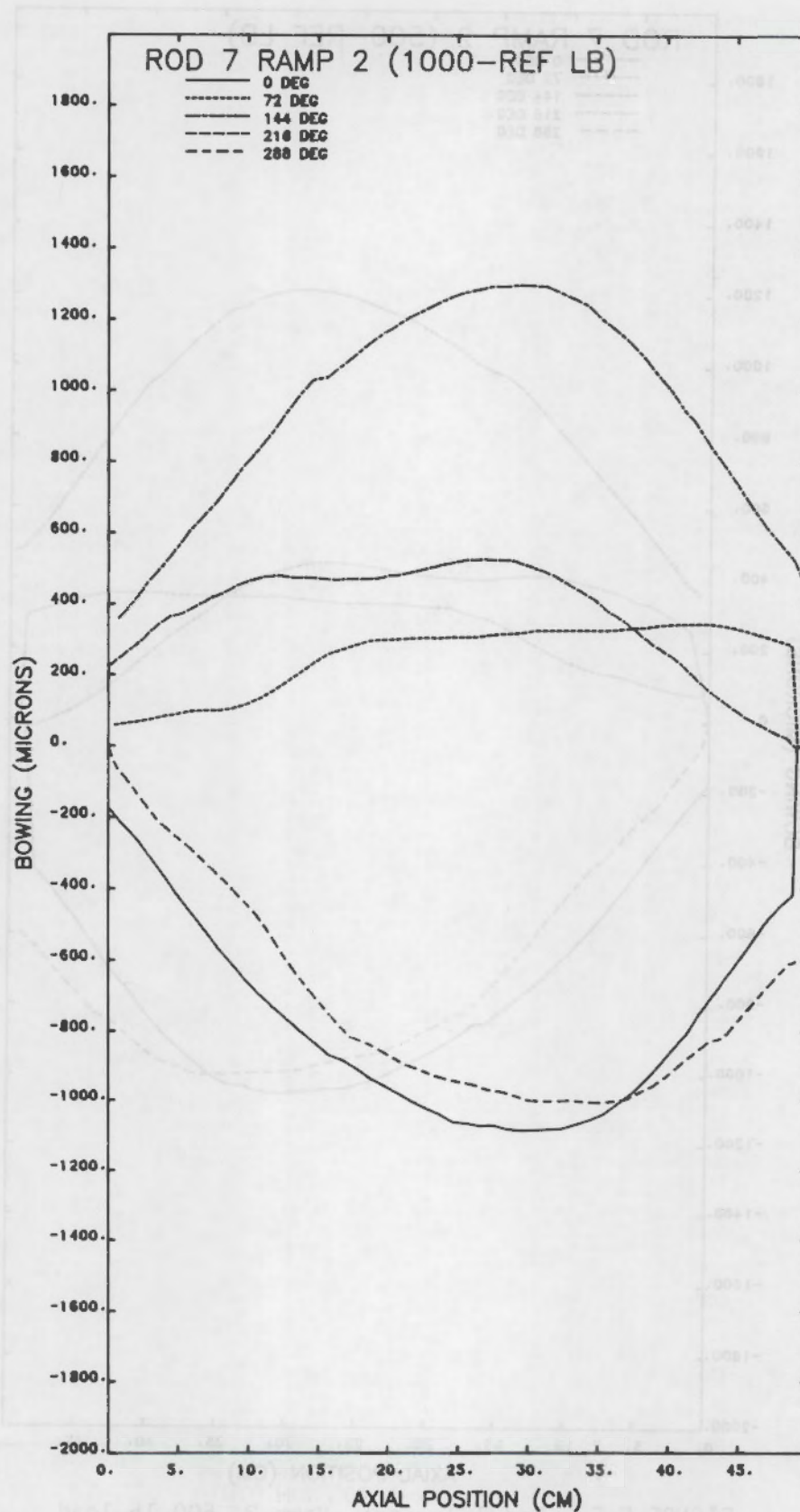
FIGURE E.6. Rod 7 Bowing: Ramp 2, 1000 lb load

E.6
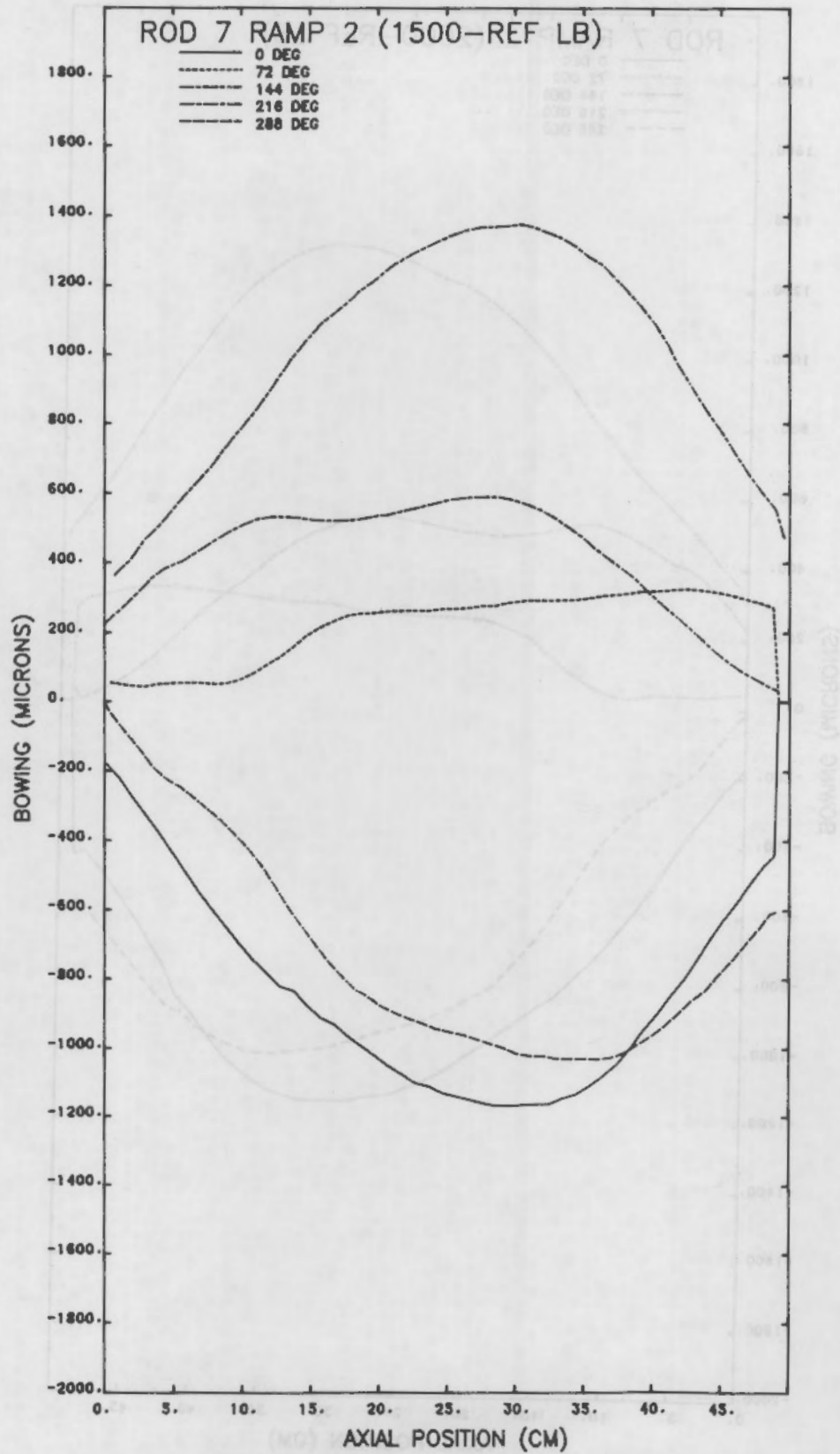
FIGURE E.7. Rod 7 Bowing: Ramp 2, 1500 lb load

E.7
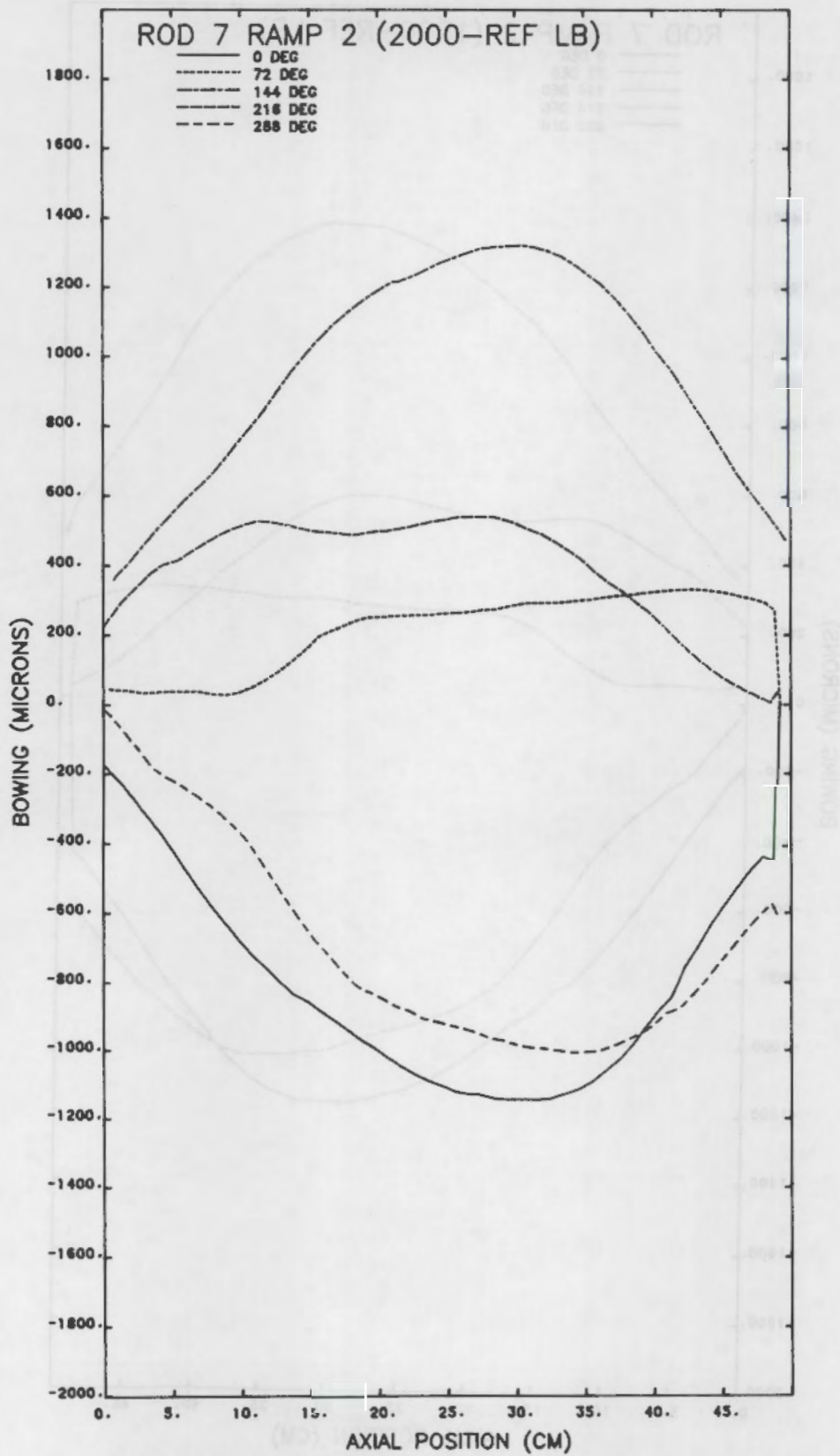
FIGURE E.8. Rod 7 Bowing: Ramp 2, 2000 lb load

E.8
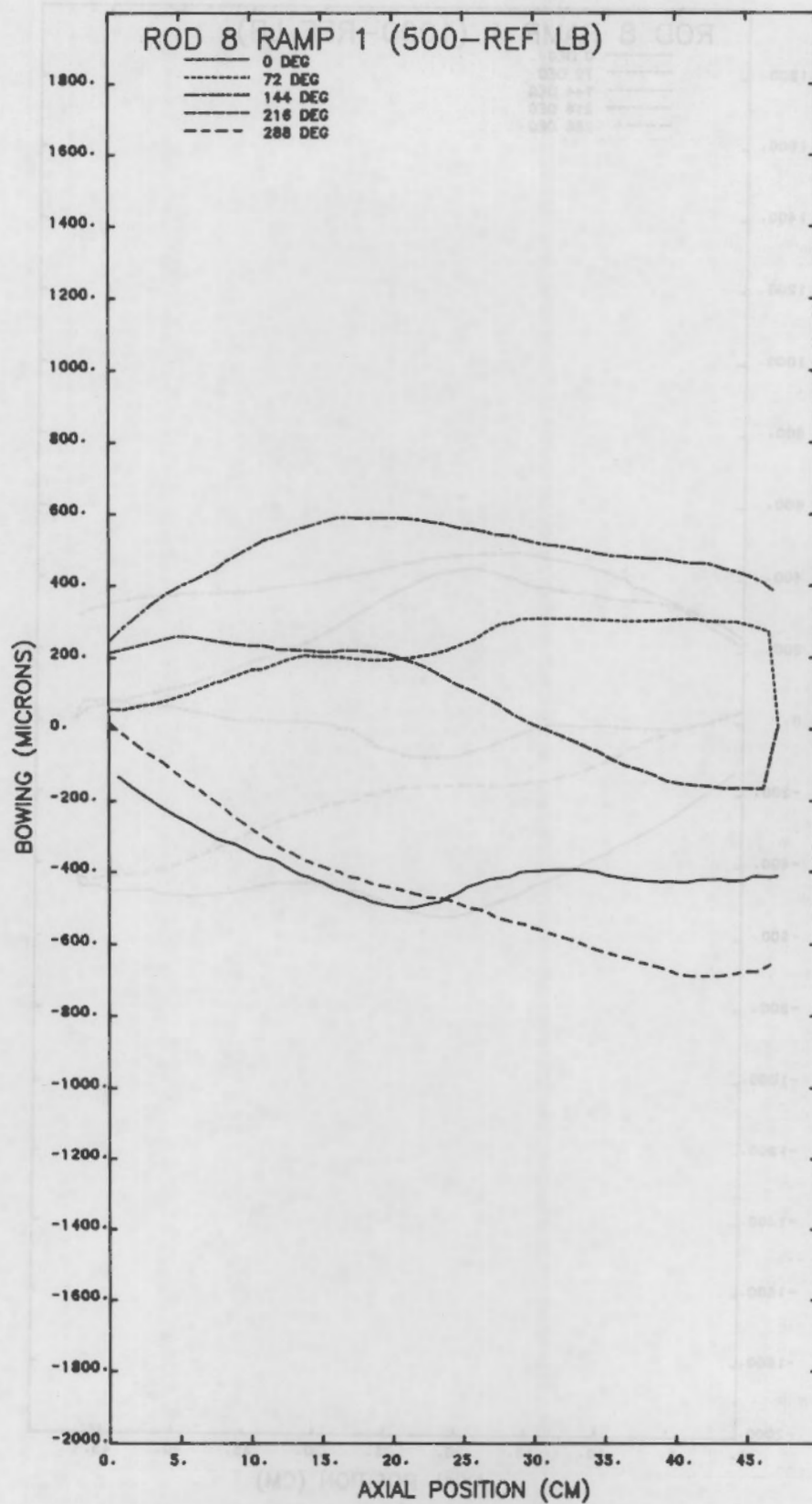
FIGURE E.9. Rod 8 Bowing: Ramp 1, 500 lb load

E.9
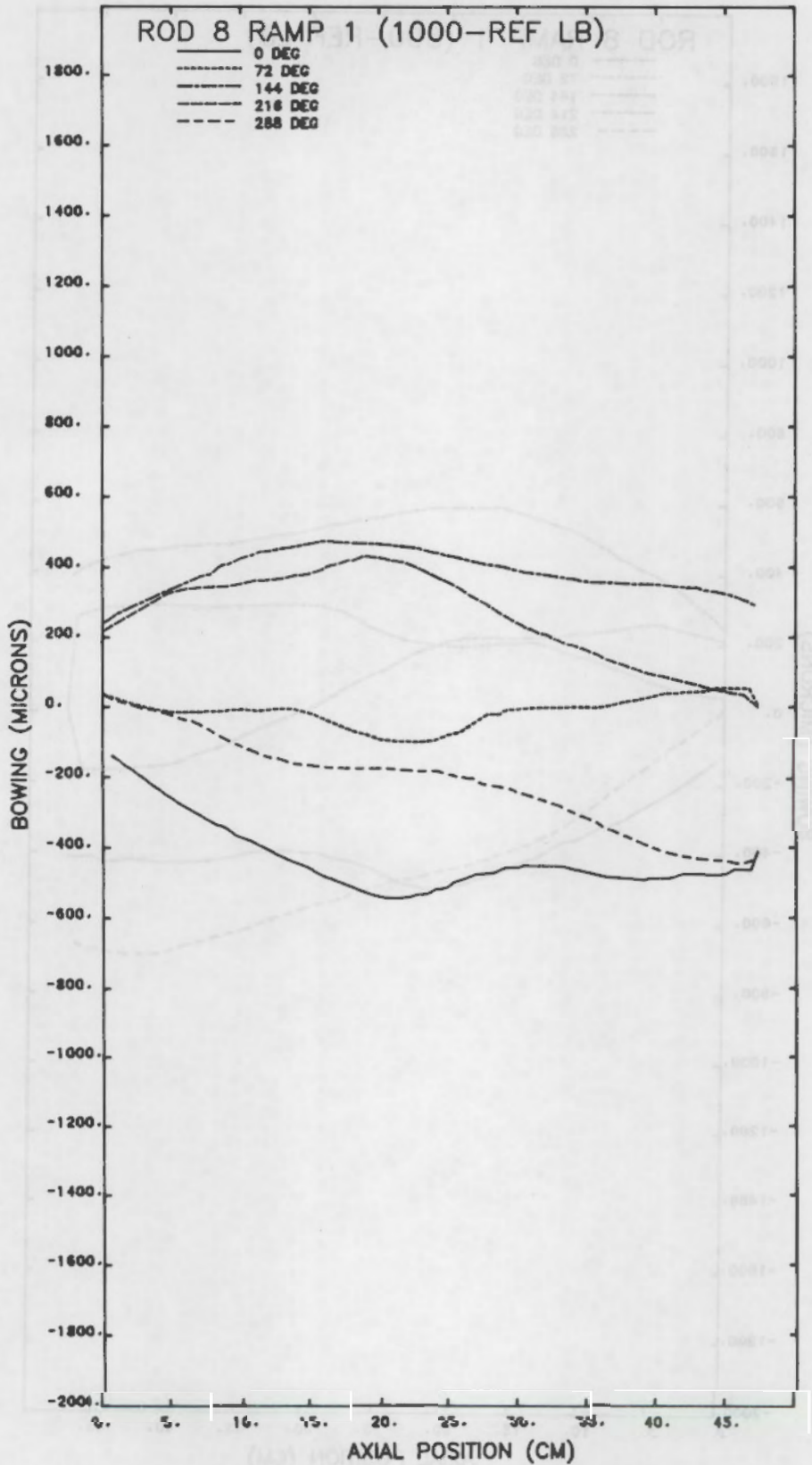
FIGURE E.10. Rod 8 Bowing: Ramp 1, 1000 lb load

E.10
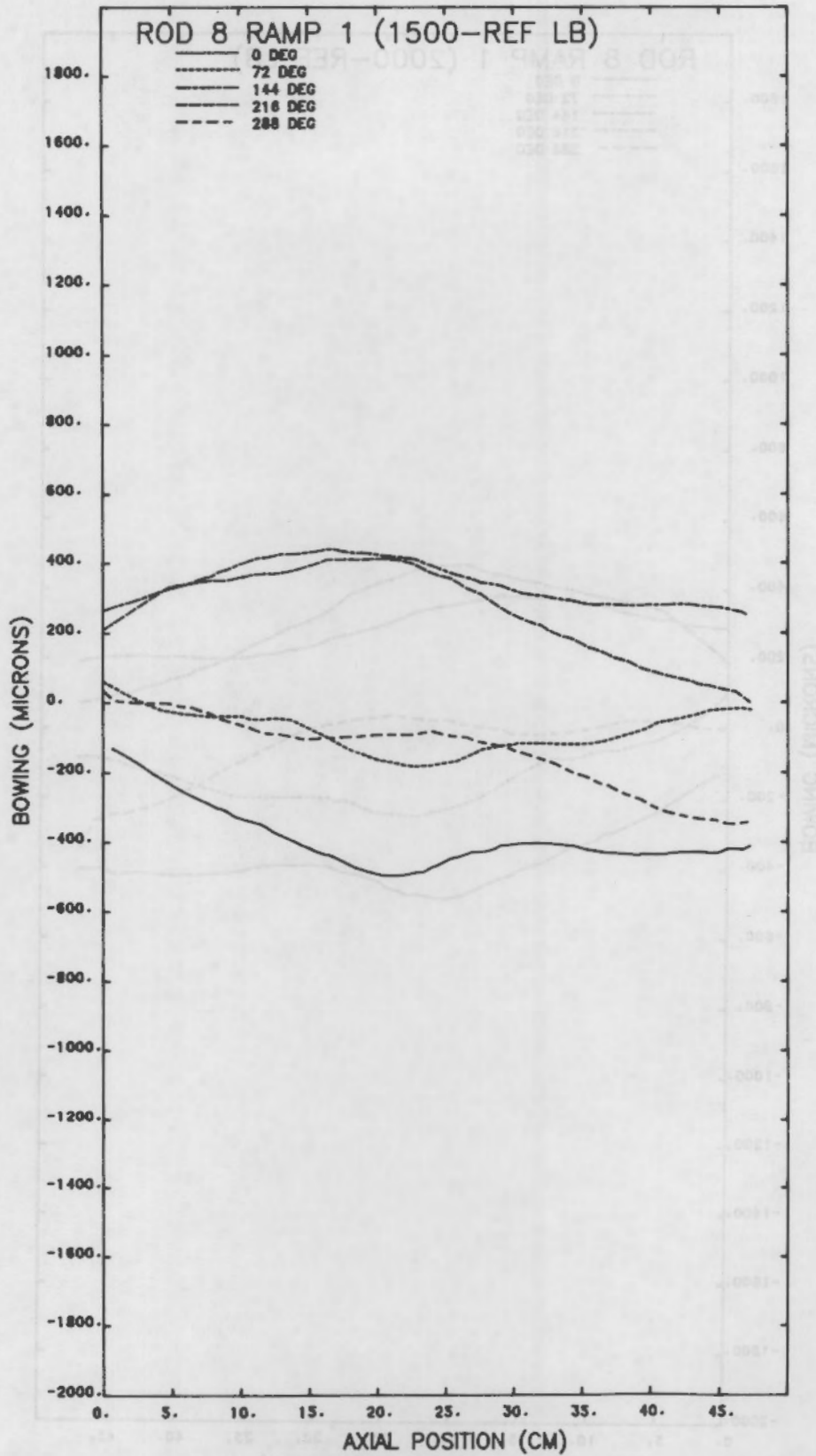
FIGURE E.11. Rod 8 Bowing: Ramp 1, 1500 lb load

E.11
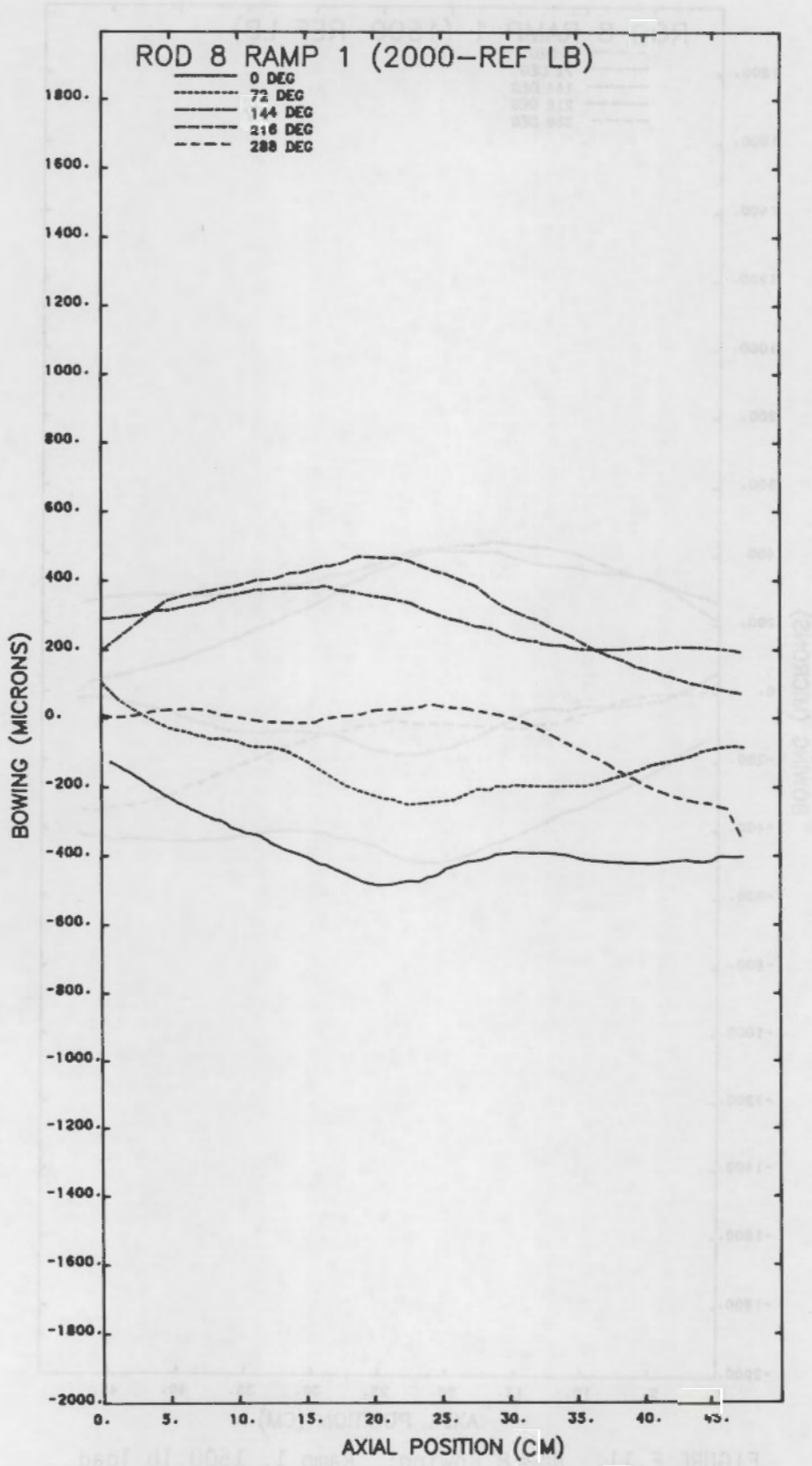
FIGURE E.12. Rod 8 Bowing: Ramp 1, 2000 lb load

E.12
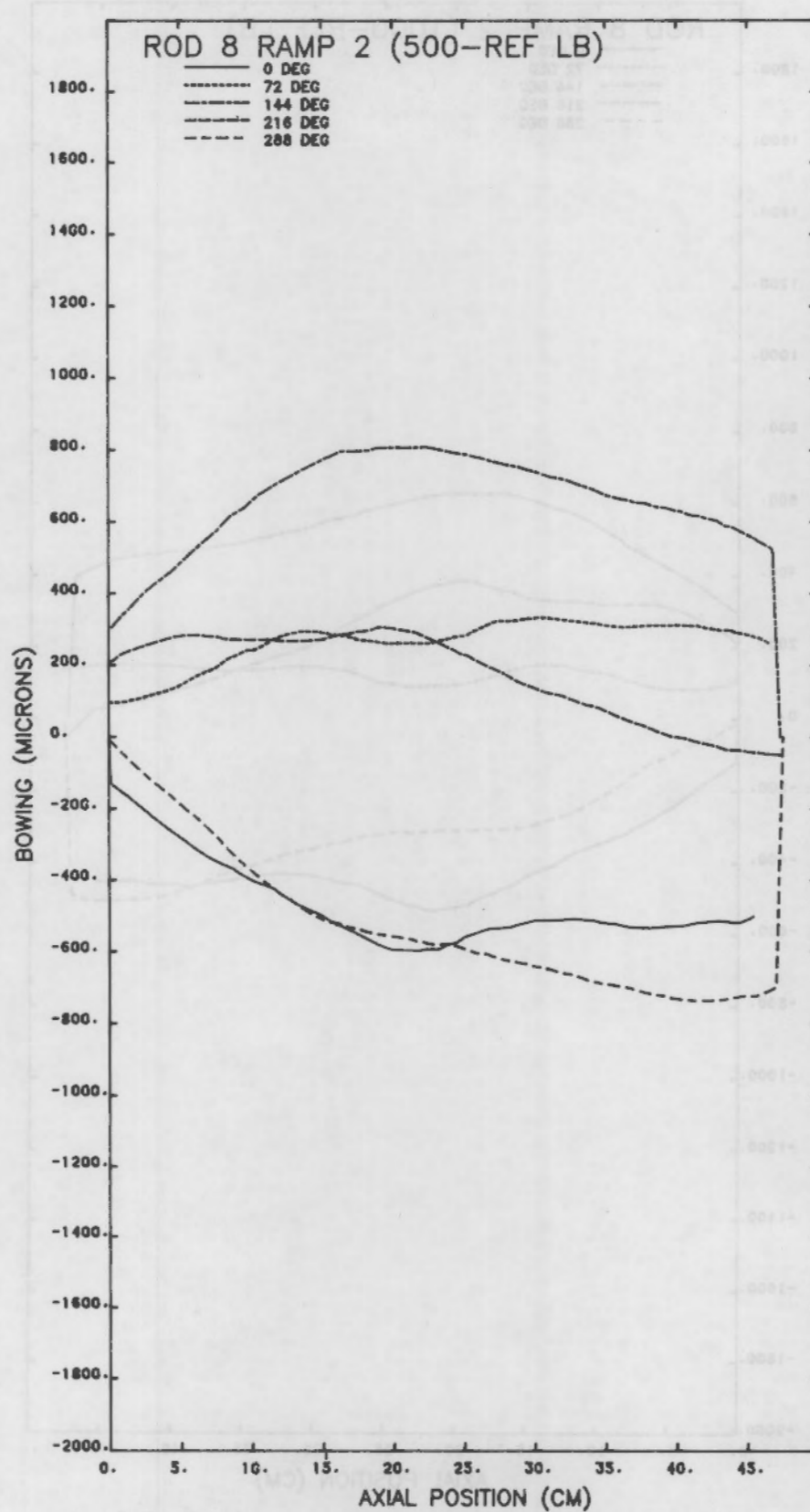
FIGURE E.13. Rod 8 Bowing: Ramp 2, 500 lb load

E.13
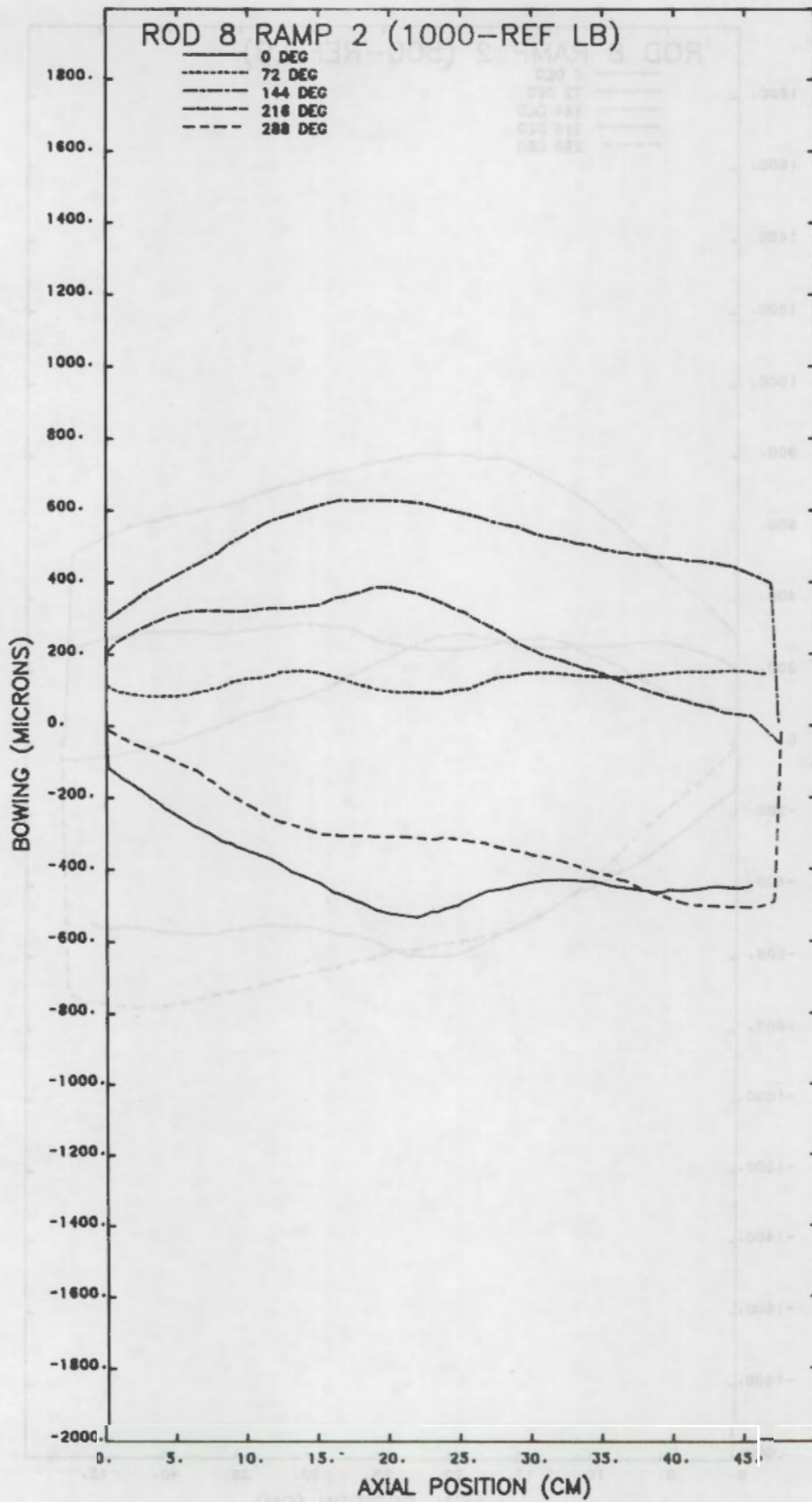
FIGURE E.14. Rod B Bowing: Ramp 2, 1000 lb load

E.14
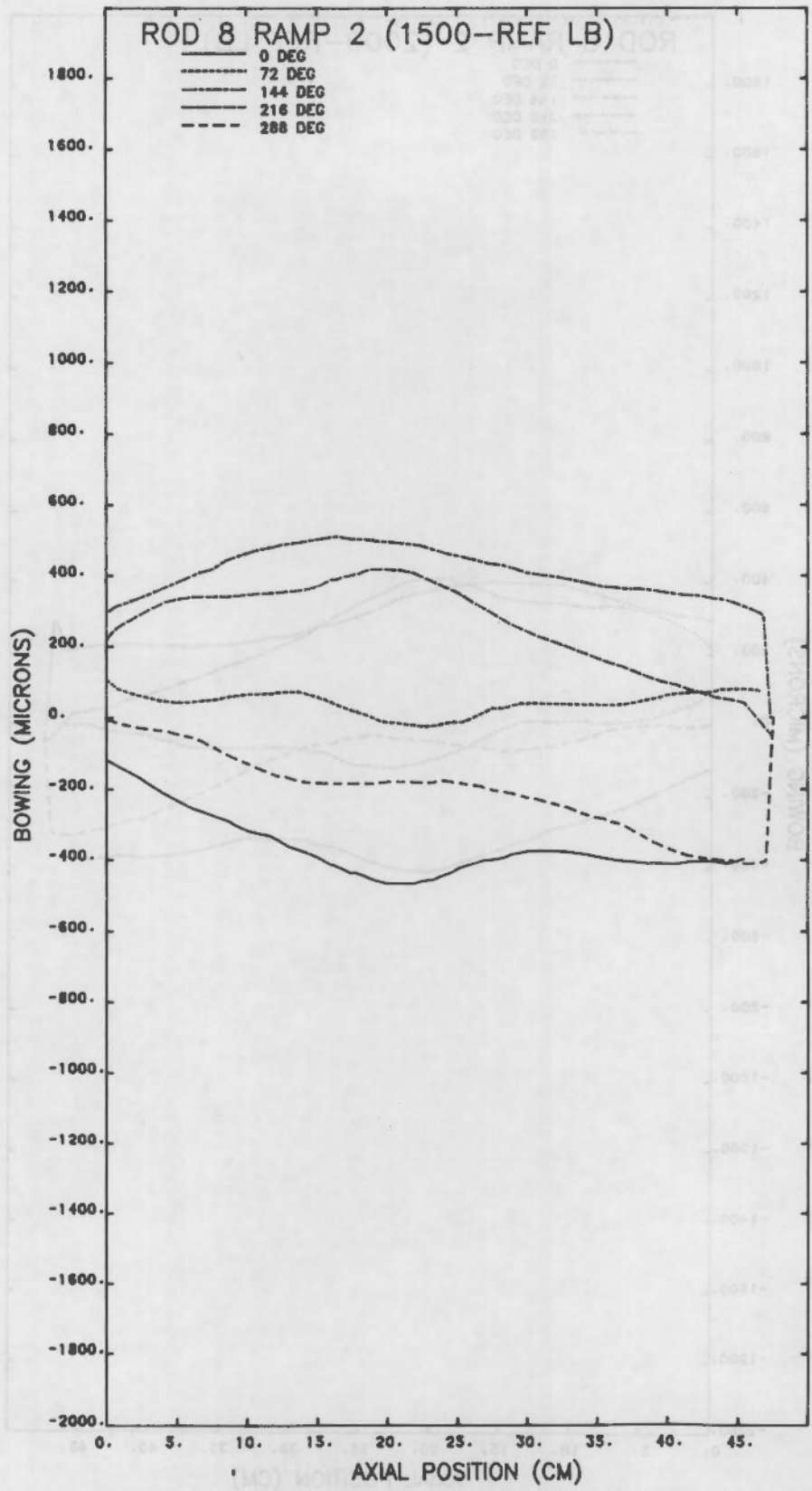
FIGURE E.15. Rod 8 Bowing: Ramp 2, 1500 lb load

E.15
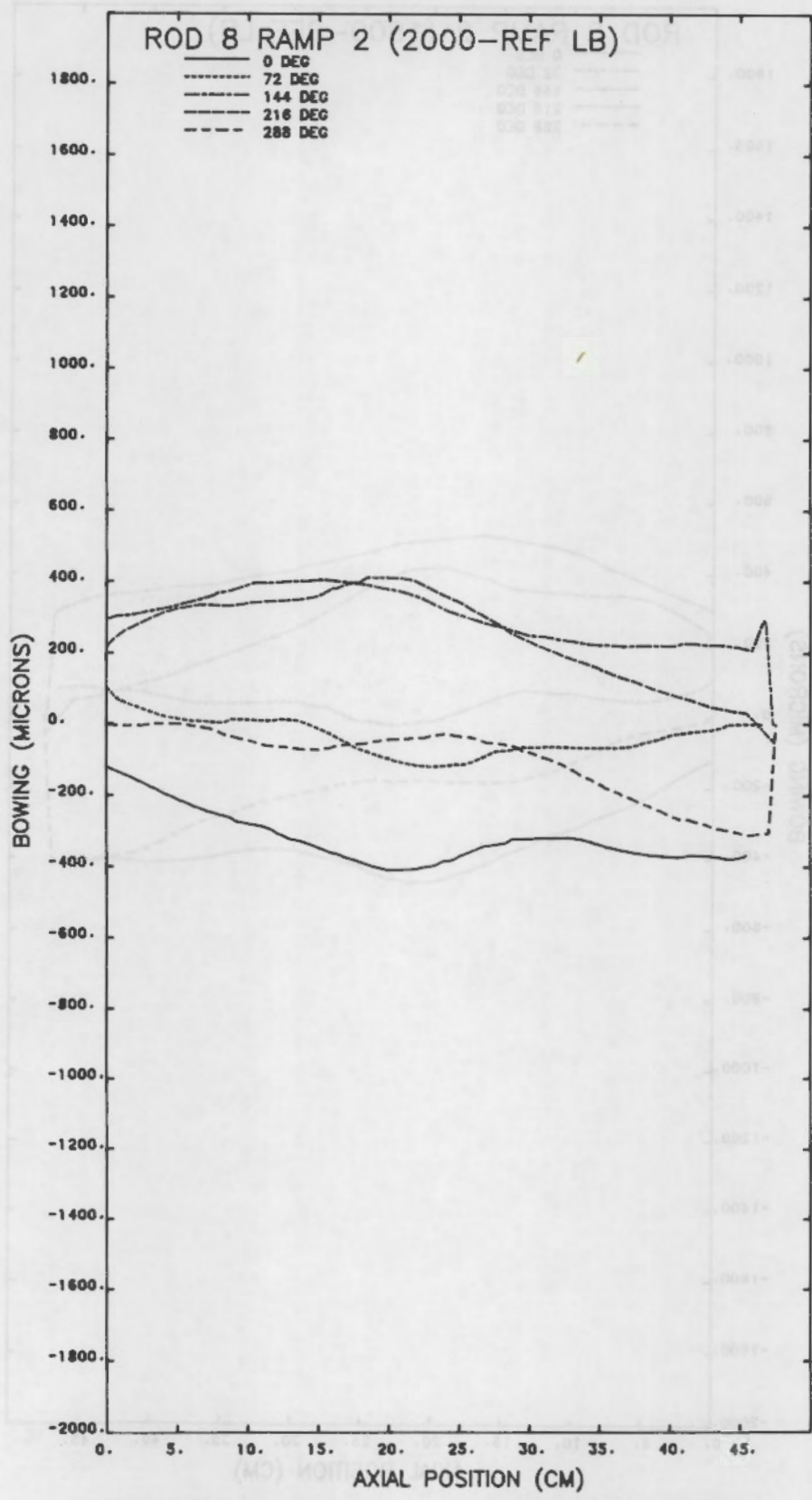
FIGURE E.16. Rod 8 Bowing: Ramp 2, 2000 lb load

E.16

DISTRIBUTION

No. of
Copies

OFFSITE

315 U.S. Nuclear Regulatory
      Commission
    Division of Technical Information
      and Document Control
    7920 Norfolk Avenue
    Bethesda, MD 20014

2   DOE Technical Information Center

4   Chief, Fuel Behavior Branch
    U.S. Nuclear Regulatory
      Commission
    Washington, DC 20555

    H. H. Scott
    Fuel Behavior Branch
    U.S. Nuclear Regulatory
      Commission
    Washington, DC 20555

No. of
Copies

ONSITE

40   Pacific Northwest Laboratory
    W. J. Bailey
    J. O. Barner
    C. E. Beyer
    E. R. Bradley
    M. E. Cunningham
    M. D. Freshley
    E. R. Gilbert
    R. L. Goodman
    R. J. Guenther
    C. R. Hann
    D. D. Lanning
    R. K. Marshall
    C. L. Mohr
    C. Nealley
    F. E. Panisko
    W. N. Rausch
    R. E. Williford (15)
    C. L. Wilson
    Publishing Coordination (2)
    Technical Information YO(5)

DISTRIBUTION

No. of Copies		No. of Copies	
	OFFSITE		ONSITE

OFFSITE

315 U.S. Nuclear Regulatory Commission
Division of Technical Information
and Document Control
7920 Norfolk Avenue
Bethesda, MD 20014

2 DOE Technical Information Center

4 Chief, Fuel Behavior Branch
U.S. Nuclear Regulatory Commission
Washington, DC 20555

H. H. Scott
Fuel Behavior Branch
U.S. Nuclear Regulatory Commission
Washington, DC 20555

ONSITE

40 Pacific Northwest Laboratory
K. J. Bailey
J. O. Barner
C. E. Beyer
E. R. Bradley
M. E. Cunningham
M. D. Freshley
E. R. Gilbert
R. L. Goodman
R. J. Guenther
C. R. Hann
D. D. Lanning
R. K. Marshall
C. L. Mohr
E. Nealley
F. E. Panisko
W. N. Rausch
R. E. Williford (15)
C. L. Wilson
Publishing Coordination (2)
Technical Information YO(5)

NRC FORM 335 (11-81)	U.S. NUCLEAR REGULATORY COMMISSION BIBLIOGRAPHIC DATA SHEET	1. REPORT NUMBER (Assigned by DDC) NUREG/CR-2872 PNL-4377	
4. TITLE AND SUBTITLE (Add Volume No., if appropriate) Experimental Verification of a Cracked Fuel Mechanical Model		2. (Leave blank)	
		3. RECIPIENT'S ACCESSION NO.	
7. AUTHOR(S) R. E. Williford		5. DATE REPORT COMPLETED	
		MONTH November	YEAR 1982
9. PERFORMING ORGANIZATION NAME AND MAILING ADDRESS (Include Zip Code) Pacific Northwest Laboratory P O Box 999 Richland WA 99352		DATE REPORT ISSUED	
		MONTH December	YEAR 1982
		6. (Leave blank)	
		8. (Leave blank)	
12. SPONSORING ORGANIZATION NAME AND MAILING ADDRESS (Include Zip Code) Division of Accident Evaluation Office of Nuclear Regulatory Research U.S. Nuclear Regulatory Commission Washington, D.C. 20555		10. PROJECT/TASK/WORK UNIT NO. TASK C2	
		11. FIN NO. B2043	
13. TYPE OF REPORT Topical	PERIOD COVERED (Inclusive dates)		
15. SUPPLEMENTARY NOTES		14. (Leave blank)	

16. ABSTRACT (200 words or less)

The report describes the results of a series of laboratory experiments conducted to independently verify a model that describes the rod average nonlinear mechanical behavior of cracked fuel under normal operating conditions. The analytical model is briefly described, and each experiment is discussed in detail. The experiments were conducted to verify the general behavior and numerical values for the three primary independent modeling parameters (effective crack roughness, effective gap roughness, and total crack length) and to verify the model predictions that the effective Young's moduli for cracked fuel systems were substantially less than those for solid pellets. The model parameters and predictions were confirmed, and new insight was gained concerning the complexities of cracked fuel mechanics.

17. KEY WORDS AND DOCUMENT ANALYSIS   17a. DESCRIPTORS

Zircaloy Cladding
Out-of-pile Experiment
Mechanical Interaction

Fuel Pellets
Effective Youngs Moduli
Crack Roughness

17b. IDENTIFIERS/OPEN-ENDED TERMS

18. AVAILABILITY STATEMENT Unlimited	19. SECURITY CLASS (This report) Unclassified	21. NO. OF PAGES
	20. SECURITY CLASS (This page) Unclassified	22. PRICE S

16. ABSTRACT (200 words or less)

The report describes the results of a series of laboratory experiments
conducted to independently verify a model that describes the rod
average nonlinear mechanical behavior of cracked fuel under normal
operating conditions. The analytical model is briefly described, and
each experiment is discussed in detail. The experiments were conducted
to verify the general behavior and numerical values for the three
primary independent modeling parameters (effective crack roughness,
effective gap roughness, and total crack length) and to verify the
model predictions that the effective Young's modulus for cracked fuel
systems were substantially less than those for solid pellets.
The model parameters and predictions were confirmed, and new insight
was gained concerning the complexities of cracked fuel mechanics.

17. KEY WORDS AND DOCUMENT ANALYSIS   17a. DESCRIPTORS

Zircaloy Cladding   Fuel Pellets
Out-of-pile Experiment   Effective Young's Moduli
Mechanical Interaction   Crack Roughness

17b. IDENTIFIERS/OPEN-ENDED TERMS

18. AVAILABILITY STATEMENT   19. SECURITY CLASS (This report)   21. NO. OF PAGES
Unlimited   Unclassified

                                             20. SECURITY CLASS (This page)   22. PRICE
                                                 Unclassified